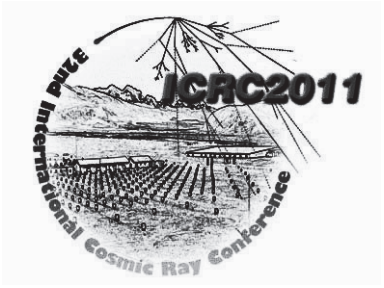
32ND INTERNATIONAL COSMIC RAY CONFERENCE, BEIJING 2011



arXiv:1204.5065v1 [astro-ph.IM] 23 Apr 2012

The JEM-EUSO Mission: Status and Prospects in 2011

THE JEM-EUSO COLLABORATION

Abstract: Contributions of the JEM-EUSO Collaboration to the 32nd International Cosmic Ray Conference, Beijing, August, 2011.

Keywords: JEM-EUSO, UHE Cosmic Rays, air showers, fluorescence technique, space observations

The Collaboration:
J.H. Adams Jr.[md], S. Ahmad[ba], J.-N. Albert[ba], D. Allard[bb], M. Ambrosio[df], L. Anchordoqui[me], A. Anzalone[dh], Y. Arai[eu], C. Aramo[df], K. Asano[es], P. Barrillon[ba], T. Batsch[hc], J. Bayer[cd], T. Belenguer[kb], R. Bellotti[db], A.A. Berlind[mg], M. Bertaina[dl,dk], P.L. Biermann[cb], S. Biktemerova[ia], C. Blaksley[bb], J. Błęcki[he], S. Blin-Bondil[ba], J. Blümer[cb], P. Bobik[ja], M. Bogomilov[aa], M. Bonamente[md], M.S. Briggs[md], S. Briz[ke], A. Bruno[da], F. Cafagna[da], D. Campana[df], J-N. Capdevielle[bb], R. Caruso[dc], M. Casolino[ev,di,dj], C. Cassardo[dl,dk], G. Castellini[dd] O. Catalano[dh], A. Cellino[dm,dk], M. Chikawa[ed], M.J. Christl[mf], V. Connaughton[md], J.F. Cortés[ke], H.J. Crawford[ma], R. Cremonini[dl], S. Csorna[mg], J.C. D'Olivo[ga], S. Dagoret-Campagne[ba], A.J. de Castro[ke], C. De Donato[di,dj], C. de la Taille[ba], M.P. De Pascale[di,dj], L. del Peral[kd], A. Dell'Oro[dm,dk] M. Di Martino[dm,dk], G. Distratis[cd], M. Dupieux[bc], A. Ebersoldt[cb], T. Ebisuzaki[ev], R. Engel[cb], S. Falk[cb], K. Fang[mb], F. Fenu[cd], S. Ferrarese[dl,dk], I. Fernández-Gómez[ke], A. Franceschi[de], J. Fujimoto[eu], P. Galeotti[dl,dk], G. Garipov[ic], J. Geary[md], U.G. Giaccari[df], G. Giraudo[dk], M. Gonchar[ia], C. González Alvarado[kb], P. Gorodetzky[bb], F. Guarino[df,dg], A. Guzmán[cd], Y. Hachisu[ev], B. Harlov[ib], A. Haungs[cb], J. Hernández Carretero[kd], K. Higashide[eq,ev], T. Iguchi [ei], H. Ikeda[eo], N. Inoue[eq], S. Inoue[et], A. Insolia[dc], F. Isgrò[df,dg], Y. Itow[en], E. Joven[kf], E.G. Judd[ma], A. Jung[fc], F. Kajino[ei], T. Kajino[el], I. Kaneko[ev], Y. Karadzhov[aa], J. Karczmarczyk[hc], K. Katahira[ev], K. Kawai[ev], Y. Kawasaki[ev], B. Keilhauer[cb], B.A. Khrenov[ic], Jeong-Sook Kim[fb], Soon-Wook Kim[fb], Sug-Whan Kim[fd], M. Kleifges[cb], P.A. Klimov[ic], S.H. Ko[fa], D. Kolev[aa], I. Kreykenbohm[ca], K. Kudela[ja], Y. Kurihara[eu], E. Kuznetsov[md], G. La Rosa[dh], J. Lee[fc], J. Licandro[kf], H. Lim[fc], F. López[ke], M.C. Maccarone[dh], L. Marcelli[di,dj], A. Marini[de], G. Martin-Chassard[ba], O. Martinez[gc], G. Masciantonio[di,dj], K. Mase[ea], R. Matev[aa], A. Maurissen[la], G. Medina-Tanco[ga], T. Mernik[cd], H. Miyamoto[ev], Y. Miyazaki[ec], Y. Mizumoto[el], G. Modestino[de], D. Monnier-Ragaigne[ba], J.A. Morales de los Ríos[kd], B. Mot[bc], T. Murakami[ef], M. Nagano[ec], M. Nagata[eh], S. Nagataki[ek], J.W. Nam[fc], S. Nam[fc], K. Nam[fc], T. Napolitano[de], D. Naumov[ia], A. Neronov[lb], K. Nomoto[et], T. Ogawa[ev], H. Ohmori[ev], A.V. Olinto[mb], P. Orleański[he], G. Osteria[df], N. Pacheco[kc], M.I. Panasyuk[ic], E. Parizot[bb], I.H. Park[fc], B. Pastircak[ja], T. Patzak[bb], T. Paul[me], C. Pennypacker[ma], T. Peter[lc], P. Picozza[di,dj,ev], A. Pollini[la], H. Prieto[kd,ka], P. Reardon[md], M. Reina[kb], M. Reyes[kf], M. Ricci[de], I. Rodríguez[ke], M.D. Rodríguez Frías[kd], F. Ronga[de], H. Rothkaehl[he], G. Roudil[bc], I. Rusinov[aa], M. Rybczyński[ha], M.D. Sabau[kb], G. Sáez Cano[kd], A. Saito[ej], N. Sakaki[cb], M. Sakata[ei], H. Salazar[gc], S. Sánchez[ke], A. Santangelo[cd], L. Santiago Crúz[ga], M. Sanz Palomino[kb], O. Saprykin[ib], F. Sarazin[mc], H. Sato[ei], M. Sato[er], T. Schanz[cd], H. Schieler[cb], V. Scotti[df,dg], M. Scuderi[dc], A. Segreto[dh], S. Selmane[bb], D. Semikoz[bb], M. Serra[kf], S. Sharakin[ic], T. Shibata[ep], H.M. Shimizu[em], K. Shinozaki[ev], T. Shirahama[eq], G. Siemieniec-Oziębło[hb], H.H. Silva López[ga], J. Sledd[mf], K. Słomińska[he], A. Sobey[mf], T. Sugiyama[em], D. Supanitsky[ga], M. Suzuki[eo], B. Szabelska[hc], J. Szabelski[hc], F. Tajima[ee], N. Tajima[ev], T. Tajima[cc], H. Takami[eu], T. Nakamura[ej], M. Takeda[eg], Y. Takahashi[er], Y. Takizawa[ev], C. Tenzer[cd], L. Tkachev[ia], T. Tomida[ev], N. Tone[ev], F. Trillaud[ga], R. Tsenov[aa], K. Tsuno[ev], T. Tymieniecka[hd], Y. Uchihori[eb], O. Vaduvescu[kf], J.F. Valdés-Galicia[ga], P. Vallania[dm,dk], L. Valore[df], G. Vankova[aa], C. Vigorito[dl,dk], L. Villaseñor[gb], P. von Ballmoos[bc], S. Wada[ev], J. Watanabe[el], S. Watanabe[er], J. Watts Jr.[md], M. Weber[cb], T.J. Weiler[mg], T. Wibig[hc], L. Wiencke[mc], M. Wille[ca], J. Wilms[ca], Z. Włodarczyk[ha], T. Yamamoto[ei], Y. Yamamoto[ei], J. Yang[fc], H. Yano[eo], I.V. Yashin[ic], D. Yonetoku[ef], K. Yoshida[ei], S. Yoshida[ea], R. Young[mf], A. Zamora[ga], A. Zuccaro Marchi[ev]

[aa] St. Kliment Ohridski University of Sofia, Bulgaria
[ba] Laboratoire de l'Accélérateur Linéaire, Univ Paris Sud-11, CNES/IN2P3, Orsay, France
[bb] APC, Univ Paris Diderot, CNRS/IN2P3, CEA/Irfu, Obs de Paris, Sorbonne Paris Cité, France
[bc] IRAP, Université de Toulouse, CNRS, Toulouse, France
[ca] ECAP, University of Erlangen-Nuremberg, Germany
[cb] Karlsruhe Institute of Technology (KIT), Germany
[cc] Ludwig Maximilian University, Munich, Germany
[cd] Institute for Astronomy and Astrophysics, Kepler Center, University of Tübingen, Germany
[da] Istituto Nazionale di Fisica Nucleare - Sezione di Bari, Italy
[db] Universita'degli Studi di Bari Aldo Moro and INFN - Sezione di Bari, Italy
[dc] Dipartimento di Fisica e Astronomia - Universita' di Catania, Italy
[dd] Consiglio Nazionale delle Ricerche - Istituto Nazionale di Ottica Firenze, Italy
[de] Istituto Nazionale di Fisica Nucleare - Laboratori Nazionali di Frascati, Italy
[df] Istituto Nazionale di Fisica Nucleare - Sezione di Napoli, Italy
[dg] Universita' di Napoli Federico II - Dipartimento di Scienze Fisiche, Italy
[dh] INAF - Istituto di Astrofisica Spaziale e Fisica Cosmica di Palermo, Italy
[di] Istituto Nazionale di Fisica Nucleare - Sezione di Roma Tor Vergata, Italy
[dj] Universita' di Roma Tor Vergata - Dipartimento di Fisica, Roma, Italy
[dk] Istituto Nazionale di Fisica Nucleare - Sezione di Torino, Italy
[dl] Dipartimento di Fisica, Universita' di Torino, Italy

[dm] Osservatorio Astrofisico di Torino, Istituto Nazionale di Astrofisica, Italy
[ea] Chiba University, Chiba, Japan
[eb] National Institute of Radiological Sciences, Chiba, Japan
[ec] Fukui University of Technology, Fukui, Japan
[ed] Kinki University, Higashi-Osaka, Japan
[ee] Hiroshima University, Hiroshima, Japan
[ef] Kanazawa University, Kanazawa, Japan
[eg] Institute for Cosmic Ray Research, University of Tokyo, Kashiwa, Japan
[eh] Kobe University, Kobe, Japan
[ei] Konan University, Kobe, Japan
[ej] Kyoto University, Kyoto, Japan
[ek] Yukawa Institute, Kyoto University, Kyoto, Japan
[el] National Astronomical Observatory, Mitaka, Japan
[em] Nagoya University, Nagoya, Japan
[en] Solar-Terrestrial Environment Laboratory, Nagoya University, Nagoya, Japan
[eo] Institute of Space and Astronautical Science/JAXA, Sagamihara, Japan
[ep] Aoyama Gakuin University, Sagamihara, Japan
[eq] Saitama University, Saitama, Japan
[er] Hokkaido University, Sapporo, Japan
[es] Interactive Research Center of Science, Tokyo Institute of Technology, Tokyo, Japan
[et] University of Tokyo, Tokyo, Japan
[eu] High Energy Accelerator Research Organization (KEK), Tsukuba, Japan
[ev] RIKEN Advanced Science Institute, Wako, Japan
[fa] Korea Advanced Institute of Science and Technology (KAIST), Daejeon, Republic of Korea
[fb] Korea Astronomy and Space Science Institute (KASI), Daejeon, Republic of Korea
[fc] Ewha Womans University, Seoul, Republic of Korea
[fd] Center for Galaxy Evolution Research, Yonsei University, Seoul, Republic of Korea
[ga] Universidad Nacional Autónoma de México (UNAM), Mexico
[gb] Universidad Michoacana de San Nicolas de Hidalgo (UMSNH), Morelia, Mexico
[gc] Benemérita Universidad Autónoma de Puebla (BUAP), Mexico
[ha] Jan Kochanowski University, Institute of Physics, Kielce, Poland
[hb] Jagiellonian University, Astronomical Observatory, Krakow, Poland
[hc] National Centre for Nuclear Research, Lodz, Poland
[hd] Cardinal Stefan Wyszyński University in Warsaw, Poland
[he] Space Research Centre of the Polish Academy of Sciences (CBK), Warsaw, Poland
[ia] Joint Institute for Nuclear Research, Dubna, Russia
[ib] Central Research Institute of Machine Building, TsNIIMash, Korolev, Russia
[ic] Skobeltsyn Institute of Nuclear Physics, Lomonosov Moscow State University, Russia
[ja] Institute of Experimental Physics, Kosice, Slovakia
[ka] Consejo Superior de Investigaciones Científicas (CSIC), Madrid, Spain
[kb] Instituto Nacional de Técnica Aeroespacial (INTA), Madrid, Spain
[kc] Instituto de Física Teórica, Universidad Autónoma de Madrid, Spain
[kd] Universidad de Alcalá (UAH), Madrid, Spain
[ke] Universidad Carlos III de Madrid, Spain
[kf] Instituto de Astrofísico de Canarias (IAC), Tenerife, Spain
[la] Swiss Center for Electronics and Microtechnology (CSEM), Neuchâtel, Switzerland
[lb] ISDC Data Centre for Astrophysics, Versoix, Switzerland
[lc] Institute for Atmospheric and Climate Science, ETH Zürich, Switzerland
[ma] Space Science Laboratory, University of California, Berkeley, USA
[mb] University of Chicago, USA
[mc] Colorado School of Mines, Golden, USA
[md] University of Alabama in Huntsville, Huntsville, USA
[me] University of Wisconsin-Milwaukee, Milwaukee, USA
[mf] NASA - Marshall Space Flight Center, USA
[mg] Vanderbilt University, Nashville, USA

Contents

1.	page 7	The JEM-EUSO mission	T. Ebisuzaki	ID1628
2.	page 11	Science objectives of the JEM-EUSO mission	G.A. Medina-Tanco	ID0956
3.	page 15	Overview of the JEM-EUSO Instruments	F. Kajino	ID1216
4.	page 19	Requirements and Expected Performances of the JEM-EUSO mission	A. Santangelo	ID0991
5.	page 23	The potential of the JEM-EUSO telescope for the astrophysics of extreme energy photons	G. Medina Tanco	ID0930
6.	page 27	Neutrino astrophysics with JEM-EUSO	G. Medina Tanco	ID0958
7.	page 31	The Focal Surface Detector of the JEM-EUSO Telescope	Y. Kawasaki	ID0472
8.	page 35	The JEM-EUSO Focal Surface Mechanical Structure	M. Ricci	ID0335
9.	page 39	SPACIROC: A Front-End Readout ASIC for spatial cosmic ray observatory	S. Ahmad	ID0236
10.	page 43	Performance of a front-end ASIC for JEM-EUSO	H. Miyamoto	ID0775
11.	page 47	High Voltage system for the JEM-EUSO Photomultipliers	J. Szabelski	ID0216
12.	page 51	The Cluster Control Board of the JEM-EUSO mission	J. Bayer	ID0836
13.	page 55	The Housekeeping subsystem of the JEM-EUSO instrument	G. Medina Tanco	ID0961
14.	page 59	Data Acquisition System of the JEM-EUSO project	M. Casolino	ID1219
15.	page 63	The Development of Photo-Detector Module Electronics for the JEM-EUSO Experiment	I. Park	ID1246
16.	page 67	The JEM-EUSO time synchronization system	G. Osteria	ID1131
17.	page 71	Technological developments in Russia for the JEM-EUSO mission	B. Khrenov	ID1261
18.	page 75	Calibration of JEM-EUSO photodetectors	P. Gorodetzky	ID0218
19.	page 79	The JEM-EUSO optics design	A. Zuccaro Marchi	ID0852
20.	page 83	JEM-EUSO lens manufacturing	Y. Takizawa	ID0874
21.	page 87	Testing of Large Diameter Fresnel Optics for Space Based Observations of Extensive Air Showers	J. Adams	ID1100

22.	page 91	Atmospheric Monitoring System of JEM-EUSO	A. Neronov	ID0301
23.	page 95	The IR-Camera of the JEM-EUSO (JAXA) Space Observatory	J.A. Morales	ID1031
24.	page 99	Cloud Coverage and its Implications for Cosmic Ray Observation from Space	M. Bertaina	ID0398
25.	page 103	A Comparison of Different Cloud Detection Methods for the JEM-EUSO Atmospheric Monitoring System	A. Anzalone	ID1152
26.	page 107	Estimation of JEM-EUSO experiment duty cycle based on Universitetsky Tatiana measurements	P. Bobik	ID0886
27.	page 111	ESAF Simulation of Ultra-High Energy Cosmic Rays in cloudy conditions for the JEM-EUSO (JAXA) Space Observatory	G. Saez Cano	ID1034
28.	page 115	The ESAF Simulation Framework for the JEM-EUSO mission	F. Fenu	ID0829
29.	page 119	The ESAF reconstruction framework for the JEM-EUSO mission	F. Fenu	ID0633
30.	page 123	Simulation framework of STM code for development of JEM-EUSO instrument	K. Higashide	ID1240
31.	page 127	Estimation of effective aperture for extreme energy cosmic rays by space-based JEM-EUSO Mission	K. Shinozaki	ID0979
32.	page 131	Very precise Fluorescence Yield measurement using a MeV electron beam	D. Ragaigne-Monnier	ID0212
33.	page 135	Fluorescence yield by electron in moist air and its application to the observation of ultra high energy cosmic rays from space	N. Sakaki	ID0520

The JEM-EUSO Mission

T. EBISUZAKI[1] FOR THE JEM-EUSO COLLABORATION
[1]*RIKEN Advanced Science Institute, 2-1 Hirosawa, Wako351-0198, Japan*

ebisu@postman.riken.jp

Abstract: The JEM-EUSO mission explores the origin of the extreme energy cosmic rays (EECRs) above 100 EeV and explores the limits of the fundamental physics, through the observations of their arrival directions and energies. It is designed to open a new particle astronomy channel. This super-wide-field (60 degrees) telescope with a diameter of about 2.5m looks down from space onto the night sky to detect near UV photons (330-400nm, both fluorescent and Cherenkov photons) emitted from the giant air showers produced by EECRs. The arrival direction map with more than five hundred events will tell us the origin of the EECRs and allow us to identify the nearest EECR sources with known astronomical objects. It will allow them to be examined in other astronomical channels. This is likely to lead to an understanding of the acceleration mechanisms perhaps producing discoveries in astrophysics and/or fundamental physics. The comparison of the energy spectra among the spatially resolved individual sources will help to clarify the acceleration/emission mechanism, and also finally confirm the Greisen-Zatsepin-Kuz'min process for the validation of Lorentz invariance up to $\gamma \sim 10^{11}$. Neutral components (neutrinos and gamma rays) can also be detected as well, if their fluxes are high enough. The JEM-EUSO mission is planned to be launched by a H2B rocket about JFY 2016 and transferred to ISS by H2 Transfer Vehicle (HTV). It will be attached to the Exposed Facility external experiment platform of "KIBO.".

Keywords: cosmic rays, neutrino, Lorentz invariance International Space Station.

1 Introduction

The "Extreme Universe Space Observatory - EUSO" is the first space mission devoted to the exploration of the Universe through the detection of the extreme energy (E >100 EeV) cosmic rays (EECRs) and neutrinos [1,2,3,4,5]; it looks downward from the International Space Station (ISS). It was first proposed as a free-flyer, but was selected by the European Space Agency (ESA) as a mission attached to the Columbus module of ISS. The phase-A study for the feasibility of that observatory (hereafter named ESA-EUSO) was successfully completed in July 2004. Nevertheless, because of financial problems in ESA and European countries, together with the logistic uncertainty caused by the Columbia accident, the start of the phase B had been pending. In 2006, Japanese and U.S. teams redefined the mission as an observatory attached to "KIBO," the Japanese Experiment Module (JEM) of ISS. They renamed it JEM-EUSO and started with a renewed phase-A study.

JEM-EUSO is designed to achieve our main scientific objective: astronomy and astrophysics through the particle channel to identify sources by arrival direction analysis and to measure the energy spectra from the individual sources, with an overwhelmingly high collecting power comparable to 1 million km^2 sr year..It will constrain acceleration or emission mechanisms, and also finally confirm the Greisen-Zatsepin-Kuz'min process [6] for the validation of Lorentz invariance up to $\gamma \sim 10^{11}$.

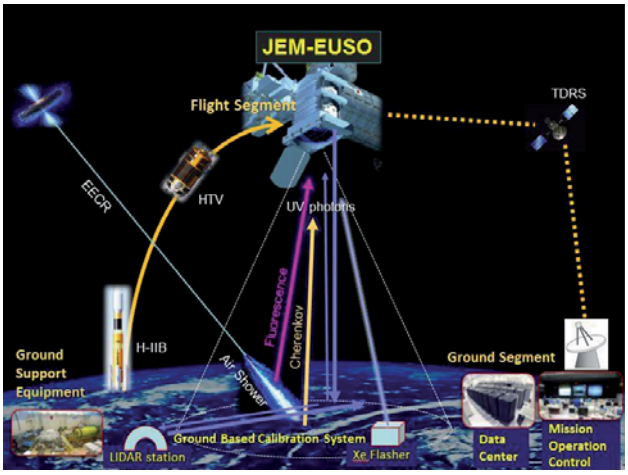


Figure 1. Principle of the JEM-EUSO telescope to detect Extreme Energy cosmic rays (EECRs).

2 Science Objectives

Science objectives of the JEM-EUSO mission are divided into one main objective and five exploratory objectives. The main objective of JEM-EUSO is to initiate a new field of astronomy that uses the extreme energy particle channel ($5x10^{19}$ eV < E < 10^{21} eV). JEM-EUSO has the critical exposure comparable to 1 million km^2 · sr · year to observe all the sources at least once inside several hundred Mpc and makes possible the followings:

- Identification of sources with the high statistics by arrival direction analysis
- Measurement of the energy spectra from individual sources to constrain the acceleration or the emission mechanisms

We set five exploratory objectives:

- Detection of extreme energy gamma rays
- Detection of extreme energy neutrinos
- Study of the Galactic magnetic field
- Verification of the relativity and the quantum gravity effects at extreme energy
- Global survey of nightglows, plasma discharges, and lightning and meteors

See [7,8,9] for the detailed discussions of scientific objectives. The success criteria of the mission are determined so as to achieve these science objectives (Table 1)

3 Instrument

The JEM-EUSO instrument consists of the main telescope, an atmosphere monitoring system, and a calibration system [10]. The main telescope of the JEM-EUSO mission is an extremely-fast (~μs) and highly-pixelized (~$3x10^5$ pixels) digital camera with a large diameter (about 2.5m) and a wide-FoV(±30°). It works in near-UV wavelength (330-400 nm) with single-photon-counting mode. The telescope consists of four parts: the optics, the focal surface detector and electronics, and the structure. The optics focuses the incident UV photons onto the focal surface with an angular resolution of 0.07 degree [11]. The focal surface detector converts the incident photons to photoelectrons and then to electric pulses [12,13]. The data electronics issues a trigger for air-shower event or other transient event in the atmosphere and send necessary data to the ground for further analysis. Atmosphere Monitoring System (AMS) monitors the earth's atmosphere continuously inside the FoV of the JEM-EUSO telescope [14]. The AMS uses IR camera, Lidar, and the slow data of the main telescope to measure the cloud-top height with accuracy better than 500 m. The calibration system measures the efficiencies of the optics, the focal surface detector, and the data acquisition electronics [15].

4 Observational Merits

In comparison with ground-based observatories, the space-based telescope may provide various merits in observations of EASs induced by EECR. One of substantially differences is that the signals of EAS from higher altitudes are efficiently observed with no or limited attenuation in cloudy cases if either the cloud lies at lower altitudes or optically thin clouds at high altitude. In order to determine the primary energy of EECRs, measurement of shower development including the signature around the maximum of the shower development is needed to be measured.

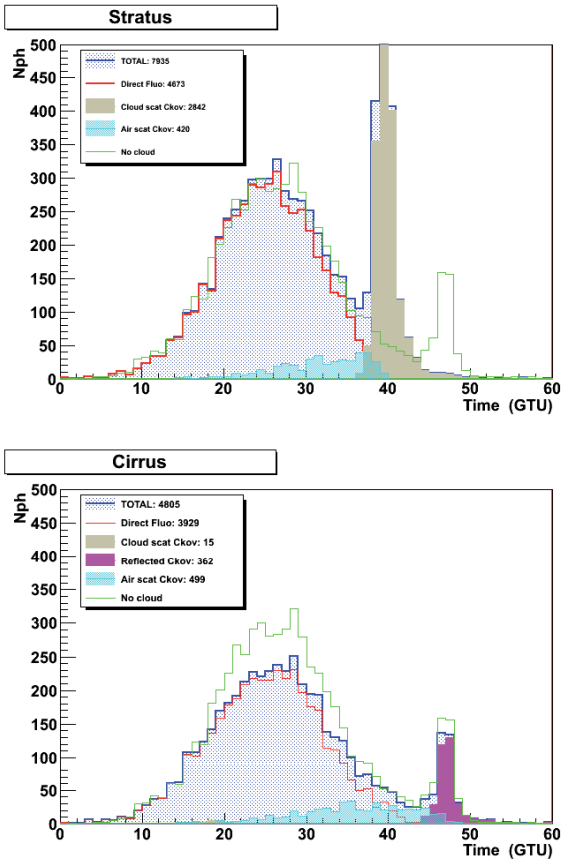


Figure 2. Typical EAS signals in cloudy conditions. Top and bottom panels show the case of the presence of stratus and cirrus. The components of signals are indicated in the legend. The green histogram is the case of EAS signal in clear sky.

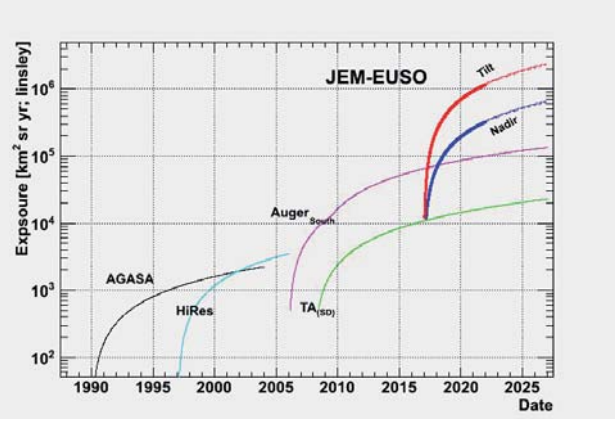


Figure 3 Expected cumulative exposure, in km2 sr yr or linsley units, of JEM-EUSO. The thick blue curve corresponds to pure nadir mode and the thick red curve to pure tilted mode; the actual exposure will depend on the final operating mode adopted and will lay between both curves. For comparison, the evolution of exposure by other retired and running EECR observatories is shown..

Fig. 2 demonstrates the typical EAS with clouds in comparison with one without clouds. In case of optically thick clouds that lie at altitudes lower than the shower maximum, such as stratus, the main part of shower development is well measured to reconstruct the energy deposit in the atmosphere. Moreover, the diffusively reflecting Cherenkov light enhances the total intensity from the shower that helps increasing the efficiency of triggering the shower at nearly threshold energies. In presence of the optically thin clouds that lie at high altitudes, *e.g.* ones categorized as cirrus, most of EAS signals penetrate the layer of the clouds and are attenuated partly and may be recognized as an lower energy event. In such a case, however, the geometry of shower axis is properly determined by the analysis of the angular velocity of the EAS signal.

Figure 3 shows the evolution of the exposures of the past and future missions devoted to research of the extremely high energy cosmic rays. The JEM-EUSO can achieve a more than one order of magnitude larger exposure compared to the Auger experiment ot Telescope array experiment.

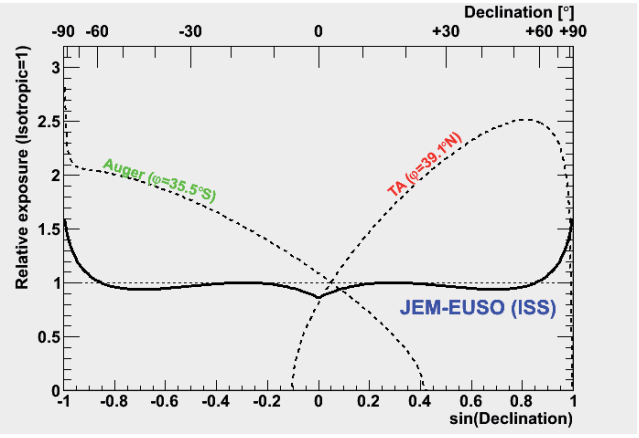


Figure 4. Relative aperture as a function of sine of declination. Dashed curves show the cases of the Auger and Telescope Array experiments for comparison. The pure isotropic exposure to solid angle is defined to 1. The horizontal axis on the top denotes corresponding declination.

Fig. 4 demonstrates the uniformity of exposure expected in the JEM-EUSO mission as a function of sine of declination (solid angle) compared with ones for ground-based experiments (Auger and Telescope Array). In addition to the significant increase of the overall exposure by about one order of magnitude compared with Auger as of today, the orbiting JEM-EUSO telescope will cover the entire Celestial Sphere. Moreover, the cumulative exposure results in high degree of uniformity thanks to inclined ISS orbit. Such an advantage is more pronounced if the EECRs from the single source are observed with angular spread. If it is the case, the gradient of exposure distributions in the Celestial Sphere may sweet over the real signals from the sources.

With wide FOV of JEM-EUSO telescopes observing from the Space, the measurements of the entire profile of the shower development is eased compared with relatively small FOV. In the case of JEM-EUSO, it is more sensitive to showers with larger zenith angles. Such a merit allows the effective measurements of neutrino-induced showers.

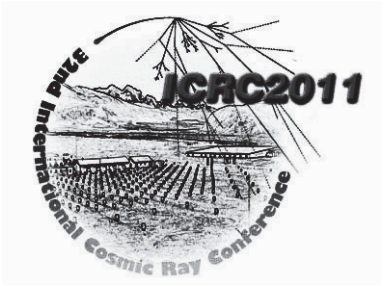
5 Conclusion

JEM-EUSO is the science mission looking downward from the ISS to explore the extremes in the Universe and fundamental physics through the detection of the extreme energy E > 10^{20} eV) cosmic rays. It is the first instrument that has a full-sky coverage and achieves an exposure compabale to one million km^2 · sr · year, the reference value of the exposure to start "astronomy and astrophysics through particle channel." The JEM-EUSO mission is planned to be launched by a H2B rocket about 2016-2017 and transferred to ISS by H2 transfer vehicle (HTV), and attached to the external experiment platform of "KIBO."

References

[1] Y. Takahashi et al., 2009, New Journal of Physics, 11, 065009.
[2] T. Ebisuzaki et al., 2008, Nucl. Phys. B (Proc. Suppl.), 175-176, 237.
[3] T. Ebisuzaki et al. (JEM-EUSO collab.) , Proc. 31st ICRC, 2009 (http://icrc2009.uni.lodz.pl/proc/html, #icrc1035).
[4] Ebisuzaki et al. 2009, Tours Symposium on Nuclear Physics and Astrophysics - VII, pp369-376.
[5] F. Kajino et al. (JEM-EUSO collaboration), 2010, Nuclear Instruments and Methods in Physics Research A 623, 422-424.
[6]K. Greisen 1966, Phys. Lett. 16, 148. G T Zatsepin, V. A.; Kuz'min 1966, JETP Phys. Lett. 4, 78.
[7] A. Santangelo et al., 2009, Tours Symposium on Nuclear Physics and Astrophysics - VII, pp380-387.
[8] K. Shinozaki, et al., 2009, Tours Symposium on Nuclear Physics and Astrophysics - VII, pp377-37.
[9] G Medina-Tanco et. al. (JEM-EUSO collab.),, proc. of this conference Proc. (ibidem #0956).
[10] F. Kajino et. al. (JEM-EUSO collab.),, proc. of this conference Proc. (ibidem #1216).
[11] J.H. Adams (JEM-EUSO collab.), Proc. of this conference ICRC, 2011 (ibidem #1100).
[12] Y. Kawasaki et al., (JEM-EUSO collab.), Proc. of this conference , 2011 (ibidem #0472).
[13] M. Casolino et al., (JEM-EUSO collab.), Proc. of this conference, 2011 (ibidem #icrc1219).
[14] A. Neronov et al., (JEM-EUSO collab.), Proc. of this conference, 2011 (ibidem #0301).
[15] P. Gorodetzky et al. (JEM-EUSO collab.), Proc. of this conference, 2011 (ibidem #0218).

32ND INTERNATIONAL COSMIC RAY CONFERENCE, BEIJING 2011



Science objectives of the JEM-EUSO mission

G. MEDINA-TANCO[1], T.J. WEILER[2], M. TESHIMA[3], T. EBISUZAKI[4], P. PICOZZA[5], A. SANTANGELO[6], E. PARIZOT[7], M. BERTAINA[8] FOR THE JEM-EUSO COLLABORATION
[1]*Instituto de Ciencias Nucleares, UNAM, Ciudad Universitaria, México D. F. 04510. (México).*
[2]*Department of Physics and Astronomy, Vanderbilt University Nashville, TN 37235 USA.*
[3]*Max-Planck-Institut fuer Physik, Föhringer Ring 6, D-80805 Munchen, Germany.*
[4]*RIKEN Advanced Science Institute, Japan.*
[5]*INFN, Sezione di Rome Tor Vergata, I-00133 Rome, Italy & University of Rome Tor Vergata.*
[6]*Institute fuer Astronomie und Astrophysik Kepler Center for Astro and Particle Physics Eberhard Karls University Tuebingen Germany.*
[7]*APC - Université Denis Diderot - Paris VII, France.*
[8]*Dipartimento di Fisica Generale dell' Università di Torino, Torino, Italy*

gmtanco@nucleares.unam.mx

Abstract: JEM-EUSO is a space telescope proposal, devoted to the observation of the ultraviolet fluorescence light emitted by extreme energy cosmic ray (EECR) atmospheric cascades [1]. The fluorescence technique has proved to be extremely successful from the ground and JEM-EUSO will be the first detector to use it from space. The telescope possesses an innovative wide field of view Fresnel optics which, combined with a highly sensitive focal surface and an observation altitude in excess of 360 km, will allow it to reach an unprecedented exposure of 10^6 km^2 sr yr at 3×10^{20} eV. These capabilities go far beyond what can be practically achieved by ground observatories. The large number of expected events will allow the identification of relatively nearby individual sources of EECR and determine their spectra. Point spread function analysis will also be used to study the Galactic magnetic field. Furthermore, baryons, photons and neutrino primaries can be discriminated with considerable accuracy, and upper limits to the fluxes of the last two will be improved by at least a factor of 10 beyond present experiments. Moreover, the mass target inside the field of view is $\sim 10^{12}$ ton which, depending on the actual astrophysics scenario, makes very likely the observation of up to a few cosmogenic neutrinos per year. Other exploratory objectives include the observation of atmospheric phenomena, like night-glow, high altitude plasma discharges and meteors.

Keywords: Extreme Energy Cosmic Rays, space detection, fluorescence technique

1 Introduction

Cosmic rays (CR) at the highest energies may be messengers of the most extreme environments in the universe. This challenging extreme energy region, at the frontier of present scientific knowledge, is the scope of the JEM-EUSO mission. JEM-EUSO is intended to address basic problems of fundamental physics and high energy astrophysics by investigating the nature and origin of extreme energy cosmic rays (EECR). JEM-EUSO will pioneer the observation from space of EECR-induced extensive air showers (EAS), making accurate measurements of the energy, arrival direction and identity of the primary particle using a target volume far greater than which is possible from the ground. The corresponding quantitative jump in statistics will clarify the origin (sources) of the EECR and, possibly, the particle physics mechanisms operating at energies well beyond those achievable by man-made accelerators. Furthermore, the spectrum of scientific goals of the JEM-EUSO mission also includes as exploratory objectives the detection of high energy gamma rays and neutrinos, the study of cosmic magnetic fields, and testing relativity and quantum gravity effects at extreme energies. In parallel, all along the mission, JEM-EUSO will systematically survey atmospheric phenomena over the Earth surface.

2 Main objectives

The CR can be considered as the Particle channel complementing the Electromagnetic one of conventional astronomy. The main objective of JEM-EUSO is to initiate a new field of astronomy and astrophysics that uses the extreme energy particle channel ($10^{19.5} eV < E < 10^{21}$ eV).

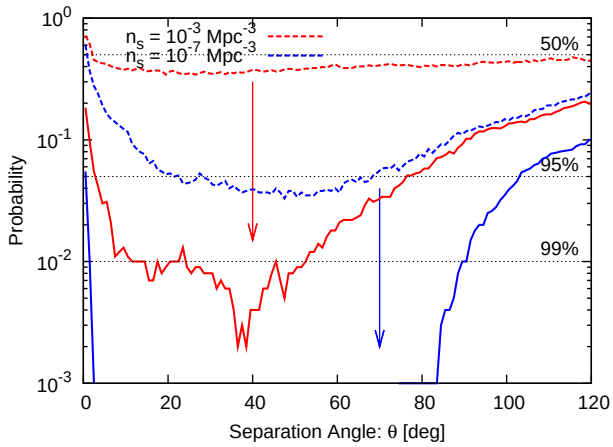


Figure 1: Probability that positive excess in the arrival distribution of EECRs (for Fe injection at LSMD from IRAS PSCz), compared to an isotropic distribution, is NOT realized (p). The probability that positive excess is realized (1-p) is indicated by numbers in the figure [8].

JEM-EUSO is designed to achieve more than 10^5 km^2 sr yr above 7×10^{19} eV during its first three years of operation which, given current uncertainties, amounts to the detection of between 500 and 800 events with energy above 5.5×10^{19} eV [2]. Such a number of events makes possible the following targets: (a) identification of sources by high-statistics arrival direction analysis; (b) measurement of the energy spectra from individual sources to constrain acceleration or emission mechanisms.

A remarkable characteristic of the EECR flux is that few astrophysical candidates are known which can attain such energies with the acceleration mechanisms we are presently aware of [3, 7]. This fact makes imperative the identification of both, those sources and of the powering mechanisms at play.

Given that a correlation between the arrival directions of EECR and the Galactic plane has never been observed, not to mention the relative calmness of the Milky Way, it is broadly accepted that the particles have an extragalactic origin. Furthermore, in all the most conservative models, the sources either follow the distribution of luminous matter or that of the associated dark matter. In either case, at large enough energies, anisotropy in the arrival directions is expected in the form of an enhanced correlation with nearby luminous matter, as data from the Pierre Auger Observatory presently implies [4]. To complicate the picture even further, the particles are widely thought to be predominantly baryons and, therefore, to posses charge during at least a significant portion of their transit through the intergalactic medium. Magnetic fields of poorly known intensity and topology are likely widespread throughout the universe, blurring any correlation between arrival directions and source position on the sky.

Particles also interact with the CMBR and the IR background. At the energies of JEM-EUSO the dominant target is the CMB which leads, in the case of HE protons, to photo-pair and photo-pion production. Above $\sim 10^{19.6}$ eV the latter dominates and can effectively decelerate particles to below the threshold for photo-pion production in few tens of Mpc, strongly suppressing the EECR energy spectrum (the GZK cut-off), and effectively setting a horizon at ~ 100 Mpc. Nuclei, on the other hand, lose energy mainly by photo-disintegration. The end result is a similar attenuation length for Fe, but shorter for intermediate nuclei. Therefore, the volume of universe sampled by EECR, regardless of their mass, is local in cosmic terms and encompasses a region where the large scale matter distribution (LSMD) is inhomogeneous. Thus, under general assumptions and given enough statistics, the footprint of the source distribution should emerge from the EECR flux.

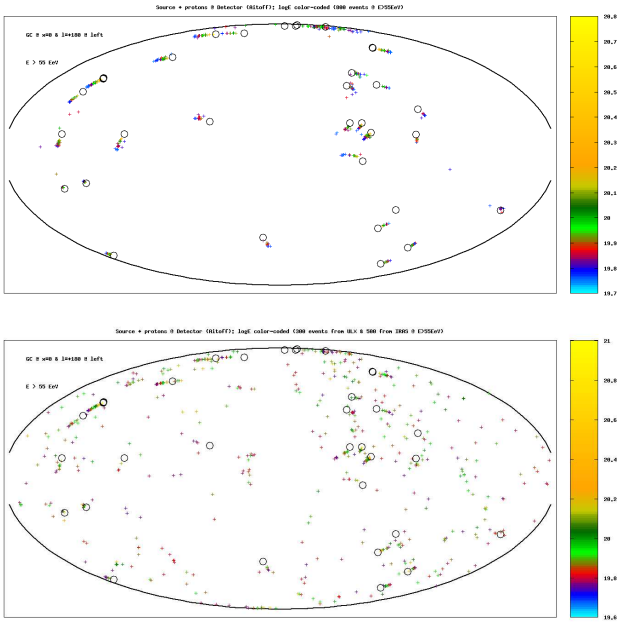


Figure 2: Simulated distribution of arrival direction of EECRs protons with $E > 55$ EeV, for (top) ULX sources and (bottom) a combination of ULX sources which contribute 37% of the events to a background originated in LSMD IRAS galaxies contributing 63% of events. Black circles denote ULX positions. The energy of events is color-coded in a log-scale. The intergalactic field (IGMF) is modeled following Faraday Rotation constraints and the LSMD traced by de IRAS PSCz. The GMF corresponds to a BSS-S disk with vertical component and $h_z \sim 250$ pc, immersed in an ASS-A magnetized halo extending up to 20 kpc. The injection at the sources follows $dN_{inj}/dE \propto E^{-2.7}$ [9].

The identification of the sources can follow different paths. First, a statistical identification can be attempted. In this case, arrival directions and source positions from candidate astrophysical catalogues are globally compared and the corresponding correlation is quantified. This has been attempted many times in the literature for the various experiments for a variety of astronomical catalogues and, most

notably, recently for Auger [4] and HiRes [5] data. However, the results are always severely bounded by the low available statistics at the highest energies and, to a lesser extent, by the small observed fraction of the sky and the strong exposure dependence on declination. JEM-EUSO, with its full sky coverage, low declination dependence of the exposure and large aperture, can significantly improve this kind of analysis.

There are several approaches to infer the density of nearby sources of EECR. If magnetic deflections are not too large, a low density of sources implies a relatively high EECR luminosity per source and, therefore, a smaller number of large multiplicity clusters of events is expected, while the opposite should occur in a large density scenario. The degree of clustering over the celestial sphere should also be dependent on the large scale spatial distribution of the sources. However, in practice, the number of parameters involved when trying to explore this avenue leads to ambiguous results due to the present limited data set [6]. Again, JEM-EUSO will have a strong impact in this arena, since its increased statistics will allow the discrimination of source densities in the interval $n_s \sim 10^{-7} - 10^{-3}$ Mpc^{-3} at more than 99% confidence level, as it is shown in Figure 2 in comparison to the present statistics of Auger above 55 EeV.

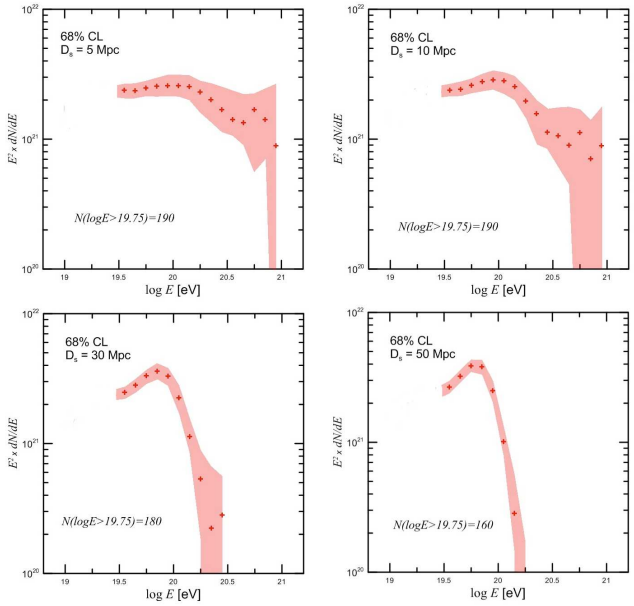


Figure 3: Simulated observed spectra of a point sources as a function of distance. The median and the upper and lower 68% CL are shown for each spectrum. The hypothetical sources have the same flux at Earth, which amounts to $\sim 160 - 190$ events above 55 EeV. If achieved in 5 yrs of operation of JEM-EUSO, it corresponds to a collection rate at Auger of < 4 yr^{-1} per source. $dN_{inj}/dE \propto E^{-2}$, IGMF $\sim$ 1 nG and $L_c \sim 1$ Mpc. Incoming events are selected with an appropriate trigger probability and their energies are convoluted with an energy and azimuth dependent error [9].

Another novel possibility is to directly observe individual sources. In this context, an individual source is a very high multiplicity cluster whose events are genetically related. Indications of such a cluster may be already popping up in the Auger data in the general direction of Cen A. Whether this enhancement is the product of a single astrophysical object or the combined effect of a compact more distant region of individual sources, e.g., the huge Shapley supercluster behind Cen A, is impossible to tell at the present level of statistics. Other relatively nearby sources may be also contributing significantly to the EECR flux, although masked at present by the limited fraction of the sky available to Auger and the strong declination dependence of its exposure. In fact, M87 and the Virgo cluster may be just such an example. JEM-EUSO, on the other hand, will be able to detect those sources if they exist. Figure shows how the JEM-EUSO sky after 3 yrs of exposure could look like if some particular class of object, ultra-luminous X-ray Galaxies (ULX), were sources of EECR contributing 37 % of the total flux originated from the LSMD as traced by the IRAS catalog (bottom). Furthermore, if several sources are found with at least dozens of observed EECR events, then the observed differences in spectral features among those sources Figure , combined with a multi-wavelength approach, will provide direct clues on the identity of the sources and the acceleration mechanism involved.

The energy dependent distortions of the sources' point spread functions as a result of the Galactic magnetic field can be clearly seen as a function of the position on the sky (top panel in Fig.). This pattern of distortions, over the celestial sphere can be used to infer the large scale structure of the Galactic magnetic field (GMF).

3 Exploratory objectives

Gamma rays at extreme energies are a natural consequence of π_0 production during EECR proton propagation through the CMB. A gamma-ray flux higher than expected from this secondary production would signify a new production mechanism, such as top-down decay/annihilation, or a breaking of Lorentz symmetry. Nuclei, on the other, would produce a much smaller gamma background. Therefore, the flux of gamma rays in extreme energy is a key parameter to discriminate origin models. Figure 3 summarizes existing limits on the gamma-ray flux and shows the sensitivity of gamma rays by five years operation of the JEM-EUSO Mission. The Auger Observatory reported the upper limit on gamma ray flux as a few percent of EECR flux above 10 EeV [12]. Under the null gamma ray assumption, JEM-EUSO is capable of putting more stringent upper limit by an order of magnitude at overlapping energies. To give the constraint on origin models or their parameters, the gamma ray flux above 100 EeV is essential and will be constrained in an unprecedented way after five years operation of JEM-EUSO.

During proton propagation through the CMBR, ν are produced. These *cosmogenic neutrinos* constitute a guaranteed

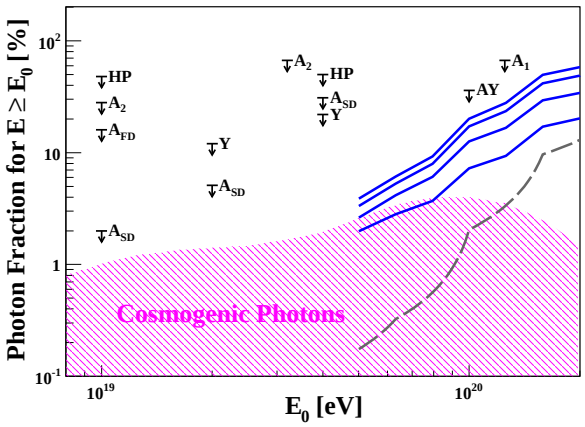


Figure 4: Upper limits on the fraction of photons in the integral cosmic ray flux at 95% of confidence level. Dashed line corresponds to the ideal case in which it is known that there is no photon in the data. Blue solid lines are the upper limits obtained by using X_{max}; from bottom to top, different X_{max} reconstruction uncertainties of 0, 70, 120 and 150 g cm^{-2} are considered. See [10] for detils.

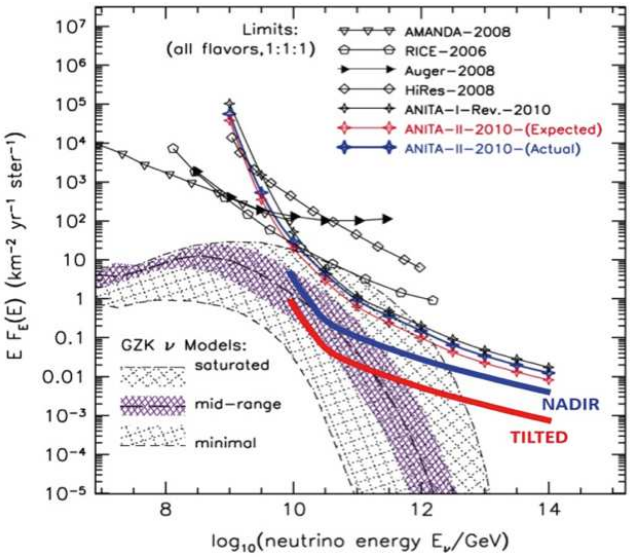


Figure 5: Flux sensitivity of JEM-EUSO detecting 1 event/energy-decade/yr. An observational efficiency of 25% is assumed. Thick blue and red curves show the case of nadir and tilted modes, respectively. Adapted from [11]

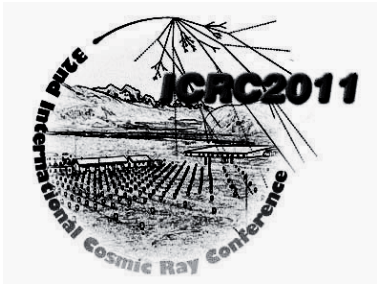
flux at Earth and contain extremely valuable information on the redshift evolution of the sources. Besides the cosmogenic flux there may also be contributions from hadronic interactions at the acceleration sites and from top-down processes. JEM-EUSO can detect neutrinos evolving deep in the atmosphere or, in the case of bursts of upward going neutrinos interacting inside the outermost layers of the crust, as expected form GRB, through direct Cherenkov. Figure shows the flux sensitivity of JEM-EUSO for several neutrino production models for both nadir and tilted mode operation of the telescope. The discovery of EE ν beyond 100 EeV has profound implications on our understanding of production mechanisms, since protons of energy > 1 ZeV at the source are required to create such energetic ν via the pion chain. Higher energy neutrinos should originate either by top-down mechanisms or by less understood bottom-up channels, like exotic plasma phenomena or unipolar induction in extreme environments.

Furthermore, the ν cross-section is uncertain and highly model-dependent. Extra-dimension models [13] in which the Universe is supposed to consist of 10 or 11 dimensions are among the favored models to unify quantum mechanics and gravitation theory. In these models, the predicted neutrino cross-section is 10^2 times larger than the Standard Model prediction. Under these conditions, JEM-EUSO should observe 100s of ν events, which would immediately validate experimentally low-scale unification. In addition, the ratio of horizontal to upward ν-originated EAS gives a quantitative estimation of ν cross-section around 10^{14} eV center of mass energies [14].

Additionally, a stringent test of relativity could be made from high multiplicity sources at known distances. If the GZK steepening functions consistently deviate at some directions in the sky, external vector fields might be emerging which are not unidirectionally Lorentz Invariant. On the other hand, verification of LI at EHE would disfavor such vector fields. [15].

References

[1] T. Ebisuzaki et al., ICRC 2011. Y. Takahashi, New J. Phys., Vol. 11, N. 065009, 2009.
[2] A. Santangelo et al., for the JEM-EUSO Collaboration, ICRC 2011.
[3] A.M. Hillas, Annu. Rev. Astron. Astr., 1984, 22(1): 425-444
[4] J. Abraham et al., Science, 2007, 318(5852): 938-943; J. Abraham et al., Astrop. Phys., 2008, 29(3): 188204; P. Abreu et al., Astrop. Phys., 2010, 34(5): 314326
[5] R.U. Abbasi et al., Astrop. Phys., 2008, 30(4): 175 269
[6] A. Cuoco et al., Astroph. J., 2009, 702(2): 825832
[7] T. Stanev, High Energy Cosmic Rays, Springer-Verlag, Berlin, 2003
[8] H. Takami, S. Inoue, and T. Yamamoto, in prep., 2011
[9] G. Medina-Tanco, T. Ebisuzaki, in prep., 2011
[10] D. Supanitsky, G. Medina-Tanco, for the JEM-EUSO Collaboration, Proc. ICRC 2011, ID0930.
[11] Gorham et al, Phys.Rev. D, 82, 022004, 2010
[12] Pierre Auger Collaboration, 2008, Astropart. Phys., 29, 243-256.
[13] Ancordoqui L. A., Feng J. L. and Goldberg H. 2002, Phys. Lett. B 525, 302.
[14] A. Kusenko, T. J. Weiler, Phys. Rev. Lett. **88**, 161101 (2002). Palimares-Ruiz S. et al. 2006, Phys. Rev. D 73, 083003.
[15] V. A. Kostelecky, Phys.Rev. D69 (2004) 105009



Overview of the JEM-EUSO Instruments

F. KAJINO[1], P. PICOZZA[2,11], T. EBISUZAKI[2], H. MASE[2], K. TSUNO[2], Y. TAKIZAWA[2], Y. KAWASAKI[2], K. SHINOZAKI[2], H. OHMORI[2], S. WADA[2], N. INOUE[3], N. SAKAKI[4], J. ADAMS[5], M. CHRISTL[5], R. YOUNG[5], C. FERGUSON[5], M. BONAMENTE[6], A. SANTANGELO[7], M. TESHIMA[8], E. PARIZOT[9], P. GORODETZKY[9], O. CATALANO[10], M. CASOLINO[11], M. BERTAINA[12], M. PANASYUK[13], B.A. KHRENOV[13], I.H. PARK[14], A. NERONOV[15], G. MEDINA-TANCO[16], D. RODRIGUEZ-FRIAS[17], J. SZABELSKI[18], P. BOBIK[19] AND R. TSENOV[20] ON BEHALF OF THE JEM-EUSO COLLABORATION

[1]*Department of Physics, Konan University, Okamoto 8-9-1, Higashinada, Kobe 658-8501, Japan*
[2]*RIKEN Advanced Science Institute, 2-1 Hirosawa, Wako351-0198, Japan*
[3]*Graduate School of Science and Engineering, 255 Shimo-Okubo, Sakura-ku, Saitama City, Saitama 338-8570, Japan*
[4] *Department of Physics and Mathematics, Aoyama Gakuin University, 5-10-1 Fuchinobe, Chuo-ku, Sagamihara-shi, Kanagawa 252-5258, Japan*
[5]*NASA Marshall Space Flight Center, Huntsville, AL 35812, USA*
[6]*Department of Physics, University of Alabama, Huntsville, AL35899*
[7]*Astronomie und Astrophysik, Universitt Tubingen, Sand 1, 72076 Tubingen, Deutschl*
[8]*Institute of Cosmic Ray Research, University Tokyo, Kashinoha 5-1-5, Kashiwa, Chiba 277-8582, Japan*
[9]*APC, Univ. of Paris Diderot, CNRS/IN2P3, 10, rue A. Domon et L. Duquet, 75205 Paris Cedex 13, France*
[10]*Istituto di Astrofisica Spaziale e Fisica Cosmica di Palermo, INAF, Via Ugo La Malfa 153, 90146 Palermo, Italy*
[11]*Department of Physics, University of Rome Tor Vergata, Via della Ricerca Scientifica 1, 00133 Rome, Italy*
[12]*Dipartimento di Fisica Generale, Università di Torino,Via Giuria 1 10125 Torino, Italy*
[13]*SINP, Lomonosov Moscow State Univ., Leninskie Gory 1 str. 2, Moscow, 119991, Russia*
[14]*Department of Physics, Ewha Womans University, Seoul 120-750, Korea*
[15]*ISDC, Data Centre for Astrophysics, Chemin d'Ecogia 16, CH-1290 Versoix ,Switzerland*
[16]*Inst. de Ciencias Nucleares, UNAM, AP 70-543 / CP 04510, Mexico D.F.*
[17]*Soltan Institute for Nuclear Studies, 90-950 Lodz, Box 447, Poland*
[18]*University of Alcala Ctra. Madrid-Barcelona, km. 33.6, E-28871, Alcala de Henares, Madrid. Spain*
[19]*Institute of Experimental Physics SAS, Watsonova 47, 040 01 Kosice, Slovakia*
[20]*St. Kliment Ohridski University of Sofia, 5, James Bourchier Boul., SOFIA 1164, Bulgaria*
kajino@konan-u.ac.jp

Abstract: JEM-EUSO mission with a large and wide-angle telescope to be mounted on the International Space Station has been planned to open up "particle astronomy" through the investigation of extreme-energy cosmic rays by detecting fluorescent and Cherenkov photons generated by air showers in the earth's atmosphere. The JEM-EUSO telescope consists of 3 light-weight optical Fresnel lenses with a diameter of about 2.5m, 300k channels of MAPMTs, frontend readout electronics, trigger electronics, and system electronics. An infrared camera and a LIDAR system will be also used to monitor the earth's atmosphere.

Keywords: cosmic rays, air shower, JEM-EUSO, telescope, International Space Station, ISS, JEM

1 Introduction

JEM-EUSO on board the International Space Station (ISS) is a new type of observatory which uses the whole Earth as a detector. Extreme-energy cosmic rays (EECR)

coming to the earth's atmosphere collide with atmospheric nuclei and produce extensive air showers (EAS). Charged particles in EAS excite nitrogen molecules and emit near ultra-violet (UV) photons. They also produce Cherenkov photons in a narrow cone of about trajectory of the EAS. JEM-EUSO mission observes these photons from the ISS orbit at an altitude of about 400 km. Reflected Cherenkov photons at the ground are observed as a strong Cherenkov mark. Viewing from the ISS orbit, the Field-of-View of the telescope ($\pm 30°$) corresponds to the observational area at the ground larger than 1.9×10^5 km^2.

Threshold energy to detect EECRs is as low as several $\times 10^{19}$ eV. Increase in exposure is realized by inclining the telescope from nadir to tilted mode, though the threshold energy becomes higher. (Figure 1) The first half of the mission lifetime is devoted to observe lower energy cosmic rays with the nadir mode and the second half to observe higher energies by the tilted mode. JEM-EUSO will be launched by H2B rocket and conveyed by H-II Transfer Vehicle (HTV) to ISS. It will be attached to the Exposure Facility (EF) of the Japanese Experiment Module (JEM) [1,2,3].

Details of JEM-EUSO mission, science objectives, requirements and expected performances are reported in [4,5,6].

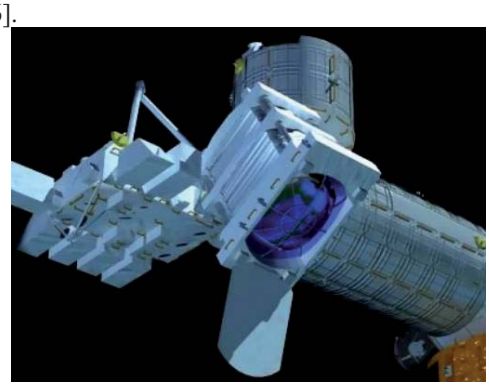


Figure 1. Illustration of the JEM-EUSO telescope on the ISS for the tilted observation mode.

2 JEM-EUSO System

Overall JEM-EUSO system consists of a flight segment, a ground support equipment and a ground segment, which is shown in Figure 2.

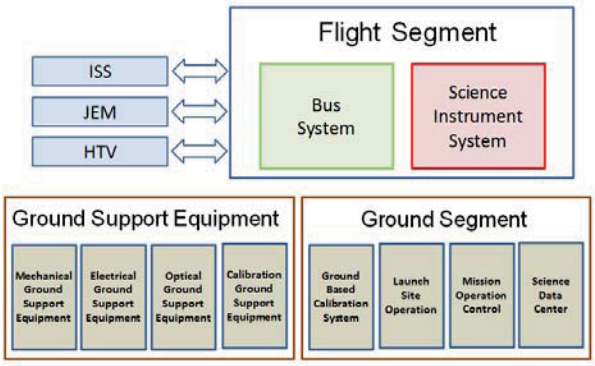


Figure 2. Overall JEM-EUSO System.

The flight segment consists of a science instrument system and a bus system. The science instrument system basically consists of the following systems:
1) The JEM-EUSO telescope which is a large diameter telescope to observe EECR
2) Atmospheric monitoring system
3) Calibration system
Details of these systems are described in the following sections.

The ground support equipment (GSE) consists of mechanical, electrical, optical, calibration GSE. GSE supports manufacturing the flight segment.

The ground segment (GS) consists of a ground based calibration system, a launch site operation, a mission operation control and a science data center. GS supports launching and mission operation, data calibration while the mission is in operation by using many flashers and LIDARs which are installed on the ground. Science data analysis is also included in GS.

2.1 The JEM-EUSO telescope

The JEM-EUSO telescope is an extremely-fast, highly-pixelized, large-aperture and large-FoV digital camera, working in near-UV wavelength range (330÷400 nm) with single photon counting capability. The telescope mainly consists of four parts: collecting optics, focal surface detector, electronics and structure. (Figure 3, 4)

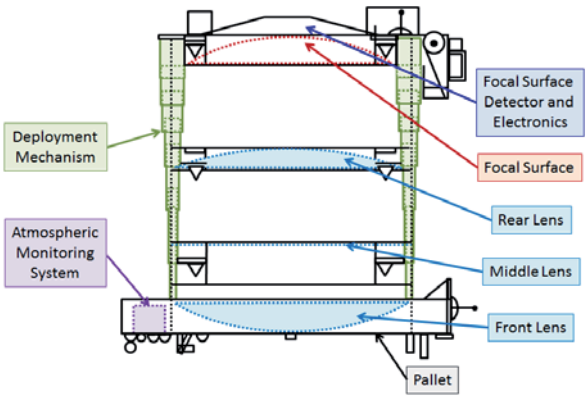


Figure 3. Side view of the JEM-EUSO telescope.

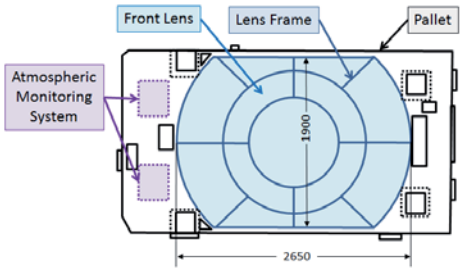


Figure 4. Bottom view of the JEM-EUSO telescope.

The optics focuses the incident UV photons onto the focal surface with an angular resolution of 0.1°. The

focal surface detector converts the incident photons to electric pulses. The electronics counts the number of the pulses in a period less than 2.5 μs and records it as a brightness data. When a signal pattern of an EAS is found, trigger is issued. This starts a sequence to send the brightness data of the triggered (and surrounding) pixels to the ground operation center. The structure encloses all the parts of the instruments and keeps them out from the outer harmful environment in space. It also keeps the optical lenses and the focal surface detector to the preset place. The telescope is stowed when it is launched and deployed in the observation mode. Main parameters of the JEM-EUSO telescope are summarized in Table 1.

Table 1. Parameters of JEM-EUSO telescope

Field of View	± 30°
Observational area	> 1.9×10^5 km^2
Optical bandwidth	330÷400 nm
Focal Surface area	4.5 m^2
Number of pixels	3.2×10^5
Pixel size	2.9 mm
Pixel size at ground	~ 550 m
Spatial resolution	0.07°
Event time sampling	2.5 μs
Duty cycle	~ 20 %

Total mass of the instruments is 1983 kg and electric power is suppressed less than 1kW in operation mode.

2.2 Optics

Two curved double sided Fresnel lenses with 2.65m external diameter, a precision middle Fresnel lens and a pupil constitute optics of the JEM-EUSO telescope. The Fresnel lenses can provide a large-aperture, wide FoV optics with low mass and high UV light transmittance. Combination of 3 Fresnel lenses realizes a full angle FoV of 60° and an angular resolution of 0.07°. This resolution corresponds approximately to 550 m on the earth.
The material of the lens is CYTOP and UV transmitting PMMA which has high UV transparency in the wavelength from 330nm to 400nm. A precision Fresnel optics adopting a diffractive optics technology is used to suppress the color aberration. Details are described in [7,8,9].

2.3 Focal Surface Detector

The focal surface (FS) of JEM-EUSO has a spherical surface of about 2.3 m in diameter with about 2.5 m curvature radius, and it is covered with about 5,000 multi-anode photomultiplier tubes [10]. The FS detector consists of Photo-Detector Modules (PDMs), each of which consists of 9 Elementary Cells (ECs). The EC contains 4 units of MAPMT. 137 PDMs are arranged in FS (Figure 5) [11].

Cockcroft-Walton type high-voltage supply will be used to suppress power consumption, which includes a circuit to protect MAPMT from an instantaneous large amount of light like lightning [12].

The MAPMTs developed for the JEM-EUSO mission are going to be tested by Russian space mission, TUS detector [13].

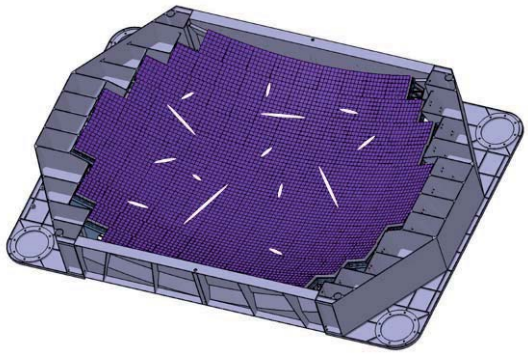


Figure 5. Illustrated images of air showers generated by EECR for various incident angles and positions on the focal surface detector.

2.4 Focal Surface Electronics

The FS electronics system records the signals of UV photons generated by EECRs successively in time. A new type of frontend ASIC has been developed for this mission, which has both functions of single photon counting and charge integration in a chip with 64 channels [14,15]. The system is required to keep high trigger efficiency with a flexible trigger algorithm [16] as well as a reasonable linearity over 10^{19}-10^{21} eV range. The requirements of very low power consumption must be fulfilled to manage 3.2×10^5 signal channels. Radiation tolerance of the electronic circuits in the space environment is also required.

The FS electronics is configured in three levels corresponding to the hierarchy of the FS detector system: front-end electronics at an EC level, PDM electronics common to 9 EC units, and FS electronics to control 137 units of PDM electronics. Anode signals of the MAPMT are digitized and recorded in ring memories for each Gate Time Unit (=2.5 μs) to wait for a trigger assertion, then, the data are read and are sent to control boards. JEM-EUSO uses hierarchical trigger method to reduce huge original data rate of ~10GB/s to 297 kbps for sending data from ISS to ground operation center [17,18].

2.5 Monitoring/Control Electronics

System control electronics consists of Data Processor (DP), Mission Data Processor (MDP) and Movement Controller (MC). Main functions of DP are: a) Communication with MDP, MC and JEM/EF, b) House Keeping (HK) data acquisition related to mission system [19], c) Interface function which distributes clock signal from GPS to MDP [20]. MDP acquires observation data from FS detector, atmospheric monitor and HK data, and then sends data to DP. MC accepts signals from DP and controls movable mechanisms.

2.6 Atmospheric Monitoring System

Atmospheric Monitoring System (AM) monitors the earth's atmosphere [21]. Intensity of the fluorescent and Cherenkov light emitted from EAS at JEM-EUSO depends on the transparency of the atmosphere, the cloud coverage and the height of cloud top, etc.. These must be determined by AM of JEM-EUSO. In case of events above 10^{20} eV, the existence of clouds can be directly detected by the signals from the EAS. However, the monitoring of the cloud coverage by AM is important to estimate the effective observing time with high accuracy and to increase the confidence level [22,23,24]. The AM consists of the followings: 1) Infrared camera [25], 2) LIDAR, 3) Slow data of the JEM-EUSO telescope.

2.7 Calibration System

The calibration system measures the efficiencies of the optics, the focal surface detector and the data acquisition electronics with a precision necessary to determine energy and arrival direction of EECR [26]. The calibration system consists of the following categories: 1) Pre-flight calibration, 2) On-board calibration, 3) Calibration in flight with on-ground instruments, 4) Atmospheric monitor calibration.

The pre-flight calibration of the detector will be done by measuring detection efficiency, uniformity, gain etc. with UV LED's. To measure efficiencies of FS detector, several diffuse LED light sources with different wavelengths in the near UV region are placed on the support of the rear lens before FS. To measure efficiencies of the lenses similar light source is placed at the center of FS. Reflected light at the inner surface of the lid is observed with FS. In this way, the gain and the detection efficiency of the detector will be calibrated on board.

The system can be calibrated with 10-20 ground light sources when JEM-EUSO passes over them. The amount of UV absorption in the atmosphere is measured with Xe flasher lamps. The systematic error in energy and direction determination will be empirically estimated, by observing emulated EAS images with a UV laser by the JEM-EUSO telescope. The transmittance of the atmosphere as a function of height will be also obtained.

The IR camera as a FoV monitoring system takes pictures periodically in observation and the effective area will be estimated [23].

2.8 Structure Analysis

To accommodate JEM-EUSO into a volume of the HTV transfer vehicle, a contractible/extensible structure is adopted. The structure is stowed at launch by H2B rocket and it is extended at JEM/EF of ISS. Structure analysis for vibration showed that the minimum natural frequency for launch mode was 25.6 Hz and that for the observation mode it was as low as 1.7 Hz. Both of them satisfied the requirements.

3 Conclusion

Phase A study (feasibility study and conceptual design) of the JEM-EUSO mission started in 2007. Many new technological items have been developed to realize the mission by inheriting ESA-EUSO. The study is now successfully in progress with an international collaboration of 13 countries.

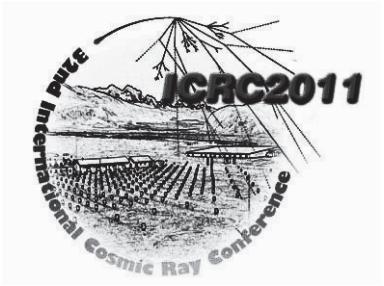
Acknowledgments

This work was supported in part by Grants-in-Aid for Science Research from the Japan Society for the Promotion of Science in Japan.

References

[1] Y. Takahashi et al., New Journ. of Phys. 11, 065009, 2009
[2] T. Ebisuzaki et al., Nucl. Phys. B (Proc. Suppl.), 175-176, 237, 2008
[3] F. Kajino et al. (JEM-EUSO collab.), Nucl. Instr. Meth. A 623, 422-424, 2010.
[4] T. Ebisuzaki et al., Proc. 32nd ICRC, 2011 (ID1628).
[5] G. Medina-Tanco et al., Proc. 32nd ICRC, 2011 (ID0956).
[6] A. Santangelo et al., Proc. 32nd ICRC, 2011 (ID0991).
[7] A. Zuccaro et al., Proc. 32nd ICRC, 2011 (ID0852).
[8] Y. Takizawa et al., Proc. 32nd ICRC, 2011 (ID0874).
[9] J. Adams et al., Proc. 32nd ICRC, 2011 (ID1100).
[10] Y. Kawasaki et al., Proc. 32nd ICRC, 2011 (ID0472).
[11] M. Ricci et al., Proc. 32nd ICRC, 2011 (ID0335).
[12] J. Karczmarczyk, et al., Proc. 32nd ICRC, 2011 (ID0216).
[13] B. Khrenov et al., Proc. 32nd ICRC, 2011 (ID1261).
[14] S. Ahmad et al., Proc. 32nd ICRC, 2011 (ID0236).
[15] H. Miyamoto et al., Proc. 32nd ICRC, 2011 (ID0775).
[16] O. Catalano et al., Proc. 31st ICRC, 2009 (ID0326).
[17] J. Bayer et al., Proc. 32nd ICRC, 2011 (ID0836).
[18] M. Casolino et al., Proc. 32nd ICRC, 2011 (ID1219).
[19] G. Medina-Tanco et al., Proc. 32nd ICRC, 2011 (ID0961).
[20] G. Osteria et al., Proc. 32nd ICRC, 2011 (ID1131).
[21] A. Neronov et al., Proc. 32nd ICRC, 2011 (ID0301).
[22] F. Garino et al., Proc. 32nd ICRC, 2011 (ID0398).
[23] A. Anzalone et al., Proc. 32nd ICRC, 2011 (ID1152).
[24] G. Saez et al., Proc. 32nd ICRC, 2011 (ID1034).
[25] J.A. Morales et al., Proc. 32nd ICRC, 2011 (ID1031).
[26] P. Gorodetzky et al., Proc. 32nd ICRC, 2011 (ID0218).

32ND INTERNATIONAL COSMIC RAY CONFERENCE, BEIJING 2011



Requirements and Expected Performances of the JEM-EUSO mission

M. BERTAINA[1], A. SANTANGELO[2,3], K. SHINOZAKI[3], F. FENU[2,3], T. MERNIK[2], P. BOBIK[5], F. GARINO[1], K. HIGASHIDE[3,4], G. MEDINA TANCO[6], G. SAEZ CANO[7], ON BEHALF OF THE JEM-EUSO COLLABORATION

[1] *Dipartimento di Fisica Generale dell' Università di Torino, Torino, Italy*
[2] *IAAT, Kepler Center für Astro- und Teilchenphysik, Universität Tübingen, Tübingen, Germany*
[3] *Computational Astrophysics Laboratory, RIKEN, Wako, Japan*
[4] *Graduate School of Science and Engineering, Saitama University, Japan*
[5] *Instutute of Experimental Physics SAS, Kosice, Slovakia*
[6] *ICN-UNAM, Mexico City, Mexico*
[7] *SPace & AStroparticle (SPAS) Group, University of Alcalá, Madrid, Spain*

Andrea.Santangelo@uni-tuebingen.de

Abstract: In this paper we describe the requirements and the expected performances of the Extreme Universe Space Observatory (EUSO) onboard the Japanese Experiment Module (JEM) of the International Space Station. Designed as the first mission to explore the Ultra High Energy (UHE) Universe from space, JEM-EUSO will monitor, night-time, the earth's atmosphere to record the UV (300-400 nm) tracks generated by the Extensive Air Showers produced by UHE primaries propagating in the atmosphere. After briefing summarizing the main aspects of the JEM-EUSO Instrument and mission baseline, we will present in details our studies on the expected trigger rate, the estimated exposure, as well as on the expected angular, energy, and X_{max} resolution. Eventually, the obtained results will be discussed in the context of the scientific requirements of the mission.

Keywords: JEM-EUSO, Ultra High Energy Cosmic Rays, Space Instrumentation.

1 Introduction

JEM-EUSO [1, 2] is an innovative space-based mission with the aim of detecting Ultra High Energy Cosmic Rays (UHECR) from the International Space Station (ISS), by using the earth's atmosphere as a fluorescence detector. JEM-EUSO consists of an UV telescope and of an atmosphere monitoring system. Orbiting the earth every $\sim$90 minutes, JEM-EUSO is designed to detect, from an altitude of 350-400 km, the moving track of the UV (300-400 nm) fluorescence photons produced during the development of Extensive Air Showers (EAS) in the atmosphere. The telescope, which contains a wide Field-of-View ($\pm 30^\circ$, FOV) optics composed by Fresnel lenses [3], records the EAS-induced tracks with a time resolution of 2.5μs and a spatial resolution of about 0.5 km ($\sim 0.07^\circ$) in nadir mode by using a highly pixellised focal surface ($\sim 3\times 10^5$ pixels) [4]. These time-segmented images allow an accurate measurement of the energy and arrival direction of the primary particles.

Since the ISS orbits the earth in the latitude range $\pm 51^\circ$, moving at a speed of $\sim$ 7 km/s, the variability of the FOV observed by JEM-EUSO is much higher than that observed by ground-based experiments. In particular the atmospheric conditions, which eventually determine the acceptance, must be carefully monitored via an atmosphere monitoring system consisting of an infrared camera [5] and a LIDAR [6].

Thanks to the ISS orbit, JEM-EUSO will monitor, with a rather uniform exposure, both hemispheres minimizing the systematic uncertainties that strongly affect any comparison between different observatories exploring, from ground, different hemispheres.

The other great advantage of JEM-EUSO, in comparison to any existing or studied ground-based observatory, is the significant increase of aperture (see Section 4). There are however other relevant advantages in using space-based UHE observatories. First, the non-proximity of the detector to the EAS considerably reduces all problems associated with the determination of the solid angle and with the different attenuation suffered by the UV light in the atmosphere. Second, the near-constant fluorescence emission rate at different heights below the stratosphere simplifies all assumptions on the energy-fluorescence yield relation at the EAS maximum as well as on the dependence of the EAS time structure on the production height [7]. Third, the observation from space minimize uncertainties due to scattering by aerosols limited to altitudes below the atmo-

spheric boundary layer. Finally, as the EAS maximum develops, for most zenith angles, at altitudes higher than 3-5 km from ground, space measurements are also possible in cloudy sky conditions. Compared to ground-based detectors, the duty cycle is therefore mainly limited by the moon phases, while the cloud impact is less relevant.

The JEM-EUSO observational approach mainly relies on the fact that a substantial fraction of the UV fluorescence light generated by the EAS can reach a light-collecting device of several square meters: typically a few thousand photons reach the JEM-EUSO detector for a shower produced by a 10^{20} eV particle. JEM-EUSO is designed to record not only the number of photons but also their direction and arrival time. It is the observation of the specific space-time correlation that allows to very precisely identify EAS tracks in the night glow background.

We wish also to observe that JEM-EUSO has considerably improved with respect to the original Extreme Universe Space Observatory [8] studied by the European Space Agency. Main improvements have to be ascribed to the new optics [3] (with $\sim$1.5 better throughput and $\sim$1.5 better focusing capability), to the photo-detector [9] ($\sim$1.6 higher detection efficiency), to the better geometrical layout of the focal surface that maximizes the filling factor [10], and to the improved performance of the electronics [11, 12], which allows to exploit more complex trigger algorithms [13].

The key element to estimate the science potential of JEM-EUSO is its exposure. This is determined by three main contributions: the trigger aperture, the observational duty cycle and the cloud impact. In the following sections the three terms are discussed in details.

2 Night-glow background and estimation of the observational duty cycle

The UV tracks of EAS must be discriminated in the night-glow background. One key parameter is therefore the fraction of time in which EAS observations are not hampered by the brightness of the sky. We define *observational duty-cycle* the fraction of time in which the sky is dark enough to measure EAS. Pavol et al. [14] have conducted an analysis of the duty-cycle using measurements performed by the Tatiana satellite rescaling them to the ISS orbit. In this estimate all major atmospheric effects, such as lightnings, meteors and anthropic lights (e.g. city lights) have been included. Results indicate that for a zenith angle position of the sun higher than 108° (120°), the fraction of time in which the night-glow background is less than 1500 ph/m^2/ns/sr is 22% (18%). In fact the mean of all background levels less than 1500 ph/m^2/ns/sr, weighted according to their relative occurrence, is equivalent to an average background of 500 ph/m^2/ns/sr: the so-called standard background actually measured by different balloon experiments. This is a conservative estimate for the highest energies where measurement could be performed even in a higher background condition. These recent studies confirms previous estimates of 18%–22% performed in the context of the EUSO studies, based on a combined analytical and simulation approach [15]. We therefore assume a value of 20% as the most probable value for the observational duty-cycle of the mission.

3 The cloud impact

Space based UHE observatories can observe EAS induced tracks also in cloudy conditions: this is typically not the case for ground-based observatories. In fact if the maximum of the shower is above the cloud top layer the reconstruction of the shower's parameters is still possible. It is clear that the same cloud top layer will affect in different ways showers of various inclination or originating from different type of primary particles (e.g. neutrino will develop much deeper in the atmosphere compared to protons). Thin clouds (τ <1, typical of cirrus) might affect the measurement of the energy but arrival direction will still be nicely measurable. Thick clouds (τ >1) will strongly impact the measurement only if located at high altitudes. As an example, a 60° zenith-angle inclined shower will reach the shower maximum at an altitude of 6–7 km, much higher than the typical range of stratus. In order to quantify the effective observational time, a study on the distribution of clouds as a function of altitude, optical depth and geographical location has been performed using different meteorological data sets [16]. Table 1 reports the results of the occurrence of each cloud typology for oceans during daytime using visible and IR information.

Table 1: Relative occurrence (%) of clouds between 50°N and 50°S latitudes on TOVS database in the matrix of cloud-top altitude vs optical depth. Daytime and ocean data are used for the better accuracy of the measurements.

Optical Depth	Cloud-top altitude			
	<3km	3-7km	7-10km	>10km
>2	17.2	5.2	6.4	6.1
1-2	5.9	2.9	3.5	3.1
0.1-1	6.4	2.4	3.7	6.8
<0.1	29.2	<0.1	<0.1	1.2

In Table 1 cloud coverage data taken during daytime are chosen since they are in general more precise. The same applies to data of clouds above the oceans, more reliable than the ones taken above land. A comparison between day and night cloud coverage has been then performed for data above land as higher variations are expected in comparison with day/night variation above the oceans. Differences however resulted to be of only a few percents. The results of Table 1 can be understood as it follows. Clear sky corresponds to $\tau < 0.1$ and this accounts for $\sim$30% of the observation time. Clouds below 3 km height do not hamper the measurements as the shower maximum will develop at higher altitudes, regardless of their τ and they account for another $\sim$30%, which gives a total of $\sim$60% of

the time when the measurement is possible with no major correction. Thick optically depth (τ >1) high clouds (h>7km) will prevent the possibility of any measurements, and they account for ∼19%. For the remaining ∼21% angular and energy measurements will be possible for very inclined showers (zenith angle >60°) which correspond to the best set of showers characterized by long tracks. For the non inclined showers of this last sample arrival direction analysis will still be possible while the energy estimation will be severely hampered by the shower attenuation in the atmosphere.

More quantitative results have been obtained by simulating showers according to the conditions of Table 1, determining the trigger efficiency in the different conditions, and by convoluting it with the corresponding aperture. Fig. 1 shows the ratio between the aperture in cloudy conditions compared to clear sky, for all events and for those events which have 'good quality' characteristics (clouds with $\tau <$ 1, and shower maximum well above the cloud top height).

More details can be found in [17]. From these results we

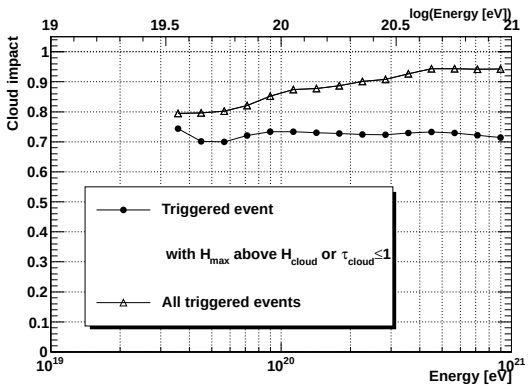


Figure 1: Ratio in the trigger efficiency for clear-sky and cloudy conditions.

conclude that 70% is a conservative estimate of the fraction of observing time in which the measurement will not be hampered by atmospheric factors. This number convoluted with the 20% duty-cycle, provides a final 14% factor to be applied to the aperture to determine the exposure Fig. 2.

4 Trigger rate and estimated exposure

The last parameter needed to estimate the aperture and the exposure is the trigger efficiency. Main objective of the trigger system is to reduce the rate of UHECR candidates to ∼0.1 Hz, limit imposed by downlink telemetry capabilities. The rejection level of the trigger algorithm determines the aperture of the instrument as a function of the energy. The rejection power depends also on the average night-glow background. In the following, the background has been assumed to be 500 ph/m^2/ns/sr.

Fig. 2 shows the full aperture, and annual exposure of JEM-EUSO in nadir mode for the entire FOV of the detector and for a few high quality conditions corresponding to "quality cuts". Quality cuts are defined by the better performance of the optics in the center of the FOV or for showers with inclined zenith angles ($\theta > 60°$ from nadir), which produce longer and less attenuated tracks.

Fig.2 shows that 80-90% of the full aperture is already reached at energies ∼2-3×10^{19} eV when the foot print of the shower is located in the central part of the FOV (R<150 km from nadir) and for showers with zenith angles $\theta > 60°$ (more details in [18]). The 80-90% is reached at ∼5×10^{19} eV if showers distributed in the entire FOV are considered.

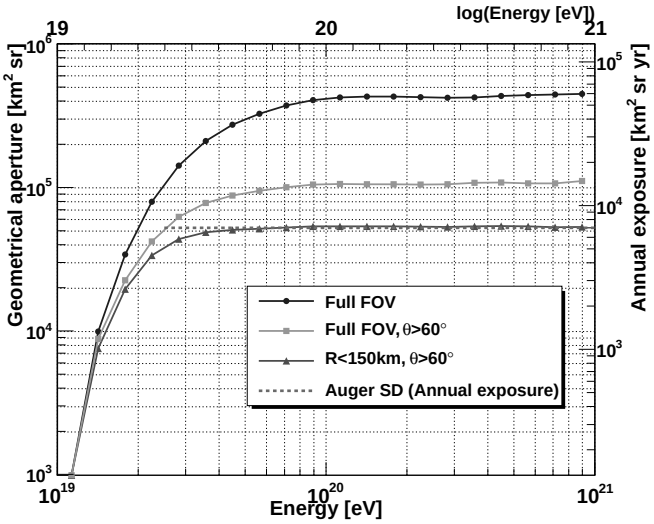


Figure 2: Aperture and annual exposure of JEM-EUSO for different quality cuts.

The convolution of the trigger aperture with the observational duty cycle and the cloud impact gives the annual exposure. In the most stringent conditions JEM-EUSO has an annual exposure equivalent to Auger (∼ 7 × 10^3 km^2 sr y) while it reaches ∼ 60 × 10^3 km^2 sr y at 10^{20} eV that is 9 times Auger. JEM-EUSO will well overlap (about one order of magnitude, starting from 2-3×10^{19} eV) with ground-based experiments to cross-check systematics and performances. At higher energies JEM-EUSO will be able to accumulate statistics at a pace per year at about one order or magnitude higher than currently existing ground based detectors. JEM-EUSO will also be operates in tilt mode to further increase the exposure at the highest energies ($E > 3 - 5 \times 10^{20}$ eV) by a factor of ∼3 compared to nadir mode. The optimization of the tilt parameters is still under evaluation.

5 Reconstruction capabilities

The JEM-EUSO reconstruction capabilities have been estimated using the ESAF code [19], a software for the simulation of space based UHECR detectors developed in the context of the EUSO ESA mission. Currently the ESAF code is being updated to the most recent JEM-EUSO configuration [20]. The technique to reconstruct the different

Table 2: Relative comparison of apertures and exposures of current and planned UHECR observatories.

Observatory	Aperture (km^2sr)	Status	Start	Lifetime	Duty Cycle × Cloud Impact	Annual Exposure (km^2 sr yr)	Relative Exposure Auger = 1
Auger	7000	Operations	2006	4(16)	1	7000	1
TA	1200	Operations	2008	2(14)	1	1200	0.2
TUS	30000	Developed	2012	5	0.14	4200	0.6
JEM-EUSO (E$\sim 10^{20}$eV)	430000	Design	2017	5	0.14	60000	9
JEM-EUSO (highest E) tilt mode $^\circ$	1500000	Design	2017	5	0.14	200000	28

shower parameters is extensively discussed in [21]. Regarding the energy reconstruction, at the current status of development of the instrument and of the reconstruction algorithms, proton showers with zenith angle $\theta > 60^\circ$ are reconstructed in clear-sky conditions with a typical energy resolution $\Delta E/E$ of $\sim 25\%(20\%)$ at energies around 4×10^{19} (10^{20}) eV. The energy resolution slightly worsen for more vertical showers where it is of the order of 30% around 10^{20} eV. This result indicates that the reconstruction of events with $E < 5 \times 10^{19}$ eV is still possible confirming the possibility of overlapping with ground based experiments over a sufficient wide energy range. Regarding the arrival direction analysis, our current results ([21]) indicate that showers of energy $E \sim 7 \times 10^{19}$ eV and zenith angle $\theta > 60^\circ$ can be reconstructed with a 68% separation angle less than 2.5°. Eventually our still preliminary results indicate that the X_{max} uncertainties the $\sigma_{X_{max}}$ are better than 70 g/cm^2 for $E \sim 10^{20}$ eV

6 Meeting the Scientific Requirements

The scientific requirements of the mission are described in detail in [2]. They can be summarized as: Observation area greater than 1.3×10^5km^2; Arrival direction determination accuracy better than 2.5° for 60° inclined showers at E $>1\times10^{20}$ eV (standard showers); Energy determination accuracy better than 30% for standard showers; $\sigma_{X_{max}} <$ 120 g/cm^2.

Results of simulations shown in the previous section confirm that the requirements can be already achieved with the current configuration.

The number of events that JEM-EUSO will observe depends of course on the UHE flux, which is uncertain especially at the highest energies. The apertures shown in fig. 2 can be however converted into number of events, assuming fluxes reported in literature by the Pierre Auger and the HiRes observatories [22, 23], and a conversion factor 0.14 between aperture and exposure (cloud impact included). We obtain more than 500 events with energy E $>5.5\times10^{19}$ eV for the flux measured by Auger and more than 1200 in the case of the HiRes spectrum.

A synthetic comparison between the JEM-EUSO aperture and exposure and the ones of other observatories is reported in Table 2.

7 Conclusions

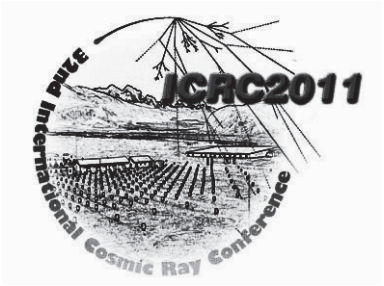
The expected performance of the JEM-EUSO mission has been reviewed. Simulations show that JEM-EUSO can reach almost full efficiency already at energies around 2.5-3×10^{19} for a restricted subset of events, and full aperture at energies E$> 5.5\times10^{19}$ eV. The expected annual exposure of JEM-EUSO at 10^{20} is equivalent to about 9 years exposure of Auger. The duty cycle and the impact of clouds has been assessed. Results indicate that the assumptions of 20% operational time and 70% cloud impact are matched by the present analysis. The angular, energy and X_{max} resolutions satisfy the requirements. The total number of events expected at energies E$> 5.5\times10^{19}$ in 5 years of operations ranges between 500 and 1200 events.

Acknowledgement: This work has been partially supported by Deutsches Zentrum fuer Luft- und Raumfahrt, and by the Italian Ministry of Foreign Affairs, General Direction for the Cultural Promotion and Cooperation.

References

[1] Y. Takahashi, New Journal of Physics, Vol. 11, N. 065009, 2009.
[2] T. Ebisuzaki, This Conference Proceedings, #120 (2011).
[3] A. Zuccaro Marchi, This Conference Proceedings, #852 (2011).
[4] F. Kajino, This Conference Proceedings, #1216 (2011).
[5] M. Rodriguez-Frias, This Conference Proceedings, #1031 (2011).
[6] A. Neronov, This Conference Proceedings, #301 (2011).
[7] K. Shinozaki, Proceedings 31^{th} ICRC, Lodz, Poland (2009).
[8] The EUSO Collaboration, EUSO: Report on the Phase A Study, Internal Note EUSO-PI-REP-002 (2003).
[9] Y. Kawasaki, This Conference Proceedings, #472 (2011).
[10] M. Ricci, This Conference Proceedings, #951 (2011).
[11] I. Park, This Conference Proceedings, #1246 (2011).
[12] J. Bayer, This Conference Proceedings, #836 (2011).
[13] M. Bertaina, Proceedings 31^{th} ICRC, Lodz, Poland (2009).
[14] P. Bobik, This Conference Proceedings, #886 (2011).
[15] C. Berat, Proceedings 28^{th} ICRC, Tsukuba, Japan (2003).
[16] F. Garino, This Conference Proceedings, #398 (2011).
[17] L. Saez, This Conference Proceedings, #1034 (2011).
[18] K. Shinozaki, This Conference Proceedings, #979 (2011).
[19] C. Berat *et al.* , *Full simulation of space-based extensive air showers detectors with ESAF* in *Astroparticle Physics*, Vol. 33, Issue 4, p. 22 (2010)
[20] F. Fenu, This Conference Proceedings, #592 (2011).
[21] F. Fenu, This Conference Proceedings, #633 (2011).
[22] F. Salamida, This Conference Proceedings, #893 (2011)
[23] R. U. Abbasi et al. (High Resolution Flys Eye Collaboration), Phys. Rev. Lett. 100, 101101 (2008)

32ND INTERNATIONAL COSMIC RAY CONFERENCE, BEIJING 2011



The potential of the JEM-EUSO telescope for the astrophysics of extreme energy photons

A.D. SUPANITSKY[1,2], G. MEDINA-TANCO[2] FOR THE JEM-EUSO COLLABORATION.
[1]*Instituto de Astronomía y Física del Espacio (IAFE), UBA-CONICET, Argentina.*
[2]*Instituto de Ciencias Nucleares, UNAM, Circuito Exteriror S/N, Ciudad Universitaria, México D. F. 04510, México.*
supanitsky@iafe.uba.ar

Abstract: Extreme energy photons are expected to be a minor component of the ultra high energy cosmic rays. Nevertheless, they are the carriers of very important astrophysical information related to the origin and propagation of such ultra energetic particles. JEM-EUSO is an orbital fluorescence telescope intended to observe the highest energy component of the cosmic rays, including photons and neutrinos. In this work we study several techniques to improve the discrimination between photon and proton showers in the context of the JEM-EUSO telescope. The most important parameter used to discriminate between protons and gammas is the atmospheric depth of the maximum of the showers, X_{max}. However, it can be demonstrated that, for a given available statistics, additional information is needed in order to take advantage of the full potential of the instrument. We propose and study additional parameters, related to the shape of the longitudinal profile, in order to obtain a better discrimination than the one given by X_{max} alone.

Keywords: Cosmic Rays; Photon Discrimination; Space Observation.

1 Introduction

Extreme high energy photons can be generated as a consequence of the interaction of the cosmic rays during their propagation through the intergalactic medium [1]. They can also be produced as by-products of the cosmic rays interactions in the acceleration sites [2] and, although disfavored by present data, they can be generated in top-down scenarios involving the decay of super heavy relic particles or topological defects [3]. At present there is no ultra high energy photon unambiguously identified.

High energy photons initiate air showers when they interact with the molecules of the atmosphere. In the high energy region the characteristics of such air showers are dominated by the LPM effect and pre-showering (i.e., photon splitting) in the geomagnetic field (see Ref. [4] for a review). In this work we present an improved version of the methods, recently proposed in Ref. [5], to calculate the upper limits on the photon fraction in the integral flux by using the X_{max} parameter, the atmospheric depth of the maximum development of the showers, in the context of the JEM-EUSO mission [6]. We also study and propose new parameters in order to improve the proton-photon separation in the energy range relevant to JEM-EUSO.

2 Upper limit calculation: X_{max}

Let us consider the ideal situation in which it is known that there is no photons in a given sample of N events. For this case, the expression for the upper limit to the photon fraction is given by [4],

$$\mathcal{F}_{\gamma}^{min} = 1 - (1-\alpha)^{1/N} \tag{1}$$

where α is the confidence level of rejection. However, in practice, the probability of the existence of photons must be realistically assessed through some observational technique which involves the determination of experimental parameters, which leads unavoidably to less restrictive upper limits than the previous one.

The method used to calculate the upper limit by using X_{max} parameter is based on the abundance estimator first introduced in [7],

$$\xi_{X_{max}} = \frac{1}{N}\sum_{i=0}^{N} \frac{f_{\gamma}(X^i_{max})}{f_{\gamma}(X^i_{max}) + f_{pr}(X^i_{max})} \tag{2}$$

where $f_{\gamma}(X_{max})$ and $f_{pr}(X_{max})$ are the photon and proton distribution functions, X^i_{max} are experimental values of X_{max} and N is the sample size. $\xi_{X_{max}}$ is an estimator of the photon abundance, $c_{\gamma} = N_{\gamma}/N$ where N_{γ} is the number of photons in the sample. The mean value and the variance of $\xi_{X_{max}}$ are given by,

$$E[\xi_{X_{max}}] = u_1 c_{\gamma} + u_2, \tag{3}$$

$$Var[\xi_{X_{max}}] = \frac{1}{N}\left[v_1 c_{\gamma} + v_2 + u_1^2 c_{\gamma}(1-c_{\gamma})\right], \tag{4}$$

where $u_1 = \alpha_1 - \alpha_2$, $u_2 = \alpha_2$, $v_1 = \alpha_3 - \alpha_4 + \alpha_2^2 - \alpha_1^2$ and $v_2 = \alpha_4 - \alpha_2^2$. Here

$$\alpha_1 = \int dX_{max} \frac{f_\gamma(X_{max})^2}{f_\gamma(X_{max}) + f_{pr}(X_{max})}, \quad (5)$$

$$\alpha_2 = \int dX_{max} \frac{f_\gamma(X_{max}) f_{pr}(X_{max})}{f_\gamma(X_{max}) + f_{pr}(X_{max})}, \quad (6)$$

$$\alpha_3 = \int dX_{max} \frac{f_\gamma(X_{max})^3}{[f_\gamma(X_{max}) + f_{pr}(X_{max})]^2}, \quad (7)$$

$$\alpha_3 = \int dX_{max} \frac{f_\gamma(X_{max})^2 f_{pr}(X_{max})}{[f_\gamma(X_{max}) + f_{pr}(X_{max})]^2}. \quad (8)$$

Note that the last term in the expression of the variance has to do with the binomial fluctuations of the process. It is assumed, for the present calculation, that the distribution functions of $\xi_{X_{max}}$ is Gaussian, which is valid for large enough values of N (due to the central limit theorem).

The upper limit to the photon fraction, for the case in which there is no photons in the sample, is given by,

$$\mathcal{F}_\gamma = \frac{1}{2u_1^2(1 + s_\alpha^2/N)} \left[\frac{s_\alpha^2}{N}(v_1 + u_1^2) + \sqrt{\frac{s_\alpha^4}{N^2}(v_1 + u_1^2)^2 + 4\frac{u_1^2 v_2}{N}(1 + \frac{s_\alpha^2}{N})} \right], \quad (9)$$

where, $s_\alpha = \sqrt{2}\,\mathrm{Erf}^{-1}(2\alpha - 1)$ and

$$\mathrm{Erf}(x) = \frac{2}{\sqrt{\pi}} \int_0^x dt \exp(-t^2). \quad (10)$$

A shower library was generated by using the last version of CONEX [8] (v2r2.3) which consist of 1.1×10^5 proton showers following a power law energy spectrum of spectral index $\gamma = -1$ in the interval $[10^{19.7}, 10^{21}]$ eV and with uniformly distributed arrival directions. Also 1.5×10^5 photon showers were generated under the same conditions but in this case cores were also uniformly distributed on the surface of the Earth in order to properly take into account pre-showering effect in the geomagnetic field. The distribution functions needed to calculate $\mathcal{F}_\gamma$ are obtained from the simulated data by using the non-parametric method of kernel superposition with adaptive bandwidth [9, 7].

Fig. 1 shows the upper limits on the fraction of photons in the integral cosmic ray flux, at 95% of confidence level, obtained in the ideal case $\mathcal{F}_\gamma^{min}$ (dashed line), by using the $\xi_{X_{max}}$ method (blue lines), and also the upper limits obtained by different experiments. The calculation is done for $E \geq 5 \times 10^{19}$ eV and $\theta \in [30^\circ, 80^\circ]$. For each method, the lines from bottom to top correspond to a Gaussian uncertainty on the determination of X_{max} of 0, 70, 120 and 150 g cm^{-2}. The number of events above a given energy, E_0, and the spectrum are obtained from Ref. [10]. The number of events corresponds to two years in nadir mode plus three years in tilt ($\alpha_{Tilt} = 38^\circ$) mode for the JEM-EUSO mission. Also, a reconstruction efficiency, taking into account the presence of clouds, of $\epsilon_R = 50\%$ is assumed (see Ref. [11]).

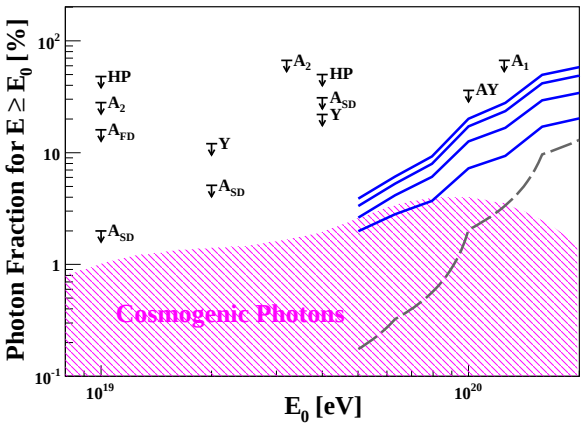
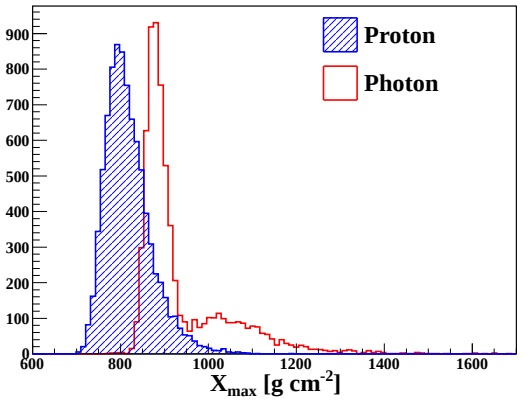


Figure 1: The upper limits on the fraction of photons in the integral cosmic ray flux at 95% of confidence level. Dashed line corresponds to the ideal case in which it is known that there is no photon in the data. Blue lines are the upper limits obtained by using $\xi_{X_{max}}$ method, they correspond, from bottom to top, to a Gaussian uncertainty of 0, 70, 120 and 150 g cm^{-2}. Shadow region is the prediction for the GZK photons [1]. Black arrows are experimental limits, HP: Haverah Park [12]; A_1, A_2: AGASA [13, 14]; A_{FD}, A_{SD}: Auger [15, 16]; AY: AGASA-Yakutsk [17]; Y: Yakutsk [18].

Note that, at the highest energies, the upper limit curves can be underestimated due to the decrease in the number of events. In this energy region the Gaussian approximation of the distribution function of $\xi_{X_{max}}$ could be not so good.

3 Photon-proton separation with skewness

In Ref. [19] it is shown that the skewness of the longitudinal profile of the showers is one of the best parameters to discriminate between primaries. However, its discrimination power depends on the part of the track of the cascade observed. Figure 2 shows the distributions of X_{max} and skewness for $\theta \in [30^\circ, 80^\circ]$ and $\log(E/eV) \in [19.7, 20]$. Skewness is calculated by using the part of the profiles between X_{max}-1000 g cm^{-2} and X_{max}+1000 g cm^{-2}. As discussed in [5] the X_{max} distribution presents two peaks, the one at lower values corresponds to the photons that suffered photon splitting in the geomagnetic field and the one at higher values corresponds to the ones that do not. From the figure it can be seen that skewness separates better photons from protons than X_{max}. The merit factor measures how good is a given parameter to discriminate between two species, it is defined as $MF = (E[x_{pr}] - E[x_{ph}])/\sqrt{Var[x_{pr}] + Var[x_{ph}]^2}$, where $E[x_A]$ and $Var[x_A]$ are the mean value and the variance of x_A with $A = \{pr,\ ph\}$ and pr = proton and ph = photon. The merit factors of X_{max} and skewness are ~ 1 and ~ 1.5, respectively, i.e., as mentioned before, the discrimination power is larger for skewness.



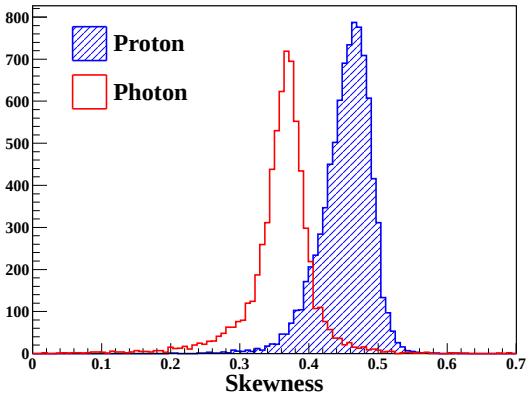


Figure 2: X_{max} and skewness distributions for $\theta \in [30°, 80°]$ and $\log(E/eV) \in [19.7, 20]$. Skewness is calculated with the part of the longitudinal profile between $X_{max} \pm$ 1000 g cm^{-2}.

The cut imposed to the events to calculate skewness has an efficiency. In particular, the profiles that passes the cut are such that they must hit the ground after propagating throughout an atmospheric depth larger than X_{max}+1000 g cm^{-2}. Figure 3 shows the efficiency of such cut for protons and for events with energy $\geq E_0$. For photons the efficiency is about a 10% smaller. Note that this cut favors showers of larger zenith angles, in particular, for protons, all the showers with $\theta > 55°$ pass the cut.

The upper limit on the photon fraction in the integral flux is obtained by using the method described above but in this case considering skewness instead of X_{max}. Figure 4 shows the results obtained, the blue curve corresponds to the result obtained for X_{max} without reconstruction uncertainty, the red curves correspond to skewness with (solid line) and without (dotted line) including the efficiency of the cut. As expected, the upper limit obtained by using skewness without including the efficiency of the cut is smaller, in almost the entire energy range, than the one obtained by using X_{max} without considering reconstruction uncertainties. However, when the efficiency of the cut is included the upper limit become larger than the corresponding to X_{max}. Note that the upper limit curves corresponding to skewness increase faster with primary energy than

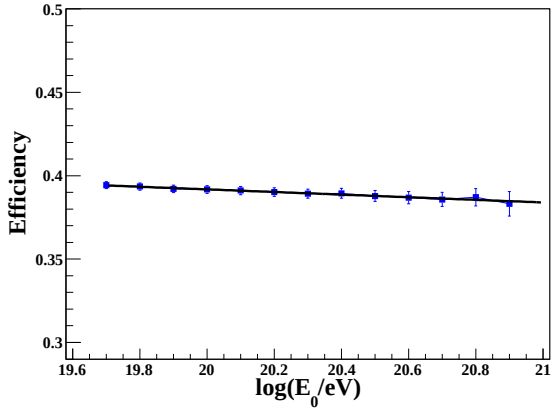


Figure 3: Efficiency of the cut imposed to the events to calculate skewness for $E \geq E_0$. Solid line: linear fit of the points.

the corresponding to X_{max}. This is due to the fact that the separation given by skewness is better for photons that do not convert in the geomagnetic field and the fraction of non converted photons decreases with primary energy.

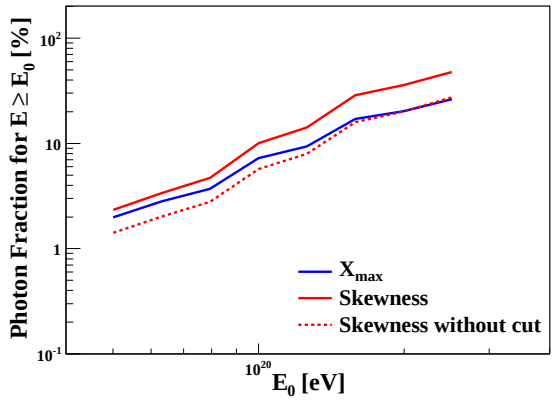


Figure 4: Upper limits on the fraction of photons in the integral cosmic ray flux at 95% of confidence level. Blue line is the upper limit obtained by using X_{max} parameter without including any reconstruction uncertainty. Red line correspond to skewness with (solid) and without (dotted) including the efficiency of the cut.

4 Two dimensional analysis

In order to improve the separation between photons and protons we introduce a new parameter intended to increase the separation power of profiles corresponding to converted photons. There is a population of converted photons for which the longitudinal profile is wider and with smaller N_{max} (number of charged particles at X_{max}). Therefore, a good parameter to separate this population should be the second derivative of the profile evaluated at the X_{max} po-

sition. For that purpose, following Ref. [20], a Gaussian fit of the profiles as a function of the age parameter $s = 3X/(X + 2X_{max})$ is performed. The second derivative at the maximum is given by,

$$a_s = \frac{N_{max}}{\sigma^2}, \tag{11}$$

where σ^2 is the variance obtained form the fit. Note that N_{max} and σ are parameters sensitive to mass composition (see references [19] and [20], respectively).

Figure 5 shows $la_s = \log(a_s/E_{19.7})$, with $E_{19.7} = E/10^{19.7}\text{eV})$, as a function of X_{max} for $\log(E/eV) \in [20.1, 20.2]$. The figure shows that, at these energies, most of the photons suffered photon splitting (the majority of the photon showers have $X_{max} < 1000$ g cm^{-2}). It also shows that la_s, in combination with X_{max}, also helps to the separation of narrower profiles with large N_{max}.

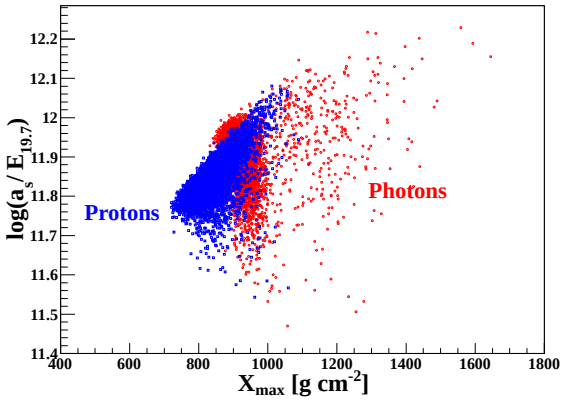


Figure 5: $la_s = \log(a_s/E_{19.7})$ as a function of X_{max} for $\log(E/eV) \in [20.1, 20.2]$ and $\theta \in [30°, 80°]$.

A two dimensional analysis is developed in order to assess the improvement on the separation between protons and photons combining different pairs of parameters. The method described in Ref. [21] is used to obtain the classification probability corresponding to different sets of parameters. The non-parametric method of kernel superposition with adaptive bandwidth [9, 7] is used to estimate the distribution functions corresponding to each primary and the leave-one-out technique [22] is used to estimate the classification probabilities for each set of parameters considered.

Figure 6 shows the classification probability as a function of primary energy, for $\theta \in [30°, 80°]$ and for the set of parameters: $\{X_{max}\}$, $\{X_{max}, \text{skewness}\}$ and $\{X_{max}, la_s\}$. From the figure it can be seen that adding skewness or la_s to the calculation with X_{max} alone, the classification probability increases. For energies of order of $10^{19.8}$ eV the skewness parameter increases the classification probability of X_{max} alone about 8% whereas la_s about 4%. This is due to the fact that skewness is good for the separation between protons and non converted photons, which at these energies are still quite abundant. As the energy increases the improvement due to the addition of skewness decreases and the corresponding to la_s increases. This is due to the fact that the fraction of converted photons increases with primary energy and la_s is good for the separation of this population whereas skewness do not.

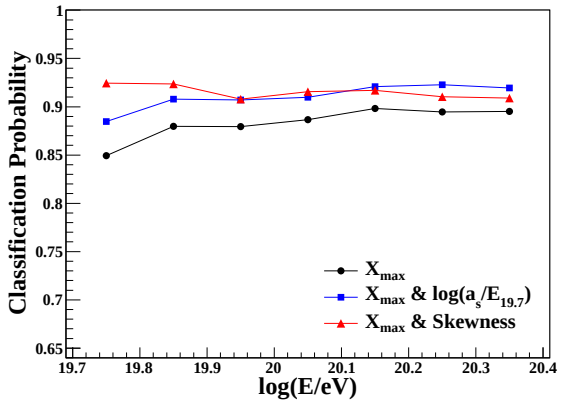


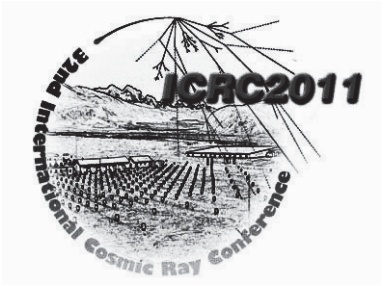
Figure 6: Classification probability as a function of primary energy for $\theta \in [30°, 80°]$.

The use of more than one parameter to calculate an upper limit to the photon fraction is a work in progress and will be presented in a forthcoming publication.

References

[1] G. Gelmini *et al.* , J. Exp. Theor. Phys., 2008, **106**: 1061.
[2] M. Kachelriess *et al.* , New J. Phys., 2009, **11**: 065017.
[3] R. Aloisio *et al.* , Phys. Rev., 2004, **D69**: 094023.
[4] M. Risse *et al.* , Mod. Phys. Lett., 2007, **A22**: 749.
[5] A. D. Supanitsky and G. Medina-Tanco, Astropart. Phys., 2011, **34**: 789.
[6] Y. Takahashi, New J. Phys., 2009, **11**:065009.
[7] A. D. Supanitsky, G. Medina-Tanco, A. Etchegoyen, Astropart. Phys., 2008, **31**: 75.
[8] T. Bergmann *et al.* , Astropart. Phys., 2007, **26**: 420.
[9] B. Silvermann: 1986, Density Estimation for Statistics and Data Analysis, ed. Chapman and Hall.
[10] K. Higashide *et al.* , Proc. 31st ICRC, 2009, #943.
[11] C. Berat et al., Astropart. Phys., 2010, **33**: 221.
[12] M. Ave *et al.* , Phys. Rev. Lett., 2005, **85**: 2244. M. Ave *et al.* , Phys. Rev., 2002,**D65**: 063007.
[13] M. Risse *et al.* , Phys. Rev. Lett., 2005, **95**: 171102.
[14] K. Shinozaki *et al.* , Astrophys. J., 2002, **571**: L117.
[15] J. Abraham *et al.* , Astropart. Phys., 2007, **27**: 155.
[16] J. Abraham *et al.* , Astropart. Phys., 2008, **29**: 243.
[17] G. Rubtsov *et al.* , Phys. Rev., 2006, **D73**: 063009.
[18] A. Glushkov *et al.* , JETP Lett., 2007, **85**: 163.
[19] F. Catalani *et al.* , Astropart. Phys., 2007, **28**:357.
[20] V. Scherini *et al.* , Proc. 30th ICRC, 2007, **4**: 523.
[21] A. Supanitsky *et al.* , Astropart. Phys., 2008, **31**: 116.
[22] A. Chilingarian, Comput. Phys. Commun., 1989, **35**: 441.

32ND INTERNATIONAL COSMIC RAY CONFERENCE, BEIJING 2011



Neutrino astrophysics with JEM-EUSO

A.D. SUPANITSKY[1,2], G. MEDINA-TANCO[2] FOR THE JEM-EUSO COLLABORATION.
[1]*Instituto de Astronomía y Física del Espacio (IAFE), UBA-CONICET, Argentina.*
[2]*Instituto de Ciencias Nucleares, UNAM, Circuito Exteriror S/N, Ciudad Universitaria, México D. F. 04510, México.*
supanitsky@iafe.uba.ar

Abstract: High energy neutrinos play a fundamental role on the understanding of several astrophysical phenomena and, in particular, on the origin and propagation of extreme energy cosmic rays. JEM-EUSO is a proposed orbital detector to be installed onboard the International Space Station. It is designed to observe the fluorescence light produced by the air showers initiated by the extreme energy component of the cosmic rays, including gamma rays and neutrinos. In this work we study the discrimination capability of the mission between nearly horizontal neutrino and proton showers, at the highest energies, by using the atmospheric depth of maximum development. We propose a new method to discriminate between electron neutrino and tau horizontal showers, developing very deep in the atmosphere, by using the multi-peak structure that they present. We also study the flux of tau leptons emerging from the Earth, including the case of the presence of oceans, produced by the interaction of tau neutrinos inside the Earth for a given model of gamma ray bursts and in the context of the JEM-EUSO mission.

Keywords: Cosmic Rays; High Energy Neutrinos; Space Observation.

1 Introduction

The astrophysical information carried by very high energy neutrinos is very important for the understanding of the origin and propagation of the cosmic rays. Such particles can be produced during the propagation of the cosmic rays in the interstellar medium [1], as by-products of the hadronic interaction in the sources [2] and as the main product of the decay of superheavy relic particles [3, 4].

In this work we study the characteristics of inclined tau and electron neutrino showers and its discrimination from the proton component in the context of the JEM-EUSO mission [5]. The main parameter used to separate the different species is X_{max}, the atmospheric depth of the maximum development of the showers.

Also, an extension of the study presented in Ref. [6] about showers initiated by neutrinos that interact in the central region of the field of view of the JEM-EUSO telescope (in nadir mode) is developed. A possible technique to identify the presence of both tau and electron neutrinos in a given sample is proposed.

Finally, the propagation of tau neutrinos inside the Earth is studied. In particular, neutrinos originated in gamma ray bursts are considered, for which the propagation in the presence of oceans is compared with the one in the mantle of the Earth.

2 Inclined neutrino showers

Neutrinos can initiate atmospheric air showers when they interact with the nucleons of the air molecules. The probability that a neutrino interact in the atmosphere increases with zenith angle because of the increase of the number of target nucleons. High energy neutrinos, propagating through the atmosphere, can suffer charge (CC) and neutral (NC) current interactions. The CC interactions are the most important for the space observations because in the NC interactions most of the energy is take by a secondary neutrino which could produce an observable air shower just in the case it suffers a subsequent CC interaction. The shower produced by the hadronic component resultant from the NC interaction is difficult to observe from the space due to the high energy threshold of the telescope.

As a result of a CC interaction, a very high energy lepton, which takes most of the energy of the incident neutrino, is generated. Typically, it takes $\sim 80\%$ of the neutrino energy at $E_\nu \cong 10^{20}$ eV, the rest of the energy goes into the hadronic component.

Proton and neutrino showers of $E = 10^{20}$ eV and $\theta = 85^\circ$ are simulated in order to study their characteristics and its possible identification. The last version of CONEX [7] (v2r2.3) with QGSJET-II [8] is used to generate the proton and neutrino showers. Electron and tau neutrino showers are considered. The program PYTHIA [9], linked with LHAPDF [10], is used to simulate the electron neutrino-nucleon interactions. The CTEQ6 [11] set of parton distri-

bution functions are used. The air showers are generated injecting the produced particles in CONEX [6]. For the case of tau neutrinos it is just consider the decay of tau leptons of $E = 10^{20}$ eV, for which the simulation program TAUOLA [12] is used.

The interaction points of the neutrino showers are simulated by taking at random values of the atmospheric depth from an exponential distribution, $P(X) \propto \exp(-X/\lambda_\nu(E_\nu))$ with $\lambda_\nu(10^{20}eV) = 3.2 \times 10^7$ g cm^{-2}, in the interval $[0, X_{end}]$ where X_{end} is the atmospheric depth from the top of the atmosphere to the core position, which for $\theta = 85°$ is ~ 10573 g cm^{-2}. Note that due to the large mean free path of the neutrinos the exponential distribution can be approximated by the uniform distribution in the interval $[0, X_{end}]$.

Figure 1 shows the profiles for some simulated events. The neutrino showers that develop deeper in the atmosphere can present more than one peak, this is due to the LPM fluctuations suffered by showers dominated by the electromagnetic component. For the case of tau leptons, just in $\sim 18\%$ of the decays a high energy electron or positron is produced, $\tau^\pm \to e^\pm \nu_\tau \nu_e$. The showers produced by this channel that develop deep in the atmosphere can have more than one peak. On the other hand, in every electron neutrino interaction a high energy electron or positron is produced, increasing the probability of finding a shower with more than one peak. This is the reason why 15% of electron neutrino showers present more than on peak whereas the same happens with just 1% of the tau neutrino showers.

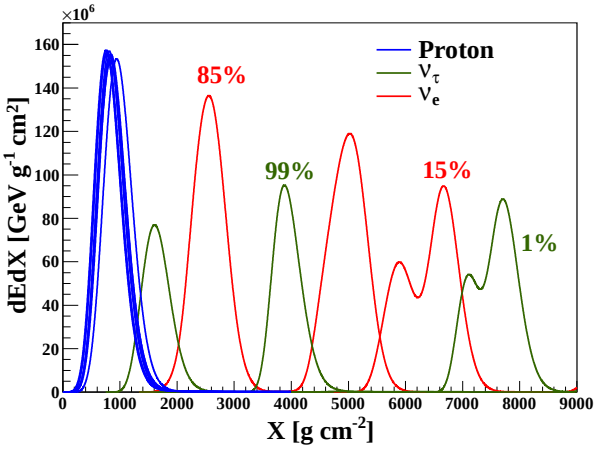


Figure 1: Simulated proton and neutrino showers of $E = 10^{20}$ eV and $\theta = 85°$.

Note that about 17.51% of the taus decay into a muon and two neutrinos, $\tau^\pm \to \mu^\pm \nu_\tau \nu_\mu$. The showers initiated by the muons are quite difficult to observe from the space because the deposited energy of these kind of showers is much smaller than the regular ones. Therefore, these type of showers are excluded from the subsequent analyses.

Figure 2 shows the distributions of the first peak of the simulated showers. Just the events with the first peak above 1 km of altitude are taken into account, which is equivalent to consider the ones whose first peak has an atmospheric depth less than ~ 9000 g cm^{-2}. It can be seen that, above ~ 1600 g cm^{-2} the distributions corresponding to tau and electron neutrinos are flat and extended over a huge interval of atmospheric depth, which allows a very efficient discrimination of the neutrino showers from the proton ones. Note that, as expected, the overlap between the X_{max} distributions of protons and taus is larger than the corresponding one to protons and electron neutrinos.

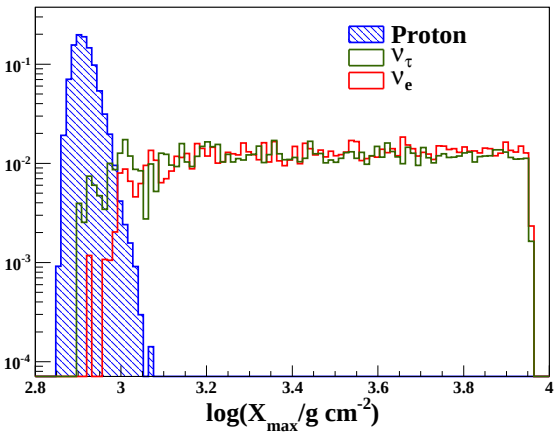


Figure 2: Distribution of the first peak of the profiles for proton and neutrinos of $E_\nu = 10^{20}$ eV and $\theta = 85°$.

3 Horizontal neutrino showers

In this section the showers generated by horizontal neutrinos that interact in the central region of the field of view of the JEM-EUSO telescope, in nadir mode, are considered. For the case of electron neutrinos, this showers are dominated by the LPM effect and can present more than one peak [6]. As mentioned before, just $\sim 18\%$ of the tau showers are initiated by electrons or positrons, diminishing in this way the probability to find showers with more than one peak. Figure 3 shows the distributions of the first peak for tau and electron neutrino showers of $E = 10^{20}$ eV and $\theta = 90°$ injected in the center of the field of view (fov) of JEM-EUSO at sea level. These distributions present two populations. The population with smaller values of X^1_{max} corresponds to showers dominated by the hadronic component and the other one corresponds to showers dominated by the electromagnetic component. As expected, the hadronic population is more important for tau showers.

Figure 4 shows the probability to find showers with exactly $N_{X^i_{max}}$ peaks for electron neutrino and tau showers. At sea level, the probability to find a tau shower with just one peak is $\sim 98\%$ whereas for electron neutrinos is $\sim 65\%$. At an altitude of 5 km, the probability to find a tau shower with just one peak is $\sim 99\%$ whereas for electron neutrinos is $\sim 76\%$. The reduction of the probability to find more than one peak with increasing altitudes has to do with the fact

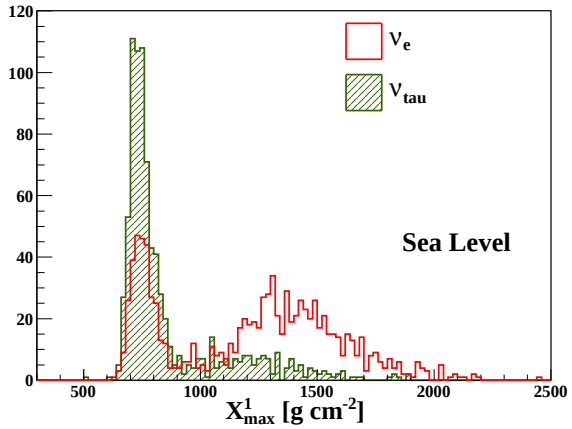


Figure 3: Horizontal tau and electron neutrino showers of $E = 10^{20}$ eV injected in the center of the field of view of the JEM-EUSO telescope and at sea level.

that the development of the showers takes place in regions with smaller values of air density, therefore, the influence of the LPM effect is also reduced.

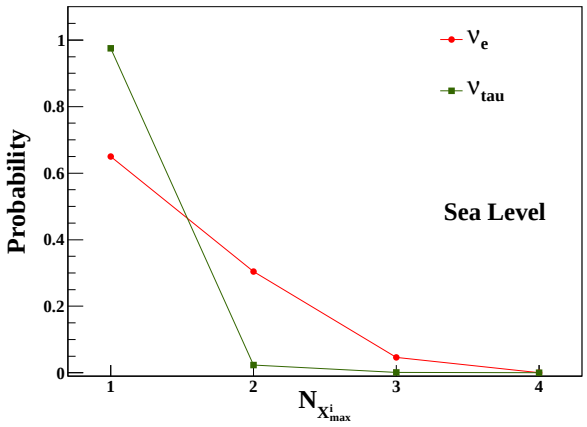


Figure 4: Probability to find showers with exactly $N_{X^i_{max}}$ peaks for horizontal tau and electron neutrino showers of $E = 10^{20}$ eV, injected in the center of the field of view of the JEM-EUSO telescope in nadir mode.

The difference between the number of showers with just one peak can be used to study the relative abundance of tau and electron neutrino showers. Due to the large decay length of the taus at 10^{20} eV ($\sim$ 5000 km), the ratio between the number of tau neutrino and electron neutrino horizontal showers (starting in the center of the fov of the telescope) is of order of $N_{sh}(\nu_\tau)/N_{sh}(\nu_e) \cong 0.07$, assuming that the relative abundances of the incident flux are equal to one. Upper panel of figure 5 shows the region (in blue) of 95% of probability to find a fraction of n_1/N showers with just one peak, as a function of the sample size N, obtained from simulations, for a mixture of equal number of incident tau and electron neutrinos. Note that showers corresponding to the muonic decay channel of the tau are not included in the analysis. Observed values of n_1/N smaller than the black solid line reject the hypothesis that the sample is composed by tau showers alone, with probability of rejection larger or equal to 0.95, depending of the particular value of n_1/N. Also, observed values of n_1/N larger than the red solid line reject the hypothesis that the sample is composed by just electron neutrino showers with probability of rejection larger or equal to 0.95, again depending on the particular value of n_1/N. From the figure it can be seen that for 95% of the cases, samples of more than 15 showers are needed to be able to reject the hypothesis of having tau showers alone. Although not shown in the figure, the number of events needed to reject the hypothesis of having a sample with electron neutrinos alone has to be grater than $\sim$ 9300.

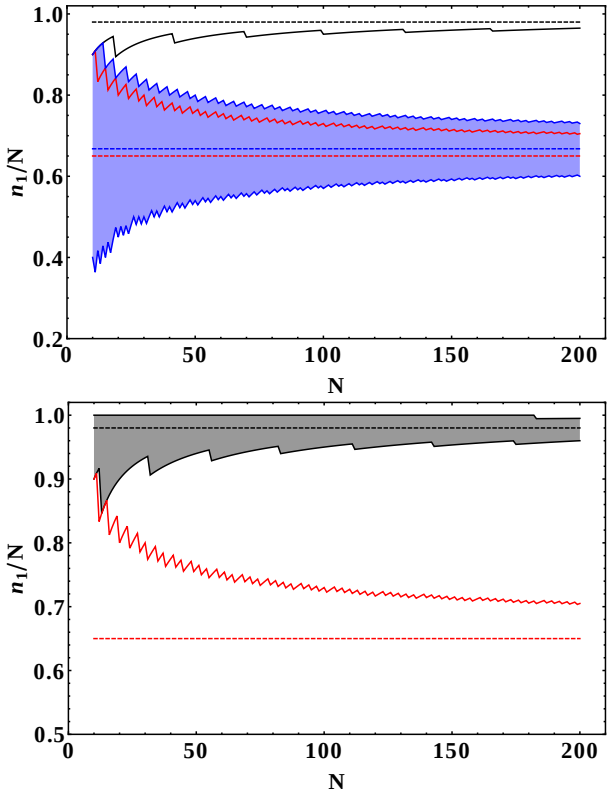


Figure 5: Shadowed region corresponds to 95% of probability to find a fraction n_1/N of showers with just one peak, for a mixture of equal number of incident tau and electron neutrinos (upper panel) and for the case in which the incident flux contains just tau neutrinos (bottom panel), as a function of the sample size N.

Bottom panel of figure 5 shows the region of 95% of probability to find a fraction of n_1/N showers with just one peak obtained from a binomial distribution, for the case in which the samples have just tau showers, as a function of the sample size N. It can be seen that for 95% of the cases, samples of more than $\sim$ 17 events are needed to be able to reject the hypothesis of having electron neutrino showers alone.

It is important to note that as the energy decreases the ratio $N_{sh}(\nu_\tau)/N_{sh}(\nu_e)$ goes to one, as a consequence the number of events needed to reject the hypothesis of having a sample with electron neutrinos alone decreases drastically.

4 Earth skimming tau neutrinos

Gamma ray bursts are potential sources of high energy cosmic rays [13, 14]. If the cosmic rays are efficiently accelerated in GRBs a neutrino flux is expected as a result of the photo-hadronic interactions of protons with the photons present in the acceleration site [15]. The detection of high energy neutrinos in coincidence with GRBs should be a proof of the acceleration of cosmic rays in this kind of events.

Depending on the redshift of the GRB, the JEM-EUSO telescope will be able to observe Earth skimming tau neutrinos, detecting the Cherenkov flashes originated by the showers produced by the decay of the taus after propagation inside the Earth [16].

A modified version of the ANIS [17] program is used to propagate tau neutrinos inside of the Earth. We have improved the propagation and energy lose of the taus in order to study the case in which the taus traverse interfaces between rock and water which is the case of taus emerging from or entering to the oceans.

Two cases are considered, for the first one, the last or external layer of the Earth, of 3 km of thickness, is composed by standard rock of density 2.6 g cm^{-3}. For the second case, this last layer is composed by water, i.e. of density 1 g cm^{-3}. Following Ref. [16] tau neutrinos of 70° of nadir angle are considered. The energy spectrum of the tau neutrinos, used in the simulations, is the one corresponding to figure 2 of Ref. [16].

Figure 6 shows the energy distributions of the tau neutrinos injected into the simulation (black lines), the ones that produced an emerging tau lepton (blue lines), the emerging taus (green lines) and the energy that effectively goes to the shower (magenta lines). This last distribution is obtained by simulating the tau decay with TAUOLA and summing the energy of the particles that contribute to the shower, i.e. all particles excepting neutrinos.

In the case of rock the probability of a tau to emerge from the Earth is $P_R(\nu_\tau \rightarrow \tau) = 5.7 \times 10^{-4}$ and the median of the energy distribution of the taus is $med(E^R_\tau) \cong 4 \times 10^{16}$ eV. For the case in which the last layer of the Earth is composed by water $P_W(\nu_\tau \rightarrow \tau) = 2.9 \times 10^{-4}$ and $med(E^W_\tau) \cong 6 \times 10^{16}$ eV. Therefore, the number of emerging taus for the case where the last layer of the Earth is made of water is about a factor two smaller than the corresponding to rock, whereas, on average, the energy of the emerging taus is larger for the case of water. This is due to the fact that the energy lose of taus is smaller in the presence of water because the density of water is smaller. In principle, the presence of oceans could deteriorate the detectability of tau showers because of the reduction of the number of emerging taus.

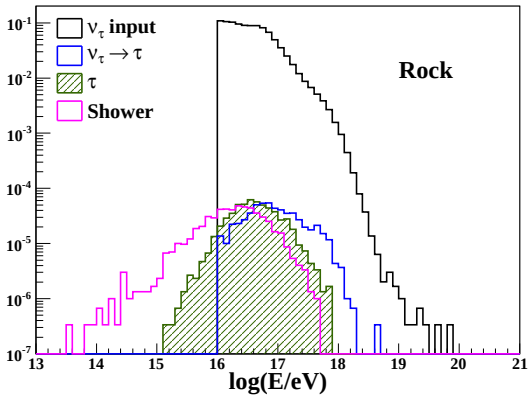


Figure 6: Energy distributions corresponding to the propagation of tau neutrinos of 70° of nadir angle following the energy spectrum of the GRB model of figure 2 of Ref. [16]. Black lines: input spectra; blue lines: neutrinos that produced an emerging tau; green lines: emerging taus; magenta lines: energy that goes to the showers (see the text for details).

The simulation of the Cherenkov photons that reach the JEM-EUSO telescope is the last step to complete the simulation chain for Earth skimming tau neutrinos (without considering the detector which is simulated with the ESAF [18] software). These simulations are under development and will allow us to study in detail the influence of the presence of oceans on the detectability of tau neutrinos from GRBs.

References

[1] V. Berezinsky et al., Phys. Lett., 1969, **28B**: 423.
[2] M. Kachelriess et al., New J. Phys., 2009, **11**: 065017.
[3] R. Aloisio et al., Phys. Rev., 2004, **D69**: 094023.
[4] P. Battacharjee et al., Phys. Rept., 2000, **327**: 109.
[5] Y. Takahashi, New J. Phys., 2009, **11**:065009.
[6] A. D. Supanitsky et al., Astropart. Phys., 2011, **35**: 8.
[7] T. Bergmann et al., Astropart. Phys., 2007, **26**: 420.
[8] S. Ostapchenko, Nucl. Phys. Proc. Suppl., 2006, **B151**: 143.
[9] T. Sjostrand et al., JHEP, 2006, **0605**: 026.
[10] M. Whalley et al., http://hepforge.cedar.ac.uk/lhapdf/.
[11] P. Nadolsky et al., Phys. Rev., 2008, **D78**: 013004.
[12] N. Davidson et al., arXiv:1002.0543.
[13] E. Waxman, Phys. Rev. Lett., 1995, **75**: 386.
[14] M. Vietri, Astrophys. J., 1995, **453**: 883.
[15] E. Waxman et al., Phys. Rev. Lett., 1997, **78**: 2292.
[16] K. Asano et al., Proc. 31st ICRC, 2009, #692.
[17] A. Gazizov and M. Kowalski, Comput. Phys. Comm., 2005, **172**: 203.
[18] C. Berat et al., Astropart. Phys., 2010, **33**: 221.

The Focal Surface of the JEM-EUSO Instrument

YOSHIYA KAWASAKI[1], MARCO CASOLINO[1,2], KAZUHIRO HIGASHIDE[3], NAOYA INOUE[3], ANDREA SANTANGELO[4], MARCO RICCI[5], FUMIYOSHI KAJINO[6], TOSHIKAZU EBISUZAKI[1] AND THE JEM-EUSO COLLABORATION[7]
[1]*Advanced Science Institute, RIKEN, 2-1 Hirosawa, Wako 351-0198, Japan*
[2] *INFN and Physics Department of Univresity of Rome ``Tor Vergata'', Via della Ricerca Scientifica 1, 00133 Rome, Italy*
[3]*The Graduate School of Science and Technology, Saitama University, Shimoohkubo, Sakura-ku, Saitama 338-8570, Japan*
[4]*Astronomie und Astrophysik, Eberhard-Karls-Universität, Sand 1, 72076 Tübingen, Germany*
[5]*INFN, Laboratori Nazionali di Frascati, Via Enrico Fermi 40, I-00044 Frascati, Italy*
[6]*Department of Physics, Konan University, Okamoto 8-9-1, Higashinada, Kobe 658-8501, Japan*
[7]*http://jemeuso.riken.jp/*
yoshiya@riken.jp

Abstract: The Extreme Universe Space Observatory on JEM/EF (JEM-EUSO) is a space mission to study extremely high-energy cosmic rays. The JEM-EUSO instrument is a wide-angle refractive telescope in the near-ultraviolet wavelength region which will be mounted to the International Space Station. Its goal is to measure time-resolved fluorescence images of extensive air showers in the atmosphere. In this paper we describe in detail the main features and technological aspects of the focal surface of the instrument. The JEM-EUSO focal surface is a spherically curved surface, with an area of about 4.5 m^2. The focal surface detector is made of more than 5,000 multi-anode photomultipliers (MAPMTs). Current baseline is Hamamatsu R11265-03-M64.

Keywords: Ultra High Energy Cosmic rays, Instrumentation.

1 Introduction

The Extreme Universe Space Observatory on JEM/EF (JEM-EUSO) is a space mission to study extremely high-energy cosmic rays [1,2,3,4]. The JEM-EUSO instrument is a wide-angle refractive telescope in the near-ultraviolet wavelength region which will be mounted to the International Space Station. Its goal is to measure time-resolved fluorescence images of extensive air showers in the atmosphere. The focal surface is a spherically curved surface, and its area amounts to about 4.5 m^2.

2 JEM-EUSO Focal Surface

The Focal Surface (FS) of JEM-EUSO has a curved surface of about 2.35 m in diameter, and it is covered with about 5,000 Multi-Anode Photomultipliers Tubes, MAPMTs, (Hamamatsu R11265-M64). It makes ±30º FOV and 0.07º angular resolution.
The FS detector consists of Photo-Detector Modules (PDM), each of which consists of 9 Elementary Cells (EC) arranged in an array of 3 × 3. About 1,233 ECs, corresponding to about 137 PDMs, are arranged on the whole FS (Figure 1).

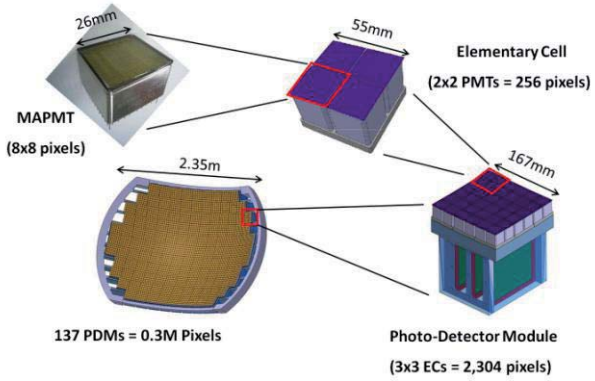


Figure 1. JEM-EUSO Focal Surface

3 Photo-detector

JEM-EUSO is a photon-hungry experiment; its expected photon ratio is <100 photons/μsec/pixel around shower maximum. And its FS detector should have high detection efficiency. The FS detector should have single photon counting capability in the near-ultraviolet wavelength region to avoid the systematic errors, which may be introduced through the gain drift. It should be reliably and stably operational in Space environment for at least 3 or 5 years mission period. For the above reason, MAPMTs with UV-glass entrance window are employed as sensors of the FS detector.

Present baseline choice is the Hamamatsu R11265-03-M64 (see Fig. 2, Fig. 3), which was developed by RIKEN in collaboration with Hamamatsu Photonics K.K.
It has an ultra-bialkali photo-cathode, which transforms photons into electrons, and amplifies photo-electrons by means of a stack of metal channel dynodes. The signals are taken from the anode which is formatted as an array of 8 × 8. The photon detection efficiency of this is about 0.3 in the near-ultraviolet wavelength region.

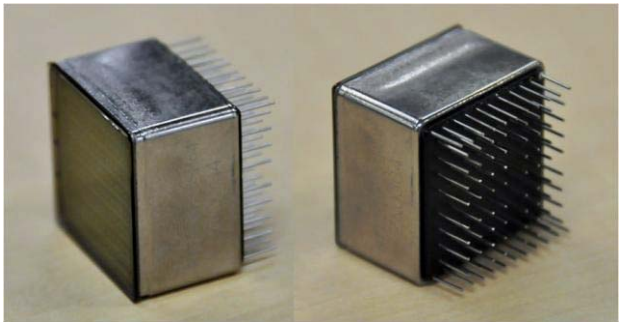


Figure 2. The MAPMT for the JEM-EUSO photo-detector (R11265-03-M64)

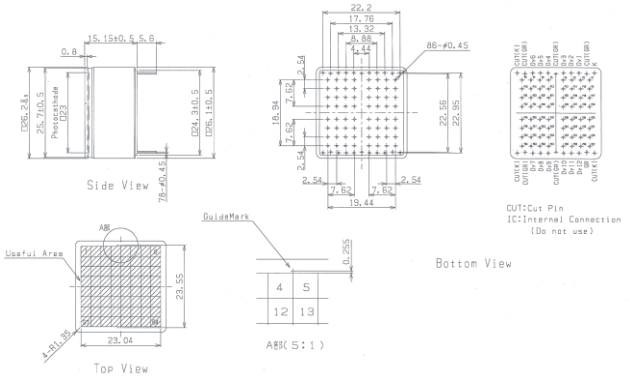


Figure 3. The Dimensional drawing of the MAPMT(R11265-03-M64)

Figure 4 shows single photo-electron spectra measured for the R11265-03-M64. Each single photo-electron peak is enough distinguished above the pedestal to use the single photon counting measurement.

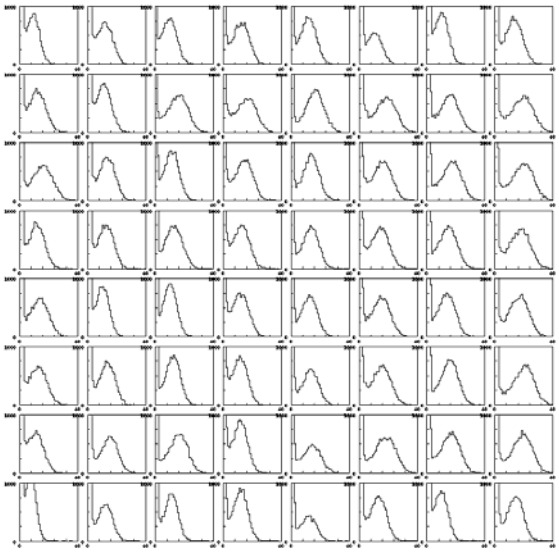


Figure 4. Sample of the single photo-electron spectra of R11265-03-M64.

Figure 5 shows the sensitivity map of the MAPMT for each pixel. The sensitivities of each pixel are clearly separated and it has almost no crosstalk.

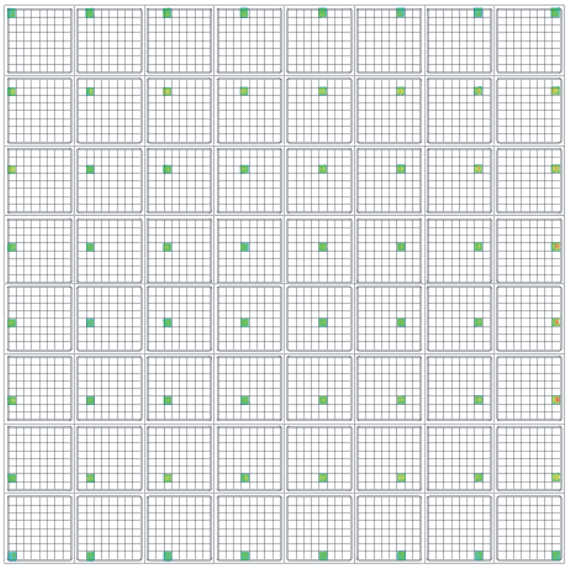


Figure 5. Sample of the pixel sensitivity map of R11265-03-M64.

4 Photo-Detector Module

PDM is the basic unit of the data acquisition of the JEM-EUSO telescope. PDM consists of the following components.

- 36 MAPMTs
- Front-End readout ASIC boards [5]
- 1st trigger board [6]
- Power Supply board
- High Voltage Supply boards [7]
- PDM Mechanical Structure [8]

Figure 6 shows Prototype of the PDM Mechanical Structure with 12 MAPMTs.

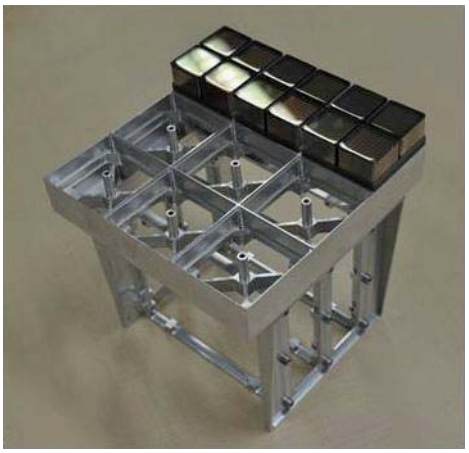


Figure 6. Prototype of the PDM Mechanical Structure with 12 MAPMTS

5 Focal Surface Mechanical Structure

The FS of JEM-EUSO is composed of a grid of ~5,000 MAPMTs arranged in modular support structures, that cover all the surface to collect the light of the optical system.

The FS is a portion of a sphere of radius 2785 mm, inserted within an in-plane section 2650 mm × 1900 mm (allowed by the HTV Exposed Pallet dimensions). We have studied the FS geometry and analyzed different PDMs distributions in order to maximize their number within the allocated space. The adopted configuration consists of a total of 137 PDMs lying in 11 rows along the parallels of the mentioned sphere, with one PDM located at the center of the FS geometry as shown in Figure 7.

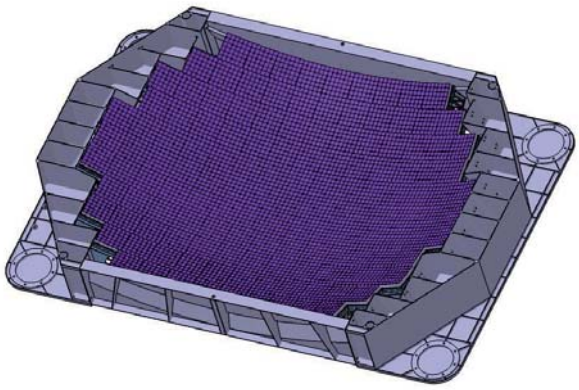


Figure 7. Focal Surface Assembly

6 Conclusion

We have developed a very large area photo-detector system for the JEM-EUSO focal surface, based on the Photo-Detector Module. We will start to build the full system when the JEM-EUSO mission is started.

Acknowledgements

These works are parts of the JEM-EUSO study of each country.

Reference

[1] Y.Takahashi et al., New J. Phys., **11**, 065009, doi: 10.1088/1367-2630/11/6/065009, 2009.
[2] T.Ebisuzaki et al., Nucl. Phys. B (Proc. Suppl.) **175–176** (2008) 237–240.
[3] T.Ebisuzaki et al., Proc. 32th ICRC, Beijing, 2011, #1628
[4] F.Kajino et al., Proc. 32th ICRC, Beijing, 2011, #
[5] S.Ahmad et al., Proc. 32th ICRC, Beijing, 2011, #0232.
[6] I.Park et al., Proc. 32th ICRC, Beijing, 2011, #1246.
[7] J.Szabelski et al., Proc. 32th ICRC, Beijing, 2011, #0216.
[8] M.Ricci, et al., Proc. 32th ICRC, Beijing, 2011, #0335.

The JEM-EUSO Focal Surface Mechanical Structure

M. RICCI[1], M.A. FRANCESCHI[1], T. NAPOLITANO[1] FOR THE JEM-EUSO COLLABORATION
[1]*INFN, Laboratori Nazionali di Frascati, Via E. Fermi 40, I-00044 Frascati, Italy*
marco.ricci@lnf.infn.it

Abstract: JEM-EUSO is a space mission devoted to study extremely high-energy cosmic rays on board of the Japanese Experiment Module on the International Space Station (ISS). The JEM-EUSO instrument is a wide-angle refractive telescope in near-ultraviolet wavelength region to observe time-resolved atmospheric fluorescence images of the extensive air showers. The Focal Surface (FS) is a spherical curved surface, area about 4.5 m^2, composed by a grid of ~5,000 Multi Anode Photo Multipliers Tubes arranged in modular support structures, Elementary Cells and Photo Detector Modules (PDM) that cover all the surface to collect the light of the optical system. The design of the FS mechanical structure is presented together with the PDM support structure. FEM analysis, to study the optimization of the overall configuration, is described as well as the acoustic and random loads evaluation, stress analysis and mass optimization. Prototypes of the first PDM modules are shown and discussed.

Keywords: Ultra High Energy Cosmic rays, Instrumentation

1 The JEM-EUSO Mission

The Extreme Universe Space Observatory on Japanese Experiment Module (JEM-EUSO) [1, 2, 3, 4] is a science mission planned to be launched by a H2B rocket about JFY 2016 and transferred to the International Space Station (ISS) by a H2 Tranfer Vehicle (HTV). It will be attached to the Exposed Facility of the Japan Experiment Module, "KIBO".
The main objective of the mission is to investigate the nature and origin of Extreme Energy Cosmic Rays (EECR) beyond energies of the order of $E_0 > 5\times10^{19}$ eV, to perform charged-particle astronomy in this energy region by collecting a large sample of events (~ 500-1000 above E_0) in 3-5 years of operation and to measure their energy and arrival direction with sufficient accuracy in order to infer the energy spectrum of the sources.
JEM-EUSO is a wide-angle telescope (60 degrees full field of view) and consists of high-transmittance Fresnel lenses 2.5 m in diameter, an advanced photo-sensitive detector at the focal surface and a suitable electronics. An infrared camera and a LIDAR system will also be used to monitor the Earth's atmosphere and provide significant information on cloud coverage.

2 The Focal Surface Mechanical Structure

The Focal Surface (FS) of JEM-EUSO (Figure 1) is composed by a grid of ~5,000 Multi Anode Photo Multipliers Tubes (MAPMT, Hamamatsu M64) arranged in modular support structures, Elementary Cells (EC) and Photo Detector Modules (PDM) (Figure 2), that cover all the surface to collect the light of the optical system. The design of FS and PDM mechanics has been studied and developed at INFN-Frascati National Laboratories.

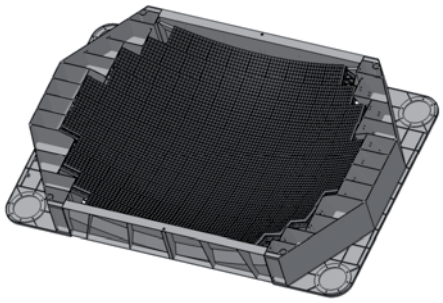


Figure 1. Focal Surface Mechanical Structure Assembly.

2.1 FS Geometry

The focal surface is a portion of sphere of radius 2505 mm, inserted within an in-plane section 2650 mm x 1900 mm (allowed by the HTV Exposed Pallet dimensions) (Figure 3).
An extensive use of CAD (Computer Aided Design, CATIA v.5) has been done to study the Focal Surface geometry and to analyze different PDM distributions in order to maximize their number within the allocated space.
The adopted configuration consists of a total of 137 PDMs lying in 11 rows along the parallels of the men-

tioned sphere, with one PDM located at the center of FS geometry as shown in Figure 4.

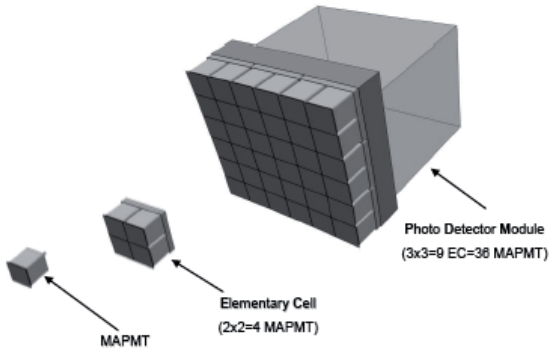


Figure 2. MAPMT Modular Arrangement, the Elementary Cell and the Photo Detector Module.

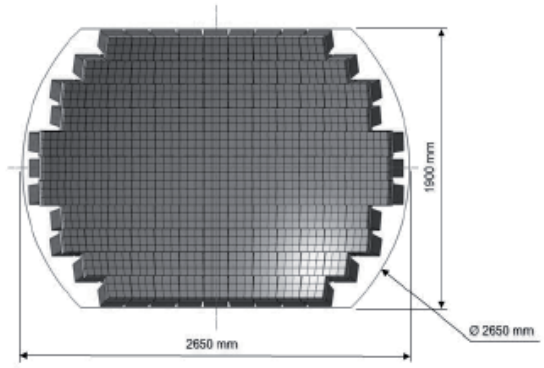


Figure 3. Focal Surface front view and overall dimensions.

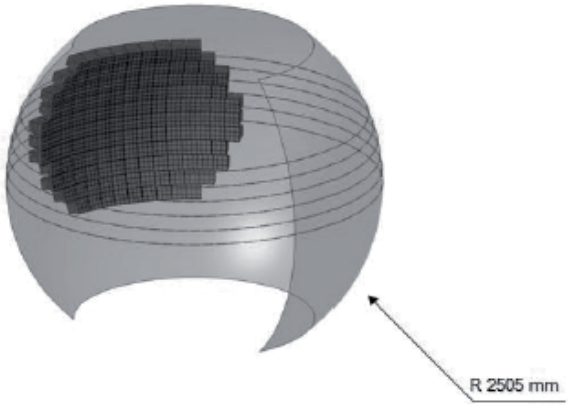


Figure 4. PDM Arrangement on the Focal Surface.

2.2 PDM Mechanical Structure

Each PDM is composed by 3x3 Elementary Cells and each EC is composed by 2x2 Multi Anode Photomultiplier Tubes.
The mechanical structure, shown in Figure 5, is designed in order to place the 9 ECs on a spherical surface (radius 2505 mm) in the same way as for the overall geometry (Figure 6).

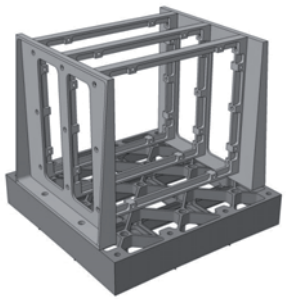


Figure 5. PDM Mechanical Structure.

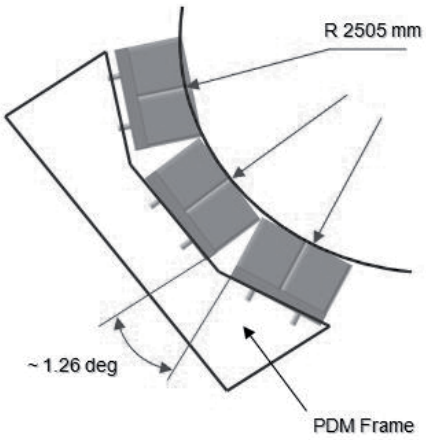


Figure 6. PDM Spherical Shape.

The frame on which the ECs are positioned presents quite a complex shape (Figure 7) and is built by machining a single aluminum alloy piece, with a mass reduction, at the end of machining, larger than 87% (from 2,7 kg to 0,330 kg).

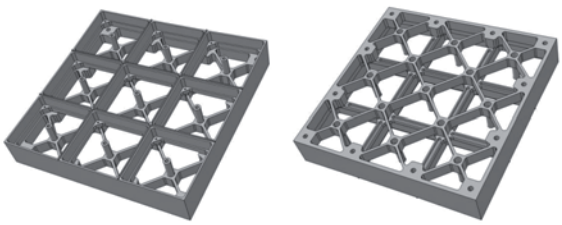


Figure 7. PDM Frame (front and rear view).

This frame, besides allocating the ECs, is rigidly connected to the main FS structure (Top Frame), contributing to the overall rigidity and strength. Each EC base can accomodate two electronic boards (MAPMT, ASIC) (Figure 8), while the PDM layout is completed by 5 aluminum alloy frames supporting 6 electronic boards: 1 board for PDM electronics, 1 board for High Voltage, 3 boards for Power Distribution and 1 optional board. The total mass of each PDM mechanics is 0,624 kg.

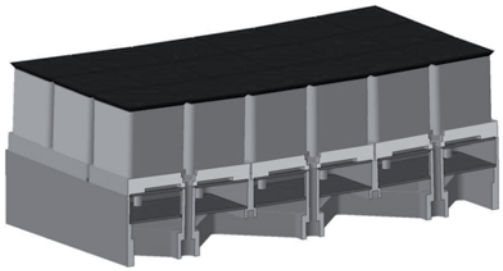


Figure 8. PDM Frame Section.

2.3 FS Structure (Top Frame)

The FS main structure, Top Frame (Figure 9), is an assembled structure, composed by 2 head Master Frames, connected by 2 Side Frames and 10 supporting "Ribs" lying along the parallels of the Focal Surface sphere, as shown in Figure 10.

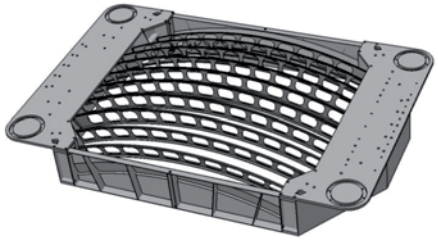


Figure 9. Top Frame – Rear View.

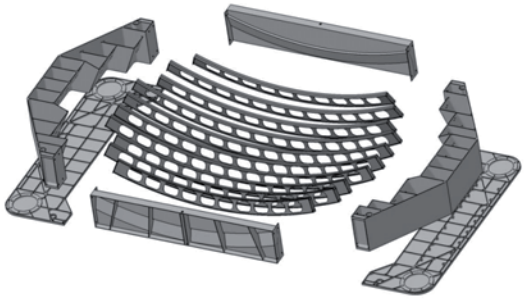


Figure 10. Top Frame – Front View (Exploded).

Locking bars housings are positioned in Master and Side Frames for a total of 6 holes: 2 in each Master Frame (∅ 50 mm) 1 in each Side Frame (∅ 20 mm). Threaded holes have been considered for Tilting Mechanism connection as well for Electronics Boxes, FRGF, GPS, etc.; reinforced zones are provided for the connection to the 4 telescopic masts foreseen for the telescope deployment to the operational configuration.

2.4 Structural Analysis and Mass Optimization

FEM (Finite Element Method) analyses have been worked out in order to evaluate the consistency of the Top Frame and optimize its mass (minimize) and first natural frequency (maximize). As already mentioned, PDMs mechanical structures, once connected with fasteners to the main structure, become part of it giving their contribution in terms of rigidity and strength (Figure 11). The material considered is aluminum alloy 7075-T7351, both for main structure and PDM structure, for its good properties in terms of strength, elongation, crack toughness and machining.

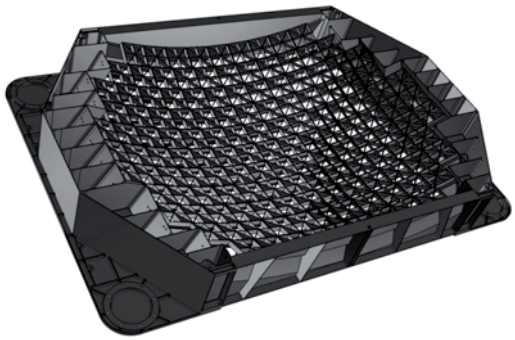


Figure 11. CAD Model for FEM Analysis (Top Frame + PDM Frames).

The Modal Analysis reports the first natural frequency of 45,7 Hz while Stress Analysis led to a maximum Von Mises stress at launch of 105 MPa localized at few points, with an average stress less than 10 MPa over most of the structure.

3 Prototypes

Besides design, simulations and FEM studies, real prototypes of the PDM modular structure have been recently produced in the INFN-Frascati National Laboratories mechanical workshop: the mechanics of few complete PDM was realized in aluminum alloy (6000 Series, Alcoa Mic-6). In particular, a sector of 3 PDMs has been worked out in order to test the assembly procedure on the main structure and to check any possible issue due to curvature (Figures 12 and 13).

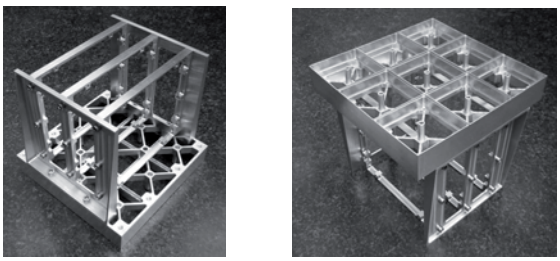


Figure 12. PDM Prototypes.

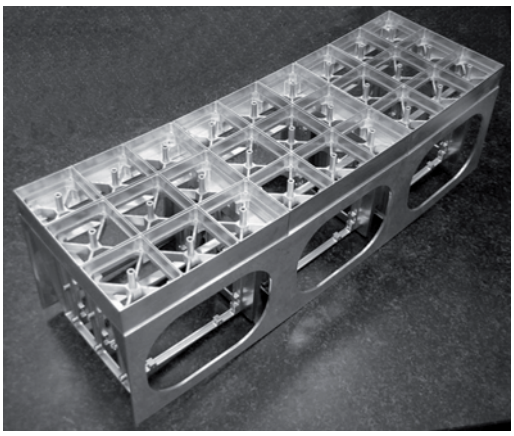


Figure 13. Focal Surface Sector Prototype (3 PDMs).

4 Space Qualification Studies

Based on the above described design, space qualification studies have started with National Aerospace Companies in order to delivery the Focal Surface Assembly consisting of:

· Structure
· Thermal Control
· On Board Data Handling
· Harness
· Integration
· Qualification
· Pertinent GSE (Ground Support Equipment)

The activities under study will comply to a System Engineering Approach and be organized in Program Phases typical of the design of a space mission.
A combined Structural/Thermal Model of JEM EUSO is being proposed for the following purposes:

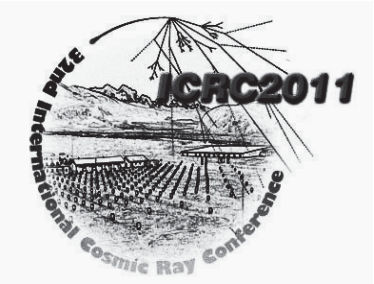
- verify the FEM model by modal survey included in sine test;
- derive, respectively confirm the structural loads for subsystems and equipment;
- achieve qualification for the spacecraft structure;
- verify the structural strength of primary/secondary structure versus qualification loads;
- verify the spacecraft thermal design;
- verify the interface to launcher adapter;
- verify the mechanical interface between PLM (Payload Module) and SVM (Service Module);
- exercise the alignment methodology and demonstrate the alignment stability.

References

[1] Y. Takahashi and the JEM-EUSO Collaboration, New J. Phys., 2009, **11,** 065009
[2] T. Ebisuzaki, “The JEM-EUSO mission”, these proceedings, ID1628
[3] G. Medina-Tanco, “ Science objectives of the JEM-EUSO mission”, these proceedings, ID0956
[4] A. Santangelo, “Requirements and Expected Performances of the JEM-EUSO mission”, these proceedings

Aknowledgments

This work was partially supported by the Italian Ministry of Foreign Affairs, General Direction for the Cultural Promotion and Cooperation.



SPACIROC: A Front-End Readout ASIC for Spatial Cosmic Ray Observatory

SALLEH AHMAD[1],PIERRE BARRILLON[1], SYLVIE BLIN-BONDIL[1], SYLVIE DAGORET-CAMPAGNE[1],CHRISTOPHE DE LA TAILLE[1], FREDERIC DULUCQ[1], GISELE MARTIN-CHASSARD[1], YOSHIYA KAWASAKI[2], HIROKO MIYAMOTO[2], HIROKAZU IKEDA[3],TATSUNARI IGUCHI[4] AND FUMIYOSHI KAJINO[4] FOR THE JEM-EUSO COLLABORATION.
[1]*Omega/LAL/IN2P3/CNRS Université Paris Sud 11,*
Laboratoire de l'Accélérateur Linéaire,
Bâtiment 200,91898 Orsay Cedex,France
[2]*Computational Astrophysics Lab, RIKEN*
Hirosawa 2-1,Wako, Saitama 351-0198, Japan
[3]*Institute of Space and Astronautical Science, JAXA,*
Yoshinodai 3-1-1, Sagamihara, Kanagawa 252-5210, Japan
[4]*Physics Department, Konan University*
Okamoto 8-9-1, Higashinada, Kobe, Hyogo 658-8501, Japan
ahmad@lal.in2p3.fr

Abstract: The SPACIROC ASIC is designed for the JEM-EUSO fluorescence imaging telescope onboard of the International Space Station. Its goal is the detection of Giant Air Showers above a few 10^{19} eV, developing at a distance of about 400 km, downward in the troposphere. From such distance, most of the time, the number of the photons expected in the pixels is very weak, ranging from a few units to a few tens. For such running conditions, we propose a low-power, rad-hard ASIC which is intended for reading out a 64-channel Multi-Anode Photomultiplier. The two main features of this ASIC are the photon counting mode for each input and the charge-to-time (Q-to-T) conversions for the multiplexed channels. In the photon counting mode, the 100% triggering efficiency is achieved for 50fC input charges. For the Q-to-T converter, the ASIC requires a minimum input of 2pC. Moreover SPACIROC is required to have a low power dissipation which is around 1mW/channel. We will describe in details the architecture of this ASIC and how the required specifications are satisfied. SPACIROC is a result of the collaboration between OMEGA/LAL-Orsay, France, RIKEN, ISAS/JAXA and Konan University, Japan on behalf of the JEM-EUSO consortium.

Keywords: Front-End, ASIC, Low-power, DAQ

1 Introduction

The primary purpose of JEM-EUSO [1] mission is the detection of the Extensive Air Showers (EAS) created by the Extreme Energy Cosmic Rays (EECR $>10^{19}$ eV), inside the atmosphere. JEM-EUSO, which is a fluorescence telescope, looking downward, that should be installed on the JEM module of the International Space Station, will detect the fluorescent photons released by the EAS. By observing these phenomena from the upper side of the atmosphere, this telescope will be able to identify the EECR.

SPACIROC (Spatial Photomultiplier Array Counting and Integrating Readout Chip) was designed according to the requirements from the JEM-EUSO consortium. Multi-anode photomultipliers (MAPMT) are proposed to be the sensitive device of the JEM-EUSO observatory focal surface. SPACIROC [2] was designed to accommodate the readout of these MAPMTs. As JEM-EUSO is intended to track the fluorescent light, this ASIC is required to count the number of photons reaching each pixel of the MAPMTs. The secondary mission of SPACIROC is to measure the intensity of photon flux by performing charge to time (Q-to-T) conversion. The layout of SPACIROC is shown in figure 1. The final dimensions are 4.6 mm x 4.1 mm (19mm²) and it was submitted to the foundry in March 2010. The chip was developed using the 0.35µm SiGe process from AMS.

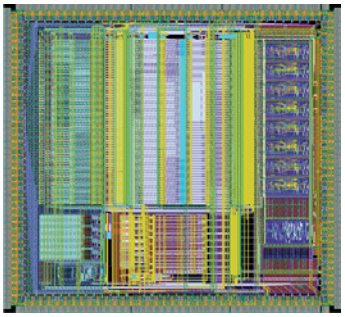


Figure 1 : SPACIROC layout

2 The ASIC

SPACIROC offers 64 inputs dedicated to the anodes of one MAPMT and 1 input for the last dynode. For the following, the MAPMT gain is assumed to be 10^6 in order to have 1 photoelectron (1 p.e.) around 160 fC.

2.1 Specifications

The specifications for the chip are the following:

- 64 channels preamplifier with independent gain (8-bit) adjustment.
- Photon Counting : 64 channels.
- Q-to-T converter : 1 channel for last dynode + 8 internal channels (multiplexed inputs).
- 100% trigger efficiency for charge greater than 50 fC (~1/3 p.e.).
- Q-to-T converter input range: 2 pC – 400 pC (12.5 p.e – 2500 p.e.).
- Power consumption : 1 mW/channel.
- 9 data serial outputs.

This circuit was designed for low-power spaceflight applications. SPACIROC is also radiation hardened by design against Single Event Latchup (SEL) and Single Event Upset (SEU).

2.2 Architecture

The general architecture of SPACIROC could be divided into 3 main blocks: the Photon Counting, the Q-to-T converter (called KI) and the digital part. The Photon Counting and KI are the analog section of this ASIC. The digital part of SPACIROC is used to count photon triggered pulses and to measure the photon intensity. The readout management are also implemented in the digital part. The architecture of SPACIROC is represented in figure 2. However figure 2 doesn't include the auxiliary components of the ASIC such as the bandgap reference, DACs and signals monitoring.

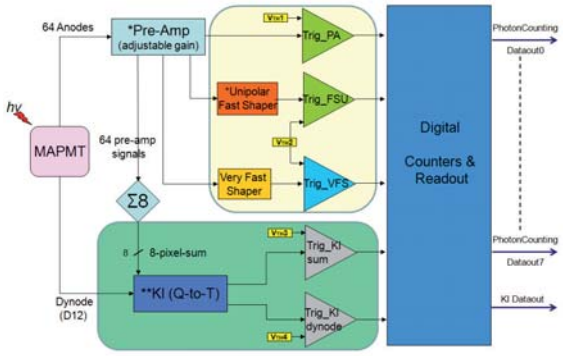


Figure 2: SPACIROC general architecture.

The 64 signals from MAPMT anodes are fed through the preamplifiers which offer adjustable gain to correct the gain non-uniformity of the MAMPT. The preamplified signals are fed to the Photon Counting and KI in order to transform these signals into discriminator pulses. These discriminator pulses will be made available at the inputs of the digital part for counting and measuring. Each mentioned block will be described in the following sections. The use of the word "trigger(s)" in the next sections will refer to the Photon triggered pulses on the outputs of the analog part.

3 Analog Design

3.1 Photon Counting

The 64-channel Photon Counting block is required to discriminate the preamplifier signal into trigger pulses. This operation is done in parallel for each channel. For this prototype, the ASIC offers three different discriminator outputs (Trig_PA,Trig_FSU and Trig_VFS) for each channel. The reason of having three different discriminators is to verify the performances of each triggering scheme under laboratory tests before choosing the design which represents the best trade-off between noise, speed and power consumption. Figure 3 shows the block diagram of the Photon Counting analog part.

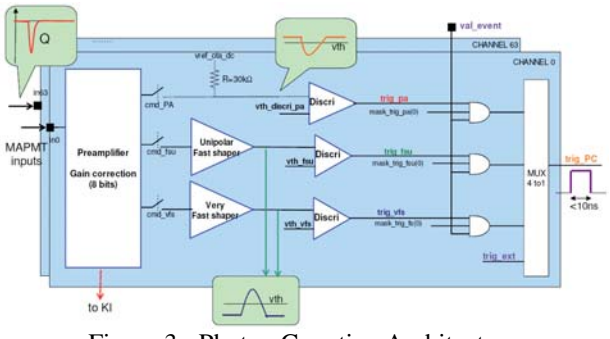


Figure 3: Photon Counting Architecture

The output for the first trigger design, which is called Trig_PA, is obtained from the preamplifier signal which is fed directly into a discriminator. Due to its simple architecture (a preamplifier and a discriminator), this design has the lowest power consumptions compared to the other trigger designs in the Photon Counting part. Estimated power consumption of Trig_PA analog part is 0.36mW/channel.

For the next two trigger designs (Trig_FSU and Trig_VFS), the preamplifier signal is fed to shapers before reaching the discriminators. The shapers will add more gain to the preamplifier signal. As for the second trigger design, Trig_FSU, a low-noise with adjustable-gain shaper called FSU from MAROC3 [3] chip is used. The output pulse of the Trig_FSU is obtained by comparing the FSU signal to a fixed threshold. The power dissipation for Trig_FSU is estimated at 0.56mW/channel.

For the last trigger design, Trig_VFS, a shaper is also used here. The shaper, which is known as VFS, has a larger gain and a faster shaping time compared to the FSU shaper. The output signal this design is obtained by discriminating the VFS signal. The power consumption for Trig_VFS is around 0.54mW/channel.

These three discriminator outputs are sent to the digital block via a 4-to-1 analog multiplexer. The fourth input of the multiplexer is for the external trigger signal which is used to test the digital block independently. Two 10-bit DACs are used in this block. One DAC is shared between Trig_FSU and Trig_VFS trigger designs as both designs will discriminate signals that have the same polarity and baseline. The other DAC is used for setting threshold in the Trig_PA trigger design because of the inverted polarity of the preamplifier signal at the discriminator input. Each trigger output could be masked independently as only one trigger could be used at one time.

3.2 KI

Another important feature of this ASIC is the ability to perform the Charge to Time (Q-to-T) conversion by measuring the signal duration over a fixed threshold. Q-to-T conversion is done by the 9-channel KI block. The first 8 inputs of the KI converters receive the pre-amplified signals of the MAPMT anodes. The pre-amplified signals are reorganised into the sum of every 8 neighbouring channels or pixels; hence the given name of 8-pixel-sum for this part. However, the 9th input of KI takes a signal coming directly from the dynode of the MAPMT. The gathered data on the dynode could be used for the MAPMT protection strategy (gain reduction against high photon flux) in the JEM-EUSO experiment. Figure 4 shows the general architecture of this converter.

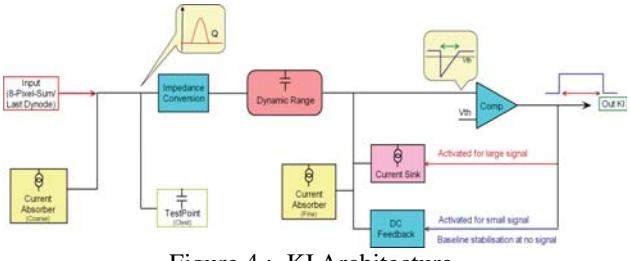


Figure 4 : KI Architecture

An impedance converter (Impedance Conversion) and a capacitive network (Dynamic Range) are used to transform the input current pulse into a voltage signal. The Impedance Conversion circuit will convert the low impedance input (~50Ω) of the KI part into higher impedance. The Dynamic Range circuit is used to scale the input dynamic range. The scaling is done via the ASIC configuration parameters in order to obtain the appropriate capacitance value for integrating the input signal. If the input signal is strong enough, it will produce a discriminator output, which in turn will deactivate the DC Feedback baseline and activate a variable gain current source (Current Sink). Once the current source takes over, the integrated signal length can be adjusted according to the selected current value. The 9-channel discriminator outputs can be masked individually or all at once. It is also possible to use external inputs for testing the digital part independently. This converter was designed in collaboration with RIKEN, Japan. The design is based on their KI02/03[4] chip.

3.3 Simulation results

The analog part of Photon Counting and KI were fully simulated. Figure 5 shows the simulations for the Photon Counting block. The injected charge are 1/3 p.e, 1 p.e and 10 p.e. The simulations results indicate that Photon Counting block could achieve 100% trigger efficiency starting from 1/3 p.e.

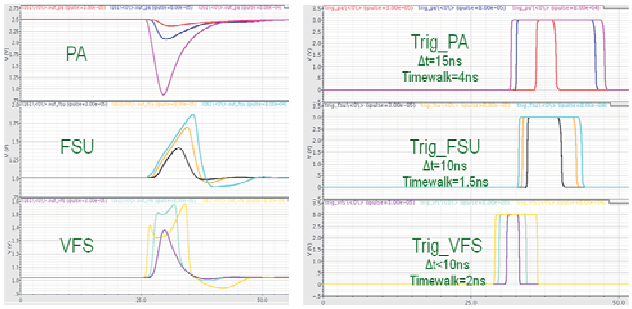


Figure 5 : Photon Counting simulations

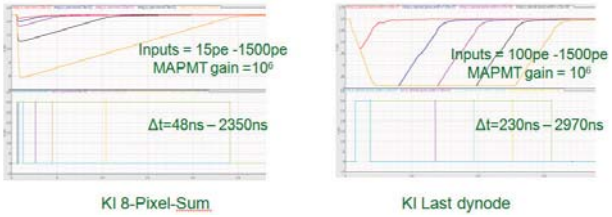


Figure 6 : KI simulations

The Figure 6 shows the simulations results of the KI block for the summed channels and the MAPMT dynode pulses. For the simulations, charges ranging from 15p.e. to 1500p.e. are injected into input of KI last dynode and 100p.e. – 1500p.e. are injected into the KI 8-pixel-sum inputs. The expected trigger widths could vary up to 2970 ns.

4 Digital Design

All the data acquisition and readout are done within a defined time slot which is call Gate Time Unit (GTU=2.5µs). This means that during every cycle of

GTU, the present data are acquired and the previously recorded data are sent out on the serial links.

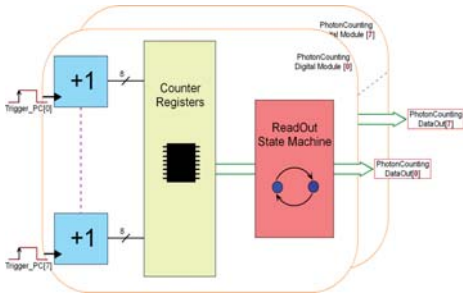


Figure 7 : Photon Counting digital

For the Photon Counting (figure 7), the digital part is organised into 8 identical modules. Each module will handle 8 triggers from Photon Counting analog part. The discriminator output's rising edge is used to clock an 8-bit counter which could operate up to 100 MHz. Each Photon Counting digital module will have 64-bit counters data and these data are transmitted on a serial data link. To summarise, 8 Photon Counting digital modules are required to manage 64 channels of Photon Counting and 8 serial links are used to send the counter data simultaneously.

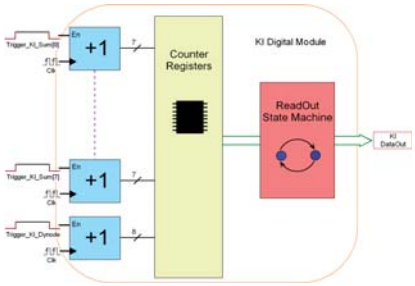


Figure 8 : KI digital

The digital part for the KI (figure 8) has the same architecture as the digital part for Photon Counting. However it has some minor differences for certain components. As the KI part has 9 channels, only one digital module is used. The KI discriminator outputs are sampled by the digital block system clock. The readout management program has been written differently so that it could accommodate a bigger channel number.

The digital part of SPACIROC was designed carefully in order to minimize area usage, to reduce power consumption and to increase the robustness of the system. Flip-flops in critical areas are implemented in Triple Modular Redundancy (TMR) configuration in order to mitigate the effects of SEU.

5 Measurements

The ASIC was received in October 2010 and extensive tests have been carried out. A test board (figure 9) and a Labview interface have been developed for testing SPACIROC.

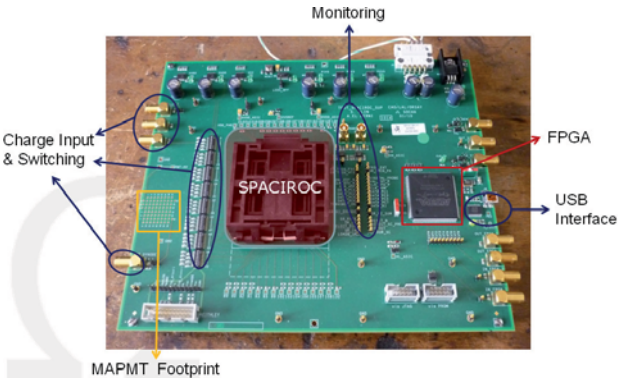


Figure 9 : SPACIROC test board

Test results have shown that the ASIC is working quite well and exhibits expected behaviours. Nearly all the important features are available and SPACIROC is capable of sending out data of Photon Counting and KI charge measurements.

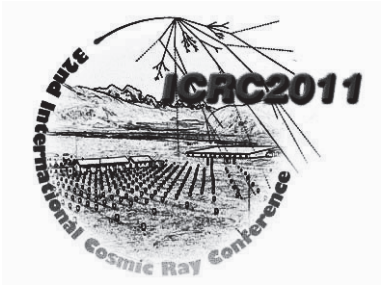
6 Conclusions

To conclude, SPACIROC ASIC has been proven to work and exhibits good behaviour. Extensive tests are being carried out in order to characterise the chip completely. Current test results have shown that SPACIROC could achieve 30 ns double pulse separation and measuring input charges up to 1000 p.e. The measured power consumption under typical operating condition is around 1.1mW/channel. Further work on improving the chip is currently underway so that it could be ready for mass production.

References

[1] Y. Takahashi et al., New Journal of Physics, Vol. 11, 2009 pp. 065009
[2] S. Ahmad et al., SPACIROC: A Rad-Hard Front-End Readout chip for the JEM-EUSO telescope, 2010 JINST 5 C12012
[3] P. Barrillon et al., MAROC3,Multi-Anode ReadOut Chip for MAPMTs, 2010 IEEE NSS/MIC.
[4] F. Kajino et al., Front-End Readout Asic for the JEM-EUSO Focal Surface Detector, 2009 ICRC icrc0711

32ND INTERNATIONAL COSMIC RAY CONFERENCE, BEIJING 2011



Performance of a front-end ASIC for JEM-EUSO

HIROKO MIYAMOTO[1], SALLEH AHMMAD[2], PIERRE BARRILLON[2], SYLVIE BLIN-BONDIL[2], SYLVIE DAGORET-CAMPAGNE[2], CHRISTOPHE DE LA TAILLE[2], FREDERIC DULUCQ[2], TATSUNARI IGUCHI[3], HIROKAZU IKEDA[4], FUMIYOSHI KAJINO[3], YOSHIYA KAWASAKI[1], GISELE MARTIN-CHASSARD[2], KENJI YOSHIDA[3] ON BEHALF OF THE JEM-EUSO COLLABORATION
[1]*Advanced Science Institute, RIKEN*
Hirokosawa 2-1, Wako, Saitama 351-0198, Japan
[2]*OMEGA/LAL/IN2P3/CNRS/Universitè Paris-Sud, Laboratoire de l'Accèlèrateur Linèaire*
Bâtiment 200, 91898 Orsay Cedex, France
[3]*Physics Department, Konan University*
Okamoto 8-9-1, Higashinada, Kobe, Hyogo 658-8501, Japan
[4]*Institute of Space and Astronautical Science, JAXA*
Yoshinodai 3-1-1, Sagamihara, Kanagawa 252-5210, Japan
hirokom@riken.jp

Abstract: The SPACIROC (Spatial Photomultiplier Array Counting and Integrating ReadOut Chip) is a Front-End ASIC designed for the space-borne fluorescence telescope JEM-EUSO[1][2]. The device is designed for features of single photon counting, dynamic range of 1 photoelectron (PE) to 1500 PEs, double pulse resolution of 10 ns, and low power consumption ($<$1 mW/ch). SPACIROC reads output signals from a 64-channel Multi-Anode Photomultiplier Tube (MAPMT). Input photons are measured in the two features as following: photon counting mode for each input and charge-to-time (Q-to-T) conversion mode for the multiplexed channels. The combination of these two features enables the large dynamic range as described above. We will report the performance of the ASIC such as power consumption, double pulse resolution, dynamic range and linearity.

Keywords: JEM-EUSO FRONT-END ASIC DAQ

1 Introduction

JEM-EUSO (Extreme Universe Space Observatory on board Japanese Experiment Module) is a mission which aims the observation of Extreme Energy Cosmic Rays (EECRs) with a space-borne fluorescence telescope on the International Space Station (ISS). The detector will consist of five thousand 1-inch-square MAPMTs, and will allow an area of about 400 kilometers in diameter of Earth's atmosphere to be imaged in the field of view. Since 2006 the Phase A study of JEM-EUSO has been continued with extensive simulations, design, and prototype hardware developments that have significantly improved the JEM-EUSO mission profile, targeting the launch of 2016 in the framework of the second phase of JEM/EF (Japanese Experiment Module/Exposure Facility) utilization.
The main physical sources of interest of JEM-EUSO are the fluorescent and Cherenkov UV photons induced by cosmic rays with energies higher than $10^{19}eV$ impinging on the atmosphere leading the development of an Extensive Air Showers (EAS) in the troposphere. The JEM-EUSO telescope will determine the energies and directions of extreme energy primary particles by recording the tracks of EAS with a time resolution of about $1\mu s$ and an angular resolution of about 0.1°.
About the JEM-EUSO status and general project information, see also [3] and [4] in this conference.

2 JEM-EUSO Focal Surface

The Focal Surface (FS) of the JEM-EUSO telescope consists of a curved surface of about 2.35 m in diameter which is covered with 5,000 of 64-channel MAPMTs (Hamamatsu R11265-M64). A JEM-EUSO FS Photo-Detector Module (PDM) consists of an array of 3×3 Elementary Cells (ECs), each of which consist of 2×2 MAPMTs. About 1,233 ECs, corresponding to about 137 PDMs, are arranged on the on the whole FS (See the Fig.1). MAPMTs capture the photons from the Earth atmosphere, convert them in its photocathode into photoelectrons and induce pulses from the charges on their anodes and dynode output. The Front-End ASIC transforms the charges from MAPMTs into digital numbers which can be processed

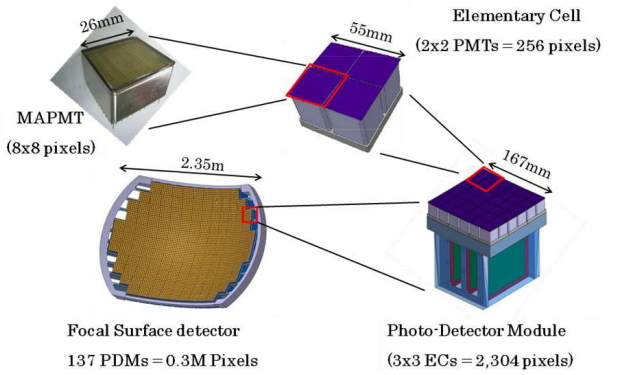


Figure 1: FS detector modules.

in next stages by digital electronics. Similarly the trigger stages process digitally those charges which have been previously converted into numbers.
About the JEM-EUSO focal surface, see also the contributions[5][6][7] in this conference.

3 Front-End ASIC : SPACIROC

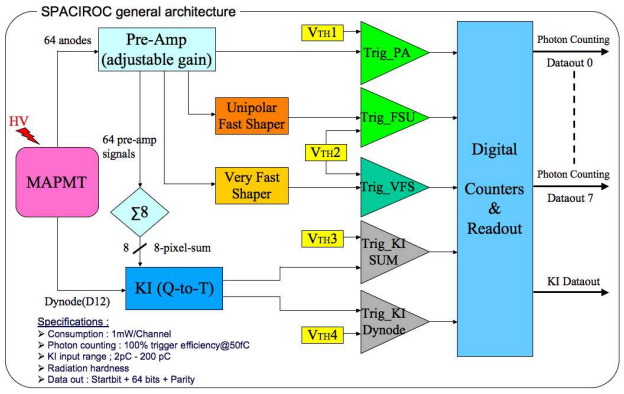


Figure 2: SPACIROC general architecture.

Fig.2 shows the general architecture of the SPACIROC. SPACIROC consists of two analog blocks and one digital part. One of the analog parts is dedicated for Photon Counting, and another is for so called "KI" Charge to Time (Q-to-T) converter. The digital part is build to count the detected photons. The 64-channel Photon Counting block discriminate the preamplifier signal into trigger pulses. Each of 64 channels of photon counting block consist of a preamplifier, two shapers and three compartors (trigger discriminators) as below:

- Trig_pa : Trigger of the signal coming directly from preamplifiers
- Trig_FSU : Trigger of signal from Unipolar Fast Shaper (FSU)
- Trig_VFS : Trigger for Very Fast Shaper (VFS).

Charge signals from 64 anodes of a PMT are first fed into preamplifiers before sent to various shapers and discriminators in the latter part of ASIC. Then divided to 3 photon counting (PC) and outputs : preamp, FSU, VFS. At the end of each acquisition window, so called Gate Time Unit (GTU=2.5μs), the counter values are readout through 8 serial links in order to reduce overhead. The first 8 inputs of KI takes the pre-amplified signals from the photon counting (sum of every 8 channels), while 9th input takes a signal coming directly from the last dynode of the MAPMT. In a similar manner to the photon counting readout, the counter data are sent through a serial link at the end of each GTU.
For more details of design and specification of SPACIROC, see also[8] in this conference.

3.1 Requirement

The electronics system is required to keep a high trigger efficiency with a flexible trigger algorithm as well as a reasonable linearity in the energy range of 4×10^{19} to $10^{21}eV$ for EECRs.
The Front-End ASIC is required to count single photoelectrons, i.e., with considering the MAPMT gain of 5×10^5, 0.08 pC.
Number of photoelectrons per GTU per pixel by the fluorescent light from EAS generated by EECR with 10^{20}eV is obtained by simulations to be roughly 250 at around the shower maximum. By multiplying a safety factor of 2, it becomes 500 PEs/GTU/pixel which correspond to 40 pC/GTU/pixel.
Also, to operate JEM-EUSO under a quite limited power in the space, a power consumption of less than 1mW/ch is essential.
SPACIROC achieves 100 % trigger efficiency for charge greater than 1/3 PEs, a dynamic range of over 1000 with having two analog processing modes as described below, low power consumption of 1 mW/channel and thus fulfills the requirement for the JEM-EUSO electronics.

3.2 Test Method

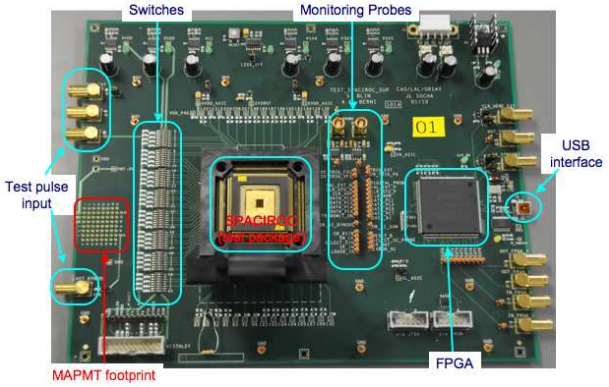


Figure 3: Test board for SPACIROC.

Various tests have been done by using a test board shown in Fig.3. The test board consists of a socket for ASIC, FPGA

and USB connection to PC, MAPMT 64 anodes and a dynode footprint, and various test points. Test pulses are fed into the board from a pulse generator. PMT signals are also fed into the board after the test pulse measurement. The registers inside the ASIC are controlled by a PC using a LabView software via an FPGA and USB connection.

3.3 Power Consumption

Due to the limited electrical power available from the ISS for the JEM-EUSO experiment, a maximum of 0.8 mW is allowed per detection channel in the ASIC. For the first prototype of SPACIROC, the measured power consumption is 1.1 mW/channel. This is partially because of the design bugs which makes some unused componet always on and non negligible power dissipation is occuring. Therefore, the next version of SPACIROC is expected to reduce the power consumption and fulfill the requirement.

3.4 Radiation Hardness

For the experiments in the space, the radiation hardness is essential. Two effects have been clearly identified as harmful to the ASIC. One is "Single Event Latchup" which can destroy the circuits, another is "Single Event Upset" which may affect the SPACIROC functionalities. In case of the analogue part of SPACIROC, it has been designed to take into account the radiation effects on electronic systems. For example, the layout is done carefully in order to minimize the single event latchup effect. Also, a mechanism to detect single event upset is added. For the total ionizing doze effect, we exposed the ASIC chip against the radiation of 70 MeV proton beam with the ASIC running with maximum gain and all the capacitors and registers on to see if it causes any effects. As a result, we confirmed no significant effect or difference in configuration parameters such as threshold and preamplifier gains before and after the test in the operation. For other effects, we are also planning to test the ASIC with a heavy ion beam near future.

3.5 Single Photoelectron response

Fig.4 shows the differential of a Trig_PA S-curve. The input charge is $80fC$ which corresponds to 1 photoelectron for a PMT gain of 5×10^5 generated by a pulse generator Tektronix AFG 3102. The single photoelectron peak is clearly seen thus we obtained the minimum threshold of 0.13 PEs on the average of 64 channel outputs. Fig.5 shows the amplitude, i.e., subtract pedestal from 1 PE peak, of all 64 channel outputs of preamplifier and FSU respectively. The fluctuation in an ASIC is $\sim$1.3 for preamplifier and $\sim$3.7 DAC unit for FSU.

3.6 Linearity and dynamic range

In photon counting mode, the measured double pulse resolutions for Trig_PA is 36ns, and 30ns for Trig_FSU. Currently, further tests with input pulses of random timing are ongoing to estimate the actual linearity and dynamic range in photon counting mode for the PMT signal readout.
Fig.7 shows the KI_SUM counts, which corresponds to the measured width of KI_SUM output pulse as a function of input charge (pC). It is shown that there is a sufficient linearity between the input charge and output pulse width within a dynamic range of the input charge of 0.3 PEs to 80 PEs. In this case KI reaches the maximum counter bit (7 bit dedicated for KI_SUM) while the linearity of KI itself still continues. The study on the optimum KI parameters

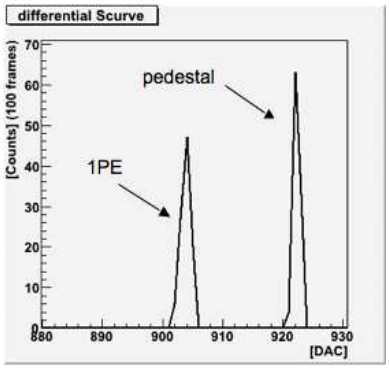


Figure 4: Differential S-curve from preamplifier output with the input charge of 80fC which is corresponding to 1PE for the gain of 5×10^5.

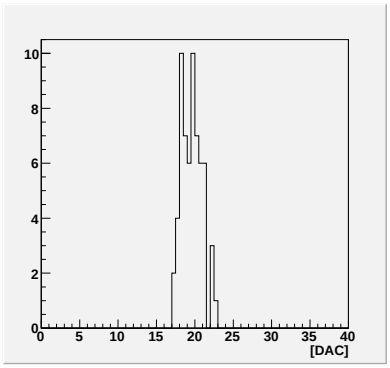


Figure 5: Amplitude of 64 ch preamp. RMS is 1.32 DAC unit.

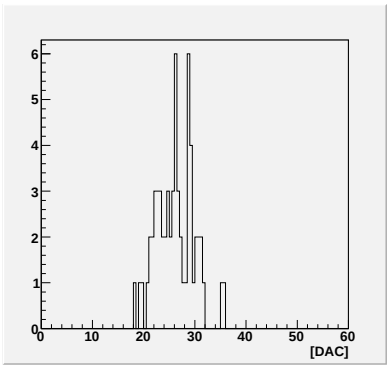


Figure 6: Amplitude of 64 ch FSU. RMS is 3.67 DAC unit.

such as of KI pulse width and dynamic range adjust for the Q-to-T conversion is still ongoing.

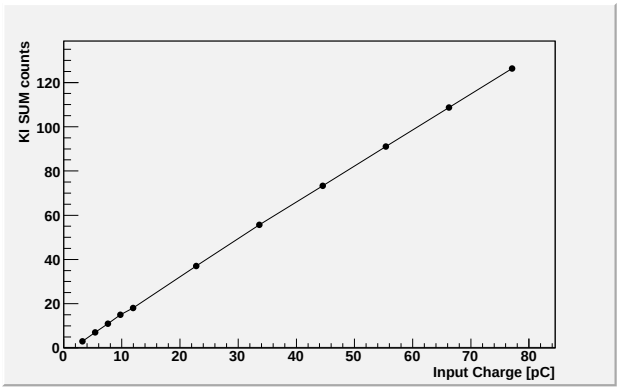


Figure 7: example of KI_SUM digital output.

3.7 PMT response

Fig.8 shows setup of the integration measurement. A 64 ch MAPMT on a PDM frame is connected to the ASIC test board which is controlled by a PC. The MAPMT is illuminated by a blue LED fired by an Agilent waveform generator 33250A to give roughly 1.8 PEs on average in 200 ns. The trigger of waveform generator is synchronized to the GTU clock on the ASIC test board. Fig.9 shows the distribution of number of photoelectrons (PEs) which is obtained by one of the 64 anodes. The width of the broad peak in the figure is roughly consistent with an error caused by the Poisson fluctuation.

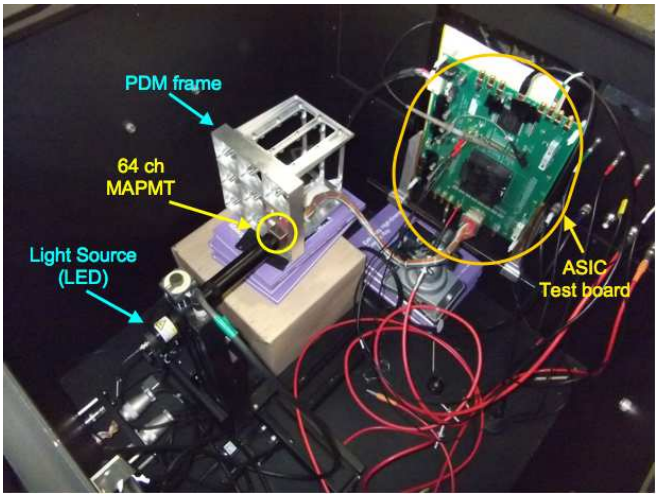


Figure 8: Integration test of MAPMT on a PDM frame connected to SPACIROC.

4 Conclusion

The first version of Front-End ASIC for the focal surface detector of JEM-EUSO mission has been examined. It has been shown that the fundamental functions of the ASIC work quite well without any critical problems. We also succeeded to readout MAPMT signals by the ASIC and we obtained the distribution of number of detected photons. More examinations such as searching for the optimum configuration parameters to achieve the largest dynamic range, best signal to noise ratio and minimum power consumption are still ongoing. Also, further work to improve the chip itself is ongoing and in the next design, the power consumption will be improved to be about 0.8 mW/ch, the noise level will be further suppressed.

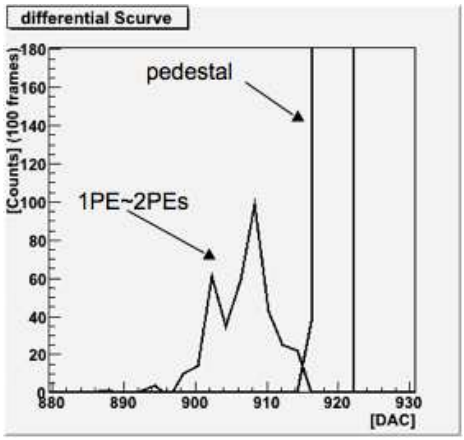
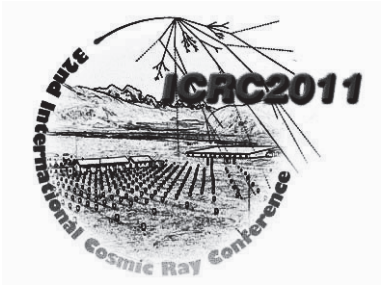


Figure 9: Distribution of number of input pulses using Trig_PA.

References

[1] T. Ebisuzaki et al., Nucl. Phys. B (Proc. Suppl.) Vol. 175-176 237(2008)
[2] <http://jemeuso.riken.go.jp>
[3] T. Ebisuzaki et al., "The JEM-EUSO mission", contribution ID1628 in this conference.
[4] G. A. Medina Tanco et al., "Science objectives of the JEM-EUSO mission", contribution ID0956 in this conference.
[5] F. Kajino et al., "Overview of the JEM-EUSO Instruments", contribution ID1216 in this conference.
[6] Y. Kawasaki et al., "The Focal Surface Detector of the JEM-EUSO Telescope", contribution ID0472 in this conference.
[7] M. Ricci et al., "The JEM-EUSO Focal Surface Mechanical Structure", contribution ID0335 in this conference.
[8] S. Ahmad et al., "SPACIROC: A Front-End Readout ASIC for spatial cosmic ray observatory", contribution ID0236 in this conference.

32ND INTERNATIONAL COSMIC RAY CONFERENCE, BEIJING 2011



High Voltage System for JEM-EUSO Photomultipliers

JACEK KARCZMARCZYK[1], PHILIPPE GORODETZKY[2], YOSHIYA KAWASAKI[3],
JACEK SZABELSKI[1], TADEUSZ WIBIG[1] FOR JEM–EUSO COLLABORATION
[1]*NCBJ, Cosmic Ray Laboratory, PL-90-950, Lodz, Poland*
[2]*APC, University Paris Diderot, 10 rue A. Domon et L. Duquet, 75013 Paris, France*
[3]*RIKEN Advanced Science Institute, 2-1 Hirosawa, Wako, Saitama 351-0198, Japan*
js@zpk.u.lodz.pl

Abstract: JEM-EUSO, the UV telescope to be installed on the ISS, has a camera (focal surface) composed of 4932 Hamamatsu new M64 photomultipliers, making a total of 315648 pixels. One pixel (2.88 x 2.88 mm) represents on the Earth surface a square of 500 m side.
Two major specifications of JEM-EUSO are:

a) the total power allocated for all the instrument should not be above 1000 W, so that the power allocated to polarize with high voltage should be less than 50 W (using normal resistive voltage dividers requires nearly 2 kW!).
b) the light intensity reaching JEM-EUSO has a dynamic range larger than 10^6 going from the background (one photo–electron per pixel per 2.5 μs) to storm lightnings.

Solution for a) is to use separate power supplies for each dynodes, regrouping identical dynodes at the same power supply. The groups can be at the level of the Elementary Cell (4 PMTs) for a total power of 50 W. The solution chosen for b) is not to shut off the telescope at the approach of the storm, but to study the events producing a lot of light (allowing for instance to measure meteors or TLEs). The voltage applied to the cathode is reduced in a fast (< 3 μs) switch driven by the integrating parts of the front–end ASICs. The focusing properties of the tubes are modified in such a way that the "gain" is reduced in a range of 10^6, by steps of 10^2.

Keywords: The highest energy cosmic rays, satellite telescope, new detection methods, multianode photomultipliers

1 JEM-EUSO telescope – TPC.

JEM-EUSO telescope is going to measure the highest energy cosmic rays by monitoring the atmosphere (at dark side of the Earth) not from the ground, as has been observed for many years, but from the top: from the altitude of the International Space Station (ISS) [1, 2, 3]. The advantage is the huge geometrical factor, as the area of radius of about 200 km would be monitored. The UV telescope (lenses and focal surface) will have the nearly circular area of about 2.3 meters in diameter. The light detector must be very fast, to monitor extensive air shower (EAS) development, which typically lasts about 30 μs, and the angular resolution (pixelisation) should be fine enough to see space development of EAS from 350–400 km altitude of ISS. To meet these requirements the light detector consists of 4932 multianode photomultipliers (MAPTM), each with 64 anodes (315648 pixels, each corresponding to about 500m x 500m at the Earth's ground level). In the basic mode, single photo–electrons would be counted in each pixel, and integrated every 2.5 μs (GTU - Gate Time Unit) (400 thousand times per second). The JEM–EUSO telescope would work as a TPC (time projection chamber) allowing 3D reconstruction of the EAS.

2 Focal Surface detector structure.

Hamamatsu – the manufacturer of M64 Multi-Anode Photomultiplier Tubes (MAPMTs) for JEM–EUSO – developed 12 stage photomultipliers with additional grid near to anodes for better focusing of internal photo–electron (pe) cascades. As the telescope will be open viewing the night atmosphere, most of measured light would come from the UV background in the telescope field of view. We expect to measure on average about 1 pe in each pixel during GTU (for UV background analysis see [4]). The gain will be about 10^6. So we expect the anode current of 4.1 μA from each MAPMT. 4 MAPMTs form the basic unit – Elementary Cell (EC), and 9 ECs form Photo Detection Module (PDM), where there are 6 x 6 photomultipliers. There would be 137 PDMs on the Focal Surface (FS).
This kind of MAPMTs requires a high voltage of about -900 – -1000 V at the cathode with grounded anodes, to achieve the gain of 10^6. One High Voltage Power Supplier (HVPS) is planned for every EC (4 MAPMTs). The anode current (background measurements) for one PDM is equal to 0.147 mA, and for the whole FS it is equal to 20.2 mA.

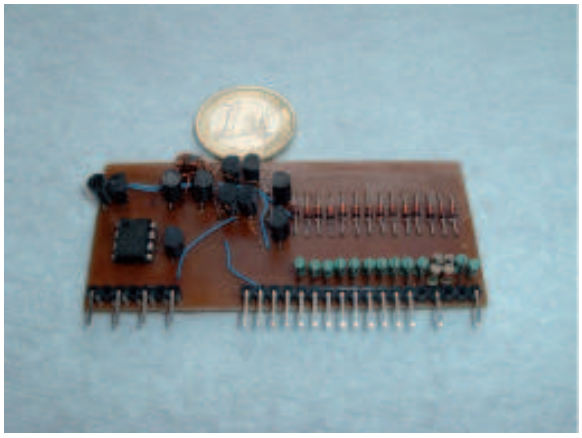


Figure 1: The Cockcroft–Walton high voltage photomultiplier supplier.

3 High voltage supply for JEM-EUSO photomultipliers – standard approach.

Standard approach requires the resistive voltage divider in parallel to the MAPMT, and, to provide stability and linearity of MAPMTs, the current in the divider should be larger than 100 times the anode current. The superposition principle acts here, so the required divider current (or sum over all dividers) shall be 100 x 20.2 mA = 2.02 A. As the required voltage is -900 V, the power which would go to the divider would be more than 1.8 kW. This value is nearly twice the limit for JEM–EUSO power consumption for all instrument devices. Therefore the standard approach to powering photomultipliers is excluded.

4 A photomultiplier model.

In photomultiplier the single pe emitted from the cathode is accelerated in electric potential U_1 between the cathode and the first dynode D_1. On average k_1 electrons are emitted from D_1 for each electron arriving from the cathode. In the next step each electron emitted from D_1 is accelerated in electric potential U_2 between the first and the second dynode (D_2), and k_2 electrons are emitted on average from D_2 per every electron from D_1, and so on. The last multiplication takes place at D_{12}, and electrons emitted from D_{12} are collected by anode. Assuming that U_n = constant (which is very common for all dynodes but 1 or 2), and k_n is proportional to U_n, we might express the phototube gain as equal to k^{12}, and for k = 3.16 we get the gain 10^6. Constant k implies constant U_n, and for 13 steps we would have U_n = 900 V / 13 = 69 V.
It is important to notice that on the last step D_{12} – anode we have the largest current i_A, then between $D_{11} - D_{12}$ the current i_{12} is k_{12} times smaller, then between $D_{10} - D_{11}$ i_{11} is still k_{11} times smaller etc. Similarly the power released in the photomultiplier itself is the largest at anode: $i_A \times U_A$, then at D_{12} is $i_{12} \times U_{12}$ then at D_{11} is $i_{11} \times U_{11}$ etc. 60% of power is deposited at anode, 20% at D_{12}, 7% at D_{11}, 2% at D_{10} and 1% at other dynodes.

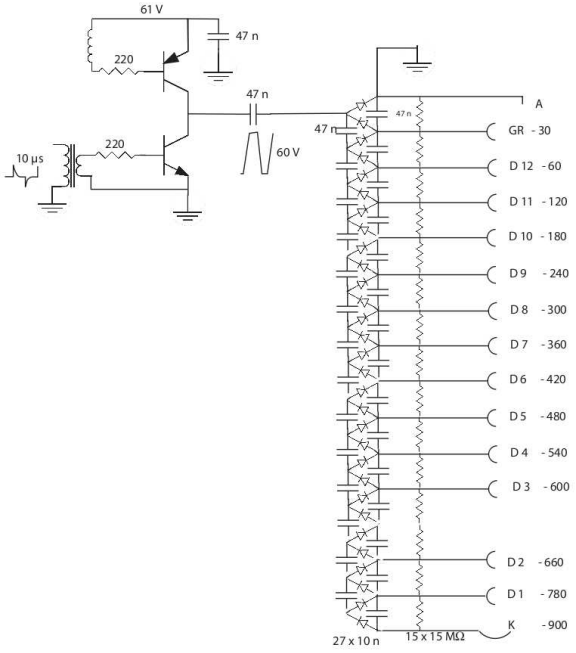


Figure 2: The Cockcroft–Walton solution for high voltage photomultiplier supplier without resistor divider.

5 The Cockcroft–Walton voltage multiplier – solution to the power problem.

The recomended photomultiplier voltage ladder is very near to the simplified description presented in the Section 4. The Cockcroft–Walton scheme shown in the Figure 2 is close to the real voltage ladder. For dynodes with large indexes the ΔU are constant, and on the first 2-3 dynodes ΔU are larger but the currents (and power) there are very small. We have made a high voltage power supply (HVPS) using the Cockcroft–Walton voltage multiplier circuit with constant ΔU approximately equal to 60 V. The idea is presented in the Figure 2. First steps near to anode (grounded) have constant ΔU and are directly connected to corresponding dynodes and near to cathode we use resistive voltage divider (however required currents are so small, that power losses there are negligible).
Large resistors presented in the Figure 2 are for diode polarization and to discharge the HVPS when turned of. For the background load as described in the Section 2 the HVPS power consumption per PDM is about 120 mW (which corresponds to about 16 W per all FS, i.e. 100 times less than a standard solution presented in the Section 3).
We have found that similar solutions for high voltage power suppliers for photomultipliers were used in the past, e.g. in CERN [5].

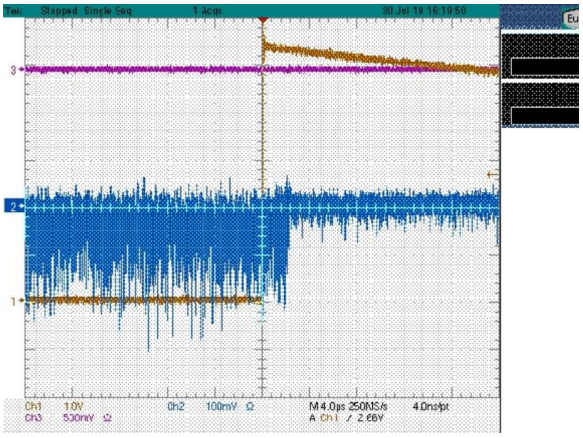


Figure 3: Oscilloscope showing the square pulses (yellow) to control the switch, and in blue the PMT anode pulses. One horizontal division is 4 μs.

6 Higher photon fluxes.

Lightnings, meteors, transient luminous events (TLE), or man made light (cities) could be very bright. During the JEM–EUSO mission we might expect to meet photon fluxes even 10^6 times higher than the background level (see Section 2). Some of them can last tens of milliseconds (i.e. long compared with GTU = 2.5 μs). As we still like to measure them, following method is applied.

When the light intensity is growing in 10 millisecond scale the HVPS should provide enough power to keep linearity of measurements up to about 200 times the background level. Laboratory measurements with calibrated light sources showed that our HVPS is capable to fulfil these conditions.

However, when the light intensity rises above 100 times the background value, then we would reduce collection efficiency in the whole PDM by about 100 times, still going on with anode current measurements. When the intensity still rises by the next 100 times, we would reduce the efficiency in the PDM by another 100 times, and the next such step can be performed (see Figure 3). This reduction shall be fast (within 1-3 GTU) to secure the tubes against potential damages or wear by large currents or charges at last dynodes and anodes. However, we would still measure the anode current and the higher gain would be restored when light flux falls below the harmful level.

7 Fast reduction of MAPMT efficiency.

In the case of increase of photon flux about 100 times above the background level we would reduce the efficiency of pe collection on the first dynode D_1. We would apply new voltage on the cathode below the voltage on the first dynode D_1 keeping all other voltages unchanged, e.g. changing the cathode voltage from -900 V to -750 V, and keeping the D_1 voltage on the level -800 V. These would provide the opposite electric field and reduce the efficiency by about 100 times. The next 100 times efficiency reduction for M64 tubes requires cathode potential equal to 500 V, and with cathode grounded the efficiency would be still at the level about $3{\cdot}10^{-5}$.

In the M64 MAPMT the cathode and metal housing box are connected. Therefore the cathode capacitance of 36 photomultipliers (PDM) is large, about 1 nF. To change the electric potential of cathode by 500 V within one GTU (2.5 μs) requires a current of 0.3 A for that time, which is a large value.

We made a two way switch controlled by low voltage circuit which has galvanic isolation from the high voltage part. It works as a current source (this or other way) providing large nearly constant current during the GTU. It requires large capacitors (0.2 μF on high voltage) in the required step of HVPS. The switch takes about 4 mW while not switching.

8 Conclusions.

We made several prototype models of HVPS and high voltage gain switches which have been successfully tested in laboratory conditions with M64 photomultipliers. Still further tests will be performed in a process of preparing engineering models and then space qualified models.

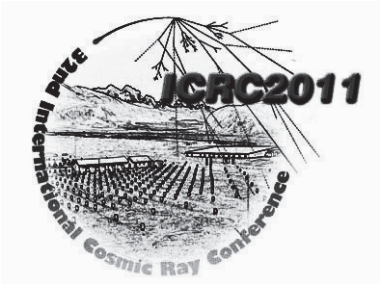
Acknowledgement

This work was supported in part by the Polish-French collaboration COPIN-IN2P3 (09-135).

References

[1] T. Ebisuzaki, this conference, ID1628
[2] G. Medina–Tanco et al., this conference, ID0956
[3] F. Kajino et al., this conference, ID1216
[4] P. Bobik et al., this conference, ID0886
[5] S. Neumaier et al., NIM in Physics Research (1995) **A360**: 593-597

32ND INTERNATIONAL COSMIC RAY CONFERENCE, BEIJING 2011



The Cluster Control Board of the JEM-EUSO mission

JÖRG BAYER[1], MARIO BERTAINA[2], GIUSEPPE DISTRATIS[1], FRANCESCO FENU[1], ANDREA SANTANGELO[1], THOMAS SCHANZ[1], CHRISTOPH TENZER[1] ON BEHALF OF THE JEM-EUSO COLLABORATION
[1]*IAAT, Kepler Center für Astro- und Teilchenphysik, Universität Tübingen , Sand 1, 72076 Tübingen, Germany*
[2]*Dipartimento di Fisica Generale, Università di Torino, Via P. Giuria 1, 10125 Torino, Italy*
bayer@astro.uni-tuebingen.de

Abstract: The Cluster Control Board (CCB) is one of the key elements of the JEM-EUSO read-out electronics, which manages the data received from eight units of the Photo Detector Module (PDM) of JEM-EUSO, performing data selection and transmission. To reduce the large amount of data produced at the detector level and to discriminate the good Extensive Air Shower (EAS) events from the spurious ones, a hierarchical trigger scheme over two levels has been developed. The first trigger level consists of three sub-levels which are implemented within the front-end Application Specific Integrated Circuit (ASIC) and the PDM electronics. The second trigger level is implemented in the CCB electronics. After the onboard processing of the data received from 8 PDMs at a rate of around 57 Hz, potentially good events are transmitted to the onboard CPU at the level of around 5 mHz. In this paper, we will firstly present the algorithm developed for the second trigger level, focusing on its implementation in hardware. The algorithm aims at distinguishing the unique patterns produced on the focal surface by the EAS from the ones produced by background events. It is based on the scan of a predefined set of directions, which covers the complete parameter space, to find good patterns associated with the EAS. The final set of directions has been carefully optimized to adapt the algorithm to the limited on-board computing power. To fulfill the requirement on the processing time, the algorithm was implemented in a Field Programmable Gate Array in order to make use of its parallel processing capabilities. After presenting the current architecture of the CCB and discussing the complex interfaces with the other elements of the read-out electronics, we will report on the performance of the laboratory model.

Keywords: JEM-EUSO, Cluster Control Board, detector, electronics

1 Introduction

The planned Extreme Universe Space Observatory (EUSO) - attached to the Japanese Experiment Module (JEM) of the International Space Station (ISS) - is a large Ultra Violet (UV) telescope to investigate the nature and origin of the Ultra High Energy Cosmic Rays (UHECR) by observing the fluorescence light produced in Extensive Air Showers (EAS).

The main instrument of JEM-EUSO is a super-wide $\pm 30^\circ$ Field of View (FoV) telescope, which will be able to trace the fluorescence tracks generated by the primary particles with a timing resolution of 2.5 μs and a spatial resolution of 0.07° (corresponding to about 550 m on ground), allowing to reconstruct the incoming direction of the UHECR with an accuracy better than a few degrees [1].

The Multi Anode PhotoMultiplier Tube (MAPMT) used as the basic detector element was developed by RIKEN in collaboration with Hamamatsu Photonics K.K. and has 64 channels in an 8x8 array.

As the electronics has to handle over $3.15 \cdot 10^5$ pixels, the Focal Surface (FS) has been partitioned into subsections - the Photo-Detector Modules (PDMs) - and a multi-level trigger scheme has been developed. In the current baseline design, there are two trigger levels: the 'first level' trigger (L1), which is implemented within the PDM electronics and the 'second level' trigger (L2) which is implemented in the CCB electronics.

2 L2 Trigger Algorithm

2.1 Overview

The fluorescence light from EASs (induced by UHECRs) looks like a thin luminous disk, which travels ultra relativistically on a straight path through the atmosphere. As the EAS produces more particles, the luminosity of the disc will also increase until the shower reaches its maximum and then fades out. A typical proton induced shower with an energy of 10^{20}eV, will be detected as several photons per pixel and μs during a typical duration of tens to hundreds μs. As the detector has some exposure time for each image - the Gate Time Unit (GTU) - the fluorescence light will appear as a small spot, which moves on a straight line from image to image. The speed and the direction of this mov-

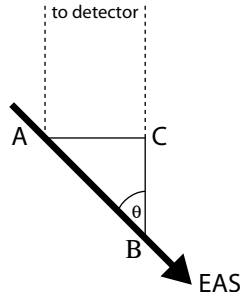


Figure 1: Kinematics of an EAS

ing spot is obviously depending on the incoming direction of the UHECR that is from the shower axis.

The principle of the L2 trigger algorithm is therefore trying to follow the movement of this spot over some predefined time, to distinguish this unique pattern from the background. In the case of an L1 trigger, the PDM electronics (see [2] for details) will send (together with the frame data) a starting point, which contains the pixel coordinates and the GTU which generated the trigger - also called 'trigger seed'. The L2 algorithm will then define a small box around this trigger seed, move the box from GTU to GTU and integrate the photon counting values. This integrated value is then compared to a threshold above the background and an L2 trigger will be issued if the threshold is exceeded.

It should be stressed, that an effective implementation of the L2 algorithm is constrained by the limited available computing power on board, due to power-, weight- and size-requirements and the space-qualification of the hardware.

Currently it is foreseen to have a total of 375 starting points for the integration, which are distributed equally over time and position around the trigger seed. Each integration will be performed over ± 7 GTUs for a predefined set of directions (see Section 2.2).

In order to follow the movement of the spot on the detector, the speed and the direction in terms of detector pixels has to be calculated.

We define in the following θ as the zenith angle ($\theta = 0^\circ$ means nadir direction of JEM-EUSO) and ϕ as the azimuth angle of the EAS ($\phi = 0^\circ$ means direction of the ISS movement). Since the EAS travels at the speed of light, the photons reaching JEM-EUSO from any point on the EAS are lagging behind the passing EAS-front by the time:

$$\Delta t = \frac{\overline{AB} + \overline{BC}}{c}$$

with c being the speed of light and $\overline{AB} + \overline{BC}$ as defined in Figure 1. Together with

$$\sin\theta = \frac{\overline{AC}}{\overline{AB}}, \quad \tan\theta = \frac{\overline{AC}}{\overline{BC}},$$

$$\tan\theta = \frac{\sin\theta}{\cos\theta} \quad \text{and} \quad \tan\frac{\theta}{2} = \frac{\sin\theta}{1+\cos\theta}$$

it follows

$$\Delta t = \frac{\overline{AC}}{c \cdot \tan\frac{\theta}{2}}$$

as can be derived from Figure 1. If we define now Δx and Δy as the projections on the focal surface along x and y expressed in number of pixels and ΔL as the FoV at ground of a pixel in a time Δt (chosen as the GTU) we find

$$\overline{AC} \quad = \Delta L \cdot \sqrt{\Delta x^2 + \Delta y^2}$$

and therefore

$$\theta = 2\arctan\left(\frac{\Delta L}{c \cdot \Delta t} \cdot \sqrt{\Delta x^2 + \Delta y^2}\right) \quad (1)$$

$$\phi = \arctan\left(\frac{\Delta y}{\Delta x}\right) \quad (2)$$

2.2 Number of Directions

Due to the fact, that the incoming direction of the EAS is unknown, the approach of the L2 trigger algorithm is simply to try out a set of directions which covers the complete space ($\theta = 0^\circ \ldots 90^\circ$ and $\phi = 0^\circ \ldots 360^\circ$). The integrated count value will have a maximum when we 'hit' the (nearly) correct direction, because in this case the integrating box will follow the spot.

As the integration over the directions is a time consuming task, a trade-off between the number of directions and the available computing power has to be found. In addition, as the hardware only works on whole pixels, some directions will produce the same offsets Δx and Δy - for example, in the extreme case $\theta = 0^\circ$ (which means the shower axis is parallel to the optical axis of the telescope), the spot is not moving at all there is no need to integrate over different ϕ angles.

Therefore, a minimum set of directions (containing 67 θ-ϕ combinations in total) was selected and evaluated with simulations aiming to optimize the design according to the constraints mentioned above.

3 Cluster Control Board

3.1 Overview

In case an L1 Trigger is issued, the data of the ring buffers from 8 PDMs are transferred to the CCB and the L2 trigger algorithm is executed. The data from the PDMs are processed independently, as it is not intended to have a fixed geometrical relationship between the PDMs connected to one CCB. In case an L2 trigger is found within any of the 8 PDMs, the complete data are transferred to the mass memory module of the Mission Data Processor (MDP).

Due to the necessity for parallel processing and the need for a high number of input/output pins (for the eight data interfaces to the PDMs and the interface to the MDP, besides

various other interfaces for control and housekeeping) it is foreseen to implement the L2 trigger algorithm inside an Field Programmable Gate Array (FPGA) chip on the CCB. As a baseline, it is planned to use a radiation tolerant Xilinx Virtex-4QV FX-140 and as an advanced option the use of a radiation hard Virtex-5QV is currently under investigation (see [3] for the specification).

The current block diagram for the FPGA is given in Figure 2, which is basically the implementation of the L2 trigger algorithm. Besides the eight Linear Track Trigger (LTT) modules it is planned to use the microcontroller cores for 'low speed' purposes, such as the configuration of the LTT modules, housekeeping and the communication with the MDP.

In order to perform the necessary calculations as fast as possible, the hardware architecture of the trigger is highly pipelined and parallelized. As it is not possible to store the raw data completely in the internal RAM of the FPGA, the data will be written to an external memory upon arrival. Only the data necessary for the trigger calculation will be stored inside the FPGA to reduce the probably slow read/write access for the external RAM. A first data 'selection' will be done by the 'Data Allocator'-module. The data will then be passed to the '3x3 Sum'-module which performs the summation of the 9-pixels blocks in two stages (horizontal and vertical) for the whole frame which reduces redundant 3x3 summation to a minimum. The new frame generated this way is then trimmed to a 19x19 pixel frame around the seed and stored in the 'Frame Buffer' for ± 14 GTUs.

After the 'Frame Buffer' is filled completely (it contains the necessary information for the integration), the 'Address Generator' allocates the different 3x3 sums - depending on the starting point for the integration and the offsets for the various directions which are stored in a Look Up Table (LUT) - to the 'Accumulator'. After each direction-integration, the accumulated value is compared to the current maximum to select the overall maximum value and is then stored along with the information to which starting-point this value belongs ('Maximum Comparator'). When the integration process is finished for all starting points, the maximum value is compared to the trigger threshold ('Threshold Comparator') and an L2 trigger is issued if the threshold is exceeded. In this case the raw data buffer (external RAM) is sent to the mass memory module of the MDP, whereas the information at which pixel the maximum value was found, could be used by the MDP to calculate the pixel coordinates on the focal surface. This information then could be used as a target for the LIDAR to monitor the atmospheric conditions around the EAS (see [4] for more details).

3.2 Interfaces

The interface between PDM and CCB for the scientific data from the detector and for controlling/monitoring the PDMs is a critical part in the processing chain as many other parts rely on the performance of this interface (e.g. the ring buffer on the PDMs, the implementation of the L2 algorithm and the dead-time of the instrument). In order to reduce the dead-time of the instrument, the event data (around 2.7 Mbit per PDM and event) has to be transferred as fast as possible within the hardware constraints. The current baseline is to implement a parallel bidirectional interface with 20 data channels running at 40 MHz. Due to the fact that the distance between the PDM and the CCB is about 1 m - as it is foreseen that the CCB is mounted on the back of the focal surface - it was decided to use the Low Voltage Differential Signaling (LVDS) standard which results in a more reliable interface, but doubles the number of lines needed. In order to reduce the weight of the harness, an advanced option is currently under investigation which uses a double buffer approach whereby a total of 4 data channels will be sufficient.

As a baseline for the interface between CCB and MDP (which will be controlled by an intermediate board - the Interface Data AcQuisition (IDAQ) board) the SpaceWire standard was chosen due to its approved reliability. To reduce the overhead of the standard, a modified protocol will be studied as advanced option.

3.3 Results from the performance tests

To verify the correct operation of the 'Linear Track Trigger' module, a first simple test was developed where the 'PDM Interface' was replaced by a 'PDM Simulator' module. This module consists of a small Finite State Machine (FSM) and an 'Event Buffer' which is basically a large RAM, filled with the simulated data of an event generated by the EUSO Simulation and Analysis Framework (ESAF).

The data from the 'Event Buffer' are sent to the input of the 'Linear Track Trigger' module where it will be processed as described in Section 3.1. To have a more detailed look into the processing, the 'Accumulator', 'Maximum Comparator' and 'Threshold Comparator' are connected either to a ChipScope Virtual Input/Output (VIO) or an Integrated Logic Analyzer (ILA) module.

The output of the 'Accumulator' is sampled by the ILA module every time the integration of one direction is finished. This allows to compare every single integrated value with the ones coming from simulations and to verify the correct operation of the 'Linear Track Trigger'. Unfortunately, the sample buffer of the ILA module is limited (as it uses the internal RAM of the FPGA) and it was not possible (with this simple test) to store all 25125 integrator values. Therefore, only around 16000 integrator values could be recorded. But as all sampled values (including the overall maximum) are equal to the ones coming from simulation, it is assumed that this test was passed successfully - also due to the fact, that the correct behavior of the the 'Linear Track Trigger' module was verified in advance with hardware simulations.

According to the current implementation, the decision of an L2 trigger could be performed within approximately 5

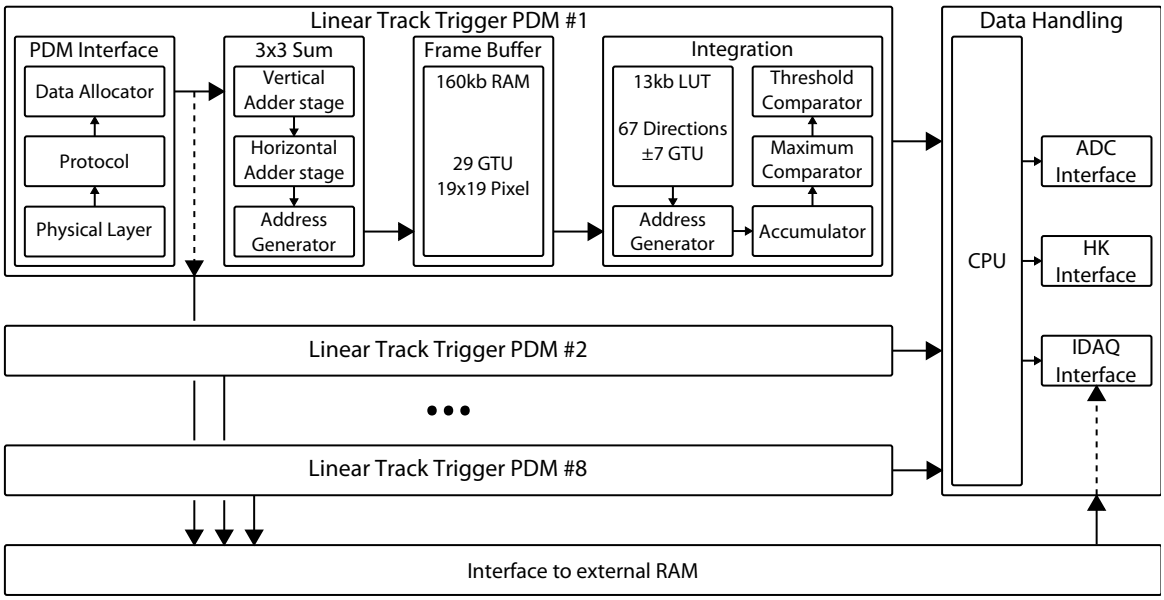


Figure 2: The current block diagram of the CCB FPGA. Most of the logic resources are needed for the eight 'Linear Track Trigger' modules which perform the L2 trigger algorithm and handle the data transfer from the PDM. As it is not possible to hold the data from all eight PDMs inside the FPGA RAM an interface to an external memory will be needed. Additionally, it is currently foreseen to use the integrated microcontrollers of the Virtex-4 FX140 to control and monitor the trigger modules and to handle the communication with the MDP and the housekeeping submodule.

ms. The time needed for the data transfer between PDM, FPGA and external RAM is not included in this number. It should be stressed, that the actual calculation time depends on the system clock of the FPGA, therefore, on the overall implementation. However, even if the system clock has to be reduced by a factor of 2 the calculation is still fast enough to meet the requirements, as 18 ms were allocated for the L2 trigger calculation.

4 Conclusion & Outlook

The developed hardware is still in phase A and a long way is necessary to reach the final space-qualified Cluster Control Board. The hardware implementation of the 'Linear Track Trigger' algorithm as L2 trigger is performing accordingly to the requirements. Based on the parallelization of the calculation process, the requirement on the processing time of the L2 trigger could be exceeded by a factor of 20. It should be stressed, that this value is highly dependent on the overall implementation of the CCB FPGA but at least the requirement was met.

In our current plan of the CCB development are the implementations of the interfaces to the Photo-Detector Module, to the Mission Data Processor and to the Housekeeping. We will then start the design of a first laboratory model of the CCB Printed Circuit Board. More information can be obtained from [5].

References

[1] Y. Takahashi and the JEM-EUSO Collaboration, New J. Phys., 11: 065009

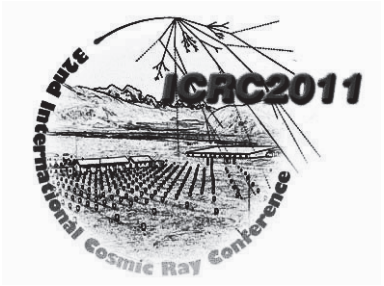
[2] I. Park, 2011, The Development of Photo-Detector Module Electronics for the JEM-EUSO Experiment, ID1246, this conference

[3] http://www.xilinx.com/

[4] A. Neronov, 2011, Atmospheric Monitoring System of JEM-EUSO, ID0301, this conference

[5] J. Bayer: 2011, Development of a Cluster Control Board for the JEM-EUSO Mission, University of Tübingen, http://astro.uni-tuebingen.de/publications/diplom/bayer-dipl.pdf

32ND INTERNATIONAL COSMIC RAY CONFERENCE, BEIJING 2011



The Housekeeping subsystem of the JEM-EUSO instrument

G. MEDINA-TANCO[1], J. C. D'OLIVO[1], A. ZAMORA[1], H. SILVA[1], L. SANTIAGO CRUZ[2], F. TRILLAUD[2], M. CASOLINO[3], K. TSUNO[4] FOR THE JEM-EUSO COLLABORATION

[1]*Instituto de Ciencias Nucleares, UNAM, Circuito Exteriror S/N, Ciudad Universitaria, México D. F. 04510, México.*

[2]*Instituto de Ingenieria, UNAM, Circuito Exteriror S/N, Ciudad Universitaria, México D. F. 04510, México.*

[3]

[4]*RIKEN Advanced Science Institute, Japan.*

gmtanco@nucleares.unam.mx

Abstract: The JEM-EUSO instrument is a refractive telescope being proposed for attachment to the Japanese Experiment Module, Kibo, onboard ISS. The instrument is substantially complex, including large Fresnel lenses, an focal surface covered by 4932 MAPMTs of 64 pixels, atmospheric monitoring subsystems (IR camer and LIDAR), low and high voltage power supply subsystems, tilting mechanism and a lid. All these subsystems must be turned on and off and monitored, and telemetry has to be conveyed between them and the principal CPU. The housekeeping subsystem (HKSS) is in charge of those tasks. In this contribution we describe the requirements and design of the JEM-EUSO HKSS.

Keywords: Cosmic Rays; High Energy Neutrinos; Space Observation.

1 Introduction

The JEM-EUSO instrument is a large refractive telescope to be installed at the Kibo module of the International Space Station (ISS) for the observation of extreme energy extensive air showers, using the fluorescence technique [1, 2]. The instrument as a whole is described in [3] and references there in.

The overall purpose of the Housekeeping Subsystem (HK) is to monitor and to relay control commands to the several subsystems that constitute the JEM-EUSO instrument. The HK sub-system is subservient to the CPU and all its activities are defined as slow control, i.e., with reaction time scales typically larger than a second. The HK subsystem architecture is conditioned by the wide variety of subsystems that constitute the JEM-EUSO instrument and with which it has to interact. The HK performs several tasks: (a) sensor monitoring of different subsystems in order to detect faults, (b) generation of alarms for the CPU, (c) distribution of telecommands to several subsystems, (d) telemetry acquisition from all subsystems, (e) monitoring of the status of the various electronic systems of the Focal Surface (FS), (f) switching between main and spares boards when appropriate, and (g) interaction with the power distribution system of the telescope, in order to turn ON and OFF the secondary power supplies, and therefore the FS, and verify adequate levels of power consumption. Fig. 1 shows schematically the architecture of the HK and its interaction with various elements of the telescope. The HK prefix denotes the main boards that constitute the HK subsystem. The core of the HK is the HK principal board (HK-PB), which centralizes most tele-command distribution and telemetry gathering. The HK-PB is the direct responsible for monitoring the FS and other subsystems, as well as providing on/off and status verification for every single component of the instrument.

The anchor points of the HK in the focal surface are the Power Supply Boards (PSB), as shown in Figure 2 and 3. The later board contains the relays that turn on and off the Points of Load (POLs) that generate the lowest voltages (1.5V, 2.5V, 3.0V and 3.3V) required by the different components of the FS (e.g., ASIC, Photo-detector Module (PDM) and High-Voltage Power Supply (HV-PS)). The PSB also contains a footprint of the HK for telemetry: the ADC responsible for the digitalization of, mostly, the temperature sensors of the FS.

Due to its pervasive interaction with different subsystems, the HK is spatially distributed throughout the telescope. Thus, the HK sub-system also possesses a secondary stage directly installed inside the main computer, the System Control Unit (SCU). The latter is divided in two boards, one of which (HK1) centralizes communication to and from the HK-PB and Power Distribution System (PDS), turning on and off and monitoring status of all the DC/DC converters of the Secondary Power Supply. The second module (HK2) receives lenses temperature data and relays tele-commands to the lid-mechanism, the tilting mechanism, the deployment mechanism, and the IR camera and LIDAR of the Atmosferic Monitoring System (AMS).

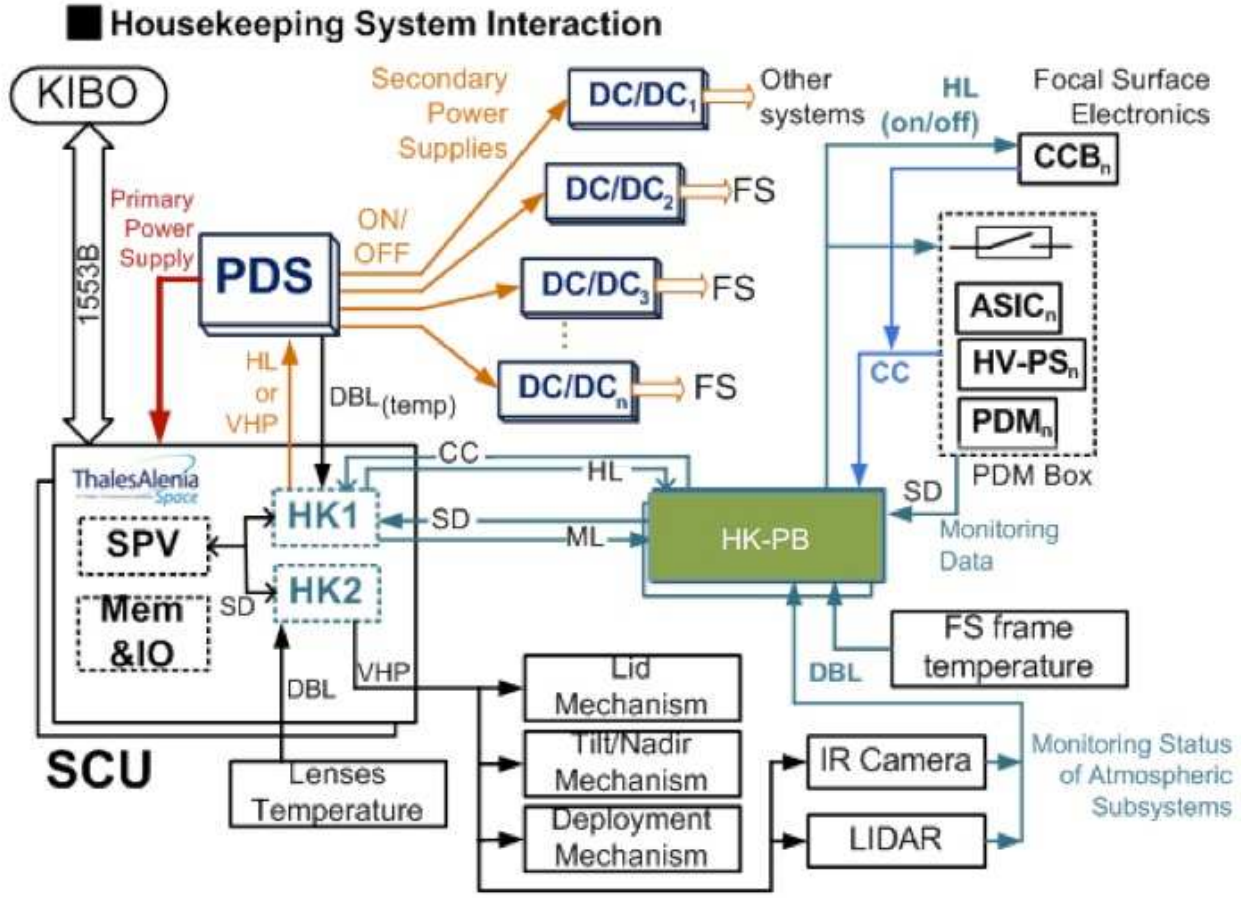


Figure 1: General architecture of the JEM-EUSO housekeeping system

The CPU and HK are turned on at the same time. HK has a direct interface with the CPU to distribute tele-commands sent from the ground by CPU users, it collects telemetry from different subsystems responsible for tasks such as atmosphere monitoring, telescope tilting, temperature measurement of lenses, and so on. Subsystem anomalies detected by the HK are reported as alarms to the CPU. In principle, HK does not take any action on these alarms, waiting for further commands from the CPU. At most, on critical instances, it can switch off a subsystem that triggered an alarm, in order to avoid possible further damage, while waiting for commands from the CPU for either restarting the reported system or its spare. The commands received and executed by the HK are either generated by the CPU itself or sent from the ground through the CPU. The HK is an auxiliary subsystem for tele-command distribution, monitoring status of the telescope's subsystems and alarms reporter.

The core of the HK subsystem is the master board HK-PB, to which all other portions of the HK report. Only slow data transmission rate is allowed between the HK-PB and any of its other components. Thus, for example, if an element of the FS is monitored at a particular time by a HK-CB, that same element will not be subsequently monitored for at least one or more seconds after the HK has established its status. FS faults, or indeed any other subsystems critical faults which require immediate shutdown in order to avoid damage, are the responsibility of the corresponding subsystem, which shall not wait for a reaction from the HK. The philosophy of monitoring and troubleshooting established for monitoring the FS will be by polling, in order to minimize power consumption by turning on sensors only when required.

An exception to the previous rule is the interaction with the power distribution subsystem. In this case, due to the critical nature of the subsystem, fault detection will be implemented by logical interruptions, which will allow fast detection and addressing of DC/DC converter failures and the consequent off-lining of the power system component in trouble. Concomitantly, HK will generate an alarm to the CPU, who is responsible for reporting operating conditions to the ground and/or deciding on an appropriate action to deal with the condition that triggered the alarm.In order to improve the offline reconstruction of the acquired scientific data, the HK will monitor the temperature of the lenses during observation. The HK will periodically activate and deactivate the conditioning and digitization board that interfaces the HK with the output signals from 15 analog

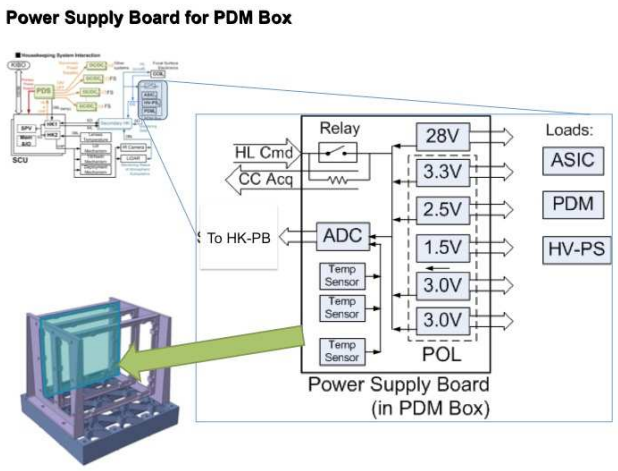


Figure 2: Focal surface monitoring scheme.

temperature sensors, which will be located at five different points on each of the three lenses of the optical system. It is estimated that cycles of measurements will take place around a dozen times per observation run.HK also includes a General Subsystems I/F Board (HK-GSB) to interact with atmospheric monitoring subsystems, and mechanical subsystems of the telescope. The HK interaction will be limited to turn on and off subsystems, to monitor any physical parameters necessary to determine whether the subsystem is within an acceptable working range and to relay commands received from the CPU.

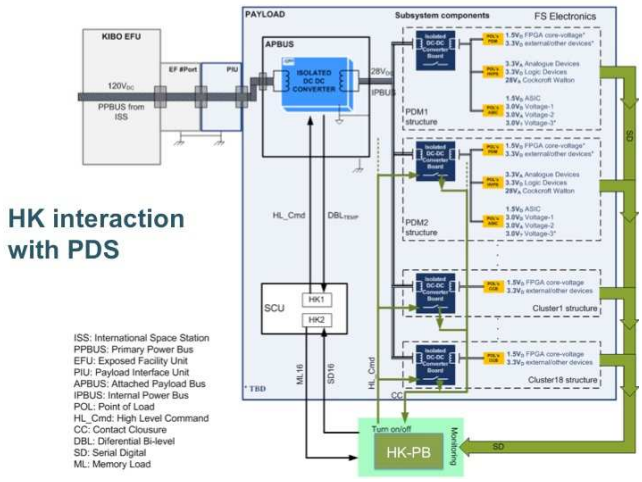


Figure 3: Interaction between the JEM-EUSO housekeeping system and the power distribution system (PDS).

References

[1] T. Ebisuzaki for the JEM-EUSO Collaboration, Proc. ICRC 2011, ID1628

[2] G. Medina-Tanco et al. for the JEM-EUSO Collaboration, proc. ICRC 2011, ID0956

[3] F. Kajino for the JEM-EUSO Collaboration, Proc. ICRC 2011, ID1216

32ND INTERNATIONAL COSMIC RAY CONFERENCE, BEIJING 2011

Data Acquisition System of the JEM-EUSO project

M. CASOLINO[1,2], T. EBISUZAKI[1], ON BEHALF OF THE JEM-EUSO COLLABORATION
[1]*RIKEN Advanced Science Institute, Wako 351-0198, Japan*
[2] *INFN, Structure of Rome Tor Vergata, Via Della Ricerca Scientifica 1, 00133, Rome, Italy*

marco.casolino@riken.jp

Abstract: The Extreme Universe Space Observatory on the Japanese Experiment Module (JEM-EUSO) of the International Space Station (ISS) is the first mission that will study from space Ultra High-Energy Cosmic Rays (UHECR). JEM-EUSO will observe Extensive Air Showers (EAS) produced by UHECRs traversing the Earth's atmosphere from above. For each event, the detector will make accurate measurements of the energy, arrival direction and nature of the primary particle using a target volume far greater than what is achievable from ground. The corresponding increase in statistics will help to clarify the origin and sources of UHECRs as well as the environment traversed during production and propagation. Possibly this will bring new light onto particle physics mechanisms operating at energies well beyond those achievable by man-made accelerators. The spectrum of scientific goals of the JEM-EUSO mission includes as exploratory objectives the detection of high-energy gamma rays and neutrinos, the study of cosmic magnetic fields, and tests of relativity and quantum gravity effects at extreme energies. In parallel JEM-EUSO will systematically perform observation of the surface of the Earth in the infra-red and ultra-violet ranges, studying also atmospheric phenomena (Transient Luminous Effects). The apparatus is a 2 ton detector using Fresnel-based optics to focus the UV-light from EAS on a focal surface composed of about 6,000 multianode photomultipliers for a total of $\simeq 3 \cdot 10^5$ channels. A multi-layer parallel architecture has been devised to handle the data flow and select valid triggers, reducing it to a rate compatible with downlink constraints. Each processing level filters the event with increasingly complex algorithms using ASICs, FPGAs and DSPs in this order to reject spurious triggers and reduce the data rate.

Keywords:

1 Introduction

JEM-EUSO is a Fresnel-optics refractive telescope devoted to the observation of Ultra High Energy Cosmic Rays showers in the Earth's atmosphere ([4]). This remote-sensing instrument will orbit the Earth every $\simeq$ 90 minutes on board of the International Space Station (ISS) at an altitude of 330 - 400 km. Its goal is the study of the sources of UHECR and the determination of the origin and nature of these particles with high precision, thanks to the increase in statistics due to the larger exposure. The observation principle is the detection of fluorescence light emitted by particles showering in the atmosphere.

The scientific goals of JEM-EUSO are described in detail by [5, 7, 3] and elsewhere at this conference.

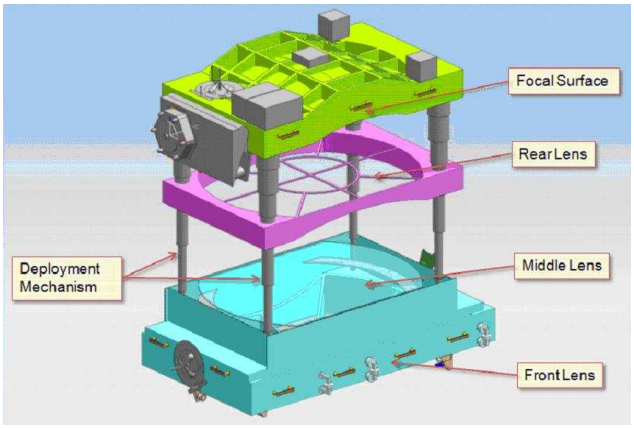


Figure 1: CAD model of the JEM-EUSO structure. The detector is attached to the ISS through the focal surface. The front lens (on bottom of the picture) looks toward Earth.(Courtesy of IHI)

2 Detector characteristics and principle of observation

JEM-EUSO (see Fig. 1) will observe from space the Earth's night atmosphere. It will measure the UV (300-400 nm) fluorescence tracks and the Cherenkov reflected

signal of the Extensive Air Shower induced by UHECR interaction in the atmosphere. JEM-EUSO captures and reconstructs the temporal and spatial evolution of the track through the fluorescent UV photon component of the EAS in the atmosphere. The light is focused through a Fresnel lens diffractive optics with a wide field-of-view ($\pm 30^o$). The light is detected by the focal plane electronics which records the track of the EAS with a time resolution of 2.5 μs and a spatial resolution of about 0.75 km (corresponding to 0.1^o). These time-segmented images allow to determine the energies and directions of the primary particles.

From the UV profile the instrument can reconstruct the incoming direction of the extreme energy particles with accuracy better than several degrees. The instantaneous geometrical area is (in nadir pointing mode) a circle of 500 km diameter, which converts to an instantaneous aperture of $6 \cdot 10^5\ km^2\ sr$. The atmospheric mass monitored, assuming the 60-degree field-of-view, is about $1.7 \cdot 10^{12}$ ton. The target mass for upward neutrino detection is $5 \cdot 10^{12}$ ton. A particle of $E \simeq 10^{20}$ eV particle penetrating the Earth's atmosphere has an interaction length of 40 g/cm^2 and generates a shower of secondary particles. The number of these secondary particles ($N \simeq 10^{11}$) is proportional to the shower maximum and is largely dominated by electrons/positrons. The total energy carried by the charged secondary particles is converted into fluorescence photons through the excitation of the air nitrogen molecules. The fluorescence light is isotropic and proportional to the number of charged particles in the EAS.

The instrument is designed to reconstruct the incoming direction of the ultra high-energy particles with an accuracy better than a few degrees.

The size of the instantaneous geometrical area depends on the tilt of the telescope, the angle between the telescope axis and nadir. The increase of geometrical area from the nadir mode to the tilted mode is a factor of 2 - 5 and depends on the energy of the events.

The depth of maximum development of a shower (X_{max}, expressed in g/cm^2) increases with energy. For a given energy, the value of X_{max} provides information on the nature of the primary particle. The JEM-EUSO objective is to reach a X_{max} resolution of $\simeq 120$ g/cm^2, which is comparable to the differences in X_{max} between showers initiated by protons and by Fe nuclei, making a distinction between protons and Fe nuclei with this kind of experiments possible.

3 Electronics

The data acquisition and handling system is designed to maximize detector observation capabilities to meet the various scientific goals, monitor system status, autonomously taking all actions to maintain optimal acquisition capabilities and handle off-nominal situations. CPU and electronics are based on hardware successfully employed in space experiments such as PAMELA, Altea, Sileye-3, etc., tak-

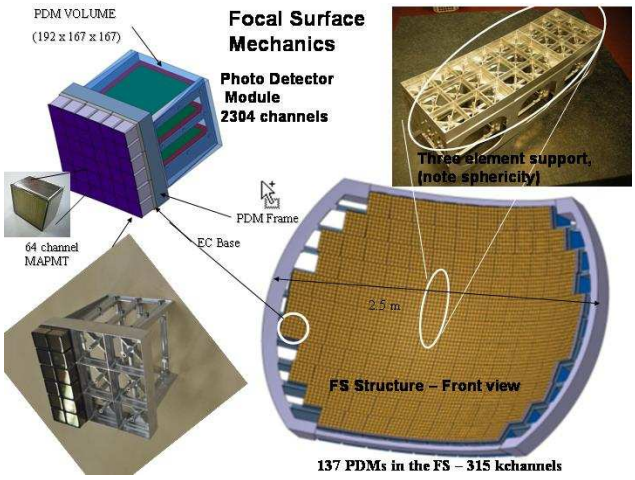


Figure 2: Bottom Right: Mechanical structure of the focal surface. The 2.5 m plane is divided in 137 PDM modules. Each PDM (Top Left) contains 36 Multi-Anode Photomultipliers (Hamamatsu Ultra-Bialkali R11265-64), each with 64 independent channels. The bottom left corner shows the prototype of the mechanical structure with two rows of 12 PMT installed. In the Top Right corner a sub-element of support beams containing three PDM is shown.

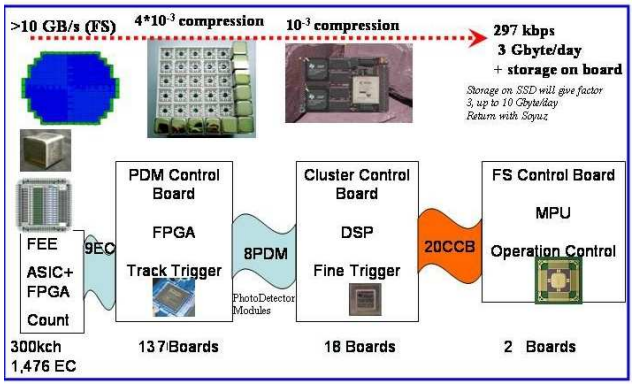


Figure 3: Data Reduction scheme. Each of the $\simeq$ 6000 Multi-Anode Photo Multiplier (MAPMT) of the focal surface is read by an ASIC digitizing the photoelectron signal. A 6*6 array of MAPMT is present and read by each of the 137 PDM modules, where an FPGA performs first level triggering and rejects noise by three orders of magnitude. 8 PDMs are read by a Cluster Control Board, each with an high performance DSP which rejects noise by other three orders of magnitude. The general acquisition and data storage is performed by the main CPU (right).

ing into account recent developments in microprocessors and FPGA technology. Acquisition techniques and algorithms are also derived from the technological development performed in these missions. Rad-hard technology will be employed, with ground beam tests at accelerator facilities such as GSI, Dubna, HIMAC to qualify and test resistance of new devices. Space qualified devices will be employed for mission-critical items.

The general approach is to use off-the-shelf technologies in the development of the laboratory models and breadboard systems to refine and test the various trigger and data reduction algorithms in parallel to hardware development and construction. The same approach will be followed in the use of communication protocols and interfaces (e.g. VHDL, spacewire, 1553, 1355 protocols) and in the realization of the ground support equipment. This will allow for a fast development of the software in parallel to the engineering and production of flight boards, reducing costs and integration time.

Hot/Cold redundancy will be implemented in all systems and in all stages of data processing with the exception of intrinsically redundant devices such as the focal surface detectors.

3.1 Data Acquisition and Reduction

The Data acquisition system (Fig. 3) is based on an architecture capable of reducing at each level the amount of data through a series of triggers controlling an increasingly growing area of the focal surface ([1]). It is necessary to reduce the 10 Gbyte/s output on the focal surface (FS) to the 3 Gbyte/day which can be downlinked on the ground. Each board and data exchange protocol is compliant to handle the data and send them to the higher level of processing if they satisfy the trigger conditions.

An ASIC chip performs photo-electron signal readout and conversion for the 64 channels of the MAPMT. An FPGA handles first level trigger data on a PDM level (reading 36 MAPMTs). The data are stored in a 100 GTU buffer (each GTU corrsponds to a 2.5 μs frame, for a total sampling of 250 μs) upon which the triggering and noise reduction algorithms are implemented. Background events are rejected by a factor 10^3. Second level triggering algorithms are implemented by the 18 CCB (Cluster Control Boards), DSPs with about 1Gflop computing capability which further process triggers coming from 8 PDMs. At this level background is rejected by another factor 10^3. The CPU has a relatively low processing power (100 MHz) since it is charged of the general handling of the experiment. The CPU is part of the Storage and Control Unit System (SCU), the evolution of a similar system used for PAMELA ([2]) and composed of a number of boards devoted to different tasks: 1. CPU mainboard 2. Mass Memory (8 Gbyte) 3. Internal and external kousekeeping interfaces (CAN bus) 4. Interfaces to ISS (1553 and Ethernet) 5. Fast bus interface for event acquisition. The CPU is devoted to the control of the apparatus and the general optimization of the performance of the instrument in terms of data budget and detector status. It is expected to function autonomously and to reconfigure the working parameters with little or no intervention from the ground. It is capable of handling alarms and contingencies in real time minimizing possible damage to the instrument. Long term mission operation and observation planning will be implemented from the ground with specific telecommands used to overrule the specific operation parameters of the instrument. By sending immediate or time-delayed telecommands it will be possible to define the various operation parameters of the instrument in terms of specific physics objectives or specific situations.

The main CPU tasks are: 1) Power on/off of all subsystems. 2) Perform periodic calibrations. 3) Start acquisition / Run. 4) Define Trigger mode acquisition. 5) Read Housekeeping. 6) Take care of real time contingency planning. 7) Perform periodic Download / Downlink. 8) Handle (slow control) 1553 commands.

3.2 Housekeeping module

The housekeeping module is connected to the CPU with the task to distribute commands to the various detectors and to collect telemetry for them in order to monitor in real-time the status of the experiment and optimize its observational parameters.

There are two modules, one internal to the CPU (I-HK), devoted to monitor critical systems, power on/off of secondary power supply etc. I-HK is turned on together with the CPU and enables power on to all subsystems. The external housekeeping board (E-HK) is devoted to the general slow control and monitoring of the status of the apparatus.

I-HK functional module capable of handling both single (upon request) or cyclic (periodic) acquisition/commanding operating both is possible according to the acquisition program and status. Different acquisitions and controls are foreseen. For instance all relays to switch on / off secondary power supplies and subsystems are controlled by High Level signals. This approach has the advantage of a great degree of flexibility keeping at the same time a strong robustness and reliability.

Some of the main electrical interfaces monitored by the module are: 1. Voltage monitor (Primary - 120V 28V; Secondary: +-5V +12V, +3.3V -700 V 2. Current monitor 3. Temperature monitor 4. Contact closure (Lid status, relays) 5. Digital Communication Protocol.

3.3 Communication Protocol

Communication between different layers of the data acquisition chain operate with LVDS (differential signal) to minimize interference and reduce power consumption. All lines are redundant, with each line employing double connectors at each end to increase reliability of the system and resistance to vibrations and thermal stresses. High level

communication protocol between CCB and CPU is based on a simplified version of the SpaceWire.

3.4 Commands from the ground

Slow control communication from/to ground is based on the MIL-STD-1553B standard. 1553 is a slow speed (1Mbit/s) bus used in space and aeronautics for transmission / reception of critical information. In JEM-EUSO the 1553 bus is employed to:

1. Switch on/off the instrument or part of its sections.
2. Issue telecommands from the ground.
3. Set general acquisition parameters based on detector status. Furthermore they can be used to patch (reprogram) part of the software at CPU, DSP or FPGA levels and dump the memory of each level in case of debugging.
4. Reception of keep-alive information from the detector, of nominal events, alarms.
5. Switch from main to spare channel (acquisition, power supply, etc.).

3.5 Storage, downlink, download

Data stored in the mass memory of JEM-EUSO are periodically sent to ISS via a high speed link based on Ethernet protocol. Data are subsequently downlinked to the ground via TDRSS satellite link or stored on hard disks. Data transmitted to the ground consists of: 1. Cosmic ray data from the focal surface 2. Atmospheric Luminous Phenomena, lightning etc... 3. Housekeeping information 4. Alarm 5. Calibration data 6. Ancillary information.

Data are sent to the ground with highest priority given to housekeeping and alarm information. Experimental data are sent to ground with main priority to high energy particle data and special trigger (e.g. Transient Luminous Phenomena, meteoroids, lightning, etc...). The amount of data downlinked to the Earth is $\simeq 3 Gbyte/day$, amounting to about 20% of the data budget. The rest of the data is stored on board ISS on a dedicated disk server. Disks are then periodically returned to the ground with Soyuz capsules. In the current configuration, it is expected to have $\simeq 5 TByte/6 months$ sent on the ground. Even though the UHECR event rate is very low, the background occupies a large part of the data. This is especially true at low energies, where shower development is shorter and more difficult to sort with on board algorithms. A higher memory capability allows to increase the trigger efficiency at low energies (around) $3 - 4 \cdot 10^{19}$ eV and improve the data bandwidth devoted to atmospheric physics (IR and UV channels).

4 Acknowledgements

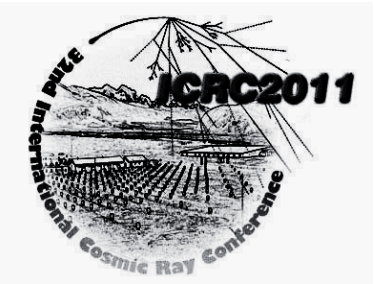
This paper is dedicated to the memory of Y. Takahashi.

This work has been partially supported by the Italian Ministry of Foreign Affairs, General Direction for the Cultural Promotion and Cooperation.

References

[1] Casolino, M., et al, NIM A: 623, 516 – 518.
[2] Casolino, M. et al.: Advances in Space Research, 37, 1857, 2006.
[3] Ebisuzaki, T., et al., Nuclear Physics B - Proc. Supp., 175-176, 237, 2010.
[4] Kajino, F.: NIM A, 623, 422, 2010
[5] Medina-Tanco, G., et al, , ArXiv e-prints, 0909.3766 2009.
[6] Santangelo, A., et al., Progress in Particle and Nuclear Physics, 64, 366, 2010.
[7] Takahashi, Y., New Journal of Physics, 11, 065 009, 2009.

32ND INTERNATIONAL COSMIC RAY CONFERENCE, BEIJING 2011



The Development of Photo-Detector Module Electronics for the JEM- EUSO Experiment

I.H. PARK[1,2], A. JUNG[1], J. LEE[1], J. NAM[1], H. LIM[2], K. NAM[2], T. EBISUZAKI[3], Y. KAWASAKI[3], H. MIYAMOTO[3], F. KAJINO[4], A. SANTANGELO[5], P. GORODETZKY[6], O. CATALANO[7], M. CASOLINO[8], G. MEDINA-TANCO[9], M. BERTAINA[10]
FOR THE JEM-EUSO COLLABORATION
[1]*Department of Physics, Ewha Womans University, Seoul 120-750, Korea*
[2]*Institute for Early Universe, Ewha Womans University, Seoul 120-750, Korea*
[3]*RIKEN Advanced Science Institute, Wako351-0198, Japan*
[4]*Department of Physics, Konan University, Kobe 658-8501, Japan*
[5]*Astronomie und Astrophysik, Universitt Tubingen, 72076 Tubingen, Germany*
[6]*APC, Univ. of Paris Diderot, CNRS/IN2P3, 75205 Paris Cedex 13, France*
[7]*Istituto di Astrofisica Spazialee Fisica Cosmica di Palermo, INAF, 90146 Palermo, Italy*
[8]*Department of Physics, University of Rome Tor Vergata, 00133 Rome, Italy*
[9]*Inst. de Ciencias Nucleares, UNAM, AP 70-543 / CP 04510, Mexico D.F.*
[10]*Dipartimento di Fisica Generale dell'Università di Torino, Italy*
ipark@ewha.ac.kr

Abstract: The JEM-EUSO focal surface detector consists of about 300,000 photodetector channels that are organized into 137 building blocks called Photo-Detector Module (PDM). A PDM is composed of 36 64-ch MAPMTs, analog ASICs, and digital electronics. The digital electronics, called PDM board, is in charge of readout of 36 MAPMTs via ASICs, control of ASICs via JEM- EUSO central data acquisition system, Level-1 trigger with decision every JEM-EUSO time unit of 2.5 μs, and buffering of a complete event of Extreme Energy Cosmic Rays typically lasting 200 μs. On positive trigger, the data of 8 adjacent PDMs is transferred to Cluster Control Board where Level-2 trigger is processed to refine the selection of interesting events. We expect the rate of Level-1 trigger is designed to be 7 Hz with 2 kHz of input data. We present the development of the PDM board for the JEM-EUSO experiment.

Keywords: JEM-EUSO, Ultra High Energy Cosmic Rays (UHECR), Trigger

1 Introduction

The JEM-EUSO space mission is devoted to the detection of Extreme Energy Cosmic rays (EECRs) including neutrinos by looking downward from the International Space Station [1,2,3]. The JEM-EUSO telescope is based on double Fresnel lens optics with a large diameter (about 2.5m) and a wide (±30°) field of view (FoV). The focal surface system identifies the track of UV photons generated by UHECR with an angular resolution of 01. Degrees thanks to a fast (~μs) and highly pixellated (~3x105 pixels) digital camera which works in single photon counting mode. Details of the optics are described elsewhere.

The focal surface (FS) of JEM-EUSO has a spherical shape with about 2.7 m curvature radius, covered with about 5,000 64-channel (8x8) multi-anode photomultiplier tubes (MAPMTs). The FS detector consists of Photo-Detector Modules (PDMs), each of which consists of nine Elementary Cells (ECs). The EC contains four units of the MAPMTs. The FS accommodates 137 PDMs. Details of the focal surface detector are described elsewhere [4]. The FS electronics system records the signals of UV photons generated by cosmic rays with high trigger efficiency and reasonable linearity in the range of 1019-1021 eV. Power consumption per channel is required to be less than 2.5mW to accommodate the 3x105 signal channels within the power budget of 1 kW.

Figure 1 shows an overview of JEM-EUSO readout, trigger and control architecture. Anode signals of the MAPMTs are counted and recorded in buffers for each GTU (Gate Time Unit~2.5 μs) to wait for a trigger. The PDM (Photo-Detector Module) electronics receives digitized data from frontend ASIC [5] and transmits to CCB (Cluster Control Board) [6] on positive triggers. PDM is connected electrically to 9 EC boards each consisting of 4 MAPMTs. The FS system is built with 137 PDMs and

therefore 2304 MAPMT channels in total. On triggering from a PDM, 8 adjacent PDMs are subject to transfer the data kept in their buffers to a CCB through high speed data protocol. PDMs are independent each other, which implies that there is no communication between PDMs. Therefore, system clocks, configuration of ASIC, run control including overall data transfer, and housekeeping (HK) should be provided to each PDM by higher level systems of CPU through CCB, as shown in Figure 1. The required clocks [7] are 40 MHz for subsystems not only PDM electronics but also frontend ASIC and 400 kHz that is the clock of the JEM-EUSO GTU.

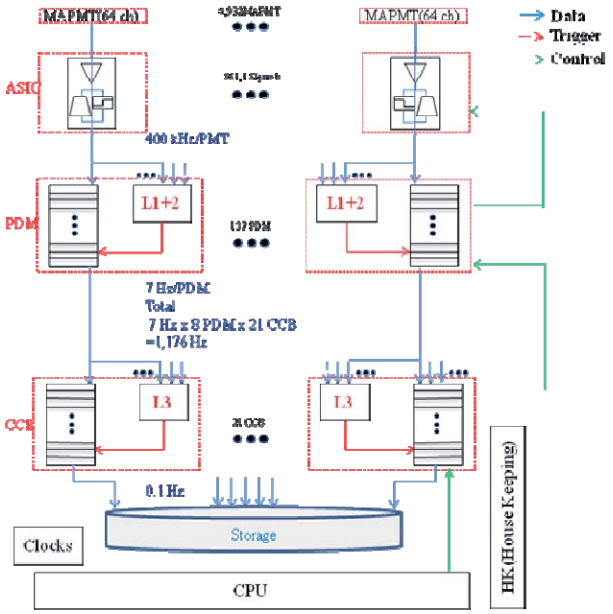


Figure 1. JEM-EUSO trigger, readout and control architecture.

In JEM-EUSO a hierarchical trigger [8] scheme has been investigated for effective reduction of raw data of ~10 GB/s down to 297 kbps, which meets the requirement of the limit in data transfer to the ground. The data reduction is made first at the PDM electronics with Level 1 (L1) trigger processor. Input rate is expected to be 400 kHz, while output is 7 Hz, so reduction of factor 6×104 is required from the trigger electronics of PDM. As shown in Figure 1, Level 2 (L2) trigger is carried out by the CCB, and described in [6]. The L1 trigger latency within PDM is expected to be only 1 GTU, 2.5 μs, which means that the trigger decision will be made every GTU. The EECR trigger will be issued typically around its shower maximum, and thus the PDM needs data buffer of about 128 GTUs to hold the data of the entire shower profile, before and after, the decision of L1 trigger. Four L1 trigger modes are under development: a) Normal mode with a GTU of 2.5 μs for routine data taking of EAS, b) Slow mode with a programmable GTU up to a few ms, for the study of meteorites and other atmospheric luminous phenomena, c) Detector calibration mode with a GTU value suitable for the calibration runs, and d) LIDAR mode with a GTU of 200 ns. Details of the FS electronics system are described in [9].

2 Requirements

The hardware of PDM electronics includes FPGA (Field Programmable Gate Array) chips and interfaces to ASIC and CCB, and thus a large number of connector pins is foreseen. Another major limitation in the design of PDM electronics comes from power consumption which is about 1.5 Watts per PDM. Therefore, the selection of FPGA chips is a non-trivial issue because power consumption, number of I/O pins enough for a large number of data transfer lines from ASICs and to CCB, space qualification for at least three years of operation in space, number of logic cells enough for of complex trigger algorithms, and cost of space grade chips must be taken into account all together.

Power consumption: Most power consumed device in the PDM electronic is FPGA. The most popular species are the ones of Xilinx, ALTERA, and ACTEL. The JEM-EUSO is considering one of ACTEL families because of its long space heritage, low power consumption. The limitation in memory size of ACTEL might be overcome with an external memory.

Clocks: The clocks, 40 MHz and 400 kHz, are received from CCB and distributed to ASICs as well. The 400 kHz clock is GTU clock and is necessary for data transfers among ASIC, PDM and CCB. The 40 MHz clock is used as an internal system clock for a various calculations and data handlings in PDMs.

Physical dimension of the PDM boards: As shown in Figure 2 (bottom right), the PDM electronics is built with 6 boards maximum, each 120mm×135mm in size where 100mm×115mm will be used for devices mount. Three boards are equipped with multi-pin connectors because the PDM needs a relatively large number of I/O pins, about 500 I/O, to connect to 9 EC boards and a CCB. The mass of 145 gram is allocated for a PDM electronics board.

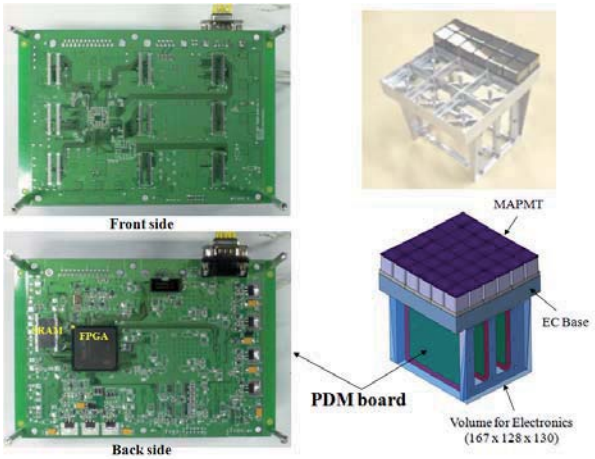


Figure 2. Fabricated PDM prototype board (left). PDM structure [10] and MAPMTs (upper right corner). PDM includes MAPMTs, EC boards and PDM board (bottom right corner).

Thermal: The required temperature for the operation of PDM is between -30°C and 50°C, so associated electronic parts should meet this standard. The PDM might be

turned off at the temperature out of range to protect itself against any possible damages.

Data rate: PDM has an input data from ASIC at the rate of 400 kHz. PDM is subject to lower the data rate down to 7 Hz that is output to CCB. So the factor of data reduction via Level 1 trigger is expected to be about 6×104.

Threshold tuning against backgrounds: As seen in Figure 3, backgrounds are different by about factor three in PDMs ranging from the center to the edge of the FS. Therefore, thresholds for trigger should be set differently depending on the location of PDMs. Those thresholds might be recalibrated and reset in space by uploading relevant parameters from ground and to take into account the varying conditions of the nightglow background.

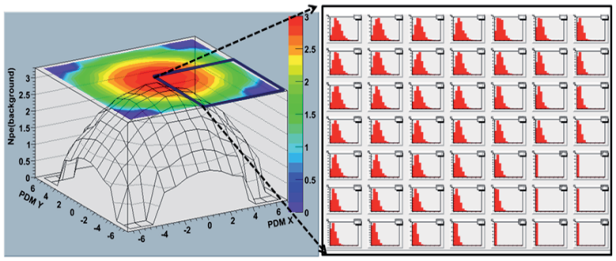


Figure 3. Simulation of background distribution in terms of number of photo-electrons/GTU/pixel (Npe) on FS (left) and for each PDM (right).

3 Design of the PDM board

The physical layout of PDM has been shown in Figure 2 (right), where the mechanical frame [10] is designed to hold 6 boards in total. Three boards are of a primary set of the PDM electronics, while the other three of a redundancy set. A board is dedicated for placing FPGAs. Connectors for cables interfacing to ASIC and CCB are mounted on the other two boards. The same power lines are connected to primary and redundancy boards, but only a set of boards are selected at a time by a switch. The redundancy boards might be switched to by issuing a special command from ground if necessary.

The schematic layout of the PDM board is shown in Figure 4 (left). The main functional blocks are as follows: ASIC for the reception of photon counting data from ASIC, KI for the reception of charge to time data from ASIC, PDM(FPGA) for logics of trigger, data readout and control, CCB for the transmission of triggered data to CCB, HK for the interface to HK for slow control monitoring [11], CPU for the interface to CPU that is the main control, PC interface for the interface to PC for standalone tests, POWER for the interface to JEM-EUSO PDM power supply, and PROM/JTAG for the download of FPGA codes.

Figure 4 (right) shows the functional blocks of the PDM FPGA which include trigger calculation unit, control of the PDM board and interfaces of ASIC, CCB, CPU and HK. Those units are briefly described as follows: SC (System Control) for the control of PDM system for operation, ABIU (ASIC Bus Interface Unit) for the interface between ASIC and PDM by customized communication, CBIU (CCB Bus Interface Unit) for the interface between PDM and CCB by customized or commercial communication, HIU (HK Interface Unit) for the interface between PDM and HK, CIU (CPU Interface Unit) for the interface between PDM and CPU, TU (Trigger Unit) for the decision of the best trigger from simultaneous trigger signals, DPU (Data Processing Unit) for the processing of PDM data, CRU (Calibration Run Unit) for the control of calibration run, RS (Run Summary) for creation of run summary.

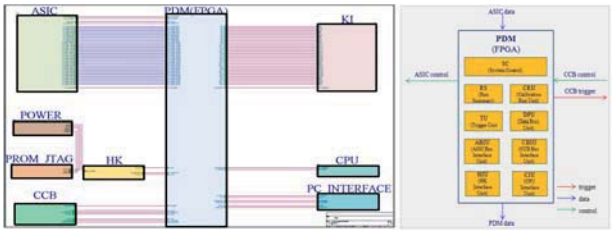


Figure 4. The schematic layout of the PDM board (left) and the functional blocks of the PDM FPGA (right).

4 PDM interfaces to ASIC and CCB

A PDM oversees 9 ECs, as shown in Figure 2 (right), and each EC board built with 4 ASICs supports 4 MAPMTs. As described earlier, two boards of PDM are equipped with connectors which receives data from ASIC, relays controls and powers to ASIC. At the beginning of power on, ASICs will be configured via a number of configuration control lines by PDM. The data from ASICs to PDM are two folds: one is photon counting data and the other KI data that is summed charge information of 8 MAPMT channels. On the other hand, each ASIC provides its prompt trigger signals which are useful for PDM to see any significance in photon counting and KI data in prior to waiting or collecting the data every GTU, which might save the power consumption of PDM. Such fast signals can be used for triggering of fast and/or large intensity event like TLEs and Cerenkov from neutrinos.

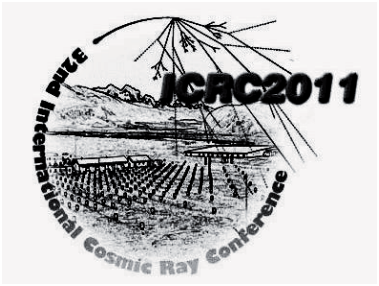
The PDM-CCB interface is similar to ASIC-PDM such that 8 PDMs are connected to a CCB as described in earlier. When any of 8 PDMs fires a Level-1 trigger, the PDM notifies the CCB which subsequently requests data transfer to the group of 8 PDMs physically neighboring each other. Although Level 1 trigger latency is 1 GTU, but the decision is made near the maximum of EECR shower, which implies that the data buffer of at least a full event is required in PDM, which is about 128 GTU, equivalently 320 μs. Therefore, total data size per PDM to be transferred to CCB is about 2.7 Mbits (= 64 ch × 8 bit × 36 PMTs × 128 samples, plus 12% additional data from the analog part - KI). The trigger output is designed to be 7 Hz per PDM, so a CCB foresees 56 Hz of input from 8 PDMs. Assuming the transfer rate from PDM to CCB via 40 MHz, it takes about 0.07 s (2.7 Mbits / 40 MHz) or 27,000 GTU per line. However, the dead time fraction of data taking will be minimized by employing a double buffering method; a buffer for data taking and the other for data transfer to CCB.

5 The PDM prototype board

The prototype board has been built as shown in Figure 2 (left) and tested mainly for interfacing to ASIC and implementation of reduced version of trigger algorithms. The USB-8451(NI) is used for the control and data transfer via PC. The test is successful as expected from the design. The PDM sends 40 MHz and GTU clocks to ASIC, then ASIC issues a series of loading of 8 bit data to be transferred to PDM. Total 64 pixels photon counting data are received at PDM via 8 lines. A text file of the data is sent from ASIC to PDM, and opened at PC, where each of 8 lines receives 8 bits data. The next step is to test the transfer of data to CCB and to implement the full Level 1 trigger algorithm in FPGA.

References

[1] Y. Takahashi et al., 2009, New Journal of Physics, 11, 065009.
[2] T. Ebisuzaki et al., 2008, Nucl. Phys. B (Proc. Suppl.), 175-176, 237.
[3] F. Kajino et al. (JEM-EUSO collaboration), 2010, Nuclear Instruments and Methods in Physics Research A 623, 422-424.
[4] Y. Kawasaki, Proceedings of this Conference, #0472
[5] S. Ahmad, Proceedings of this conference, #0236
[6] J. Bayer, Proceedings of this conference, #0836
[7] G. Osteria, Proceedings of this conference, #1131
[8] O. Catalano, Proceedings 31st ICRC, Lodz, Poland (2009)
[9] M. Casolino, Proceedings of this conference, #1219
[10] M. Ricci, Proceedings of this conference, #0335
[11] G. Medina Tanco, Proceedings of this conference, #0930



The JEM-EUSO time synchronization system

GIUSEPPE OSTERIA[1] ON BEHALF OF THE JEM EUSO COLLABORATION
[1]*Istituto Nazionale di Fisica Nucleare Sezione di Napoli*
contact.giuseppe.osteria@na.infn.it

Abstract: The JEM-EUSO instrument is a wide-angle refractive telescope in near-ultraviolet wavelength region being proposed for attachment to the Japanese Experiment Module, Kibo, onboard ISS. The instrument consists of high transmittance optical Fresnel lenses with a diameter of 2.5m, a focal surface covered by 4932 MAPMTs of 64 pixels, frontend readout, trigger and system electronics. The tracks generated by the Extensive Air Showers produced by UHE primaries propagating in the atmosphere, are reconstructed on the focal surface by registering in a cyclic memory, every 2.5 microseconds, the data coming from the 315648 pixels and by selectively retrieving only the interesting ones on the occurrence of a second level trigger. The second level trigger has a latency of the order of 10 ms and it is asserted from one or more of the 18 CCB units looking at different zones of the focal surface. In order to guarantee the correct time alignment of the events and to measure the arrival time of the event with a precision of few microseconds a clock distribution and time synchronization system for the focal surface electronics has been developed. We will discuss the status and the technical solutions adopted so far.

Keywords: Extreme High Energy Cosmic ray, electronics for space environment.

1. Introduction

JEM-EUSO (Extreme Universe Space Observatory on Japanese Experiment Module) is a project for a new type of observatory that uses the whole Earth as a detector[1]. The sensor is a super wide-field telescope that detects transient luminous phenomena taking place in the Earth atmosphere caused by particles coming from Space.
The main objective of JEM-EUSO is to investigate the nature and origin of the Extreme Energy Cosmic Rays, EECRs ($E > 5\times10^{19}$ eV), which constitute the most energetic component of the cosmic radiation. [2]
This remote-sensing instrument orbits around the Earth every ~90 minutes on board of the International Space Station at the altitude of 300-400 km. The instrument is planned to be attached to JEM/EF of ISS and will be launched by H2B rocket and conveyed to ISS by HTV (H-II transfer Vehicle).

2. The JEM EUSO apparatus

The instrument consists of high transmittance optical Fresnel lenses with a diameter of 2.5m, a focal surface covered by 4932 MAPMTs of 64 pixels, focal surface electronics and system electronics. A LIDAR and an IR camera assembly will also be provided for atmosphere sounding, which is an important complement for the main data analysis.
The telescope has to be capable to detect fluorescence and Cherenkov photons from the Extensive Air Showers (EAS) and to observe space-time development from 430 km altitude above sea level.
The fluorescence and Cherenkov photons coming from EAS are converted to electric charge by 64 pixel MAPMTs. The signals from the MAPMT are discriminated from electrical noise and digitalized by a front-end ASIC [3]. The ASIC counts the number of photoelectrons produced in a fixed time window for each pixel. The recorded amount of light is nearly proportional to the shower size at the various depths in the atmosphere. By imaging the motion of the streak every few microseconds, it allows to determine the arrival direction of the primary EECR. The integral of light recorded is correlated to the energy of the primary EECR
Since the total number of pixels in the array is very large ($\sim 3\times10^{5}$), a multi-level trigger scheme was developed [4]. This trigger scheme relies on the partitioning of the Focal Surface in subsections, named PDM (Photo Detector Module), which are large enough to contain a substantial part of the imaged track under investigation. The general JEM-EUSO trigger philosophy asks for a System Trigger organized into two main trigger-levels. The two levels of trigger work on the statistical properties of the incoming photon flux in order to detect the physical

events hindered in the background, basing on their position and time correlation. In Figure 1 a scheme of the FS electronics and trigger flow diagram is reported. The First-level trigger is implemented in a dedicated board (PDM board) [5]. Each PDM board is connected to 9 pieces of ECs (36 MAPMTs), handling 2304 channels in total. The output from each 8 PDM board is transmitted to one of 21 Cluster Control Boards (CCB) [6], then CCBs in turn transmit pixel information which passed the fine trigger conditions via Intermediate Data Acquisition Board to the main CPU.

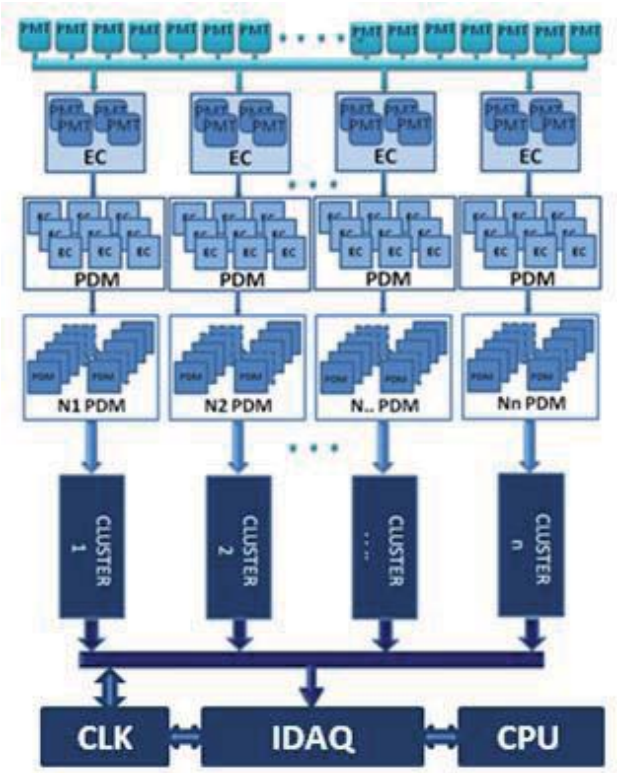


Figure 1. Focal Surface electronics hierarchical scheme

The data acquisition is based on the same hierarchical architecture designed to reduce the amount of data at each level of trigger. All the signals produced by MAPMTs are registered and stored in cyclic buffer waiting for the trigger signal before to be transmitted to the next level for further analysis. The two trigger levels have different latencies in particular the second level trigger has a latency of the order of 10 ms. The data has to be stored for such a long period before to be rejected of acquired. The apparatus is segmented in various zones and in each of these zones different units process independently different sets of data. In order to correctly assign to an event all its own data sets (distributed in space and time) and in order to keep under control the dead time of the apparatus (at level of PDM) is mandatory to perfectly synchronize the whole system and to tag properly the data sets. The role of manage the synchronization of the system is performed by a dedicated board (CLK board) which will be described in the next sections.

3. The clock board

3.1 Requirements

The clock and time synchronization board (CLK board) is mainly devoted to generate and to distribute the system clock and the synchronization signal (GTU clock) to all the devices of the Focal Surface (FS) electronics. However, in order to provide the time synchronization of the events, further and more complex functionality has to be added to the board. The board generates or receives all the signals needed to control the timing of data acquisition. These same signals can be used for measuring the absolute arrival time of the events with a precision of few microseconds if the board is interfaced with the GPS system of the apparatus.

The requirements for CLK board are:

- Generating and distributing system clock (40 MHz) and GTU clock (400 KHz)
- Time synchronization of the event
- Interfacing with the JEM EUSO GPS system
- Interfacing with the Time provided by ISS/JEM (to be used in case of failure of GPS system)
- Receiving the CCB 2nd level trigger signals and registering the trigger pattern
- Live-time and dead-time measurements

A block diagram of the CLK board is shown in Figure 2.

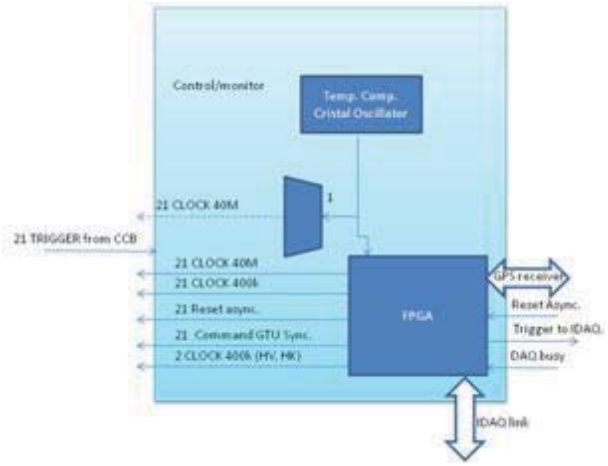


Figure 2. Clock board block diagram.

3.2 Clock signals

The main function of the CLK-board is the generation and distribution of the system clock and the GTU clock to all the devices of the Focal Surface (FS) electronics.
The distribution of these signals through the chain CCB-PDM-FE is considered the baseline design.
According to this scheme the clock signals go through three levels of boards before reaching, for example, the FE-ASIC. The responsibility of the signal integrity, as well as the total power budget, is shared among the three

levels. Prescriptions shall be imposed at each level to keep the total jitter and the total skew inside the requirements.

The master clock is generated by a space qualified crystal oscillator. Frequency stability of +/-0.1 ppm is easily achievable making use of TCXO, Temperature Compensated Crystal Oscillator. Better performance could be guaranteed by using space qualified OCXO, Oven Controlled Crystal Oscillator, with the frequency stability of +/-5 ppb.

An FPGA (Xilinx Virtex4/5 or ACTEL) will be used to fan out the signals. The system clock signals and the GTU clock signals are sent to the CCB boards.

Differential LVDS as output protocol and point to point connections will be used.

The static power dissipation is 10 mW/line for 2.5 V typical driver plus 145 microW/MHz of dynamic power. Cables of equalized length and system blocks like PLL, DLL or clock network of the Virtex family shall be used on the CLK, CCB and PDM boards in order to minimize the total skew of the clocks.

An alternative approach in which the CLK-board generates and distributes only the GTU clock and each CCB and PDM board has an own 40 MHz crystal oscillator will be carefully studied. In this case the synchronization between the two clocks signal will be performed by using double latches technique or PLL system block of the Xilinx Virtex devices.

3.3 Synchronization with GPS system and Time system from ISS/JEM

The measurements of the arrival time of the particles on a scale of few microseconds by our instrument may be possible if each trigger correlated with a detected cosmic particle, acquires a precise time stamp provided by a spatial GPS receiver or, in case of failure of the GPS system, with less precision, by the Time reference provided by the ISS/JEM. The time stamp will be also used to calibrate the internal clocks of the experiment. The slow signal PPS (1 Hz) will be used to open a communication gate to get the UTC time. This time, associated with the internal clock, will provide a stamp of a physical event. In order to associate to each 2nd level trigger the appropriate time stamp, the 2nd level trigger signals coming from the CCB board shall be sent to the CLK-board. On each 2nd level trigger the CLK-board stores in a register the trigger configuration and send a trigger signal to the IDAQ board. The timing of this last operation should be carefully defined in order to take into account the L2 trigger latency. The information on the trigger pattern could be used by the IDAQ board in order to start different data acquisition procedures.

3.4 Event synchronization

Events which trigger simultaneously two CCBs can be correctly reconstructed only if the time information on the development of the event is present in the data structure and it is synchronized with a precision of one GTU. A possible way to obtain such a time synchronization on all the CCB cards at level of one GTU is to implement GTU counters on the CCB boards and on the CLK board. If a trigger rate of 0.1 Hz is assumed, the CCB and Clock board counters should have ≥ 24 bits to avoid over flow between two consecutive triggers.

In this scheme the 2nd level (L2) trigger lines from all CCB boards are connected to the CLK-board.

After receiving the appropriate command, the CLK board initializes all the GTU counters (Time-sync signal) and starts to count the GTUs.

On the occurrence of each 1st level trigger, the PDM transfers a block of data. The CCB latches the GTU number present in its own GTU counter and associates this information to the data packet. In case of an L2 trigger the content of GTU counter of the CLK board is latched. In such a way the difference in the arrival time of different L2 trigger signals can be measured. Furthermore the CLK board can associate to each L2 trigger a time stamp with UTC time obtained from the GPS receiver. The arrival time of the event will be reconstructed, with the time accuracy of the GTU clock, by adding to the UTC time the appropriate number of GTUs as evaluated from the GTU number relative to the L1 and L2 triggers and from the position of the GTU relative to the L1 trigger in the transferred data from a PDM. In this regard it is worthwhile to note that the PDM data block, in the baseline design, contains a fixed number of consecutive GTUs acquired half before and half after the GTU relative to the trigger. However, in case of slow events, it could be useful to transfer data relative to non consecutive GTUs, for example a data every 10, 100 GTUs. To address this situation and to improve the flexibility of the system, additional information on the number of GTU transferred, on the position inside the transferred block of the GTU relative to the L1 trigger and on the sampling rate will be added to the header of the data block.

A *Time-sync* signal, synchronous with the GTU clock, will be distributed to each CCB to initialize all the GTU counters and restart the acquisition after the data transfer from CCB to IDAQ –CPU.

3.5 Live/dead time counters

The main CPU measures the time length of the run with a precision of the order of 1 ms.

To measure a flux is necessary to know the live-time T_{live} of the apparatus during all the period of data taking. If we measure, for each event, the time between event and event t_{ev} and the time needed to acquire the data relative to the event (dead-time) t_m then the total live time of a run can be evaluated by:

$$T_{life}^{(1)} = T_{CPU} - \sum_{i=1}^{N} t_m^{(i)}$$

Where N is the total number of events or by

$$T_{life}^{(2)} = \sum_{i=1}^{N} t_{ev}^{(i)}$$

The possibility of measuring two different ways T_{live} on the entire run allows controlling and possibly correcting off-line, any drift in the clock of the board. The verification can be done by checking that:

$$T_{CPU} = \sum_{i=1}^{N} (t_{ev}^{(i)} + t_m^{(i)})$$

The dead time of an event and the time between two events can be easily measured with a couple of counters implemented on the clock board. The start-stop logic is driven by the trigger signal sent to the IDAQ board and by the busy signal received in response to this signal from the CPU

A 18 bit counter clocked by a 100 KHz signal guarantees an error on the single measure of dead time $\Delta t_m = 10^{-5}$ s with overflow reached after 2.62 s (typical dead times of the order of tens of milliseconds).

The time between two events can be measured by a 18 bits counter clocked at lower frequency (400 kHz clock divided by a factor 128 (3.125 KHz) . The error on the single measurement of live time is in this case: $\Delta t_{ev} = 3.2\ 10^{-4}$ s with overflow reached after 83.9 s (expected trigger rate 0.1 Hz).

The approach just described is valid in cases where the whole apparatus is stopped at the arrival of each trigger. If it is decided to acquire only the CCB that has triggered leaving the rest of the apparatus in operation, the live time and the dead time should be measured separately for each CCB.

4. Prototype board and test

The CLK board laboratory prototype, currently tested at INFN Section of Naples, is implemented in a Virtex-5 FPGA (XC5VLX50T, package FFG1136) hosted on a Virtex®-5 LXT ML505 development board. The device is not space qualified so this prototype board is used mainly to develop and test interfaces to other devices.

In order to measure the jitter and the skew of clock and GTU signals along the chain of three board (CLK board, CCB board and PDM board), the setup shown in Figure 3 has been used. The CCB board has been simulated by using a Virtex-4 FPGA (XC4VFX20, package FF672) mounted on a Virtex®-4 ML405 development board. The PDM board has been simulated by using a M1A3P1000L-FGG484 ACTEL FPGA mounted on an ACTEL M1A3PL development board. Obviously this configuration allow us to test only the solution in which all the clock signals are transmitted and received on the I/O pins of the FPGA without use of any LVDS buffer. More realistic test will be performed when the maximum length of cables will be better known.

The interface with the GPS system is simulated by using a Vincotech A1080-A SiRFStar III-based GPS receiver.

The device supports a subset of the NMEA-0183 standard for interfacing marine electronic devices as defined by the National Marine Electronics Association (NMEA).

A bi-directional serial interface with Vincotech's GPS module has been implemented by use of the full duplex UART (Universal Asynchronous Receiver Transmitter) interface of the GPS processor.

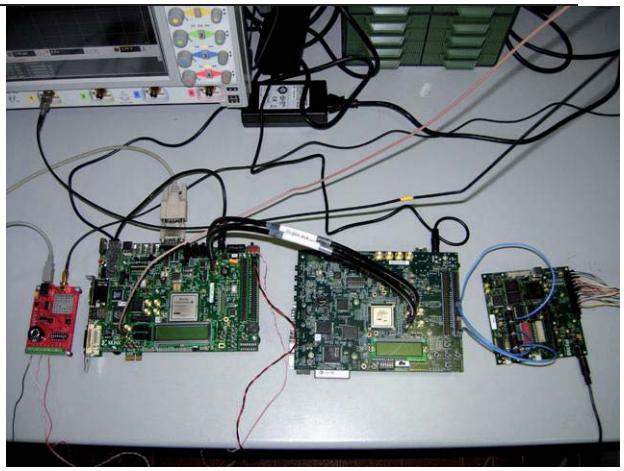


Figura 3. The setup used to test the CLK board.

This interface allows to acquire the output of the GPS modules (NMEA sentences, etc.) roughly 300 ms after the PPS pulse and store in a memory the relevant information (UTC time, longitude, latitude, number of satellites, etc), on the other side the UART interface is used to send commands to Vincotech's GPS modules.

The communication link between CLK board and IDAQ board is based on a serial protocol developed according the Spacewire standard but tailored for the specific characteristics and constraints of the PAMELA mission.

5. Conclusions

The time synchronization system for the JEM-EUSO project has been discussed in this paper. The system distributes the clock signals to the FS electronics and manages all the signal needed to take correctly aligned in time the data packets produced in different parts of the apparatus at different time. The system, for each event, provides the measurement of the arrival time with a precision of few microseconds, the measurement of the time elapsed since the previous event (live time) as well as the time needed to acquire the previous event (dead time). The CLK board described in this paper is now under development, and it will be further tested in laboratory in this year.

References

[1] Y. Takahashi, New Journal of Physics, Vol. 11, N.065009, 2009.

[2] G. A. Medina Tanco et al., Proc. 32nd ICRC, 2011 (ID0956).

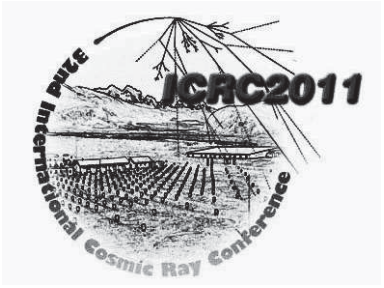
[3] S. Ahmad et al., Proc. 32nd ICRC, 2011 (ID0236).

[4] O. Catalano et al., Proceedings of the 31st ICRC, Lodz, Poland (2009)

[5] I. Park et al., Proc. 32nd ICRC, 2011 (ID1236).

[6] J. Bayer et al., Proc. 32nd ICRC, 2011 (ID0836).

32ND INTERNATIONAL COSMIC RAY CONFERENCE, BEIJING 2011



Moscow State University Satellite "Mikhail Lomonosov" – the Multi-Purpose Observatory in Space. Technological Developments in Russia for JEM-EUSO Collaboration

M.I. PANASYUK[1]
FOR THE "LOMONOSOV" COLLABORATION, FOR THE JEM-EUSO COLLABORATION
[1]*D.V. Skobeltsyn Institute of Nuclear Physics of Moscow State University*
panasyuk@sinp.msu.ru

Abstract: The new mission "Mikhail Lomonosov" is dedicated to founder of Moscow State University M.V. Lomonosov. Its scientific program is devoted to extreme phenomena in the Universe (extreme energy cosmic rays EECR and gamma ray bursts GRB) and to study of phenomenon in near Earth space and upper atmosphere. The scientific payload consists of the fluorescence detector TUS for study EECR, GRB detectors measuring optical, X-ray and gamma ray radiation and other detectors described in the presentation. Mikhail Lomonosov instruments contain the parts (many-anode PM tubes, specific chips) developed for the JEM-EUSO mission which will be tested in space before use in large scale (thousands copies) in JEM-EUSO mission. TUS detector will provide first data on EECR events measured from space and is considered as "pathfinder" for JEM EUSO detector.

Keywords: Mikhail Lomonosov, Space Observatory, TUS, EECR

1 "Mikhail Lomonosov" general description

It is a medium scale satellite with full mass less than 400 Kg, platform mass 200 Kg and scientific payload 120 Kg. The payload consists of several detectors (figure 1) and information block. The detectors are:

- TUS (a box in focus of the mirror concentrator in figure 1) – UV telescope for measuring extreme energy cosmic ray particles.
- BDRG (shown in figure 2) – 3 identical detectors for measuring X-ray and gamma-ray fluxes and selection of GBR. Detector parameters: energy range – from 10 KeV to 3 MeV, time resolution – 100 μs, source sensitivity – up to 10^{-7} Erg·sm^{-2}, source angular resolution – 1–3°, field of view – 2π sr.
- SHOK (shown in figure 3) – 2 fast wide-angle cameras for measuring GBR in optical wavelengths. Field of view of each camera – 1000 sq.deg, maximum frame rate – 5–7 frame per second.
- UFFO + UBAT – 20-cm UV-optic telescope and X-ray camera for selection and measuring GRB in UV, X-ray and G-ray bands and forming "alerts" for ground-based optical observatories.
- DEPRON – detector for measuring charge particle flux on orbit and determining radiation environment on the satellite. Device includes: 1) charged particles dosimeter based on semiconductor detector; 2) thermal neutrons detector based on gas-discharge counter SI13N.
- ELFIN – instrument for measuring variations of the Earth magnetic field and charge particle flux on orbit. It consist of a Flux Gate Magnetometer, an Energetic Particle Detector for Electrons, and an Energetic Proton Detector for Ions.

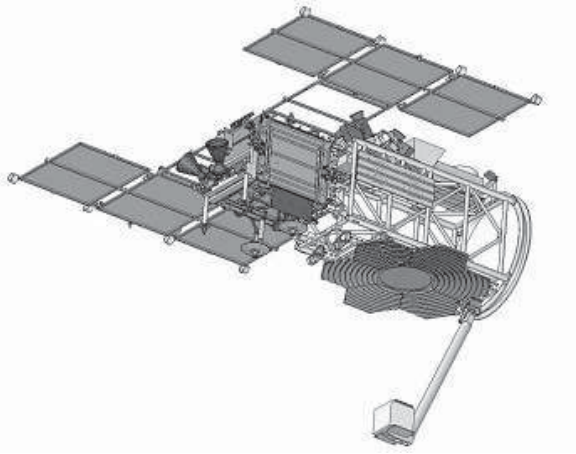


Figure 1: Mikhail Lomonosov satellite.

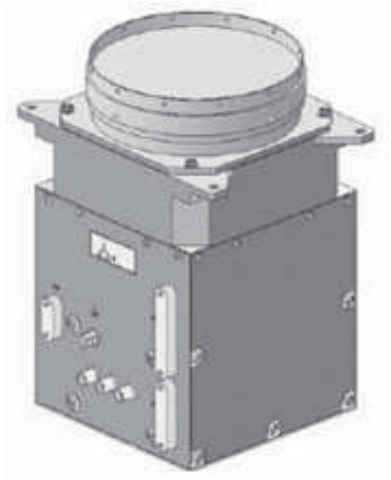


Figure 2: Detector BDRG.



Figure 3: Detector SHOK.

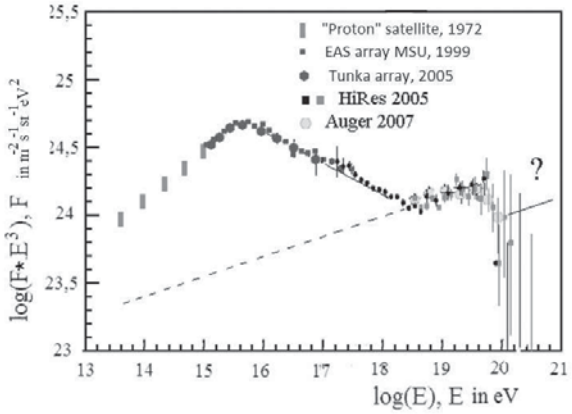


Figure 4: Cosmic ray energy spectrum. Line with a question mark indicate the energy range under investigation in the TUS experiment.

2 The TUS detector

The TUS detector is the largest part of scientific instruments on board "Mikhail Lomonosov" satellite, figure 1. It is the first space detector of extreme energy cosmic rays in line of the "Airwatch" concept, suggested by John Linsley [1]. Today the most advanced Airwatch projects are JEM-EUSO [2] and KLYPVE [3] with its prototype: the TUS detector. TUS is abbreviation of "Track Ultraviolet Set-up". TUS mass is 60 Kg, electric power 60 Wt, orientation to nadir $\pm 3^\circ$. Two main parts of TUS are: mirror-concentrator and photo receiver. The mirror area is ~ 2 m^2, focal spot RMS is < 7 mrad in FOV of 4.5° (for details see [4]). Photo receiver comprising 256 pixels everyone of 10 mrad covers the atmosphere area $(H \times 0.16)^2$ km^2 (H will change from 550 to 350 km during of 3 years operation). In this period expected exposure factor for EECR of energy more than 200 EeV is 12,000 km^2 sr. EAS energy threshold of the TUS detector is ~ 70 EeV, expected EAS event statistics in 3 years: 60 events.

The main goal of the TUS experiment is a search for the EECR energy spectrum in region beyond the GZK "cut-off" and a search for EECR sources in all sky measurements. In previous experiments there were indications on existence of events beyond the GZK limit – among them the event with energy 300 EeV detected by Fly-Eye detector [5] was widely discussed. The TUS experiment will search for events in this energy range, figure 4.

The TUS photo receiver contains 256 pixels. They are grouped in 16 clusters every of which contains 16 PMTs with common HV and electronics. The electronics is designed for a multi-purpose scientific program. The time sampling starts from 0.8 μs as needed for EAS measurements. Slower developing objects (atmospheric electric discharges, sub-relativistic dust grains, micrometeors) will be observed with larger sampling 64 μs, 0.4 ms given by digital integration.

In two "Universitetsky-Tatiana" satellite missions [6] the TUS pixel and electronics were tested in measurements of the atmosphere glow and atmospheric flashes in near UV range (wavelengths 300-400 nm). They operated in polar orbits, heights 830-950 km.

The measured map of the UV glow intensity showed that at moonless nights the atmosphere UV intensity in different Earth regions varies from $3 \cdot 10^7$ to $2 \cdot 10^8$ ph cm^{-2} s^{-1} sr^{-1}. At full moon nights the intensity rises to 2-3$\cdot 10^9$ ph cm^{-2} s^{-1} sr^{-1}.

The short (1 ms) flashes with small photons numbers ($< 10^{22}$) were found to be uniformly distributed over the Earth, figure 5. Their rate in the TUS FOV is estimated as 0.01 per minute. Flashes with larger photons numbers ($> 10^{22}$) are concentrated in the equatorial region (latitudes $\pm 30^\circ$) above the continents, figure 6. Their rate in the TUS FOV is estimated as 0.1 per minute.

Rather high intensity of the atmosphere glow and the rate of atmosphere flashes put a difficult problem for selection of EAS events and suppression of the "not useful" triggering. One should remember that EAS fluorescent photon number at $E = 100$ EeV is four order of magnitude less than photon number $\sim 10^{20}$–10^{22} in "small" flashes. At the early stage of a flash it may accidently give imitation of EAS event. For reliable distinction of flash events a pin-

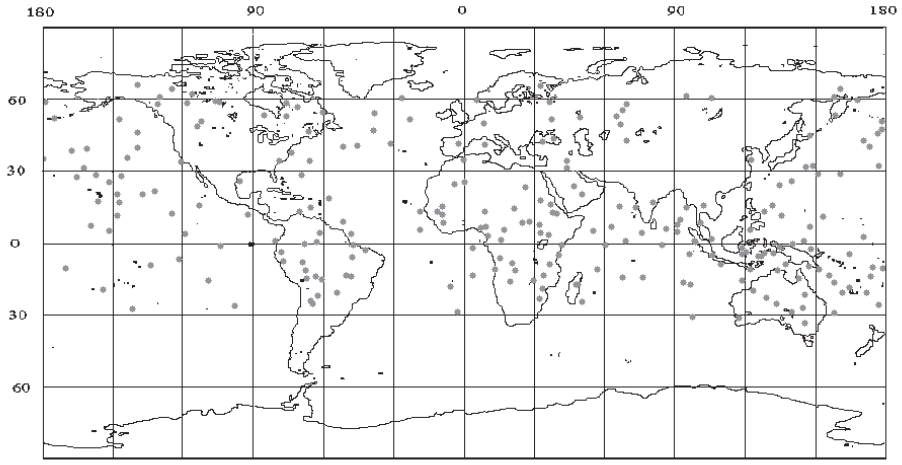


Figure 5: Global map of UV flashes with photon number less than 10^{22}.

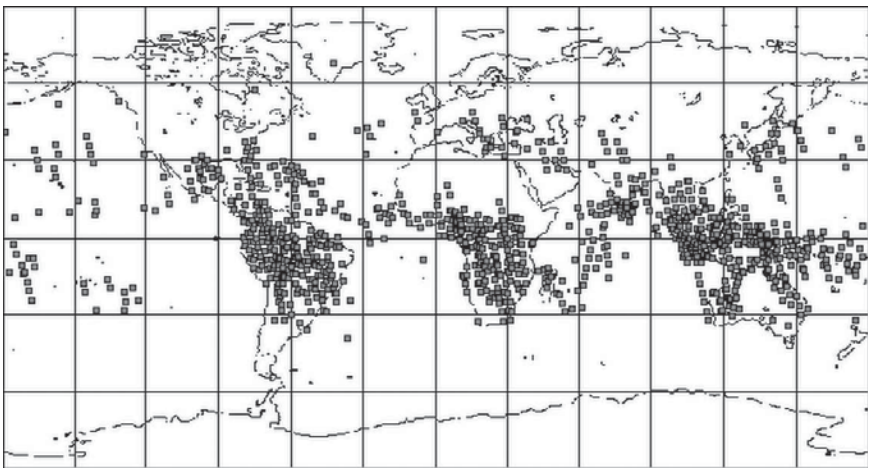


Figure 6: Global map of UV flashes with photon number larger than 10^{22}.

hole camera with aperture four order of magnitude less than aperture of TUS is installed in the TUS detector in cooperation with JEM-EUSO group (see figure 7). The many-anode PM tube, selected for the JEM-EUSO photo receiver will be used as the pinhole camera imaging detector and so tested in real space environment before use in large scale (thousands of tubes) in JEM-EUSO detector.

The pinhole camera will select and measure the atmospheric UV flashes in time scale of 1 msec started from photon number in the atmosphere of 10^{22}. The same events will be selected by the main TUS detector at much earlier stage – in time scale of about 0.1 msec. Comparison of the early flash rate and developed flash rate will give information on possible genetic connection between atmospheric flashes and EECR events.

3 Conclusions

- In near future (2011-2012) Space Observatory "Mikhail Lomonosov" will start to operate.
- Experience of the TUS detector operation will be important for final design of the next space detectors: JEM-EUSO and KLYPVE.

References

[1] Linsley J. and R. Benson. , Proc. ICRC 17-th, Paris, 1981, **8**: page 145

[2] Takahashi Y. et. al., New J. Phys., 2009, **11**: doi:10.10881/1367-2630/1116 06509

[3] Khrenov B.A , Panasyuk M.I., Garipov G.K. et. al., Proc. of Workshop on Observing of Extremely High Energy Cosmic Ray from Earth and Space, AIP Conf. Proc., Melville, N.Y., 2001, **566**: page 207

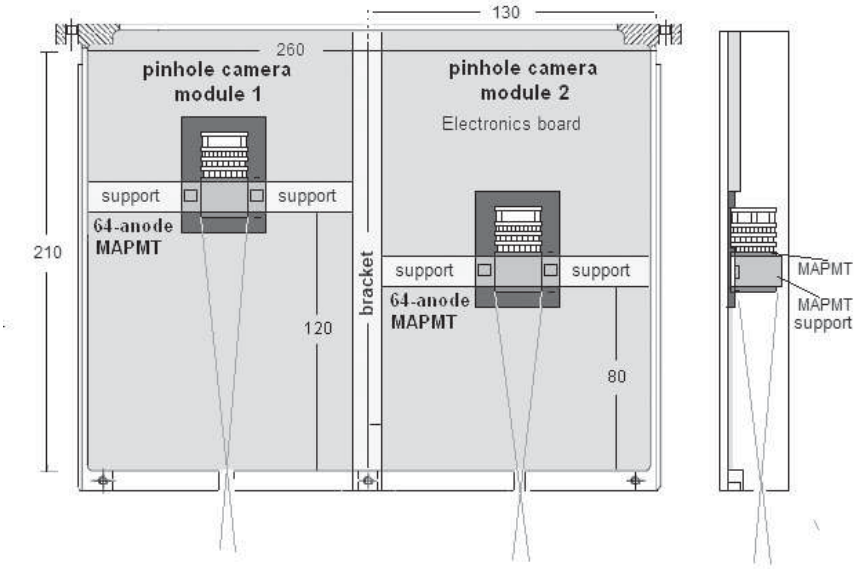


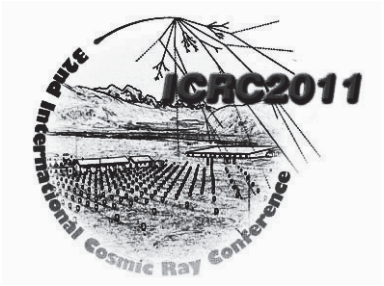
Figure 7: View of 2 pinhole cameras in a special section of the TUS photo receiver.

[4] Tkatchev L.G. et. al, The TUS Fresnel mirror production and optical parameter measurement. This conference, ID=0297

[5] Bird D. J. et. al., Detection of a cosmic ray with measured energy well beyond the expected spectral cutoff due to cosmic microwave radiation. Astrophysical Journal, 1995, **441**: page 144

[6] Sadovnichii V.A. et. al., Investigation of Space Environment aboard the "Universitetsky-Tatiana" and "Universitetsky-Tatiana-2" satellites. Solar System Research, 2011, **45**(issue 1): page 3-29

32ND INTERNATIONAL COSMIC RAY CONFERENCE, BEIJING 2011



Calibration of JEM-EUSO photodetectors

P. GORODETZKY[1], N. SAKAKI[2], M. CHRISTL[3] FOR THE JEM-EUSO COLLABORATION
[1]*Laboratoire AstroParticule et Cosmologie, APC, Paris, France*
[2]*Department of Physics and Mathematics, Aoyama Gakuin University, Sagamihara, Kanagawa 252-5258, Japan*
[3]*NASA Marshall Space Flight Center, Huntsville, Alabama 35812 USA*
Philippe.Gorodetzky@cern.ch

Abstract: The calibration of the JEM-EUSO focal surface (FS) about 5000 photomultipliers (PMTs) we will made in two steps: a) on earth, PMTs will be sorted out according to their gain and efficiency. Then identical PMTs will be used to make the Photo Detector Modules (PDM) consisting of 36 PMTs (2304 pixels). Immediately after the PDM assembly, the gain and absolute efficiency of each pixel will be measured with the PDMs own front end electronics working in single pho-electron mode. A X-Y-Z-θ-ϕ (PDM has a spherical shape) movement will support the illuminating device consisting of UV LEDs with wavelength of 330-430 nm inside an integrating sphere whose exit port will feed a collimator with 0.3 mm holes. The light will be monitored with a NIST photodiode mounted on a third port of the sphere. This set-up will be calibrated by replacing the PMT with another NIST. b) in space, during the day, when the JEM-EUSO lid is closed, the focal surface will be illuminated in a uniform way by a set of 1 inch spheres set on the periphery of the last lens (at one meter from the FS). The spheres will be equipped with LEDs and monitored by NIST photodiodes. Another set of identical spheres will be put at the FS periphery and will illuminate the lenses. The light will bounce back on the lid covered with diffusive reflector, to reach the FS which has been previously calibrated. Other means of in flight calibration will use ground sources (Xenon flashers) and finally the moon light reflected by earth albedo.

Keywords: Ultra high energy cosmic ray, International space station, JEM-EUSO, Calibration

1 Introduction

JEM-EUSO is a mission to observe ultra high energy cosmic rays (UHECRs) above 10^{20} eV[1, 2]. The JEM-EUSO telescope will be attached to the International Space Station (ISS) and will detect fluorescence photons from extensive air showers (EASs) induced by UHECRs. It is necessary to understand the instrument very well to discuss their origins. The JEM-EUSO instrument consists of Fresnel lens optics with a diffractive lens and the focal surface detector with photon counting capability[3, 4].

The number of observed photo-electrons (ΔS) from a luminous phenomena (with emitting number of photons of ΔQ) at distance r is expressed as:

$$\Delta S = \frac{\epsilon\kappa\eta T_l T_f T_e T_\alpha A}{4\pi r^2}\Delta Q, \qquad (1)$$

where,

- ϵ quantum efficiency of the detector
- η collection efficiency of the detector
- κ the probability to be contained in a pixel
- T_l throughput of the Fresnel lens system
- T_f transmission of the optical filter
- T_e trigger efficiency of the electronics
- T_α atmospheric transmission
- A aperture of the telescope.

The terms related to the instrument among above are $\epsilon, \eta, \kappa, T_f, T_e$ and T_l. Here, let's consider the calibration of the instrument with the following four cases.

- Pre-flight calibration
- On-board calibration
- In-flight Calibration with ground light sources
- Atmospheric monitor

For the atmospheric monitor, a dedicated subsystem is organized[5]. A ultra violet(UV) LASER and an infrared camera are under preparation to measure the cloud coverage in the field of view and the cloud heights. The other three calibrations are included in the "calibration system" and are being prepared by the collaboration of Japan, France, United States, Italy and Mexico.

The energy of 10^{20} eV has not been reached until now artificially, so that it is difficult to determine the absolute energy scale directly by any calibration. However, JEM-EUSO is expected to detect more than 1000 UHECRs in the mission period. If there are sources in our vicinity, the energy spectrum for each source will be obtained. Since ultra

high energy cosmic rays interact with cosmic microwave background photons and lose energy, the spectrum will be suppressed above $\sim 4 \times 10^{19}$ eV (GZK suppression). If the suppression threshold energy is obtained as a function of distance, the absolute scale might be determined.

2 Pre-flight calibration

2.1 Outline

The JEM-EUSO optics consists of two Fresnel lenses, a diffractive lens and a focal surface[3, 4, 6]. The focal surface is covered with about 5000 pieces of 1" multi-anode photomultiplier tubes (MAPMTs) developed for JEM-EUSO[7, 8]. The focal surface detectors are grouped, to make it easy for manufacturing and the data handling. A module of four PMTs is called "Elementary Cell" (EC) and a photo-detector module (PDM) consists of 9 ECs. Each PDM has a capability to detect EASs induced by cosmic rays by itself. The stand-alone performance and the functions of optics, electronics, etc. will be checked in each dedicated subsystem in principle. The calibration subsystem is in charge to measure the efficiency of the focal surface, especially efficiency of the MAPMTs.

2.2 Calibration of MAPMTs

The gain of a MAPMT will be measured at various voltage to determine an appropriate voltage for the input to the front-end electronics. As shown in Figure 1(a), LED light will be diffused with an integrating sphere to illuminate the photo-cathodes of 5-10 MAPMTs. Three kinds of wavelength will be used in the range of 330 nm and 430 nm. Pulse height distribution will be taken with photon-counting method with the electronics developed for night glow measurement by the EUSO Italy group. All the PMTs will be sorted out by their gain and efficiency, and every four PMTs with similar characteristics will be packed as an EC.

2.3 Calibration of PDMs

In order to measure the position and angular dependences of the photon detection efficiency of PDMs, an integrating sphere with UV LED at 375 nm and a monitor photo-diode is mounted on a XYZ$\theta\phi$ stage and the PDM surface will be scanned with 1 mm step with various incident angles (Figure 1(b)). The light is collimated to 1 mm in diameter. The photo-diode is calibrated precisely by the manufacturer. The efficiency of not only MAPMTs but the whole system (=quantum efficiency$\times$collection efficiency$\times$electronics efficiency) can be obtained. In this measurement, the variation of the intensity is monitored by a well-calibrated photo-diode, and that the attenuation of light to single photo-electron level is determined by the geometrical factor of the collimator. Therefore, the efficiency can be obtained better than a few percent.

Next, to check the trigger efficiency of PDM, fluorescence image from a cosmic ray air shower will be emulated with an array of UV LEDs. UV beam reflected by a rotating mirror is another candidate to emulate EAS image. The rotating speed will be adjusted to reproduce the light spot speed of EAS on the focal surface.

2.4 End-to-End calibration

The total performance of the instrument will be checked at this stage. One of the possible methods is that EAS image generated with a LED array for the PDM calibration is projected to the entrance pupil by a large parabolic mirror(Figure 1(c)). UV LASER light reflected by a rotating mirror is another candidate light source at this stage, too.

3 In-flight calibration

3.1 Outline

Absolute values of efficiency, gain, etc. will be measured on ground before launch, and only the relative changes will be monitored in flight in principle. Several light sources will be put in the JEM-EUSO instrument to monitor the efficiency and the detector gain. Ground light sources and the reflection of the moonlight by the Earth will also be utilized to make the calibration more reliable.

3.2 On-board calibration

The light source consists of a small integrating sphere equipped with UV LED in 330-430 nm and a NIST photo-diode to monitor the variation of the light intensity. Several identical light sources will be settled behind the rear lens and illuminate the whole focal surface (Figure 2 (a)). The intensity will be set at single photo-electron level and the photon detection efficiency of the system and the gain of MAPMT will be measured. If large change of gain is found, the threshold level for the counting will be adjusted.

Other several light sources will be set along the edge of the focal surface to illuminate the rear lens. The light passes through the lenses and is reflected back at the diffuse surface on the lid. A certain amount of the emitted light will be detected by the focal surface detector. The time variation of the efficiency of the optics and the detector will be obtained in this measurement. Therefore, after subtracting the degradation of the detector itself, the decrease in the optics throughput will be obtained.

3.3 From-ground calibration

3.3.1 Ground light source (Flasher)

There will be a dozen ground-based units deployed at host stations in different geographical locations to cover various atmospheric conditions, and one airborne unit. ISS will fly

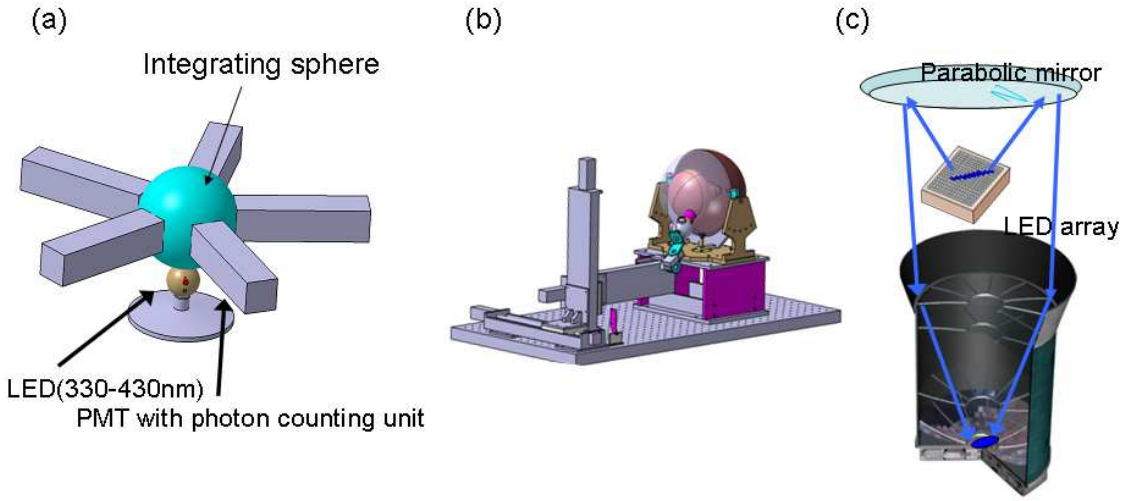


Figure 1: Apparatus for the pre-flight calibration. (a) Uniform light made with an integrating sphere illuminate ten MAPMTs. Single photo-electron spectrum will be taken with photon counting and MAPMTs will be sorted according to the gain and the efficiency. (b) A light source made of an integrating sphere is mounted on a stage to measure the PDM efficiency at various positions and with various incident angles. (c) An emulate air shower image with a LED array will be seen with the JEM-EUSO instrument to check total performance.

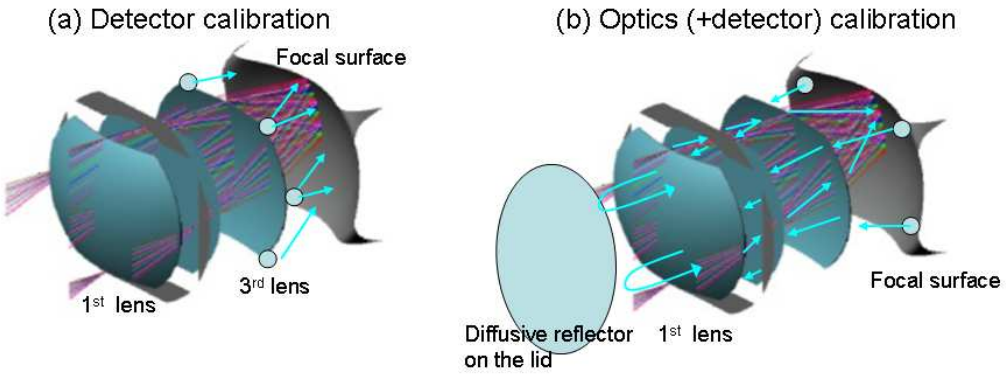


Figure 2: On-board calibration system. Diffused UV light sources made of integrating spheres will be set at the position shown in the panels (a) and (b), and the time variation of the efficiency of the optics and the detector will be monitored. (a) Several light sources will be set along the edge of the rear lens to illuminate the focal surface directly. The relative change of the detector efficiency will be taken. (b) The same light sources are placed along the edge of the focal surface to illuminate the rear lens. The light is reflected back at the diffuse surface on the lid and is detected by the focal surface detector. Here, convolution of the efficiency of the optics and that of the detector will be obtained.

over one flasher in average every night, the lamp will be lit by remote control for the cross-check of the JEM-EUSO photon detection efficiency, atmospheric transmittance, focusing quality of the JEM-EUSO optics. The airborne unit is to be installed on an upward directed portal of a P3B research aircraft stationed at NASA Wallops Flight Facility. It flies under the orbit of ISS at the altitude of 1-6 km above both land and sea every month during the JEM-EUSO mission. The Hamamatsu flash lamp L6404 has an light intensity of 2J per flash. The expected signal detected by JEM-EUSO is about 500 photo-electrons for clear nights. The maximum flash-to-flash variation for this lamp is 3% and the spatially non-uniformity is less than 5% over a 60° field of view. The duration of over-flights range from 5 to 70 seconds, so that typically 100 flashes per over-flight will be observed by JEM-EUSO. Atmospheric transmittance will be determined with a few percent accuracy by repeating measurements. Each ground flasher consists of four lamps with band pass filters at 337 nm, 357 nm and 391 nm, which corresponds to the wavelength of main N_2 fluorescence lines, and one broad band filter similar to that on JEM-EUSO. The intensity of the lamps is monitored by

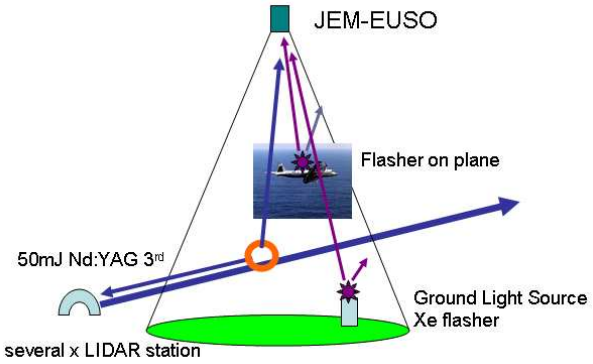


Figure 3: In-flight calibration with ground light sources. JEM-EUSO will fly over one of the 10-20 Xe flasher stations in average every night, and atmospheric transmittance and the JEM-EUSO efficiency will be checked. Artificial extensive air showers generated by LIDAR will be used to study the reconstruction accuracy experimentally.

a photo-diode precisely calibrated at NIST. These lamps will be controlled by way of the Internet and be flashed at $\sim$30 Hz when JEM-EUSO flies over the station. The image of a ground flasher moves at $\sim$0.03°/0.03 s. If a light source passes through at the center of the FoV, about 2000 flashes will be observed by JEM-EUSO.

3.3.2 Ground LIDAR

Since we can emulate EASs with the third harmonic of NdYAG Laser (355 nm), ground LIDARs may be an effective tool for calibration. In order to emulate the EAS of 3×10^{20}eV with an elevation angle of $\sim$20°, we need the output of 50 mJ at least. Once the power and the elevation angle of the Laser are fixed, we can determine the size of the receiver (1 m in diameter). The signals back-scattered at 30 km and 60 km are about 800 photo-electrons and 20 photo-electrons in GTU (2.5 μs). If we shoot 100 times, for example, more than 1000 photo-electrons will be observed and the atmospheric properties are determined well. We can measure the transparency with an accuracy of 5-10% after 100 shots. As a ground light source the shot in the elevation angle of 20-30° is optimum and probably the fixed directional Laser may be robust and minimize the maintenance of the mechanical parts of the system. The Laser can be tunable up to 10-30 Hz. In these horizontal shots, the Laser beam reaches the top of the atmosphere after traveling 30 km, where the Rayleigh scattering is dominant. The beam travels in pure molecular region for another 30 km and we can get the boundary condition for the LIDAR equation, because we can know the ratio of the back-scattered intensity to the beam intensity in the pure molecular region. Then we can solve the LIDAR equation to obtain the transmittance of the atmosphere as a function of height. The Laser beam with an elevation angle of 20° can be seen as a track of 30-50 km long from JEM-EUSO. If the scattering is dominated by the Rayleigh process, the number of photons at the entrance of JEM-EUSO can be calculated. The scattering angles of photons that JEM-EUSO will receive are always larger than 40°. In such large scattering angles, Rayleigh process usually dominates under good weather condition. We will use photons scattered above 3 km where the scattering is better described only by the Rayleigh process. Simultaneous operation of the on-board LIDAR system and the ground LIDAR system gives us more detailed information about the atmosphere and more redundant measurements. It will also reduce the systematic error in the measurement significantly. The systematic errors and the resolutions of arrival direction and energy determinations by JEM-EUSO can be evaluated experimentally by reconstructing LIDAR events.

4 Summary

Calibration of the instrument plays a key role to open a new era of "Particle Astronomy" by JEM-EUSO. In order to achieve better than a few % accuracy, several methods for pre-flight and in-flight calibrations are proposed and the preparation is in progress.

Acknowledgments

This project was partially supported by JSPS and CNRS under the Japan-France Research Cooperative Program.

References

[1] Y. Takahashi et al., New Journal of Physics, 11, 065009, 2009.
[2] T. Ebisuzaki et al. (JEM-EUSO collab.), This conference proceedings, 2011, (ID 1628).
[3] F. Kajino et al. (JEM-EUSO collab.), Nucl. Instr. Meth. A 623, 422-424, 2010.
[4] F. Kajino et al. (JEM-EUSO collab.), This conference proceedings, 2011 (ID 1216).
[5] A. Neronov et al., (JEM-EUSO collab.), This conference proceedings, 2011, (ID 0301).
[6] A. Zuccaro Marchi et al. (JEM-EUSO collab.), This conference proceedings, 2011, (ID 0852).
[7] Y. Kawasaki et al. (JEM-EUSO collab.), This conference proceedings, 2011, (ID 0472).
[8] M. Casolino et al., (JEM-EUSO collab.), This conference proceedings, 2011 (ID 1219).

The JEM-EUSO optics design

ALESSANDRO ZUCCARO MARCHI[1], YOSHIYUKI TAKIZAWA[2], YOSHIYUKI TAKAHASHI[3]
FOR THE JEM-EUSO COLLABORATION

[1]*CNR- INO (National Institute of Optics), largo E. Fermi 6, 50125 Firenze, Italy*
[2]*RIKEN, Hirosawa 2-1, Wako, Saitama, Japan*
[3]*The University of Alabama in Huntsville, 301 Sparkman dr., Huntsville 35899, AL, USA*
alessandro.zuccaro@ino.it

Abstract: The Extreme Universe Space Observatory onboard the Japanese Experiment Module is an international mission devoted to the detection of ultra high-energy cosmic particles with energies $E > 7x10^{19}$ eV. They are revealed through emission in the atmosphere of Cherenkov and fluorescence light in the near-UV region, by using an optical system with 60° field of view and a 2.3m entrance pupil. One of the challenges consists in developing an unusual combination of large and lightweight refractive optics: two double-sided curved Fresnel lenses and a central curved Fresnel + diffractive lens, whose maximum dimensions are 2.65m. This paper describes the development of such an optical system and its performances of the latest configurations.

Keywords: Refractive optics, Diffractive optics, Ultra high-energy cosmic rays, Extensive air shower.

1 INTRODUCTION

Accommodated on the Japanese Experiment Module (JEM) of the International Space Station (ISS), the Extreme Universe Space Observatory JEM-EUSO is the first planned space mission devoted to the exploration of the outermost bounds of the Universe through the detection of the Ultra High Energy ($E > 7x10^{19}$eV) Cosmic Rays (UHECRs), the most energetic particles coming from the Universe, by using the Earth atmosphere as a giant detector [1]. Looking downward the Earth, JEM-EUSO will detect such particles observing the fluorescence signal produced during their pass in the atmosphere. In particular, an UHECR collides with a nucleus in the Earth atmosphere, mainly Nitrogen, and produces an Extensive Air Shower (EAS made of electrons, positrons and photons. JEM-EUSO will capture the moving track of the fluorescent and Cherenkov ultraviolet (UV) photons, reproducing the calorimetric development of the EAS. At these energies the probability of detection is very low (~1 Km^{-2} $century^{-1}$). Since the volume of Earth atmosphere targeted from the ISS orbit is huge (~1 Teraton or more, observing on ground a circle of ~250 km radius or more), this observatory will increase the UHECR detection statistics with respect to the existing ground- based experiments, allowing to detect at least 500 UHECRs in three-year operation. Besides, its threshold energy is about 10^{19} eV, thus yielding cross calibration with the other experiments [2].

The instrument concept is a fast, high-pixelized, large-aperture and large Field-of-View (FoV) digital camera, working in the near-UV wavelength range with single photon counting capability. The telescope will record the track of an EAS with a time resolution of 2.5 μs and a spatial resolution of about 0.75 km (corresponding to ~0.1°), thus allowing the determination of energy and direction of the primary particles.

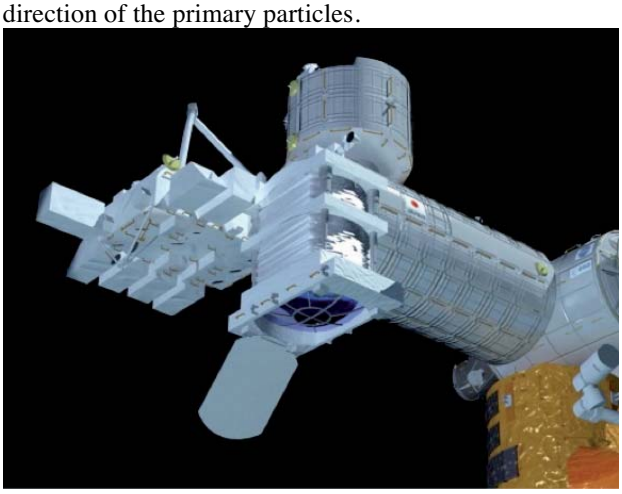


Figure 1. The telescope on the ISS.

Optics		Focal surface	
FOV	±30°	Focal surface area	~4.5 m^2 (curved)
Optical bandwidth	330 ÷ 400 nm	Number of pixels	~2.0×10^5
Entrance Pupil Diameter (EPD)	≥ 2.3 m	Pixel size	2.8 mm for "M64" MAPMT
F/number (F/#)	≤1		

Table 1. JEM-EUSO instrument parameters

2 THE JEM-EUSO TELESCOPE

In order to collect enough signals at the requested energies, the optical system must have a large aperture, wide FoV (Tab. 1). Besides, the system must be necessarily lightweight since the overall dimensions of the instrument, related to the maximum allowable stowing room on the launcher, let optical elements to be as big as 2.65m in diameter. Also for this reason reflective optics, in the form of a properly designed Schmidt camera, does not have yet a technological readiness, since the optical requirements would need a large, deployable, primary mirror, with some sort of active control on the shape [3], and with all the constraints of movable parts onboard the ISS. The main components of the telescope are: collecting optics, focal surface detector, electronics and structure (shown schematically in Fig. 2). The proposed optics system is essentially based on refractive elements: two Fresnel lenses and another one with a diffractive surface. The focal surface detector is covered by a grid of ~6000 multi-anode photomultipliers (MAPMTs), which convert the energy of the incoming photons into electric pulses with duration of 10 ns. The electronics counts-up the number of the electric pulses in time periods of 2.5 μs and records them to the memory; when a signal pattern coming from extreme energy particle events is found, the electronics issues a trigger signal and transmits all the useful data to the ground operation center, tracking back the image information stored in the memory.

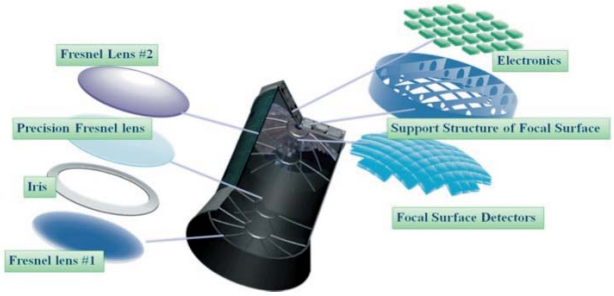


Figure 2. The main components of JEM-EUSO telescope concept.

3 THE OPTICS MODULE

The Optics Module (OM) is formed by two curved double-sided Fresnel lenses and a central lens with a Fresnel surface and a diffractive one for chromatic aberration reduction. Indeed, because of the scientific requirements, a large aperture, wide FoV system is needed. Besides, a small F/number condition helps controlling the focal surface dimensions. A Fresnel optical system is the challenging solution adopted for this mission: the Fresnel lens basically works as its prescription lens, with the advantage of being lighter and consequently less radiation absorbing, which is a critical feature especially in the UV. A lightweight design is really compulsory, since for the considered operative conditions a normal (i.e. prescription) lens system would be too expensive, not adequate and also difficult to carry into space. However, a combination of lenses cannot avoid the chromatic aberrations in the waveband of interest, for which the refractive index shows a steep behavior with respect to longer wavelengths; therefore a diffractive lens was added, with the purpose to reduce those aberrations. Being in the vicinity of the Aperture Stop, this optical element serves also as a sort of field lens, which helps gaining signal in particular on the wide fields.

3.1 Lens Materials

Two materials have been chosen to prove the feasibility of the optics: CYTOP and PMMA (000 grade). CYTOP is an amorphous, soluble perfluoro polymer (by Asahi Glass Co. LTD, Japan). It combines the excellent properties of highly fluorinated polymers with solubility in selected perfluorinated solvents to provide outstanding coatings for optical, electronic and other applications. CYTOP has a 95% transmittance between UV and near-IR. PMMA-000 is a special Grade UV-transmitting polymetyl methacrylate (by Mitsubishi Rayon Co. LTD, Japan). Fig. 3 shows the refractive index and transmittance (for a 15-mm sample measured by RIKEN) of CYTOP and of PMMA-000. CYTOP provides less dispersion and more transmittance, and its refractive index is generally lower than PMMA-000.

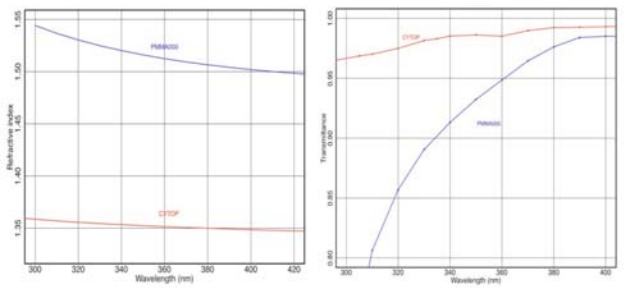


Figure 3. Left: refractive index for CYTOP and PMMA-000. Right: transmittance for CYTOP and PMMA-000 for 15-mm thickness.

3.2 Optics design

After many efforts both in optimization and in searching for optimal materials, only in the last few years the option on CYTOP and PMMA UV grade has been decided. Recently, only two designs have been adopted and analyzed: the so-called "Baseline" optics and the "Advanced" optics (see their cross sections in Fig. 4). Both are F/1 on-axis, with 2.3 m EPD and 60° overall FoV. Both use two curved double-sided and rotationally symmetric Fresnel lenses and one curved diffractive + Fresnel lens, the former design being all in PMMA-000, the latter having the front lens in CYTOP and the two others in PMMA-000. As previously stated, the optical advantages of CYTOP are evident; however, it is heavier and more expensive, therefore a system all made in CYTOP has not been considered as a valuable option. In both designs an intermediate lens is positioned, with a rotationally symmetric diffractive surface from one side and Fresnel one on the other side. Since a diffractive surface introduces dispersion with opposite sign with respect to a refractive one, this element helps taming the chromatic aberration. This lens acts also as a field lens, which assures the minimum possible loss due to vignetting. Indeed, the available room on the HTV transfer vehicle stowing area necessarily limits the lenses' diameter dimensions, while the wide-angle and large EPD conditions would require even bigger diameters to avoid vignetting (Fig. 4). In both designs, all the three lenses are 10-mm thick, with 2.65 m maximum diameter. As for all the parameters, also the base curvature is a result of the optimization, which is also related on the considered material. The corresponding prescription lenses are all convex- concave positives, therefore for each curved Fresnel lens there is one prescription surface curvature that does not follow the bending direction of the Fresnel, thus resulting in an increased number of back-cuts, typical of Fresnel designs. At this stage, base curvature is spherical, while all the surface curvatures are slightly aspheric.

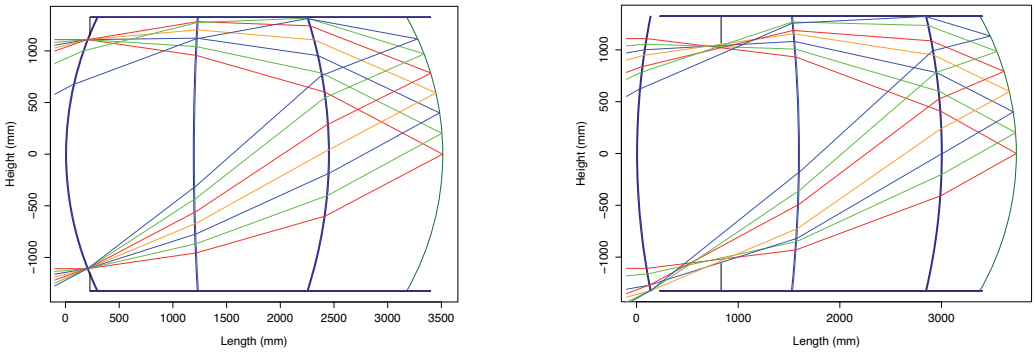


Figure 4. Baseline (left) and Advanced (right) designs.

3.3 Optics performance

The scientific goals do not need diffraction-limited conditions for the optics: with the described requirements, geometrical aberrations and back-cuts losses and scatterings are the main drivers. The performance of the optics designs is given in terms of geometrical Encircled Energy (EE) and Throughput (Fig. 5). The EE is defined as the ratio between the number of photons in the spot area and the those reaching the whole focal surface for a given field, while the Throughput is the ratio between the number of photons in the spot area and those passing through the Aperture Stop (i.e. the iris of Fig. 2). EE and Throughput are estimated using a ray-tracing code that takes into account the different material absorptions, Fresnel structures and surface reflections. Besides, the considered losses due to the surface roughness and the depth error of the diffractive + Fresnel structure were previously estimated by formulas and then verified via simulations. Manufacturing trials on plastic samples have also helped defining some of these maximum tolerable conditions. Fig. 5 shows how better the Advanced design performs with respect to the Baseline. This behavior depends on several issues, as well as on the fact that the advanced optics average RMS spot size is smaller than the one of Baseline optics, since CYTOP presents smaller refractive index dispersion than PMMA-000. Throughput necessarily drops with bigger angles, since the back-cuts' geometrical obscuration tends to increase, as well as scattering losses.

3.4 Performance of the HTV stowing type

So far, two designs with 2.65 m diameter have been presented. However, more realistic considerations on the true available volume lead to edit both the designs and the corresponding performance. Indeed, the HTV unpressurised stowage area constrains the layouts to a maximum 2.65 x 1.9 m^2 (Fig. 1). After a re-optimization, the so-called "side- cut" optics has ~82% aperture of the original 2.65 m design. It keeps the performance up to 15°, while the FoV on the side-cut direction is limited to ~24°, since beyond that angle there is no more focal surface.

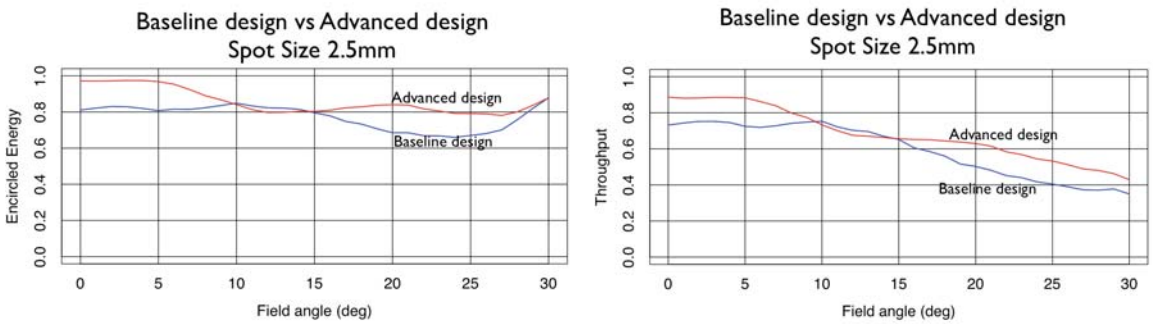


Figure 5. Performance of Baseline and Advanced optics designs. Left: EE, right: Throughput.

3.5 Tolerance analysis

The angular resolution tolerance can be roughly 300 thousand times larger than the diffraction limit. Consequently, tolerance of the optics is much lower than for astronomical telescopes. Preliminary tolerances with 2.5-mm spot sizes have been verified via ray- tracing code. For each lens and for the focal surface the axial displacement, the lateral displacement and the tilt have been considered. Another source of error comes from thermal issues. Since JEM-EUSO orbits around the Earth in ~90 minutes, each lens has a thermal cycle synchronized with the orbit. Refractive index is shifted by temperature changes, causing de- focusing effect. Thermal analyses predict that the front lens shifts ±2°C from the equilibrium temperature, vs. a requirement of max ±10°C. On the other hand, tolerance analysis (with numerical ray-tracing method) allows the refractive index to vary no more than 0.0013/10°C. The measurement results of temperature dependence of refractive index state that the temperature shift amount is 0.0007/10°C (CYTOP) and 0.0009/10°C (PMMA-000), which are below the requirement. A further study on simulations regarding the temperature difference between lenses, due to the environment, is under way.

3.6 Manufacturing

Manufacturing procedures give a feedback on the design and tolerances of the Fresnel lenses. Since June 2008, a large diamond turning machine is being used in Japan to manufacture lenses up to 3.4 m in diameter. This machine has already successfully cut three 1.5-m diameter PMMA-000 Fresnel lenses, being the central portion of a 1:1 scale JEM-EUSO prototype [4]. These lenses will be shipped to NASA - MSFC to undergo complete optical tests. These tests will be used as a feedback for detailing the optical design as well as for improving manufacturing of future lenses.

4 CONCLUSIONS

The construction of an all-refractive space-based telescope for detection of Ultra High Energy Cosmic Rays is on its way. Intensive simulations of the optics are being conducted for the last years, in connection with the development of the other subsystems, and two possible designs are presented: a Baseline (with all PMMA-000 lenses), and an Advanced one (with two PMMA-000 and one CYTOP lens). Their performances show that Science with such a challenging optical system is not only possible but almost a reality. Once the prototype will be tested, more information and a stronger feedback for simulations and opto-mechanical issues will be provided, thus reinforcing the reliability of the ray- trace and stray light simulations in view of building the final telescope.

[1] Y. Takahashi et al. “The JEM-EUSO mission”, New Journal of Physics 11 (2009) 065009.
[2] http://www.auger.org/index.html.
[3] A. Zuccaro Marchi et al. “A Technology demonstrator for development of ultra-lightweight, large aperture, deployable telescope for space applications”, Proceedings of the 7th International Conference on Space Optics, Toulouse, France, 14-17 October 2008.
[4] Y. Hachisu et al., “JEM-EUSO lens manufacturing”, 32nd ICRC conference, Beijing, China, 2011

JEM-EUSO lens manufacturing

Yosuke Hachisu [1], Naoki Tone [1], Yoshihiro Uehara [1], Hitoshi Ohmori [1], Kazutoshi Katahira [1], Yoshiyuki Takizawa [1], Zuccaro Marchi Alessandro [2], for the JEM-EUSO collaboration
[1] *RIKEN, Japan*
[2] *CNR-INOA Firenze, Italy*

Abstract: We are manufacturing full-scale JEM-EUSO lenses by using a large ultra precision diamond turning machine. This machine is able to manufacture up to the lens diameter of 3.4 m and control the vertical and horizontal position of tool bit with a resolution of 10 nm. JEM-EUSO optics has two curved-doublet-Fresnel lenses and a precision Fresnel lens for chromatic aberration correction. The size of each lens is 2.65 m in diameter. Each lens consists of a center part and an annular part. We have manufactured the center 1.5 m of all three lenses that will act as the Bread Board Model optics. The material of these lenses is UV-grade PMMA. Another candidate lens material is CYTOP. We manufactured a 1m CYTOP lens. In this paper, we report the details of manufacturing the 1.5 m PMMA lenses and 1m CYTOP lens.

Keywords: Fresnel lens optics, International space station, PMMA, CYTOP, Cutting

1 Introduction

The Extreme Universe Space Observatory on the Japanese Experiment Module (JEM-EUSO) will be transported on the JAXA HTV and attached to the Exposure Facility on the JEM located on the International Space Station (ISS), and observe the earth's atmosphere with a field of view approximately 250 km radius. The ISS orbit period is approximately 90 minutes at an altitude of ~400 km. From this platform, JEM-EUSO can observe the extensive air shower (EAS) created by cosmic ray with the highest energy. Figure 1 shows the observation method. Cosmic rays with extreme energy that collide with nuclei in earth's atmosphere produce an EAS that mainly consists of electrons and positrons and lasts for several microseconds. JEM-EUSO acquires images of these UV emissions, from the excited nitrogen atoms in the atmosphere, as a function of time to produce 3D images of the air shower development. This data allows determining its energy and trajectory. This mission will help discover the origin and acceleration processes responsible for producing this natural phenomena and potentially open a door to new physics studies(1).

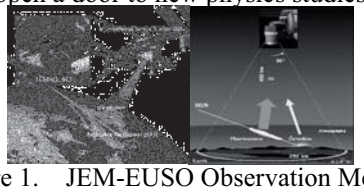


Figure 1. JEM-EUSO Observation Method

2 Optical System of JEM-EUSO Telescope

The JEM-EUSO telescope is composed of two double-sided curved Fresnel lenses, a precision Fresnel lens (diffraction lens), and focal surface detectors as shown in Figure 2. Table 1 shows the specification of the telescope. The diameter of the lens is 2.65 m and the operational bandwidth is in the UV-A (λ=330 to 400 nm). EAS within ±30° of the optical axis are concentrated on to the focal plane. The front and rear lenses are meniscus shaped curves, with a large number of Fresnel facets on both sides on the lens surfaces. This unique design helps to achieve wide angle, lightweight optics. Although the middle lens is flat, it has 700 nm deep diffraction patterns that cover the entire surface. The manufacturing of this surface is requires a high degree of precision machining. The base material for the lens must be low density due to the weight restrictions and vibration resistance. The materials considered are 1) acryl PMMA (Mitsubishi Rayon) of the UV transmittance grade that allows high transmittance in the targeted observation wavelength range, and 2) amorphous fluorocarbon polymers CYTOP (Asahi Glass)(2). The large Fresnel lenses are a critical element of the JEM-EUSO instrument. For this reason, we started our research and development of the machining process for large Fresnel lens shaping at an early stage. For development of this large size Fresnel lens, we applied the direct cutting method using an ultra-precision cutting machine. We machined a 1.5 m

diameter Bread-board model (BBM) lens as the first step of the process development.

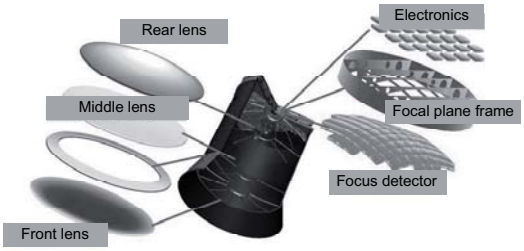


Figure 2. JEM-EUSO Telescope Abstract

Table 1. JEM-EUSO Telescope Specification

	Front lens Curved doublet fresnel		Middle lens Flat fresnel(Precision lens)		Rear lens Curved doublet fresnel	
	S1 (Convex)	S2 (Concave)	S4 (Concave)	S5 (Convex)	S6 (Concave)	S7 (Convex)
Lens material	CYTOP or PMMA		PMMA		PMMA	
Substrate profile	Spherical surface (R=2278mm)		Flat plane		Spherical surface (R=4052mm)	
Lens diameter	2650mm		2200mm		2650mm	
Groove Height	1.0mm		1.0mm	700nm	1.0mm	
Groove Width	296～5mm	80～1mm	119～3mm	0.5～0.01mm	56～1mm	260～3mm

Required Machining Accuracy
○Front lens and Rear lens
Surface roughness ＜20nm(RMS)
Profile accuracy ±0.1mm
○Middle lens
Surface roughness ＜20nm(RMS)
Groove Depth accuracy ±70nm(10% of groove depth)

3 Large Lens Machining Experiment

3.1 Front and Rear Lens Creation

A large size Fresnel lens with diameter 2.65 m can be produced in two separate parts – a center area in diameter 1.5 m and an outer ring lens in diameter 1.5 m – 2.65 m. Since it is a BBM lens, we machined the both-side spherical Fresnel lens in diameter 1.5m, which serves as each central area.

Table 2 shows the specification of this Fresnel lens shape, and Table 3 shows the machining parameters. PMMA material was used for the lens. The required machining accuracy for the Fresnel lens is 1) lens surface roughness <20 nm RMS, and 2) profile accuracy <0.1 mm. The lens blank curvature was formed using a heat press method. For this process, convex and concave wooden molds shaped to the approximate radius of curvature of the Fresnel lens were installed in a press-forming machine. The flat PMMA blank was formed by placing it on the wooden mold and in a heating chamber. It was then pressed and allowed to cool. This process allowed reducing the amount of material that had to be trimmed in the machining process as well as the time required for this process[3]. Figure 3 shows the Fresnel lens machining process. As a single crystallized diamond tool bit was used for machining, an extended life diamond was built with consideration to the crystal orientation. By using this specially built tool, although this large-size machining takes considerable time, we managed to achieve a surface roughness less than 20nm on the machined area. Figure 4 shows the measurement result obtained by AFM. Due to the size of the lens, the measurement values could only be obtained in a few locations. In the past, we used optical interferometer measurements as the evaluation criteria[4]. However, a recent study established a correlation with the AFM measurement result, we concluded that we achieved our optical measurement target, 20 nm RMS based on the AFM measurement result. In addition to the measurement result, Figure 5 and Figure 6 show the high clarity of the lens even when it is on the cutting machine. The optical performances of these lenses are also demonstrated by the image of each person standing behind the lens.

Table 2. Fresnel Lens Profile Specification

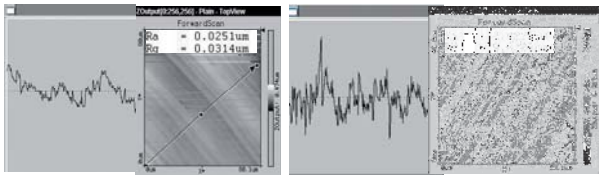
	Front lens (Curved doublet fresnel)		Rear lens (Curved doublet fresnel)	
	S1 (Convex)	S2 (Concave)	S6 (Concave)	S7 (Convex)
Lens material	PMMA		PMMA	
Effective lens dia	1500mm		1500mm	
Substrate profile	Spherical surface (R=2278mm)		Spherical surface (R=4052mm)	
Center sag	60.9mm		60.9mm	
Center thickness	15mm		15mm	
Groove depth	1.0mm		1.0mm	
Groove Width	296mm~5mm	80mm~1mm	53mm~2mm	179mm~23mm

Table 3. Fresnel Lens Machining Specification

Bit profile	R0.05mm
Machining feed rate	0.2 – 10 mm/min
Cutting depth	0.010 – 0.050 mm/pass
Work piece material	PMMA



Figure 3. Fresnel Lens Machining



（Front lens） （Rear lens）

Figure 4. AFM Measurement Result on Machined Area of Fresnel lens

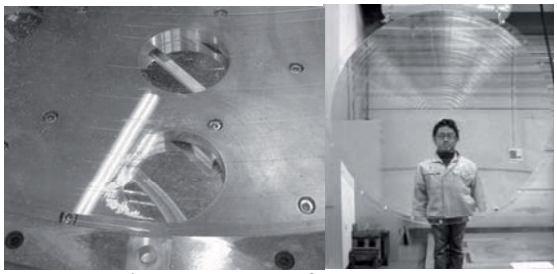


Figure 5. Image of Front Lens

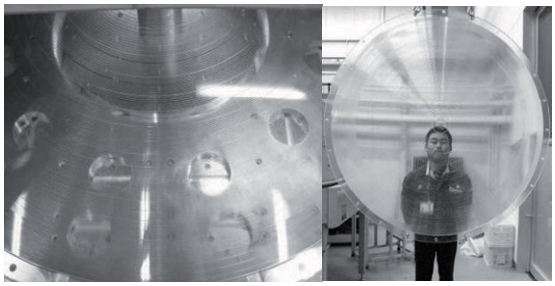


Figure 6. Image of Rear Lens

3.2 Middle Lens Production

After the front and rear lenses were created, we fabricated a middle lens with 1.5m diameter. A large flat Fresnel lens serves as the middle lens in accordance with the lens specification. The middle lens has Fresnel facets on one side and a diffraction grating on the other. The lens design is shown in Table 4. First, the Fresnel lens surface with a facet depth of 1 mm was machined. Then, the diffraction lens surface with a groove depth of 700 nm was machined. The machining parameter used for the Fresnel surface is same as the one shown in 3.1. Figure 7 shows the outcome of this machining process. The surface roughness was also measured in the same way as described in 3.1, and it was confirmed that the target had been achieved (Figure 8).

This lens was created with a diffraction pattern with grooves 700 nm deep on the entire 1.5m surface, requiring high precision machining. Therefore, the machining parameter was determined (See Table 5) based on the machining stability. For the diffraction lens machining, the groove depth was designed as 700 nm with a tolerance <70 nm. The lens was machined in several sessions and the machining performance was measured and evaluated each time. In order to minimize the impact of vibration and temperature change that may happen during the day, the machining was done at night. Figure 9 shows a microscopic view of the diffraction lens surface after machining. Based on this image, the proper diffraction pattern was confirmed. Also, the profile measurement result of the diffraction surface (Figure 10) showed that the groove depth deviation is within 70 nm, and therefore satisfy the requirement.

Table 4. Fresnel and Diffraction Groove Lens Profile Specification

	Middle lens Flat fresnel(Precision lens)	
	S4 (Fresnel)	S5 (Diffraction)
Lens material	PMMA	
Effective lens dia	Flat plane	
Substrate profile	Flat plane)	
Center sag	60.9mm	
Center thickness	15mm	
Groove depth	1.0mm	0.0007mm
Groove Width	119mm~3mm	0.5mm~0.01mm

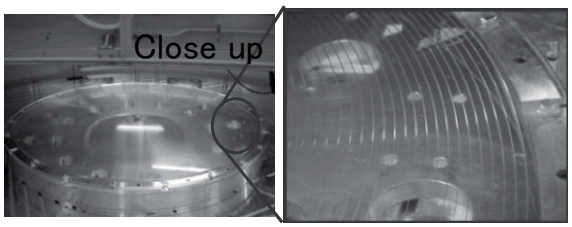


Figure 7. Middle Lens – After Fresnel Machining

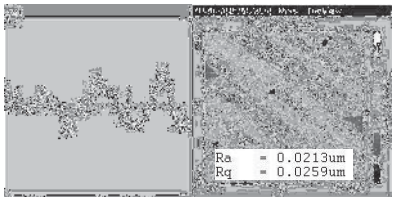


Figure 8. AFM Measurement Result of the Machined Surface of Fresnel Lens

Table 5. Diffraction Lens Surface Machining Parameter

Bit profile	Tip R0.0005mm
Machining feed rate	0.2 – 10 mm/min
Cutting depth	0.005 – 0.010 mm/pass



Figure 9. Microscopic Image of Diffraction Machined Surface

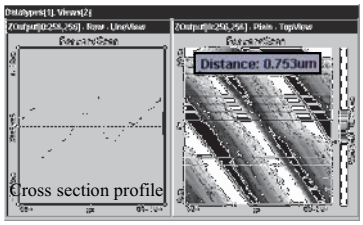


Figure 10. Diffraction Lens Machining Result

3.3 CYTOP 1m Lens Production

First, as a part of the basic experiment, we studied the feasibility of using the direct cutting method using an ultra-precision machine on approximately 100 mm diameter CYTOP material blank for Fresnel and diffraction patterns. As there are almost no case studies on CYTOP direct machining done in the past, we needed to verify the cutting ability and surface roughness of the Fresnel grooves for the front and rear lens design. The machine uses a slide plane for hydraulic static pressure and bolt nut for the linear axes. This is an ultra-precision cutting machine with a complete no-contact drive, which realized the locating resolution of 1.4 nm. We machined a flat surface on the 100 mm diameter CYTOP substrate. In order to measure the surface roughness, White Light

Interferometer, "New View (Zygo Corp.)" was used. Table 6 shows the machining parameters and Figure 11 shows the machining process and a sample after machining. The sample surface after machining had good clarity, and the surface roughness was 10 nm RMS as shown in Figure 12, and satisfied the target <20 nm RMS. After this stage, Fresnel patterns were machined on the surface of CYTOP substrate. The depth of the Fresnel pattern was set to 1 mm, and the groove width ranged from 1to 10 mm, as this width frequently appears on the full size 2.65m Fresnel lens design. Table 7 shows the machining parameters and Figure 13 shows the profile and image of the machined material. This photo shows a good outcome of the machining. Based on this result, we concluded that the CYTOP machining is feasible and that it can satisfy the required precision.

In the next step, we performed a basic experiment using a large-size precision cutting machine that is used for large size lens. Table 8 shows the machining parameters and Figure 14 shows the machining process and a sample after machining. The sample's surface after machining had good clarity. Figure 15 shows the measurement result obtained by AFM.

Table 6. Surface Cutting Parameter

Work piece material	CYTOP (dia.100mm)
Bit profile	R0.5mm
Work piece RPM	600 rpm
Machining feed rate	1mm/min
Cutting depth	0.001mm/pass

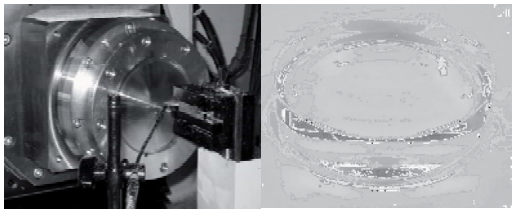


Figure 11. Machining Process and CYTOP Substrate after Machinin

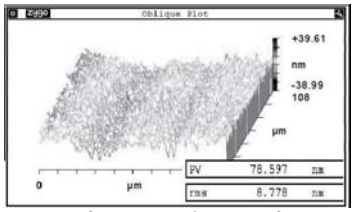


Figure 12. Surface Roughness of CYTOP after Flat Plane Machining

Table 7. Fresnel Profile Machining Parameter

Work piece material	CYTOP (dia.100mm)
Bit profile	R0.05mm
Work piece RPM	600 rpm
Machining feed rate	0.5mm/min
Cutting depth	2.0 μm/pass

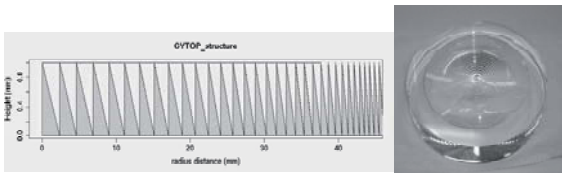


Figure 13. Fresnel Profile Chart after machining a work piece after machining

Table 8. Surface Cutting Parameter

Bit profile	Tip R0.05mm
Work piece RPM	40 −70rpm
Cutting depth	0.005 − 0.020mm/pass

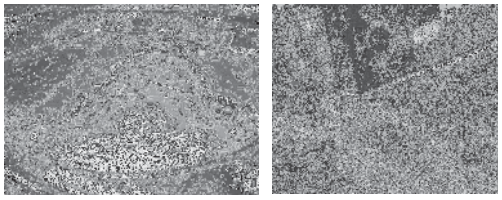


Figure 14. Ultra-precision machining (Lathing)

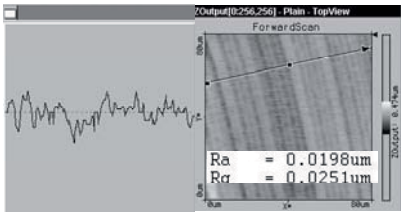


Figure 15. AFM Measurement Result of the Machined Surface of Fresnel Lens

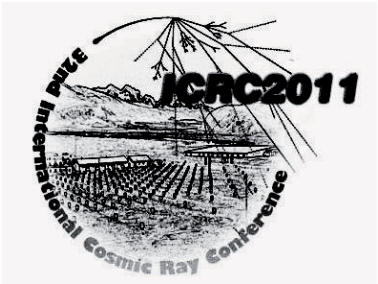
4 Performance Test

Currently large size BBM lenses made from PMMA, which consist of the central part of the JEM-EUSO optical module, have been completed, and they are undergoing performance testing in the laboratory environment and will eventually be tested in a simulated space environment using a large thermal vacuum chamber.

5 Conclusion

This study shows that it is possible to produce large CYTOP lenses with 1.0 m diameter and 3 large PMMA lenses with 1.5 m diameter 1 for the JEM-EUSO telescope. In the future, we would like to verify machining parameters and environment for larger lenses and continue our experimental machining study.

[1] Y. Takahashi et al. "The JEM-EUSO mission", New Journal of Physics 11 (2009) 065009.
[2] Y.Takizawa et al. 31th ICRC,Lodz,Poland.2009
[3] Y. Hachisu, K. Maekawa, et al. Large size both-side spherical type Fresnel lens creation, Abrasive Technology Conference (ABTEC). 2009
[4] Y. Hachisu, K. Maekawa, et al. Large size both-side spherical type Fresnel lens creation, The Physical Society of Japan. 2009



Testing of Large Diameter Fresnel Optics for Space Based Observations of Extensive Air Showers

JAMES H. ADAMS, JR.[1], FOR THE JEM-EUSO COLLABORATION
[1]*NASA Mashall Space Flight Center*
James.h.adams@nasa.gov

Abstract: The Extreme Universe Space Observatory on the Japanese Experiment Module (JEM-EUSO) mission will detect extensive air showers (EAS) produced by extreme energy cosmic rays. It operates from the ISS looking down on Earth's night time atmosphere to detect the nitrogen fluorescence and Cherenkov light produced by the charged particles in the extensive air showers. JEM-EUSO's science objectives require a large field of view and sensitivity below 50 EeV and must fit within available ISS resources. To accomplish this, JEM-EUSO uses refractive optics consisting of three large lenses with Fresnel surfaces. A bread-board model (BBM) of the optic has been manufactured and has undergone preliminary tests. We report the results of these tests and evaluate the present capability to manufacture these optical elements.

Keywords: JEM-EUSO, EAS, Fresnel, ISS.

1 Introduction

The JEM-EUSO mission uses a large telescope on the ISS to observe Extensive Air Showers (EAS) produced by Extreme-Energy Cosmic Rays (EECR) incident on Earth's nighttime atmosphere [1,2]. The Optic Module (OM) for JEM-EUSO consists of 3 2.5 m diameter Fresnel lenses made from polymethylmethacrylate (PMMA). This unique OM design provides a large field of view (±30°) and sensitivity to low photon fluxes in the near UV (330 to 400 nm) to measure key properties of the EAS [3].

The present level of maturity of the OM has been achieved by designing and manufacturing test articles for the OM, including lenses of 10 cm, 20 cm, 40 cm and 1 m diameter. Recently, a bread-board model (BBM) of the central 1.5 meters of the OM, with a flight-like design, has been completed [4]. The BBM includes two double-sided curved Fresnel lenses (front and rear) and a single flat lens (middle) with one Fresnel and one diffractive surface. The front lens is shown in Figure 1. Each lens was mounted in a frame and installed in a metering structure that provides proper spacing and alignment of the lenses, aperture stop and detector (Figure 2). The testing completed thus far includes evaluation of the current manufacturing parameters and processes used during the BBM fabrication, transmission and focusing. These key performance factors also have been simulated using commercial optical design software and custom routines developed for the JEM-EUSO OM.


Figure 1. Picture of one BBM lens after manufacturing.

2 Testing

2.1 Surface Roughness

A key performance parameter in the manufacturing of these plastic lenses is the resulting surface roughness. The roughness of the finished surface was sampled using a replication process. Commercial replication clay, Reprocil, was applied at several locations on the surface of the front lens. After drying the molds were lifted off of the lens surface and measured with a Wyko profilometer. Three parallel traces measured from one of these surface impressions are shown in Figure 3. The surface rough-

ness was measured at several locations and found to be ~40 nm RMS. The front lens was the last lens fabricated and included some improvements to the manufacturing process identified during the fabrication of the other two lenses.



Figure 2. Picture showing the assembled BBM.

2.2 Transmission measurements

The transmission of the front lens was measured using a parallel beam produced by a parabolic mirror with a focal length of 183 cm and diameter of 60 cm. A source pallet was assembled for transmission measurements using a laser diode (LD) with a wavelength of 405 nm, focusing optics, a single mode optical fiber (<100 microns diameter) and an attenuation filter. The LD output was focused on one end of the fiber optic and the other end was positioned at the mirror's focal point. A neutral density filter with an optical density of 3.0 was used to reduce the intensity of the beam. The resulting collimated beam was circular with an azimuthally symmetric Gaussian-shaped intensity profile and a half intensity width of 12.3 cm. The intensity of the collimated beam was measured using a power meter (Newport model 918D-UV-OD3). The transmission of the front lens was measured at normal incidence in 5 positions along a radius and offset from the optical axis: offset = 0 (optical axis), 10, 20, 30, 40 and 50 cm. These measurements included losses from surface reflection, absorption within the lens material (nominal thickness of 1.5 cm), scattering from the Fresnel backcuts and losses due to the residual surface roughness resulting from the manufacturing of the lenses.

The front lens performance was simulated to determine the best focal position to measure the transmitted power. Simulations show the focal length of just the front lens is 575 cm. The image formed at this position is not a sharp point but is diffuse with the majority of light falling within a spot 1 cm^2. The transmitted power was measured at several different depths to find the best focus. The transmitted power was found to be only weakly dependent on the depth of the measurement within a few centimeters about the predicted focal depth (Figure 4). The results of the measured transmission are given in Table 1.The measured transmission value of 69% at 30 cm offset should be compared with 72% that was predicted by simulations based on the detailed characterization of the BBM lens and surface roughness.

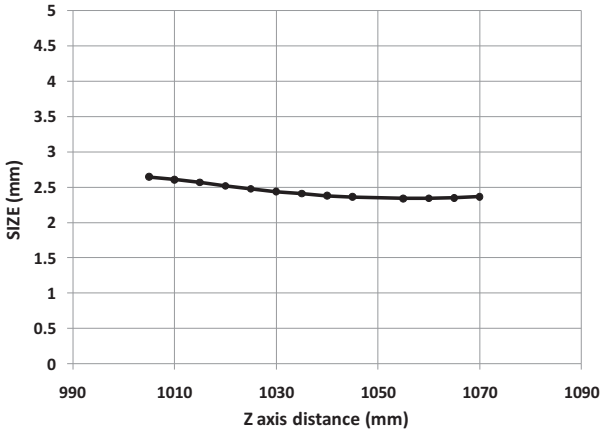


Figure 4. Image size as a function of detector depth. The image formed is weakly dependent on the precise position of the detector along the optical axis.

2.3 Imaging performance

The focusing power of the BBM (all three lenses) was studied with sub-aperture exposures using a collimated beam produced by a parabolic mirror as well as full aperture exposures using an extended source. The sources used in this testing included the LD at 405 nm and a broadband xenon lamp together with narrowband filters. The strongest emission lines from atmospheric fluorescence produced by the EAS are at 337, 357 and 391 nm. The filters used to evaluate the imaging performance had pass bands at 340±5 nm, 360±5 nm, and 390±5 nm. A single bandpass filter between 300-400 nm (Schott UG1) was also used to determine the performance of the BBM over the full bandwidth. A digital camera produced by Photometrics SensSys was used to record the images produced by the BBM at the predicted focal distance. Optimization of the JEM-EUSO instrument has lead to a curved focal surface design. The camera's Charge-Coupled Device (CCD) was mounted on a 2 dimensional stage with 5 cm of travel parallel and perpendicular to the optical axis. This stage is then mounted to a 258.9 cm swing arm that matches the predicted radius of curvature of the focal surface (Figure 2). The central element of the CCD is a Kodak 1401e chip with 6.8 μm square pixels. The CCD has 1317x1035 pixels, covering an area 9x7 mm^2. The integration time for each exposure is computer-controlled and adjustable from 25 milliseconds to several minutes.

The JEM-EUSO science objectives require a focal spot of less than 5 mm diameter with a design goal of <3 mm. Simulations predicting the imaging performance of the BBM design are shown in Figure 5. CCD images of the focused images recorded during various testing of the BBM are shown in figures 6, 7 & 8. A composite image representing the principal atmospheric fluorescence lines was formed by adding separate images produced using spike filters at 340, 360 and 390 nm and the collimated xenon source. The intensity for each image was normalized to 1.0 before adding the images. The resulting RMS

width of the composite image was 2.4 mm (Figure 6). The width of the image formed with just the 360 nm filter was 2.3 mm. This test result demonstrates that the peaks from each band line up well in this sub-aperture test.

Full aperture testing of the BBM used the same sources but without the 60 cm collimator. For these tests the source was located at a distance of 40 m from the BBM. This setup provided a full exposure of the 1.5 m diameter lenses and produced an approximate parallel beam of light. Images were recorded on–axis (Figure 7) and tilted at 10° with respect to the optical axis (Figure 8). The resulting image size was 2.5 mm RMS for the on-axis image and 2.7 mm RMS at 10°.

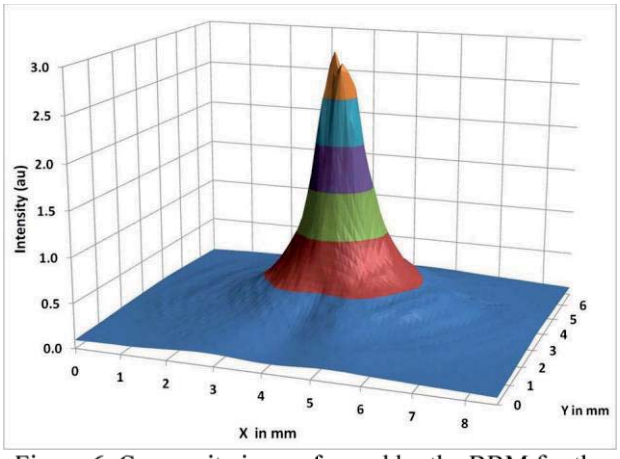


Figure 6. Composite image formed by the BBM for the principal nitrogen fluorescence wavelengths.

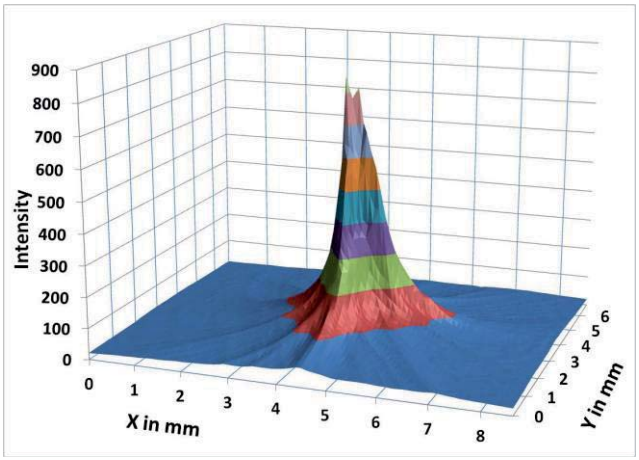


Figure 7. Full aperture image for bandpass 300-400nm.

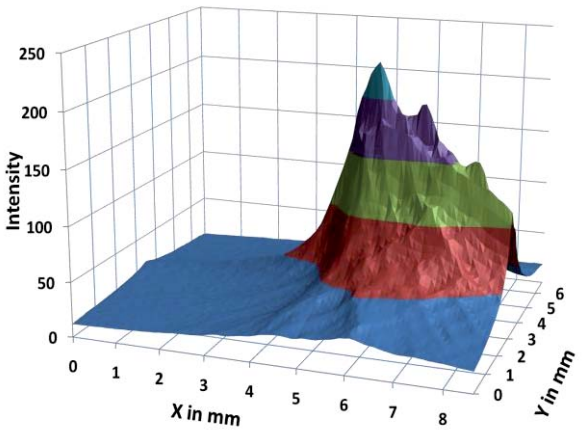


Figure 8. Image formed with full aperture exposure and source 10° off the optical axis. Compare with simulations.

3 Summary

These preliminary tests on the BBM support the technology and approach used to meet the OM requirements for the JEM-EUSO mission. The data shows that the BBM OM meets the expected performance as manufactured. Furthermore the performance meets or exceeds the instrument requirements for this scaled model. A more thorough and complete set of tests have been included in a proposal to NASA for participation in the JEM-EUSO mission. More detailed tests will likely provide the data necessary to understand the 2% increase in the focal length measured compared to simulations. The surface roughness analysis will help improve the manufacturing process in order to reduce the surface roughness to 20 nm RMS or less.

Acknowledgements

The BBM design and fabrication were supported by RIKEN. The testing was a collaborative effort between Marshall Space Flight Center & University of Alabama Huntsville personnel. Funding was provided jointly by MSFC & UAH. Laboratory test facilities were provided by UAH.

References

[1] Y. Takahashi, The JEM-EUSO Mission, New Journal of Physics, **Vol. 11**, No. 065009, (2009)
[2] T. Ebisuzaki, these proceedings
[3] A. Zuccaro Marchi, ID:0852, these proceedings
[4] Y. Hachisu, ID:0874, these proceedings

Offset (cm)	Incident Power	Transmitted Power	Transmission (%)	note
0	288	171	60	Center hole exists from manufacturing
10	328	189	58	
20	364	207	57	
30	368	254	69	
40	368	231	63	Source begins to illuminate the BBM frame
50	368	158	43	Source is further off the edge of the lens.

Table 1. Transmission measurements for the front lens

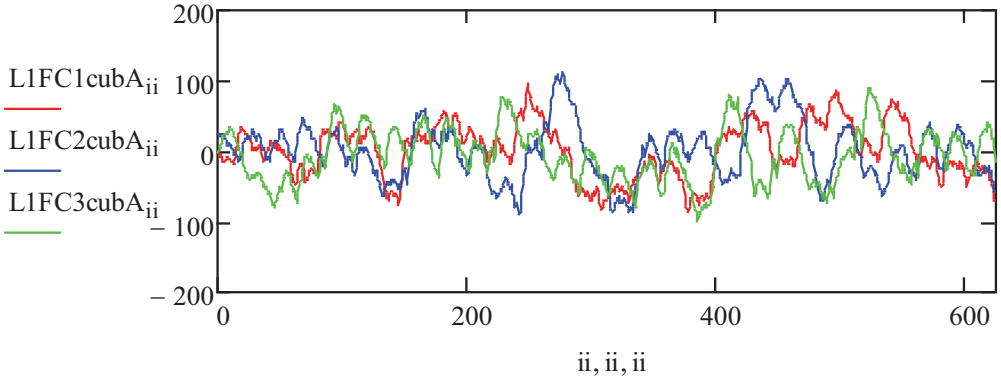


Figure 3. Traces of the lens surface to evaluate the manufacturing process.

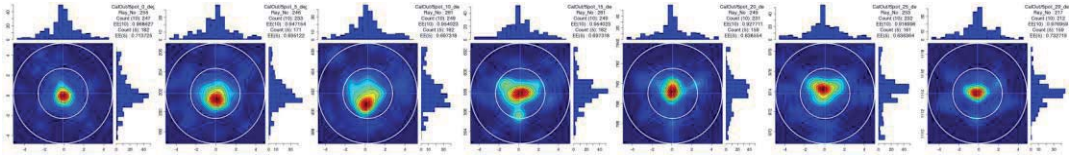
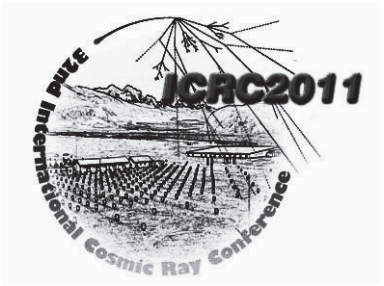


Figure 5. Simulated performance of the BBM. The columns show predicted images at 0°, 5°, 10°, 15°, 20°, 25° and 30° off the optical axis. Circles with diameters of 2.5 and 5.0 mm are superimposed on the images.

32ND INTERNATIONAL COSMIC RAY CONFERENCE, BEIJING 2011



Atmospheric Monitoring System of JEM-EUSO

A.NERONOV[1], S.WADA[2], M. D. RODRÍGUEZ FRÍAS[3], A. MORALES DE LOS RÍOS[3], G. SÁEZ CANO[3], H. PRIETO[3], J. PIÑEIRO[3], L. DEL PERAL[3], J. HERNÁNDEZ[3], N. PACHECO[3,4], M. D. SABAU[5], T. BELENGUER[5], C. GONZÁLEZ[5], M. REINA[5], S. BRIZ[6], A. DE CASTRO[6], F. CORTÉS[6], F. LÓPEZ[6], G. HERRERA[7], J. LICANDRO[7], E. JOVEN[7], M. SERRA[7], O. VADUVESCU[7] A.ANZALONE[8], F.ISGRÒ[9], R.CREMONINI[10], C.CASSARDO[10], A.MAURISSEN[11], C.URBAN[11], T.OGAWA[2] K.SHINOZAKI[2] FOR JEM-EUSO COLLABORATION
[1]*ISDC Data Centre for Astrophysics, Versoix, Switzerland*
[2]*RIKEN Advanced Science Institute, Japan*
[3] *SPace & AStroparticle (SPAS) Group, UAH, Madrid, Spain*
[4]*Instituto de Física Teórica (IFT), Universidad Autónoma de Madrid (UAM), Spain*
[5] *LINES laboratory, Instituto Nacional de Tecnica Aeroespacial (INTA), Madrid, Spain*
[6] *LIR laboratory, University Carlos III of Madrid (UC3M), Spain.*
[7] *Instituto Astrofisico de Canarias, Tenerife, Spain*
[8] *INAF-IASF, Istituto di Astrofisica Spaziale e Fisica Cosmica,Palermo, Italy*
[9] *Dipart. di Scienze Fisiche, Università degli Studi di Napoli Federico II, Napoli, Italy*
[10] *Dip.di Fisica, Università degli Studi di Torino, Italy*
[11] *Centre Suisse d'Electronique et Microtechnique, Switzerland*
Andrii.Neronov@unige.ch

Abstract: JEM-EUSO telescope on International Space Station will detect UV fluorescence emission from Ultra High Energy Cosmic Rays (UHECR) induced Extensive Air Showers (EAS) penetrating in the atmosphere. The accuracy of reconstruction of the properties of the primary UHECR particles from the measurements of UV light depends on the extinction and scattering properties of the atmosphere at the location of the EAS and between the EAS and JEM-EUSO. The Atmospheric Monitoring system of JEM-EUSO will use the LIDAR, operating in the UV band, and an infrared camera to detect cloud and aerosol layer features across the entire 60° field of view of JEM-EUSO telescope, to measure the cloud top altitudes with the accuracy of 500 m and the optical depth profile of the atmosphere in the direction of each EAS with the accuracy $\Delta\tau \leq 0.15$ and resolution of 500 m. This should ensure that the energy of the primary UHECR particles and the depth of EAS maxima are measured with the accuracy better than 30% and 120 g/cm^2, respectively.

Keywords: Ultra-High-Energy Cosmic Rays; Fluorescence Telescope; International Space Station; LIDAR; Infrared Camera.

1 Introduction

JEM-EUSO is a next-generation fluorescence telescope for detection of Extreme Energy Cosmic Rays (EECR, cosmic rays with energies $\sim 10^{20}$ eV and higher) which will be installed at International Space Station (ISS) in 2016 [1, 2]. It is a refractive telescope with the aperture $\simeq 2.5$ m which will detect fluorescence UV emission from Extensive Air Showers (EAS) produced by EECR penetrating in the atmosphere within the 60° Field of View (FoV). At the altitude of the ISS $H \simeq 400$ km the area over which the EAS events will be detected is $\simeq (400\ \mathrm{km})^2$. The ISS orbits the Earth with the period $P \simeq 90$ min along an inclined orbit extending between $\pm 52°$ from Equator.

The properties of the primary EECR particles (energy, type, arrival direction) will be derived from the imaging and timing properties of the UV emission from the EAS trace in the atmosphere. The Earth atmosphere absorbs and scatters UV light. The amount of absorption and scattering depends on the air column density between the emission and detection point and also on the type of absorbing and scattering centers. Scattering and absorption properties of the atmosphere are strongly affected by the presence of clouds and aerosol layers [3]. Cloud- and aerosol-induced variations of the scattering and absorption properties at the locations of EAS events distort the UV signal from EAS detected by JEM-EUSO. In the absence of detailed information on the presence and physical properties of the cloud and aerosol layers in JEM-EUSO FoV, distortions of the UV signal from EAS lead to systematic errors in determination of the properties of EECR from the UV light profiles.

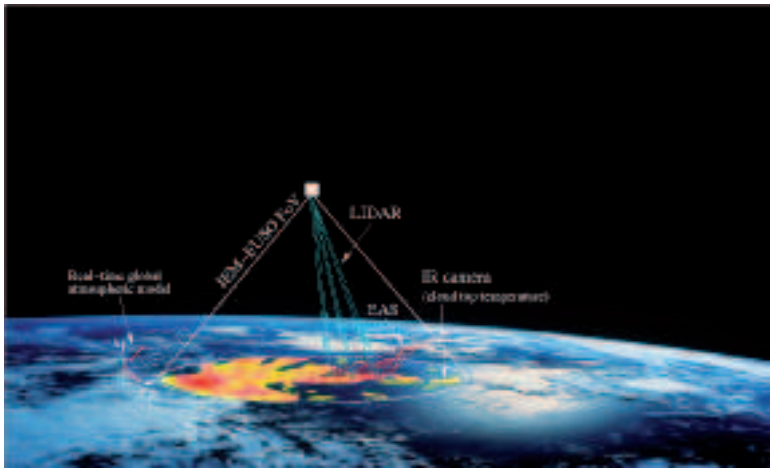


Figure 1: The principle of Atmospheric Monitoring in JEM-EUSO

In particular, presence of optically thin cloud layers between the EAS and JEM-EUSO telescope reduces the overall intensity of UV light leading to an under-estimate of the EECR energy. EAS penetration into an optically thick cloud produces strong enhancement of the scattered Cherenkov light emission from EAS, which can be misinterpreted as Cherenkov light reflection from the ground/sea. This again leads to a wrong estimate of the depth of EAS maximum in the atmosphere. Statistics of the Earth cloud coverage known from the satellite measurement [4, 5] indicates that as much as 70% of EAS profiles might be affected by the presence of the clouds.

Cloud and aerosol layer induced distortions of the EAS profiles could be corrected if the detailed information on distribution and optical properties of the cloud/aerosol layers in JEM-EUSO FoV is known. This information will be provided by the Atmospheric Monitoring (AM) system of JEM-EUSO. The ISS orbital speed is $\simeq 7$ km/s so that the atmospheric volumed monitored by JEM-EUSO changes every $400\ \mathrm{km}/7\ \mathrm{km/s} \simeq 60$ s. This means that the distribution of clouds and aerosol layers in JEM-EUSO FoV is continuously changing. The AM system will continuously monitor the variable atmospheric conditions in JEM-EUSO FoV during all EECR data taking periods.

In this contribution we describe the set up of the AM system of JEM-EUSO and its expected performance.

2 Atmospheric Monitoring system

The goal of the AM system of JEM-EUSO is to provide information on the distribution and optical properties of the cloud and aerosol layers within the telescope FoV. The basic requirements on the precision of measurements of the cloud and aerosol layer characteristics are determined by the requirements on the precision of measurement of EAS parameters [7]: *(A1)* measurement of EECR energy with precision 30%; *(A2)* measurement of the depth of the shower maximum with precision 120 g/cm^2.

Precision of the measurement of the energy of EECR is affected by the absorption of UV light cloud and aerosol layers. Precision of the measurement of the depth of shower maximum is additionally affected by the uncertainties of location of clouds and aerosols in the atmosphere. Imposing the requirements on the performance of the AM system: *(B1)* measurement of the optical depth of atmospheric features with precision down to $\Delta\tau \leq 0.15$; *(B2)* measurement of the altitude of the boundaries of atmospheric features with precision $\Delta H \leq 500$ m. assures that the systematic error of the measurement of the energy and the depth of the EAS maximum introduced by the uncertainty of atmospheric conditions is significantly below that of requirements *A1, A2*.

The required precision of measurement of the altitude and optical depth of the cloud and aerosol layers will be achieved with the following dedicated AM system which will consist of (Fig. 1)

1. LIght Detection And Ranging (LIDAR) device,
2. Infrared (IR) camera and
3. global atmospheric models from the post-analysis of all available meteorological data by global weather prediction services like ECMWF [8] and GMAO [9].

JEM-EUSO will take the cosmic ray data during the ISS nighttime. To reveal the overall picture of cloud distribution in the FoV an IR camera will be used. The IR camera is an infrared imaging system used to detect the presence of clouds and to obtain the cloud coverage and cloud top altitude during the observation period of the JEM-EUSO main instrument. Measurement of the temperature of the clouds will be used to estimate the altitude of the cloud top layers. Such an estimate is possible in the troposphere in the altitude range $0 - 10$ km where the atmosphere is characterized by a steady temperature gradient of $dT/dH \simeq 6^\circ/\mathrm{km}$. To achieve the precision of measurement of the cloud top altitude $\Delta H \simeq 0.5$ km the precision

of the temperature measurements by the IR camera will be $\Delta T = (dT/dH)\Delta H = 3$ K.

The AM system will additionally use a LIDAR device. The LIDAR will measure the optical depth profiles of the atmosphere in selected directions, with the ranging accuracy of $375/\cos(\theta_z)$ m, where θ_z is the angle between the direction of the laser beam and nadir direction. The power of the laser will be adjusted in such a way that cloud/aerosol layers with optical depth $\tau \geq 0.15$ at 355 nm wavelength will be detectable.

The IR camera and LIDAR measurements will provide complementary information with the amount of details sufficient to

- select the EAS events appearing in the clear sky conditions;
- provide information on the optical properties of the clouds needed for correction of the cloud affected EAS profiles which could be retained for further analysis;
- reject EAS events occurring in the complicated atmospheric conditions (multi-layer cloud/aerosol structures).

3 IR camera

The IR camera on board of JEM-EUSO will consist of a refractive optics made of germanium and zinc selenide and an uncooled microbolometer array detector [11]. Interferometer filters will limit the wavelength band to 10-12 μm. In the current configuration, two $\delta\lambda = 1$ μm wide filters will be used centered at the wavelengths 10.8 μm and 12 μm two increase the precision of the radiative temperature measurements.The FoV of the IR camera is 60°, totally matching the FoV of the main JEM-EUSO telescope. The angular resolution, which corresponds to one pixel, is about 0.1°. A temperature-controlled shutter in the camera and mirrors are used to calibrate background noise and gains of the detector to achieve an absolute temperature accuracy of 3 K. Though the IR camera takes images continuously at a video frame rate (equal to 1/30 s), the transfer of the images takes place every 30 s, in which the ISS moves half of the FoV of the JEM-EUSO telescope.

Fig. 2 shows the precision of the measurement of the cloud temperature for different cloud altitudes, reachable with the current IR camera design. The precision is within the required 3 K limit almost everywhere down to the altitude of $\sim$ 1 km. Three different columns show the error derived from the measurements in the shorter (B1) and longer (B2) wavelength bands as well as in the combined ($B_{\rm TIR}$) measurement (see [6] for more details).

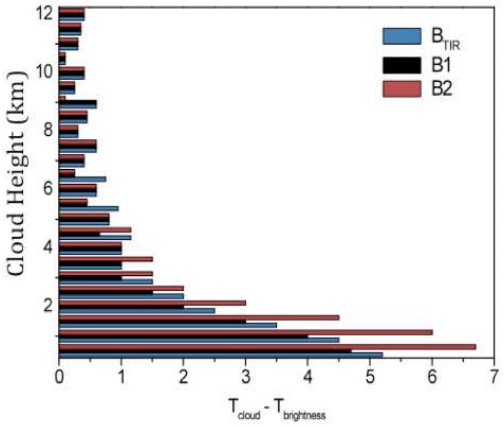


Figure 2: Error in the determination of temperature of clouds with the IR camera as a function of the cloud altitude.

4 LIDAR

The most relevant information about the absorption and scattering properties of clouds and aerosols is at the locations around the EAS events. To get this information, the LIDAR will have a re-pointing capability. The laser beam will be repointed in the direction of EAS candidate events following each EAS trigger of JEM-EUSO telescope. The average trigger rate of JEM-EUSO will be ~ 0.1 Hz. During the time interval between subsequent triggers, the LIDAR will

- re-point to the direction in which the EAS trigger occurred and
- take the measurements of laser backscattering signal in several directions around the supposed EAS maximum.

Re-pointing of the laser beam will be done with the help of a steering mirror with two angular degrees of freedom and maximal tilting angle $\pm 15^\circ$. The laser backscatter signal will be received by the main JEM-EUSO telescope which is well suited for detection of the 355 nm wavelength. Any Multi-Anode Photo-Multiplier Tube (MAPMT) in the focal surface of JEM-EUSO telescope could temporarily serve as the LIDAR signal detector, a special LIDAR trigger is foreseen in the Focal surface electronics of JEM-EUSO detector [10]. Measurements of the laser backscatter signal with time resolution of 2.5 μs (time unit of the focal surface detector) will provide ranging resolution of 375 m in nadir direction. The energy of the laser pulse will be adjusted in such a way that the backscatter signal will have enough statistics for the detection and measurement of the optical depth of optically thin clouds with $\tau \leq 0.15$ at large off-axis angles. Examples of the simulated laser backscatter signal as it would appear in the JEM-EUSO detector are shown in Fig. 3. The upper panel shows the signal in the presence of an optically thin cloud with $\tau = 0.06 \pm 0.04$

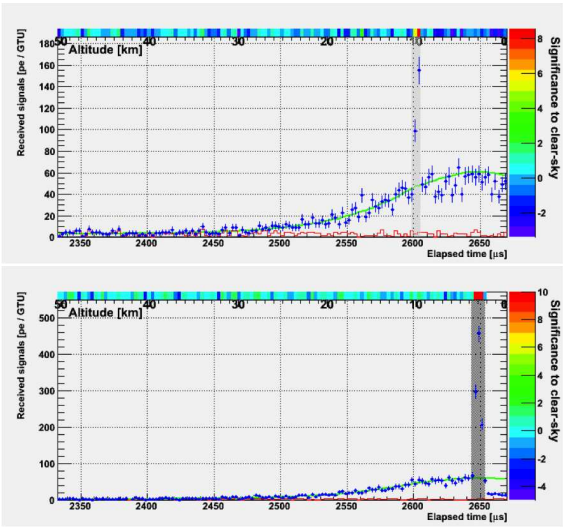


Figure 3: Simulated LIDAR backscatter signal in the presence of an optically thin (top) and optically thick (bottom) clouds.

Parameter	**Value**
Wavelength	355 nm
Pulse repetition rate	> 1 Hz
Pulse width	15 ns
Pulse energy	20 mJ/pulse
Steering of output beam	$\pm 30^\circ$
Receiver	JEM-EUSO telescope
Detector	MAPMT (JEM-EUSO)
Range resolution	375 m
Mass	17 kg
Power	< 70 W

Table 1: Characteristics of JEM-EUSO LIDAR

($\tau = 0.05$ was assumed in the simulation) at the altitude of 10 km. Laser pulse energy $E = 20$ mJ is assumed. Bottom panel shows an example of optically thick low altitude cloud. Assuming the same laser pulse energy $\tau = 0.8 \pm 0.2$ is derived from the simulated data, while $\tau = 0.9$ was assumed in the simulation.

Parameters of the LIDAR system of JEM-EUSO are summarized in Table 1.

5 Global Atmospheric Model data.

Precision of the analysis of both IR camera and LIDAR data is largely improved when the basic atmospheric parameters of the atmosphere (temperature and pressure profiles, humidity etc) in the monitored region are known. Such parameters will be systematically retrieved from the global atmospheric model resulting from the post-analysis of weather models, calculated on regular basis by global meteorological service organizations (GMAO, ECMWF). These models also provide information on the presence and altitude distribution of cloud and aerosol layers, information which is directly relevant for JEM-EUSO data analysis. This justifies the incorporation of real time global atmospheric models in the AM data of JEM-EUSO.

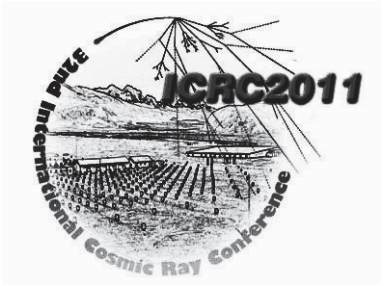
6 Conclusions.

The AM system of JEM-EUSO, which includes the IR camera, the LIDAR and global atmospheric model data will provide sufficient information on the state of the atmosphere around the location of EAS events. This information will be used to correct the profiles of cloud-affected EAS events for the effects of clouds and aerosol layers, so that most of the cloud-affected events could be retained for the in the EECR data analysis.

References

[1] T.Ebisuzaki et al., These Proceedings, 2011, ID1628
[2] Y. Takahashi, New Journal of Physics, 2009, **11**, 065009
[3] G. Sàez-Cano et al., These Proceedings, 2011, ID1034
[4] H.Chepfer et al., 2010, J.Geophys.Res., **115**, D00H16
[5] M.Bertaina et al., These Proceedings, 2011, ID0398
[6] A.Anzalone et al., These proceedings, ID1152
[7] A.Santangelo et al., These Proceedings, 2011, ID0991
[8] `http://www.ecmwf.int/`
[9] `http://gmao.gsfc.nasa.gov/`
[10] Kawasaki Y., et al., These Proceedings, 2011, ID0472
[11] J.A. Morales de los Rios et al., These Proceedings, 2011, ID1031

32ND INTERNATIONAL COSMIC RAY CONFERENCE, BEIJING 2011



The IR-Camera of the JEM-EUSO Space Observatory

J.A. MORALES DE LOS RÍOS[1], G. SÁEZ-CANO[1], H. PRIETO[1], L. DEL PERAL[1], J. PIÑEIRO[1], K. SHINOZAKI[1,2], J. HERNÁNDEZ[1], N. PACHECO[3], M.D. SABAU[4], T. BELENGUER[4], C. GONZALEZ[4], M. REINA[4], S. BRIZ[5], A.J. DE CASTRO[5], F. CORTÉS[5], F. LOPEZ[5], J. LICANDRO[6], E. JOVEN[6], M. SERRA[6], O. VADUVESCU[6], G. HERRERA[6], S. WADA[2], K. TSUNO[2], T. OGAWA[2], O. CATALANO[7], A. ANZALONE[7], M. CASOLINO[8,2] AND M.D. RODRÍGUEZ-FRÍAS[1], FOR THE JEM-EUSO COLLABORATION.

[1]*SPace & AStroparticle (SPAS) Group, UAH, Madrid, Spain.*
[2]*RIKEN, 2-1 Hirosawa, Wako, Saitama 351-0198, Japan.*
[3]*Instituto de Física Teórica (IFT). Universidad Autónoma de Madrid (UAM), Spain.*
[4]*LINES laboratory, Instituto Nacional de Técnica Aeroespacial (INTA), Madrid, Spain.*
[5]*LIR laboratory, University Carlos III of Madrid (UC3M), Spain.*
[6]*Instituto de Astrofísica de Canarias (IAC), Tenerife, Spain.*
[7]*INAF/IASF Istituto di Astrofisica Sapziale e Fisica Cosmica di Palermo, Italy.*
[8]*University of Rome Tor Vergata, Rome, Italy.*
josealberto.morales@uah.es

Abstract: The JEM-EUSO space observatory will be launched and attached to the Japanese module of the International Space Station (ISS) in 2016. Its aims is to observe UV photon tracks produced by Ultra High Energy Cosmic Rays (UHECR) and Extremely High Energy Cosmic Rays (EHECR) developing in the atmosphere and producing Extensive Air Showers (EAS). JEM-EUSO will use our atmosphere as a huge calorimeter, to detect the electromagnetic and hadronic components of the EAS. The Atmospheric Monitoring System plays a fundamental role in our understanding of the atmospheric conditions in the Field of View (FoV) of the telescope and it will include an IR-Camera for cloud coverage and cloud top height detection.

Keywords: JEM-EUSO, Ultra High Energy Cosmic Rays, Atmospheric Monitoring, Infrared Camera, Clouds Temperature Retrieval, End to End Simulation.

1 Introduction

JEM-EUSO (Extreme Universe Space Observatory on Japanese Experiment Module) [1] is an advanced observatory onboard the International Space Station (ISS) that uses the Earth's atmosphere as a calorimeter detector. The instrument is a super wide-Field Of View (FOV) telescope that detects UHECRs and Extremely High Energy Cosmic Rays (EHECRs) with energy above 10^{19} eV. This instrument orbits around the earth every $\approx$ 90 minutes on board of the International Space Station (ISS) at an altitude of $\approx$ 430 km.

An extreme energy cosmic ray particle collides with a nucleus in the Earth's atmosphere and produces an Extensive Air Shower (EAS) that consists of a huge amount of secondary particles generating flourescence light of atmospheric N_2. JEM-EUSO captures the moving track of the fluorescence UV photons and reproduces the calorimetric development of the EAS [2], [3]. At the energies observed by JEM-EUSO, above 10^{19} eV, the existence of clouds will blur the observation of UHECRs. Therefore, the monitoring of the cloud coverage by JEM-EUSO Atmospheric Monitor System (AMS), is crucial to estimate the effective exposure with high accuracy and to increase the confidence level in the UHECRs and EHECRs events just above the threshold energy of the telescope. Therefore, the JEM-EUSO mission have implemented the AMS as far as the impact onto mass and power budget is insignificant. It consists of 1) Infrared (IR) camera, 2) LIDAR, 3) slow data of the JEM-EUSO telescope.

The Atmospheric Monitoring System (AMS) IR Camera is an infrared imaging system used to detect the presence of clouds and to obtain the cloud coverage and cloud top altitude during the observation period of the JEM-EUSO main instrument. Cloud top height retrieval can be performed using either stereo vision algorithms (therefore, two different views of the same scene are needed) or accurate radiometric information, since the measured radiance is basically related to the target temperature and therefore, according to standard atmospheric models, to its altitude [4].

Parameter	Target value	Comments
Measurement range	200 K - 320 K	Annual variation of cloud temperature plus 20 K margin
Wavelength	10-12 μm	Two atmospheric windows available: 10.3-11.3 μm and 11.5-12.5 μm
FoV	60^o	Same as main instrument
Spatial resolution	0.25^o@FOV center 0.22^o@FOV edge	Threshold values.
Absolute temperature accuracy	3 K	500 m in cloud top altitude
Mass	$\leq$ 7 kg	Inc 30% margin.
Dimensions	$200 \times 280 \times 320$ mm.	$300 \times 300 \times 500$ mm. Max
Power	$\leq$ 11 W	Inc 30% margin.

Table 1: Requirements for the IR camera.

2 Requirements for the infrared camera measurements

The Atmospheric Monitoring System (AMS) IR Camera is an infrared imaging system used to detect the presence of clouds and to obtain the cloud coverage and cloud top altitude during the observation period of the JEM-EUSO main instrument. Moreover, since measurements shall be performed at night, it shall be based on cloud IR emission. The observed radiation is basically related to the target temperature and emissivity and, in this particular case, it can be used to get an estimate of how high clouds are, since their temperatures decrease linearly with height at 6 K/km in the Troposphere. Table 1 summarizes the current scientific and mission requirements for the JEM-EUSO AMS IR camera.

Although there are no formal requirements for data retrieval, it has been assumed that the IR camera retrieval of the cloud top altitude could be performed on-ground by using stereo vision techniques or radiometric algorithms based on the radiance measured in one or several spectral channels (i.e. split-window techniques). Therefore, the IR camera preliminary design should be complaint with both types of data processing. Moreover, in this work, we have considered two methods for the data retrieval based on the use of one or two IR bands.

3 The infrared camera preliminary design

The IR-Camera can be divided into two main subsystems: a) Opto-mechanical unit, including the components necessary for the manipulation of the optical signal (magnification, spectral filtering), the detection of light (sensor) and the calibration of the sensor. b) Electronic subsystem, providing the instrument control and HouseKeeping (HK) functions, scientific data processing, redistribution of the power supply to IR camera components and electronic interfaces with the JEM-EUSO Instrument.

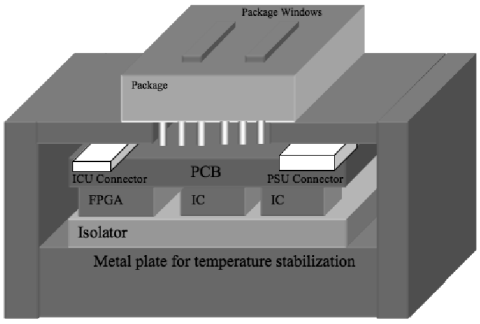


Figure 1: Detail view of the temperature stabilizer and the arrangement of the diferent components.

The optical system will be a refractive objective based on a modified IR Cooke triplet, with an aperture of 15mm, made of composed materials to save weight. This type of lens is especially interesting because has enough available degrees of freedom to allow the designer the correction of primary aberrations. For the detector, the baseline is an uncooled microbolometer pixel array, with a size of 640 x 480 pixels, and a Read Out Integrated Circuit (ROIC) as well, that is in charge of reading the values of the photodetector array. The ROIC has on-chip programmable gain for optimization of the performance over a wide range of operating conditions. The system is uncooled, although a temperature stabilizer is required with a thermistor close to the detector array for accurate temperature measurements, and a Peltier cooling system, as is show in figure 1.

In the Electronic subsystem, we can find the image channel wich is formed by an optic element, used to focus the image, and the IR detection unit (detector plus video electronics). The data generated by the image channel is processed by the Data Processing Unit (DPU) within the Instrument Control Unit (ICU), which is in charge of controlling several aspects of the system management such as the electrical system, the thermal control, the calibration subsystem and the communication with the platform computer. The actuators of the instrument are managed by the ICU through an interface with the Centralized Control Unit (CCU). The Power Supply Unit (PSU) provides the required power regulation to the system. The management of the PSU is controlled by the ICU as well.

Most of the digital circuit implementation is based on FPGAs. The design contains two FPGAs which are located inside the ICU and inside the CCU respectively. Both FPGAs offer a control interface to the microprocessor to deal with basic functions such as actuator manipulations and data processing functions. All the commands are transmitted through a common data interface.

Therefore, the system architecture can be split into four different blocks: the optic with the detector and video electronics, the CCU with the power drivers and the mechanisms controller FPGA, the PSU which is in charge of provide the power supply to the instrument, and the ICU that controls and manages the overall system behavior. A cold redundancy scheme has been selected for the design.

4 Infrared data retrieval

The radiation emitted by the Earth's surface and the atmospheric clouds is measured by the IR sensor and the system retrieves the temperature of the emitter from this measurement. However the radiation collected by the IR sensor is not emitted by one single source. On the contrary, the atmosphere between the emitter and the sensor absorbs and emits energy. Therefore, the temperature obtained directly is not exactly the temperature of the emitter. These effects involve some uncertainties in the emitter temperature obtained from the direct radiation measurements. The objective of this part is the estimation of the errors associated to several factors: temperature and water vapor profiles deviations and cirrus effect. For this purpose some retrievals simulations have been carried out.

The simulations are based in a radiative model that consists of an atmospheric model, with the Earth surface emitting at 300K and a cloud at a certain height. In order to define the atmospheric model, the atmosphere is split into layers and values of temperature, pressure and gases concentrations have to be assigned. In this study, the atmosphere has been divided in 0.5 km thick layers from the bottom to the top of the atmosphere assumed at 150 km. Far away from this altitude, it is assumed that there is not physical effects on the IR radiation transport through the medium. In this way, the atmospheric model is described by vertical profiles of temperature, pressure and density. As a good approximation, clouds can be considered as blackbody emitters. For this reason, the clouds would absorb the energy emitted by the Earth surface and by the atmosphere beneath the clouds. For the same reason, the cloud can be modeled by a thin layer located at the top of the cloud that behaves as a blackbody at the temperature of the atmospheric layer at the same level. Figure 2 shows the vertical profiles describing the atmosphere model used.

4.1 Results of the one-band analysis

The main conclusions can be summarized as follow: a)The effect of the temperature vertical profiles is not significant (errors $<$3 K). b)The effect of water vapor vertical profile is significant for low-level clouds and atmospheres with high water vapor concentrations. c)The effect of thin clouds (cirrus) cannot be neglected since errors in retrieved temperatures are higher than 3 K for low and medium-level clouds. d)The temperatures retrieved by only one band are not accurate enough due to the effect of water vapor profiles and thin clouds.

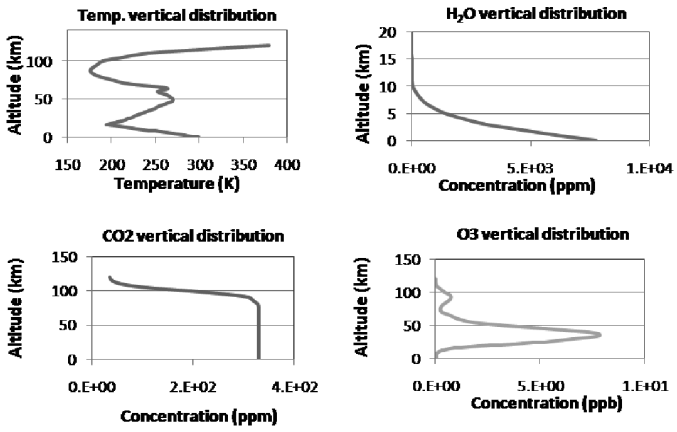


Figure 2: Examples of vertical profiles that describe the atmosphere model used in radiance calculations.

Cloud Height	$T_{cloud}(K)$	$T_{band-1}(K)$	$T_{band-2}(K)$	$T_{SWA}(K)$
0.5 km	296.7	293.6	292.0	297.4
1 km	293.7	291.5	290.3	294.0
2 km	287.7	286.7	286.1	287.7

Table 2: Comparison between retrieved temperatures by the one-band algorithm and the SWA. Although clouds have been studied from top heights of 0.5 km to 12 km in 0.5 km steps, in this table only the worst cases are shown

4.2 Results of the two-band analysis

In order to take advantage of the two-bands, a Split-Window Algorithm (SWA) has to be applied to the brightness temperatures retrieved from B1 and B2 bands. These algorithms have been used since latest 70s to measure the Earth's surface temperature from satellites to minimize the effect of the atmosphere. There are plenty of SWA that have been developed to retrieve the surface temperature from satellite measurements [5] [6]. All these algorithms are based on linearization of Planck's law and on the Radiative Transfer Equation (RTE). They have been applied to radiances obtained in two spectral bands and all of them consist of linear or quadratic functions of the temperatures retrieved in two bands. A comparison between retrieved temperatures by the one-band option and the SWA is shown in table 2. For blackbody clouds, the coeficients only depend on the atmospheric transmittance and they can be calculated because atmospheric profiles are known in simulations studies.

For real cases, the transmittance is not always known and, for this reason, different algorithms have been developed by different authors. The differences between algorithms lies in the SWA parameters and different authors propose different parameters to retrieve the surface temperatures in different conditions [7]. The algorithms have to be validated for different examples and environmental conditions but there is not an universal algorithm that can be applied

to any problem with enough accuracy. The same methodology can be applied to measure clouds temperatures, especially to low-level and thick clouds. In fact, there are also some SWAs devoted to retrieve clouds temperatures from satellites such as AVHRR, MODIS, etc. [8]. These algorithms are able to retrieve top-cloud temperature (Nieman, 1993), cloud emissivity and type of clouds (Pavolonis, 1985 and Inoue, 1987) and cloud microphysics (Inoue 1985). However the results attained when semitransparent cirrus are found in the FOV are not so accurate [8]. Therefore still open points remain to be adressed in order to retrieve top-cloud temperatures accurately.

Summarizing the results of this SWA preliminary study we can state: a) SWA is as accurate as the transmitances calculated with specific known atmospheric profiles. b) In order to study the effect of a cirrus (semitransparent cloud) in the temperature retrieval of a blackbody cloud, some simulations have been performed considering a cirrus between the cloud top and the IR camera. The examples show that the one-band option temperature retrievals have stronger uncertainties than SWA option, although SWA error is still above 3K. c) Not all SWAs from the bibliography always give good results. d) For higher clouds the coefficients of SWA have to be checked because the distance between the cloud top and the sensor decreases. These are only preliminar results, other factors like partially-covered pixels, semitransparent clouds, and some other issues will be estudied in the future.

5 End to end simulation of the IR-camera

End to end simulation of the infrared camera will give us simulated images of those we expect to obtain with the instrument. Therefore this simulation together with the data analysis will be included in the AMS detector simulation module of the JEM-EUSO analysis software. First the simulated radiation produced by the Earth's surface and atmosphere have been considered, taking in account the effect of the optics and the detector, and finalizing in the electronics and image compresion algorithm. A data analysis module is foreseen to take the data from simulator, and real data from the IR-Camera to perform the analysis tasks with the algorithms for data retrieval. The output from this analysis module will be used as an input in the official codes for the event reconstruction of the main telescope.

So far we have just started with the IR simulations, emitted by the ground and the atmosphere, using a modified version of the SDSU [9] software developved in the Hydrospheric Atmospheric Research Center, Nagoya University, to simulate the wavelenght of our detector, and thanks to the capabilities of this code we are simulating the UV(Ultraviolet) range of our main instrument (250-500 μm) to get an aproach for the slow data of JEM-EUSO. At the end, the output from this work will be images similar to what we expect from our camera, that would allow us to test the data retrieval algorithms and calculate correction factors for the IR-Camera. A preliminary example of the IR simulations done by the SDSU software is shown in the figure 3.

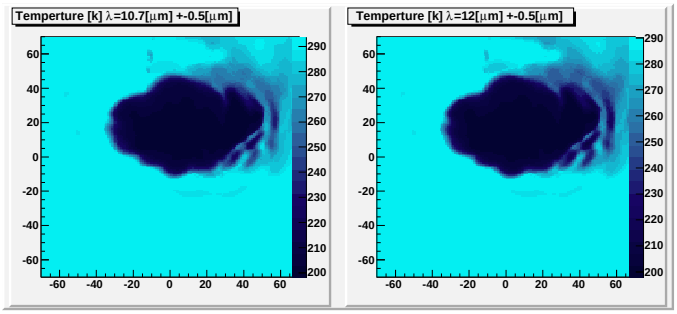


Figure 3: Examples of simulated cloud with SDSU modified for the IR-Camera bands.

6 Acknowledgments

The Spanish Consortium involved in the JEM-EUSO Space Mission are funded by MICINN under projects AYA2009-06037-E/ESP, AYA-ESP 2010-19082, CSD2009-00064 (Consolider MULTIDARK) and by Comunidad de Madrid (CAM) under project S2009/ESP-1496. J.A. Morales de los Ríos wants to acknowledge the University of Alcalá for his Phd fellowship.

References

[1] The JEM-EUSO International Collaboration website, http://jemeuso.riken.jp/en/index.html

[2] JEM-EUSO Collaboration, Nuclear Physics B (Proc. Suppl.), 175-176, (2008), 237-240.

[3] The JEM-EUSO Mission, New Journal of Physics, 11, (2009), 065009.

[4] S. Wada, T. Ebisuzaki, T. Ogawa, M. Sato, T Peter, V. Mitev, R. Matthey, A. Anzalone, F. Isgro, D. Tegolo, E. Colombo, J.A, Morales de los Ros, M. D. Rodrguez Fras, Park II, Nam Shinwoo, Park Jae and JEM-EUSO Collaborators, Potential of the Atmospheric Monitoring System of JEM-EUSO Mission, Proc 31st International Cosmic Ray Conference (2009).

[5] M.D. King et al, Cloud Retrieval Algorithms for MODIS. MODIS Algorithm Theoretical Basis Document N ATBD-MOD-05, 1997

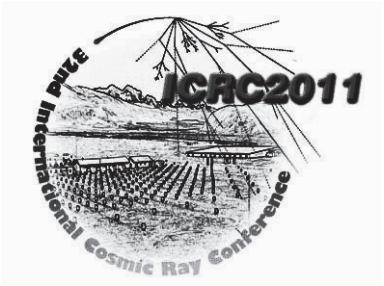
[6] Z. Wan and J., Dozier, A Generalized Split- Window Algorithm for Retrieving Land-Surface Temperature from Space, IEEE Transactions on Geoscience and Remote Sensing, Vol. 34, NO. 4, JULY 1996

[7] J. M. Galve et al, Tethys, 2007, 4, 2934.

[8] A.K. Heidiger and M.J. Pavolonis. Journal of Applied Meterology and Climatology, 2008, Vol. 48, 1100-1116.

[9] Hirohiko Masunaga et al, Satellite Data Simulator Unit, A multisensor, multispectral Satellite Simulator Package, 2010, American Meteorological Society.

32ND INTERNATIONAL COSMIC RAY CONFERENCE, BEIJING 2011



Cloud Coverage and its Implications for Cosmic Ray Observation from Space

F. GARINO[1], A. GUZMAN[2], M. BERTAINA[1], C. CASSARDO[1], R. CREMONINI[1], C. DE DONATO[2], G. MEDINA-TANCO[2], K. SHINOZAKI[3], ON BEHALF OF THE JEM-EUSO COLLABORATION
[1] *Dipartimento di Fisica Generale dell' Università di Torino, Torino, Italy*
[2] *ICN-UNAM, Mexico City, Mexico*
[3] *RIKEN, Wako, Japan*

tapozio@gmail.com,bertaina@to.infn.it

Abstract: JEM-EUSO is an International mission planning to observe Extreme High Energy Particles from Space. Flying on the ISS, during its operation, JEM-EUSO will experience all possible weather conditions inside its field of view. In order to estimate the effective aperture of the detector, one key point is the evaluation of the role of clouds, in particular their frequency as a function of altitude and optical depth for the different geographical areas of the planet. The probability of occurrence of a defined atmospheric condition has been assessed in this study by means of different meteorological databases: TOVS, ISCCP and CACOLO data. Because of the specific peculiarities of each dataset, the comparison of the different results is used to assess the systematic uncertainty on the derived conclusions.

Keywords: JEM-EUSO, meteorological databases, cloud information.

1 Introduction

JEM-EUSO [1, 2] is a new type of observatory under development with the aim of detecting Extreme Energy Cosmic Rays (EECR) from the International Space Station (ISS), by using the whole Earth as a detector. JEM-EUSO telescope will orbit around the Earth every $\sim$90 minutes at the altitude of 350-400 km to capture the moving track of the Ultra Violet (UV) photons produced during the development of Extensive Air Showers (EAS) in the atmosphere. The telescope has a super-wide ($\pm 30^\circ$) Field-of-View with optics composed by Fresnel lenses [3]. The telescope records the track of an EAS with a time resolution of 2.5μs and a spatial resolution of about 0.5 km (corresponding to 0.07°) in nadir mode by using a highly pixelized focal surface (3×10^5 pixels) [4]. These time-segmented images allow determining energy and direction of the primary particles [5].
During its operation JEM-EUSO will experience all possible weather conditions. The amount of both fluorescence and Cherenkov signals reaching JEM-EUSO depends on the extinction and scatteringt of UV light in atmosphere. Correct reconstruction of EECR energy and of the type of the primary cosmic ray particle requires, therefore, information about absorption and scattering properties of the atmosphere. For this reasons the JEM-EUSO observatory will include an Atmospheric Monitoring System (AM) [6] which will consist of an infrared camera [7], and a LIDAR device. Moreover, it will benefit from the real time global atmospheric models like those generated by the Global Modeling and Assimilation Office (GMAO) [8], the European Center for Medium range Weather Forecasts (ECMWF) [9] and other similar services.
The cloud coverage in the FoV of JEM-EUSO will be continuously monitored by the infrared camera, which will also measure the altitude of the top of optically thick clouds. LIDAR will determine the detailed scattering and extinction properties of the atmosphere at the location of each triggered EAS event. Real-time models of the atmosphere are used to deduce the parameters relevant for the modeling of the transmission and extinction properties of the air, neeeded for the analysis of the LIDAR data, for the calibration of the infrared camera, and for the modeling of development of EAS in the atmosphere.
The peculiarity of the observation from space is the possibility of observing CR also in some cloudy conditions, which is tipically not the case for ground-based telescopes. In a simplified way, we can assume that if the maximum of the shower is above the cloud layer the reconstruction of the shower parameters will be possible. It is clear that the same top cloud layer will affect in a different way showers of various inclination or originating from the different type of primary particles (i.e. neutrino will develop much deeper in the atmosphere compared to EECR). Thin clouds ($\tau < 1$, typical of cirrus) will affect the energy estimation but the measurement of the arrival direction will still be possible with acceptable uncertainty. Thick clouds ($\tau > 1$) will compromise, or prevent, the measurement only if

located at high altitudes. As an example, 60° zenith-angle inclined showers will have the shower maximum at 6-7 km altitude, much higher than the typical range of stratus [10]. As the location of the clouds will affect either the duty cycle or the effective aperture of the instrument, and, consequently, the exposure, a detailed analysis of the probability of occurrence of the differect atmospheric conditions has been evaluated by means of different meteorological databases. The main reason is that each database has its own peculiarity, therefore, their comparison will allow to study the variability of the results and assess an uncertainty on the cloud distribution.

2 The meteorological databases

TOVS, ISCCP and CACOLO meteorological databases have been used in the following analysis. The NASA project TOVS (TIROS Operational Vertical Sounder) [11] on board NOAA's TIROS series of polar orbiting satellites consists of three instruments: a high-resolution infrared radiation sounder modification 2 (HIRS/2), a stratospheric sounding unit (SSU) and a microwave ounding unit (MSU). The three instruments have been designed to determine the radiance needed to calculate temperature and humidity profiles of the atmosphere from the surface to the stratosphere. These data have a good spectral distribution and provide optical depth and altitude of clouds. They are distributed irregularly and to obtain a complete data-set, the application of the transport radiative model has been necessary. In this study, data from January 1988 to December 1994 have been used, divided between land and ocean data.
The International Satellite Cloud Climatology Project (ISCCP) [12] was established in 1982 as part of the World Climate Research Program (WCRP) to collect and analyze satellite radiance measurements to infer the global distribution of clouds, their properties, and their diurnal, seasonal and interannual variations. Data collection is still on. The resulting data-sets and analysis products are being used to improve the understanding and the modeling of the role of clouds in climate, the primary focus being the elucidation of the effects of clouds on the radiation balance. These data can be also used to support a number of other cloud studies, including the understanding of the hydrological cycle. The data are collected from the suite of weather satellites operated by several nations and processed by groups in government agencies, laboratories, and universities. ISCCP has developed cloud detection schemes using visible and infrared window radiance (infrared during nighttime and daytime, while visible during daytime). The data from July 1983 to June 2008 have been used in this analysis. The data have the following characteristics: a) possibility to obtain monthly, seasonal and annual means; b) the cloud types are defined by the VIS/IR (visible/infrared) top pressure and optical depth and they are divided in 3 levels (low clouds with a top pressure greater than 680 mb, about 3.2 Km, high clouds with a top pressure minor than 440 mb, about 6.5 Km, and middle clouds with a pressure between the other types); c) no division between ocean data and land data; d) frequency of occurrence of cloudy conditions in individual satellite image pixels, each of which covers an area of about 4 to 49 square kilometers; e) data are given on a 2.5 degree square latitude-longitude grid, so we obtained a map divided in 10368 boxes (144 X 72 - longitude X latitude). As the data of this dataset can be extracted also on a monthly basis, they allow to reconstruct the interannual variability of cloud coverage for low, middle and high clouds.
The CACOLO (Climatc Atlas of Clouds Over Land and Ocean data) database [13] presents maps introduced in the atlases of cloud climatological data obtained from visual observations from Earth. The cloud averages presented on these maps have been extracted from a digital archive of gridded land and ocean cloud climatological data. Maps are given for total cloud cover, clear-sky frequency, and the average of nine cloud types within the low, middle, and high levels of the troposphere. The amount of cloud is defined as the fraction of the sky-hemisphere covered by the cloud. Maps of precipitation frequency are also included. Monthly, seasonal, and annual averages are given for both daytime and night-time. Land and ocean data have been analyzed separately, and are mapped separately for most quantities. Two grid sizes are used to display the cloud averages. Most data are given at 5-degree latitude-longitude resolution. A 10-degree grid is used to map some ocean data. The land data are based on analysis of 185 million visual cloud observations made at 5388 weather stations on continents and islands over a 26-year period (1971-1996). The ocean maps are based on analysis of 50 million cloud observations made from ships over a 44-year period (1954-1997).
In this sense CACOLO is a truly complementary database compared to the other two as the information is coming from ground observations instead from space.

3 Data analysis

A first study has been conducted in order to evaluate the differences between night-time and daytime, oceans and lands, using the TOVS data-set. Data have been used only in the range of latitudes 50N-50S since this is the range of latitudes spanned by the ISS. Clouds have been classified into 16 categories, according to their top altitude (h) (h <3 km, 3< h <7 km, 7< h <10 km, h > 10 km) and optical depth (OD) ($OD < 0.1$, $0.1 < OD < 1$, $1 < OD < 2$, $OD > 2$). Table 1 reports the results of the occurence of each cloud tipology for oceans during daytime. This configuration has been chosen as data taken during daytime are in general more reliable and the same applies to the ocean data compared to the land ones. The comparison between day and night has been performed then on lands as higher variations are expected on land surface compared to oceans. Slight differences among the tables exist, however, the general trend seems to be indepen-

Table 4: Distribution of the cloud properties (%) for 5 different geographical areas using ISCCP data. Data refer to daytime.

Sky condition	Geographical area									
	ocean					land				
	51.6-35N	35-15N	15N-15S	15-35S	35-51.6S	51.6-35N	35-15N	15N-15S	15-35S	35-51.6S
high clouds	23.5	18.9	27.8	17.2	20.1	26.1	19.4	33.5	24.2	28.1
middle clouds	24.2	12.4	12.1	13.6	24.2	22.0	12.4	14.8	11.8	18.9
low clouds	35.7	28.7	21.0	33.1	38.9	18.4	18.6	15.2	16.0	22.8
clear sky	16.6	40.0	39.1	36.1	16.8	33.5	49.6	36.5	48.0	30.2

Table 1: Relative occurrence (%) of clouds between 50°N and 50°S latitudes on TOVS database in the matrix of cloud-top altitude vs optical depth. Daytime and ocean data are used for the better accuracy of the measurement.

Optical Depth	Cloud-top altitude			
	<3km	3-7km	7-10km	>10km
>2	17.2	5.2	6.4	6.1
1-2	5.9	2.9	3.5	3.1
0.1-1	6.4	2.4	3.7	6.8
<0.1	29.2	<0.1	<0.1	1.2

dent from the geographical and temporal conditions. Table 2 shows the highest deviations from tab. 1 obtained in all possible combinations spanned with TOVS data (oceans, land, day, night). The results of tab. 1 can be classified

Table 2: Highest deviations from tab. 1 obtained in all possible combinations spanned with TOVS data (oceans, land, day, night)

Optical Depth	Cloud-top altitude			
	<3km	3-7km	7-10km	>10km
>2	-5.1	+1.6	-0.6	+2.7
1-2	-2.9	-0.2	+0.4	+0.3
0.1-1	-2.0	-0.8	-0.4	+0.3
<0.1	+7.6	+0.1	<0.1	+1.4

in the following way. OD<0.1 corresponds to clear sky and it accounts for $\sim$30%. Clouds below 3 km height do not hamper the measurements as the shower maximum will develop at higher altitudes, regardless of their OD and they account for another $\sim$30%, which gives a total of $\sim$60% of the time when the measurement is clearly possible. Thick (OD>1) and high (h>7km) will prevent the possibility of measurement, and they account for $\sim$19%. The remaining $\sim$21% will limit the measurement to very inclined showers (zenith angle >60°, which by the way correspond to the best category of data in terms of light intensity, angular accuracy and energy resolution - see [5]), or to the study of the arrival direction analysis, as the energy estimation will be worsened by the shower attenuation in atmosphere.

The study performed with TOVS data is important to have a first estimation of the uncertainty of the cloud distribution and its effects on shower-reconstruction capabilities, however, possible systematic effects of the technique employed in the TOVS measurement can not be inferred. For this reason, the same type of study has been applied to ISCCP and CACOLO data and results have been compared. As previously explained, the ISCCP and CACOLO data divide the clouds only in low, middle and high type, without distinguish according to their OD. In order to compare these data with the TOVS ones, the latter data were grouped only on the basis of their top altitude: clear sky, low clouds (h<3 km), middle clouds (3-7km), high clouds (h>7km). Tab. 3 shows the comparison between the 3 data sets in the case of lands and oceans during day-time. Results look

Table 3: Comparison among TOVS, ISCCP and CACOLO databases for the relative cloud occurence (%) in the different meteorological situations. Data refer to day-time, with a weighted average between oceans and lands.

Sky condition	Database		
	TOVS	ISCCP	CACOLO
high clouds	32.7	23.3	17.9
middle clouds	8.4	16.0	25.0
low clouds	28.4	26.0	40.4
clear sky	30.5	34.7	16.7

quite different at a first glance. However, if clear sky and low clouds are averaged together, they give almost similar results, with a minimum of 57.1% for CACOLO to a maximum of 60.7% in case of ISCCP. As a consequence also the sum of middle and high clouds gives similar results. More in detail, TOVS data seem to overestimate high clouds meanwhile CACOLO data tend to overestimate the low ones. This overestimation might be due to the fact that CACOLO data are taken by ship and weather stations in the visual band only (so they tend to underestimate high clouds, especially in presence of low and middle clouds), while TOVS data are taken by satellites (for a similar reason, the low and middle clouds tend to be underestimated, because 'masked' as high clouds). ISCCP data are a sort of average of the other two data sets, since they are taken from satellite in the visual and infrared bands and this fact facilitates to distinguish the various levels. In this sense, as the TOVS data provide the highest value for high clouds, the results presented before can be considered as a conservative estimation of the fraction of events that could be measured by JEM-EUSO.

Finally, ISCCP data have been used to check the dependence of the above mentioned results according to their geographical area. Data have been divided into 5 latitude layers, separating among equatorial area, tropics and middle latitudes. Results are provided in tab. 4. In general the combination of low clouds and clear sky is slight higher onto oceans, which by the way account for the higher fraction of time. High clouds are particularly frequent in the equatorial region. This is normal, as it is correlated also with the big storms occurring in that area.

4 Conclusions

Flying on the ISS, during its operation, JEM-EUSO will experience all possible weather conditions inside its field of view. In order to estimate the effective aperture of the detector, one key point is the evaluation of the role of clouds, in particular their frequency as a function of altitude and optical depth for the different geographical areas of the planet.

The probability of occurrence of a defined atmospheric condition has been assessed in this study by means of different meteorological databases: TOVS, ISCCP and CACOLO data. The peculiarity of the observation of cosmic rays from space is the fact that the presence of low clouds ($h < 3$ km) is de facto equivalent to clear-sky conditions as the shower maximum will be located at altitudes higher than the cloud top altitude. The results of the present analysis, which is based on visible and infrared data, indicate that showers will develop in the atmosphere in clear-sky conditions for at least $\sim$60% of the time. The results are marginally dependent on the database adopted in the analysis ($\sim$5%). A precise evaluation of the effective fraction of time in which shower observation will be possible as a function of the arrival direction of the primary cosmic rays and how this will impact on the exposure of the experiment is reported in [10].

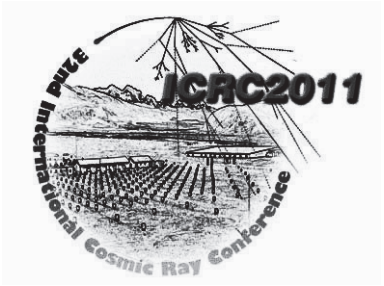
In the future we plan to extend the analysis by using other databases such as MERIS and CALIPSO. Furthermore, CALIPSO data will be used to assess the effects of the ISS orbital displacement on the inferred cloud structure along the effectively probed line of sight.

Acknowledgement: This work was partially supported by the Italian Ministry of Foreign Affairs, General Direction for the Cultural Promotion and Cooperation.

References

[1] Y. Takahashi, New Journal of Physics, Vol. 11, N. 065009, 2009.
[2] T. Ebisuzaki et al., This Conference Proceedings, #1628(2011).
[3] Y. Takizawa et al., This Conference Proceedings, #0852(2011).
[4] F. Kajino et al., This Conference Proceedings, #1216(2011).
[5] A. Santangelo et al., This Conference Proceedings, #0991(2011).
[6] A. Neronov et al., This Conference Proceedings, #0301(2011).
[7] J.A. Morales et al., This Conference Proceedings, #1031(2011).
[8] http://gmao.gsfc.nasa.gov/
[9] http://www.ecmwf.int/
[10] G. Saez et al., This Conference Proceedings, #1034(2011).
[11] http://www.ozonelayer.noaa.gov/action/tovs.htm/
[12] http://isccp.giss.nasa.gov/
[13] http://www.atmos.washington.edu/CloudMap/

32ND INTERNATIONAL COSMIC RAY CONFERENCE, BEIJING 2011



A study of different cloud detection methods for the JEM-EUSO atmospheric monitoring system

A. ANZALONE[1], M. BERTAINA[2], R. CREMONINI[2], M.D. FRÍAS RODRÍGUEZ[3], F. ISGRÓ[4] FOR THE JEM-EUSO COLLABORATION
[1]*INAF-IASF, Palermo, Italy*
[2]*Dipartimento di Fisica, Universitá degli Studi di Torino, Italy*
[3]*SPACE & AStroparticle (SPAS) Group, UAH, Madrid, Spain*
[4]*Dipartimento di Scienze Fisiche, Universitá degli Studi di Napoli Federico II, Italy*
anna.anzalone@ifc.inaf.it

Abstract: The observation of the atmosphere is a crucial task for the JEM-EUSO mission, and a module for the atmospheric monitoring is included in the design of the whole system. In this paper the retrieval of cloud coverage in the field of view of the telescope is addressed considering both radiative methods commonly used in the meteorological field and methods of image analysis, with the aim of studying the feasibility of these approaches to the data that the JEM-EUSO infra red camera will provide. The complementarity of the two approaches will be further investigated, together with a different set of techniques, to contribute to achieve the best cloud estimation in JEM-EUSO.

Keywords: JEM-EUSO experiment, atmospheric monitoring system, cloud detection, cloud height.

1 Introduction

The strength of the fluorescent light and the Cherenkov signal received from EAS, as well as the reconstruction efficiency and errors, depend on the transparency of the atmosphere, the cloud coverage and the height of the cloud top. A crucial task for the success of the JEM-EUSO mission [1] is to observe the conditions of the atmosphere in the field of view of the telescope. To this end a dedicated atmospheric monitoring (AM) system [2] is being designed. The system includes an infrared camera, that will be used to estimate cloudiness and height maps in the field of view of the telescope.

This paper reports on current work to identify optimal cloud detection algorithms from infrared data, that will be implemented into the JEM-EUSO observing system for accurate estimations of cosmic-ray energy. To this end here we revise the performance of different methods for cloud detection: threshold algorithms, radiative, and methods exploiting image analysis techniques. The experiments are run on scenes under different conditions, retrieved by operational atmospheric sensors similar to the JEM-EUSO atmospheric monitoring system.

2 Radiative methods

Geostationary (i.e. GOES, MSG) and LEO satellites (i..e. Terra/Aqua, HIRS) provide multi-spectral observations with good spatial and temporal resolution. CALIPSO mission combines an active lidar instrument with passive infrared and visible images to probe the vertical structure and properties of thin clouds and aerosols over the globe. The cloud mask (CMa) allows the identification of cloud free areas where other products (total or layer precipitable water, stability analysis imagery, snow/ice cover delineation) may be computed. The main aim of the CMa is therefore to delineate all cloud-free pixels in a satellite scene with a high confidence. In addition, the typical CMa product provides information on the presence of snow/sea ice, dust clouds and volcanic plumes. SEVIRI is a multi-band sensors operating on MSG satellite series by EUMETSAT [12]: starting from SERIVI radiance observations, it has been developed an algorithm for identifying cloud presence and cloud contamination. The algorithm is based on several and differential band threshold tests, using only infra red bands as JEM-EUSO work during nighttime: some difference band tests are specific for thin cirrus detection. Thresholds depend on pixel background (land, water and coast) and on Numerical Weather Prediction (NWP) model temperature at surface and at standard levels. Starting from four categories

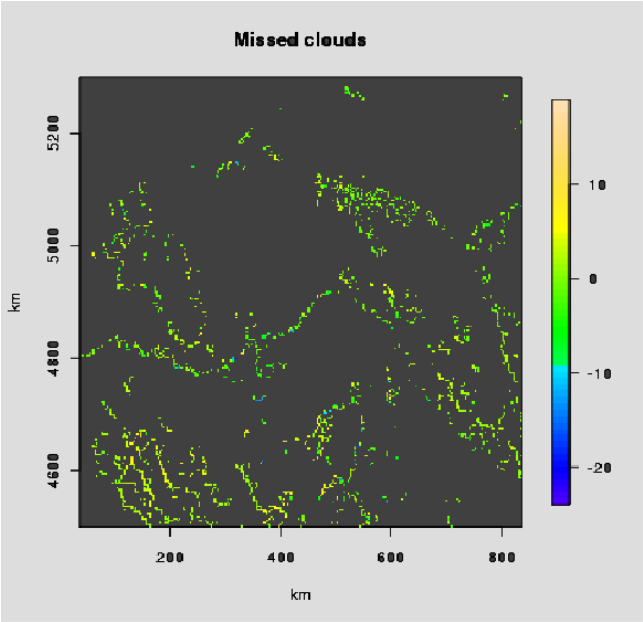


Figure 1: Single IR band cloud detection respect all IR channel CMa

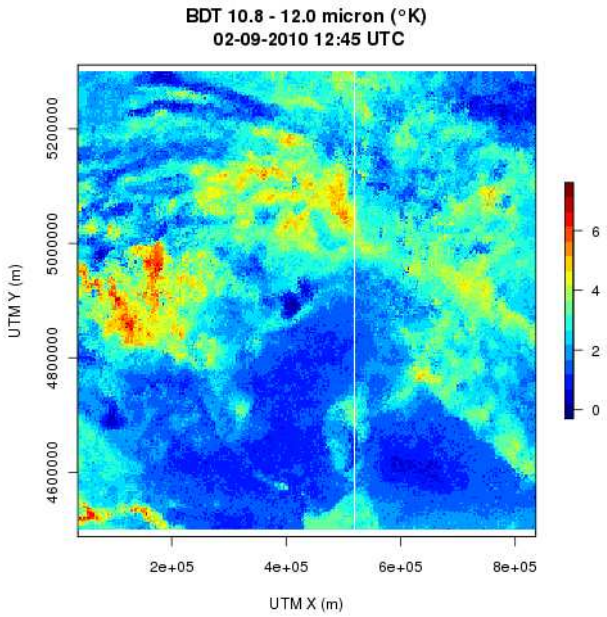


Figure 2: Band difference from SEVIRI for 10.8 μm and 12.0 μm at 12:45 on 2th sept 2010

of tests a probability of clear sky is defined as follow:

$$cloud\,sky\,probability =^3 \sqrt{P_{ir} \cdot P_{thin} \cdot P_{diff-ir}}$$

Where P_{ir} test is the probability that for a given band/threshold the pixel is cloudy or cloud contaminated; P_{thin} and $P_{diff-ir}$ have the same meaning but for band differences and thin cirrus specific tests. As JEM-EUSO will work with at least with a two band infrared camera, the tests performed on SEVIRI have been limited to 10.8 and 12.0 μm bands. Single infrared algorithm can detect only thick and extended clouds, with better performance during summer and over warm sea due to high thermal contrast [10].

Figure 1 shows undetected clouds when only 10.8 μm IR band is used: major problems occur near coastal borderline, with thin cirrus and at border of cloud desk, where pixels and not fulfilled. Well-known split window channels are essential to detect thin cirrus or broken clouds and to estimate Earth's surface and cloud top temperatures. The 12.0 μm band is more sensitive for high thin cirrus but it is not easy to recognise through visual inspection, while it is highlighted by band difference [11].

Figure 2 shows the difference between Brightness Temperature (BT) at 10.8 μm and 12.0 μm at 12:45 on 2th sept 2010: BT differences greater than $3°K$ distinguish between semi-transparent thin clouds and thick ones.

3 Image analysis methods

The methods discussed in this Section exploit the image content of the infrared data, not considering its physical meaning. That is that the content of a pixel is regarded as a colour information only, and not as related to the temperature.

In this Section we consider two different methods: a supervised image segmentation algorithm, and a second method that follows a geometric approach.

3.1 Feature based method

In this method the classification of the cloudy pixels is performed using a state of the art machine learning tool: a Support Vector Machine (SVM) [6], for which we chose a Gaussian kernel. In particular we use a public available implementation of the SVM [5].

The classification using SVM is a supervised method, and it needs a training set of data. This means that a relatively large number of pixels must be manually labelled. A simple graphical interface has been created to facilitate this task.

The classification is not performed in the gray-level space, but each image pixel is mapped into a higher dimensional space, that is usually called feature space. In our case the feature vector associated to each pixel (i,j) is

$$\mathbf{f_{i,j}} = (v, \mu, \sigma, D_x, D_y, h_1, h_2, h_3, h_4, h_5, h_6, h_7, h_8)$$

where v is the gray-level of pixel (i,j), μ and σ are mean and standard deviation respectively in a 5×5 neighbourhood centred in the pixel, D_x and D_y are the gradient

components, and h_1 to h_8 are the entities of the eight-bin histogram of the 5×5 neighbourhood in the image.

The classifier has been tested on more than 2000 images from different sensors. The training set includes 610 points belonging to both *cloud* and *not-cloud* classes, manually selected from the first 1000 frames of the image set. From the remainder of the sequence we selected further 609 points that have been used as test set for evaluating the performance of the classifier. As it can be seen from the ROC curve shown in Figure 3 the performances are particularly good, since the test set is temporally close to the training set. We are planning to use more data for a better evaluation.

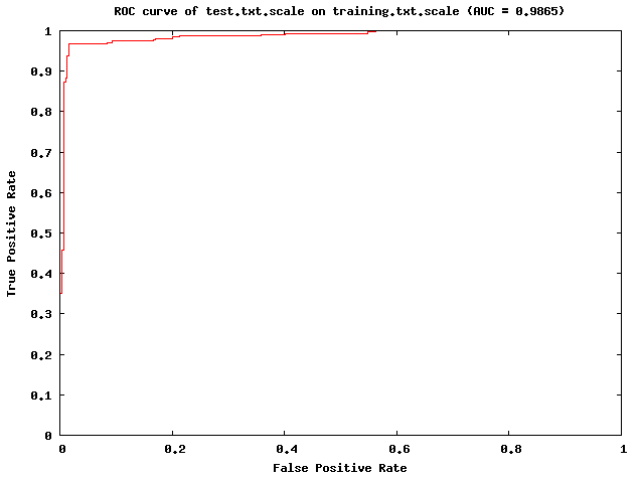


Figure 3: ROC curve for the SVM classifier.

3.2 Stereo based method

In this section the possibility of retrieving maps of cloudiness from maps of heights is presented supposing that stereo acquisition was enabled by the use of the infra red camera. Using stereo methods, the depth of the imaged points can be recovered from two, or more, images, in this way, in presence of clouds, the cloud-top height (CTH) can be recovered [8, 7, 4]. Stereo could be achieved in JEM-EUSO exploiting the ISS movement. While the ISS flies along its orbit, the IR camera acquires an image of the FoV at every fixed time interval.

Exploiting this information, and the fact that the images can be geo-located, we can mark as clouds all those pixels for which the recovered height is higher than the altitude of the corresponding ground.

We analyse the feasibility of this method studying the theoretical reconstruction error for the depth, as a large error in reconstruction may lead, especially for lower clouds, to mis-classification.

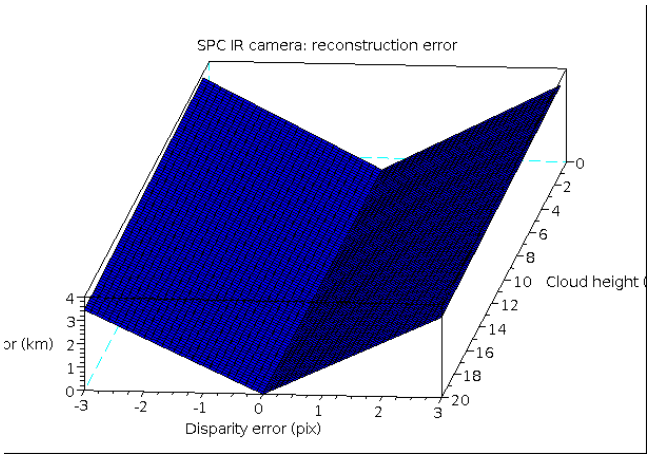


Figure 4: Plot of the CTH estimate error against the disparity error and the true CTH. ISS station altitude at 430 Km.

The depth Z of a point can be obtained by triangulation as

$$\hat{Z} = \frac{b}{\hat{d}_x}$$

where b is the baseline of the stereo system (the distance covered by the ISS between the two views), and $\hat{d}_x$ is the estimated disparity [9]. If d_x and Z are the true disparity and the true depth respectively we have that

$$\hat{d}_x = d_x + \delta x$$

and

$$Z = \frac{b}{d_x}$$

We can write the depth error δZ as a function of δx by Taylor expansion as

$$\delta Z = \frac{b}{d_x^2}\delta x = \frac{Z^2}{b}\delta x$$

which shows that for a fixed baseline b and δx then the error in the depth measurement rises as the square of distance from the camera. Therefore we need a large baseline b to get a good depth resolution, but also we can expect a poor depth resolution for distant objects.

The error function is plotted in Figure 4. For this simulation we used the specs for the infrared camera given in Table 1, the altitude of the sensor fixed at 430 Km, and a time interval between the two images of 32 sec, which ensures a 50% overlap.

From the analysis of the results of the simulations we can conclude that we have an accuracy within 500 meters with a disparity error of 0.5 pixels, that can be achieved for most pixels with a good matching strategy. With higher disparity error, say 1-2 pixels, we have an error in the depth estimation that is within 2 Km.

	FoV	IFoV	Pixel resolution	Number of of pixels	Focal length	Pixel pitch
	$60°$	$0.1°$		640×480	15 mm	20μm
ISS_h=350 Km			$\simeq 0.58$ Km			
ISS_h=430 Km			$\simeq 0.72$ Km			

Table 1: Specification for the IR camera used for this experiment

4 Conclusions

Radiative and image methods for cloud detection and cloud height estimation have been preliminary considered as candidates for JEM-EUSO atmospheric monitoring system. While performance of radiative methods depend on IR camera thermal resolution and available bands - especially when the scene is thin cirrus contaminated - the image methods described in this contribution depend on spatial angular resolution of the sensors, and on the quality of the features or on the quality of the matching. Both radiative and image methods need to be deeper investigated and moreover other well known techniques and features in image analysis will be investigated. Radiative and image approaches can be considered as complementary, an their integration to best achieve cloud coverage estimation for JEM-EUSO will be considered.

References

[1] T. Ebisuzaki et al.: 2011, The JEM-EUSO mission, 32nd ICRC (ID1628)

[2] A. Neronov et. al: 2011, Atmospheric Monitoring System of JEM-EUSO, 32nd ICRC (ID301)

[3] J.A. Morales et. al.: 2011, The IR-Camera of the JEM-EUSO (JAXA) Space Observatory, 32nd ICRC (ID1031)

[4] Anzalone A. et al.: 2004, Proceedings of MDIC04, 75-86

[5] Chih-Chung Chang et al.: LIBSVM:a library for support vector machines, 2001 http://www.csie.ntu.edu.tw/˜cjlin/libsvm

[6] Shawe-Taylor J. et al.: 2000, Support Vector Machines and other kernel-based learning methods. Cambridge University Press

[7] J.P. Muller et al.: 2007, Journal of Applied Meteorology and Climatology, International Journal of Remote Sensing, **28**(9), 1921-1938

[8] G. Seiz et al: 2006, Journal of Applied Meteorology and Climatology, 2006, **46**, 1182-1195

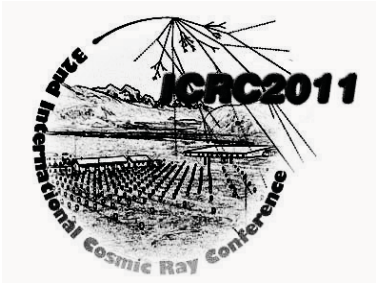
[9] E. Trucco and A. Verri: 1998, Introductory Techniques for 3-D Computer Vision, Prentice Hall

[10] Stanley Q., Kidder and Thomas H. Vonder Haar., San Diego, CA: Academic Press, **1995**.

[11] Krebs, W. Mannstein, H., Bugliaro, L., and Mayer, B., Atmos. Chem. Phys., 2007, **Volume**(7): 6145,6159

[12] Schmid, J., **1999**, available at www.eumetsat.int/groups/ops/documents/document/pdf_ten_msg_seviri_instrument.pdfhttp://www.eu

32ND INTERNATIONAL COSMIC RAY CONFERENCE, BEIJING 2011



Estimation of JEM-EUSO experiment duty cycle based on Universitetsky Tatiana measurements

BOBIK P.[1], GARIPOV G.[2], KHRENOV B.[2], KLIMOV P.[2], MOROZENKO V.[2], SHINOZAKI K.[3], BERTAINA M.[4], SANTANGELO A.[5], KUDELA K.[1], PASTIRCAK B.[1], URBAR J.[6] FOR THE JEM-EUSO COLLABORATION
[1]*Institute of Experimental Physics SAS, Slovakia*
[2]*Skobeltsyn Institute of Nuclear Physics, Moscow State University, Russia*
[3]*RIKEN Advanced Science Institute, Japan*
[4]*Dipartimento di Fisica Generale, Università di Torino, Italy*
[5]*Institute fuer Astronomie und Astrophysik Kepler Center for Astro and Particle Physics, Eberhard Karls University Tuebingen, Germany*
[6]*Department of Surface and Plasma Science, Charles University, Czech Republic*
bobik@saske.sk

Abstract: JEM-EUSO experiment will search for UV light produced by UHECR interaction with atmosphere from International Space Station. We have estimated a duty cycle for JEM-EUSO experiment from UV light measurements provided by Universitetsky Tatiana satellite. The duty cycle and stability of UV light signal during measurements are presented. An alternative method based on the real ISS trajectory and the analytical evaluation of UV moonlight intensity for the estimation of JEM-EUSO duty cycle is also presented.

Keywords: JEM-EUSO, nightglow, UV background light, UHECR.

1 Introduction

1.1 JEM-EUSO duty cycle

The JEM-EUSO experiment [1] will search for UV light produced in interactions of ultra high energy cosmic rays (UHECR) with atmosphere on the Earth's night side. The duty cycle of JEM-EUSO detector on low earth orbit was estimated some years ago from the calculations [2,3] based on ISS trajectory simulation and moonlight intensity simulations along this trajectory. ISS trajectory was simulated for one year long period with minute time-steps. The moonlight was estimated from the Moon position and phase at evaluated positions. The duty cycle was evaluated as a time during the night when UV intensity from moon light was less than the selected value. This approach do not take into account another sources of UV light on the Earth night side (i.e. zodiacal light, integrated faint star light) and partly also changes in ISS trajectory due to loosing altitude because of a slight atmospheric drag and the following boosts to higher altitude of ISS occurring from time to time. To take into account another sources of UV light and their influence to the duty cycle estimation of JEM-EUSO experiment we have used an Universitetsky Tatiana [4,5,6] data from the measurements in the period from 2005 till 2007. To estimate an effect of the real ISS trajectory we have used the data from [7] and the moonlight simulation along the real trajectory.

1.2 Universitetsky Tatiana satellite

The Universitetsky Tatiana was a satellite of Moscow State University launched on 20th January 2005 from the Plesetsk spaceport in RF, measuring near UV (310-400nm) light on the orbit with the inclination of 82^o and the altitude 950 km [4,5,6]. The detector field of view (15^o) corresponds to observing atmospheric surface of 250km in diameter. Satellite was operational until March 2007.

2 Method and Results

2.1 JEM-EUSO duty cycle simulation for ISS orbit

ISS trajectory was provided by NASA SSCweb [7]. For every position of ISS during the period of Universitetsky

Tatiana measurements we have evaluated a position of the Sun (solar zenith angle) and Moon (Moon phase and lunar zenith angle) and calculated the UV moonlight intensity I_{Moon} (θ, α) at low orbit in the range 300-400 nm by formula (1) from [3].

$$I_{Moon}(\theta,\alpha) \approx 1.55\times10^{4} \times \cos\theta \times \\ \times 10^{-0.4(1.5|\alpha|+4.3\times10^{-2}\alpha^{4})}\ ph/(m^{2}.ns.sr) \quad (1)$$

Where θ is lunar zenith angle and α is Moon phase. For the night defined by solar zenith angle bigger than 109.18° we have evaluated the duty cycle for a set of moonlight induced background values. The results are presented in figure 1.

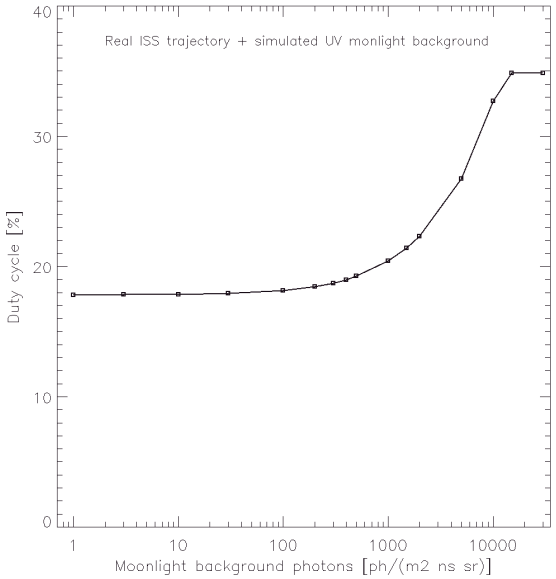


Figure 1. Duty cycle evaluated from real ISS trajectory in years 2005 till 2007 and simulated moonlight BG light.

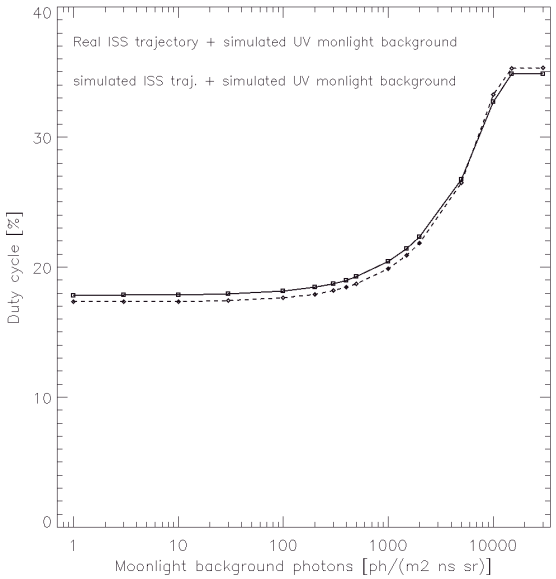


Figure 2. Duty cycle evaluated from real ISS trajectory (solid line) in comparison with simulated ISS on Keplerian orbit (dashed line).

It is possible to simulate the ISS trajectory by several ways. The simulation with a simple Keplerian orbit with an inclination of ISS trajectory gives the results similar to those evaluated with real ISS trajectory. Figure 2 shows the comparison between duty cycle for simulated and real ISS trajectory. Figure 3. show radius of in this article so called real ISS trajectory [7].

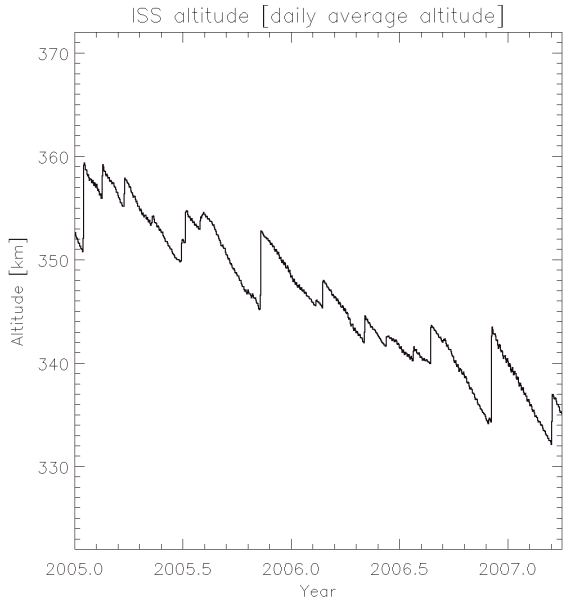


Figure 3. ISS altitude in 2005 till 2007. Boosts to higher altitudes.

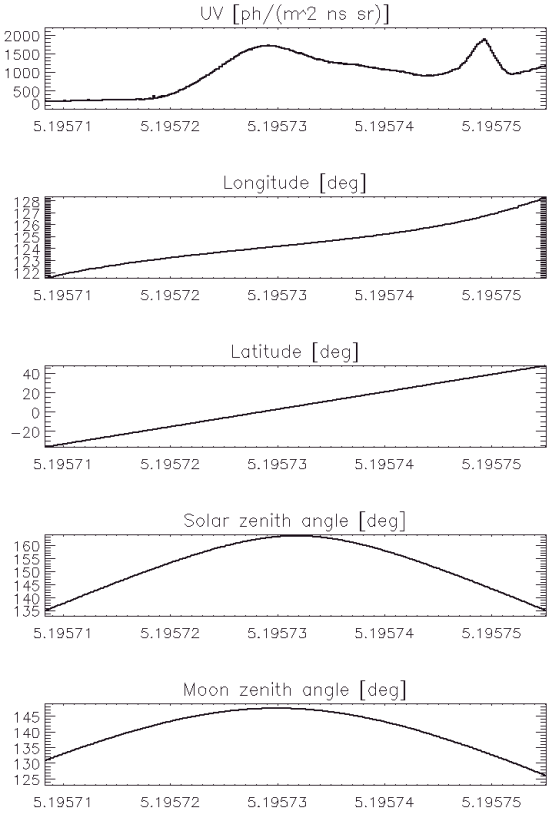


Figure 4. Example of Universitetsky Tatiana measurement. 24 minutes measurement starting at 14:34:44 11. march 2005. Time on figure in year units.

2.2 Tatiana duty cycle evaluation

We have evaluated a Sun position and Moon position for every Tatiana satellite measurement. We have used an integrated 4 second UV intensity data. Example of Uniersitetsky Tatiana measurements is presented on the figure 4. For the analysis we have used a data in latitudinal range of ISS trajectory i.e. (-51,6°, 51,6°). We have selected only the night-time measurements. . As the night for Tatiana orbit we consider simple cut on the zenith angle [3] by solar zenith angle higher than 119.5°. We apply the correction for UV intensity on Tatiana orbit to ISS orbit (~16.89% - the precise value depends on the exact Tatiana altitude) and the correction taking into account the difference between night definition for Tatiana orbit and ISS orbit. Figure 5 shows a duty cycle evaluated from Tatiana data corrected to ISS orbit together with duty cycle evaluated for real ISS trajectory and simulated moonlight (see the previous part of the article). The comparison shows the effects of other sources of UV background light to the duty cycle of the detector. For lower intensities of UV light limits i.e. under 1500 photons/(m^2 ns sr), other sources of UV light play significant role during moonless nights, that lead to decreasing duty cycle for lower allowed UV background thresholds.

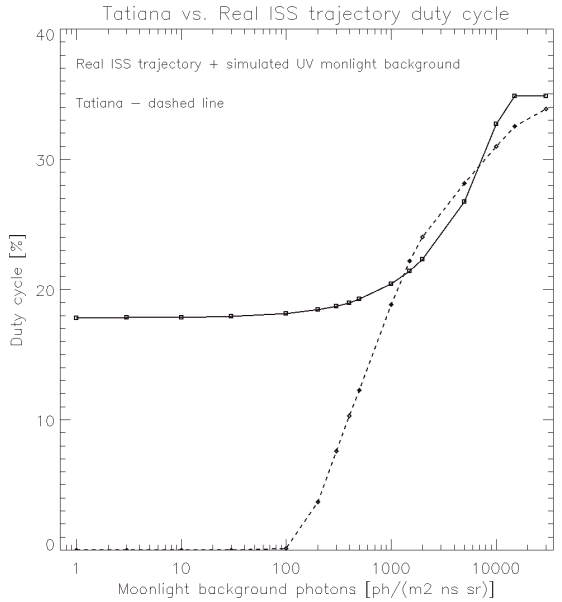


Figure 5. Duty cycle evaluated from real ISS trajectory (solid line) in comparison with duty cycle from Tatiana data (dashed line).

2.3 Night definition for JEM-EUSO duty cycle

The night definition by simple cut on the zenith angle could not be very precise approximation for JEM- EUSO measurements. It is possible that we will need to redefine night by shifting the Sun position 19.18° under horizon as used in this article to a higher value. We have estimated a JEM-EUSO duty cycle for a set of solar zenith angles for allowed background of UV intensity less than 1500 photons/(m^2 ns sr). The estimation from Tatiana measurements is presented in Table 1. The change of solar zenith angle limit from 108° to 120° degrees decreases the JEM-EUSO duty cycle by about 3.8%.

Solar zenith angle (deg.)	Duty cycle (%)
108	22.2
109	22.1
110	21.9
111	21.7
112	21.5
113	21.3
114	21.0
115	20.6
116	20.3
117	19.9
118	19.5
119	19.0
120	18.4

Table 1. The change of duty cycle with different night definition i.e. with different solar zenith angle threshold.

2.4 Time stability of UV background light

We evaluate average length $T_{AVG,Sza}$ of one continuous measurement during Tatiana operation period for different Sun zenith angles thresholds. Average length $T_{AVG,Sza}$ on the night Earth side is roughly 10 minutes and decrease with increasing solar zenith angle threshold.

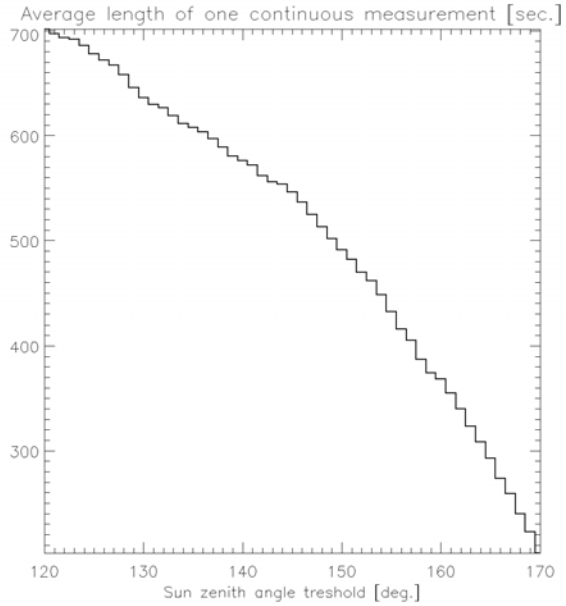


Figure 6. Average length of one continous Tatiana measurement as function solar zenith angle treshold.

The average length of measurements when UV intensity not change more than preselected percentage level we

evaluate for plusminus 10, 20, 30 and 40% as function of Sza threshold. Results are presented on figure 7.

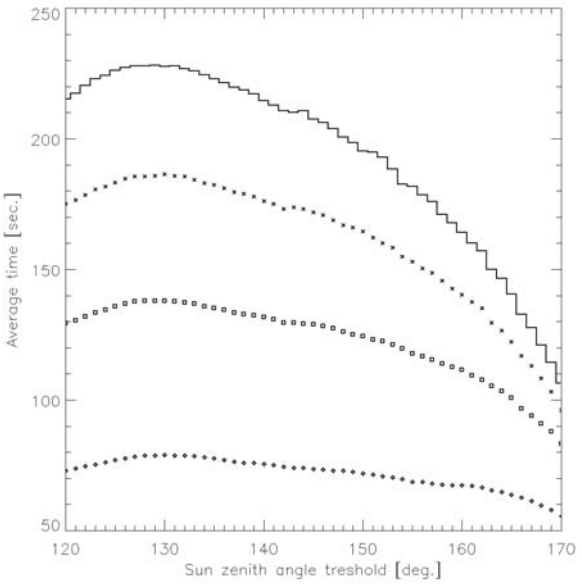


Figure 7. Average length of measurement when UV signal not change more than ±10% (diamonds), not more than ±20% (squares), ±30% (crosses) and ±40% (solid line).

Summary

We have estimated a duty cycle for JEM-EUSO detector at ISS orbit from Universitetsky Tatiana measurements for the set of allowed UV background thresholds. For the allowed background less than 1500 photons/(m^2 ns sr) we have got the duty cycle as 22% for the operational time of experiment. The influence of different night definitions to the duty cycle was presented. Alternative estimations based on simulation of ISS trajectory together with evaluation of amount of moonlight reaching ISS orbit leads for 1500 photons/(m^2 ns sr) to similar values of duty cycle. Difference between the real ISS trajectory and previously used trajectory simulations do not change the estimated values of duty cycle significantly. A more conservative estimation of the duty cycle which includes further cut on the Sun location lowers the duty cycle to 18.4%. This result is in agreement with the value assumed so far by the collaboration (19%).

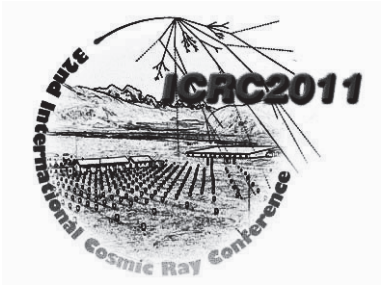
Acknowledgements

This work was supported by Slovak Academy of Sciences MVTS JEM-EUSO.

References

[1] Y Takahashi, the JEM-EUSO Collaboration, New Journal of Physics, 2009, **Volume 11**: page 065009
[2] C Berat, D Lebrun, F Montanet, J Adams, Proceedings of the 28th International Cosmic Ray Conference, 2003, page 927
[3] F Montanet, EUSO-SIM-REP-009-1.2, 2004
[4] G K Garipov, B A Khrenov, M I Panasyuk, V I Tulupov, A V Shirokov, I V Yashin, H Salazar, Astroparticle Physics, 2005, **Volume 24** (4-5): page 400-4008
[5] G K Garipov, M I Panasyuk, V I Tulupov, B A Khrenov, A V Shirokov, I V Yashin, H Salazar, Journal of Experimental and Theoretical Physics Letters, 2005, **Volume 82** (4): page 185-187
[6] V A Sadovnichy et. al., Cosmic Research, 2007, **Volume 45** (4): page 273-286
[7] NASA SSCweb, http://sscweb.gsfc.nasa.gov/cgi-bin/sscweb/Locator.cgi

32ND INTERNATIONAL COSMIC RAY CONFERENCE, BEIJING 2011



Observation of Ultra-High Energy Cosmic Rays in cloudy conditions by the JEM-EUSO Space Observatory

G. SÁEZ CANO[1], J. A. MORALES DE LOS RÍOS[1], K. SHINOZAKI[2,1], F. FENU[3], H. PRIETO[1], N. PACHECO GÓMEZ[4], J. HERNÁNDEZ[1], L. DEL PERAL[1], A. SANTANGELO[3] & M. D. RODRÍGUEZ FRÍAS[1] FOR THE JEM-EUSO COLLABORATION

[1]*SPace & AStroparticle (SPAS) Group, University of Alcalá, Madrid. Spain.*
[2]*RIKEN, 2-1 Hirosawa, Wako 351-0198, Japan.*
[3]*Institut für Astronomie und Astrophysik, Eberhard-Karls Universität Tübingen, Tübingen, Germany.*
[4]*Instituto de Física Teórica (IFT), Universidad Autónoma de Madrid, Spain.*
lupe.saez@uah.es

Abstract: Source of Ultra-high Energy Cosmic Rays (several times 10^{19} eV) are still unidentified. Overcoming their extremely small fluxes, a detector with huge observation areas is needed to investigate the energy and arrival direction distribution of EECRs. JEM-EUSO is a unique experiment that will be located in the International Space Station to observe extensive air showers (EAS) by monitoring night part of Earth atmosphere. In addition to clear sky condition, the extensive air showers in cloudy condition are also observable by taking advantage of the certain fraction of EAS develop above the cloud. In the preset work, using Monte Carlo simultions for test clouds, the cloud impact to the trigger efficiency was estimated taking into account the statistics of cloud property.

Keywords: JEM-EUSO, Ultra-High Energy Cosmic Rays, Extensive Air Shower simulation

1 Introduction

Cosmic rays origin is not identified, specially for Ultra-High Energy Cosmic Rays (UHECRs), despite of the limited numbers of astrophysical objects that can accelerate particles to such energies [1]. Properties of the primary UHECR can be measured by the observation of Extensive Air Showers (EAS). These EAS are developed when cosmic rays come through the atmosphere. The primary energy is shared among secondary particles. Most of them are electrons which carry about 90% of the primary energy. These electrons excite nitrogen molecules in the atmosphere that results in fluorescence light through the de-excitation of the molecules. Also Cherenkov component is produced, due to the relativistic velocity of the particles. These components have been measured by ground-based ultra-violet (UV) telescopes. However, with a steep power-law energy spectrum and possible Greisen-Zatsepin-Kuzmin effect, UHECR flux at highest energy (above $\sim 5 \times 10^{19}$ eV) [2, 3] is such small, that their origin cannot be investigated by these ground-based experiments.

JEM-EUSO (Extreme Universe Space Observatory on Japanese Experiment Module) is a new type, space-based experiment that will be launched in 2017, aiming to identify origin sources by detecting UHECRs at large statistics [4, 5]. JEM-EUSO telescope will cover a much larger area than ground-based experiments with a wide field of view (FoV) of 60°. From the orbit on the International Space Station (ISS) an altitude of ~ 400 km, it will search the Earth's atmosphere as a detector for light produced by EAS. In order to determine the energy and arrival direction of the primary particle as well as its composition, the light profile is needed to be measured. This profile depends on atmospheric conditions, such as absorption and scattering. The atmosphere is also the source of UV background such as subsistence airglow and transient luminous events, artificial sources, etc. Therefore, JEM-EUSO will need a dynamical trigger system capable of continuously adapting the triggering requirements [6, 7]. Furthermore, the FoV of JEM-EUSO varies as ISS orbits with sub-satellite speed of ~ 7 km/s and therefore presence and properties of clouds change significantly. To acquire such information, LIDAR (LIght Detection And Ranging) device and an infrared (IR) camera will be installed on JEM-EUSO [8, 9]. The former will measure transmittance as a function of the altitude and the latter will be accommodated to obtain cloud coverage overview and cloud-top altitude (H_C) in JEM-EUSO's FoV that provide data for evaluate exposure of the observation.

In this paper, the impact to the trigger aperture was investigated by Monte Carlo simulation taking into account cloud conditions. The presence of the clouds may affect vary-

ing by their altitude and optical depth τ. The effect due to clouds may also depend on the fraction of EAS develops above the typical altitude of cloud over the orbit. Effectively observing such EAS events helps increase the statistics of UHECR events. As conclusion, the cloud impact to the exposure will be presented.

2 Simulations

In this work, ESAF (Euso Simulation and Analysis Framework) [10] was used. It is a software framework to simulate space-based cosmic observations, including showers generation, emission and transport of photons, ray trace of optics, photodetector response and telemetry, as well as reconstruction. Key parts of ESAF were developed in EUSO project [11] and nowadays, it is adapted and optimized for JEM-EUSO instrument [12].

In the ESAF, EAS event is generated along with fluorescence and Cherenkov photons emission and their propagation in the atmosphere. In present work, fluorescence yield, one of uncertainty in energy scale, is assumed by the measurement of Reference [13] from the available options. Even in case of clear sky condition, UV photon propagation through atmosphere severely involves Rayleigh scattering and absorption by ozone in shorter wavelengths ($\sim$ 320 nm). The transmittance of these processes are modeled by LOWTRAN package [14].

In consideration of the effect of photon scattering in clouds which consists of droplet below ~ 8 km altitude, Mie scattering is more dominant since the scattering particle size well larger than wavelength. Scattering can be considered as independent of wavelength range of our interest (300-450 nm). The same behavior is observed for cirrus, made of ice crystals [15]. In the software, analytical formulation of scattering process including phase function is modeled and implemented in ESAF [10].

To include clouds in ESAF, there are two different options in its atmospheric model: with TOVS (TIROS Operational Vertical Sounder) database [16] including τ and H_C or as a uniform and homogeneous layer. The database was analysed to understand the global distribution of clouds within the range of the JEM-EUSO orbit and was analyzed in [19]. For the last option, physical parameters considered for the cloud layer are the optical depth τ, that yields transparency by $\exp(-\tau)$, the top altitude of the cloud and its physical thickness. For our study, the latter option was chosen for the discrete test values in τ and H_C.

3 Results

3.1 Shower simulation in cloudy conditions

In Figure 1, light curves (arrival time distribution of photons to the telescope pupil) of typical EAS events with zenith angle of 60° are shown for cirrus- (top panel) and stratus- like test clouds (bottom). Note that the horizontal axis is in unit of GTU (gate time unit = 2.5 μs. In each panel dark most shaded histogram denotes the total number of photons. Other histograms indicate the different components of scattered Cherenkov photons in atmosphere of from cloud or Earth's surface . For comparison, light curve for clear sky for EAS at similar energy is drawn (dashed histogram).

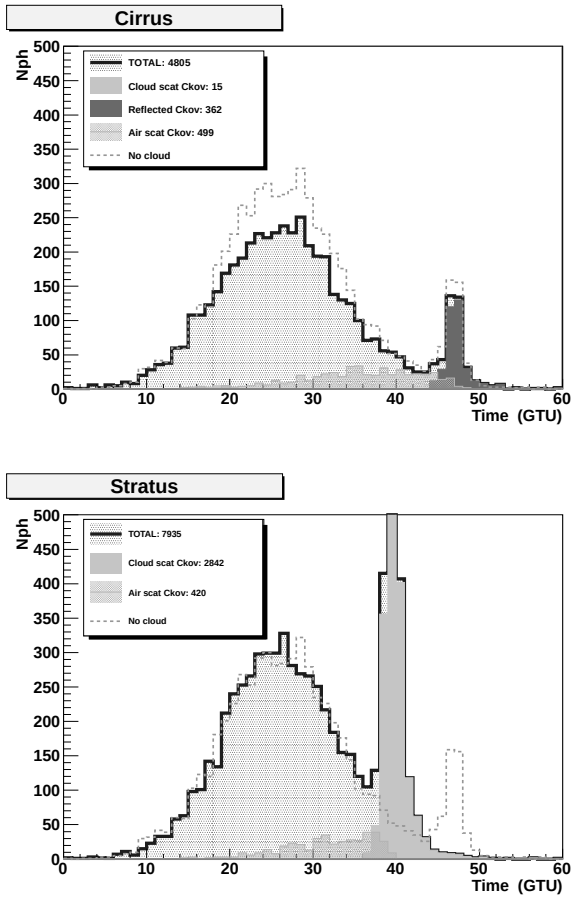


Figure 1: Light curve (arrival time distribution of photons to the telescope pupil) of typical EAS events. Note that the horizontal axis is in unit of GTU (gate time unit) corresponding 2.5 μs. Top and bottom panels correspond to the cases of cirrus- and stratus- like test clouds, respectively. In each panel, dark most shaded histogram denotes the total number of photons. Other histograms indicates the different components of Cherenkov photons. For comparison, light curve for clear sky for EAS at similar energy is drawn (dashed histogram).

For cirrus-like cloud at lower altitudes, signals from EAS are attenuated according to the optical depth, while the shower image and its time evolution will allow the arrival direction analysis. The scattered signals of Cherenkov from the ground is also observed.

For stratus-like clouds with large τ at lower altitudes, most of signals from EAS are observed without attenuation when the altitude of the cloud is well below the altitude of EAS

development. Such clouds also produce a very intense reflected Cherenkov signals and the detected signal is even larger, due to higher albedo of clouds, than that for the clear sky case. This may enhance the better capability of triggering for particular case such as low zenith angle event. It is more pronounced in reconstruction of the EAS geometry since the location of the impact on the cloud is more accurately determined.

3.2 Trigger efficiency in cloudy conditions

In order to evaluate the impact of clouds in FoV into trigger efficiency, shower simulations for different cloudy cases were made. To characterize the test cloud property, four altitudes have been considered (H_C = 2.5 km, 5 km, 7.5 km and 10 km), as well as four optical depths (τ= 0.05, 0.5, 1.5 and 5). For each of the sixteen cases, incident angles from 0° to 90° and energies of the primary particles (protons) with energies of $\log E = 19.5$ to 21 have been considered. For comparison, simulation for clear sky case was also made.

In this paper, 'trigger efficiency' $\epsilon(E)$ is referred to the ratio to the trigger aperture at energy E in comparison to the nominal semi-saturated aperture. The semi-saturated aperture is meant to be the product of solid angle (π for $\theta = 0° - 90°$) and observation area determined by the result of the optical ray trace simulations [17, 18]. Note that the efficiency can be slightly higher than 1 since some EAS that cross a part of FOV may trigger. To quantitatively estimate the effect of clouds, we first calculate the ratio ϵ of given cloudy condition to that of clear sky case. The ratio, to be called 'cloud impact' hereafter that represents the ratio of the number of events in comparison to the one expected for clear sky condition. For a given cloud condition (H_0, τ), the average cloud impact $\epsilon(E; H_0, \tau)/\epsilon(E; \mathrm{clear})$ is defined taking into account the assumed UHECR flux.

In Table 1, the average cloud impacts are summarized for the different tested clouds with different energy thresholds of 5×10^{19} (top) and 7×10^{19} eV (bottom) with an assumed differential spectrum of $dN/dE \propto E^{-3}$.

In case of optically thick clouds with $\tau \geq 1$, the presence of clouds affect the trigger efficiency depending on H_C. Especially high-altitude clouds absorb EAS signals emitted beneath the cloud that significantly result in lowering the trigger efficiency. In the middle altitudes such as ~ 5 km, the influence of the clouds are limited to EAS from lower zenith angles, which develop even lower altitudes.

In the presence of similarly high clouds but with $\tau < 1$, signal from EAS below such clouds is only attenuated by a factor of $\exp(-\tau)$ and the effect to the trigger efficiency is limited.

If H_C is well below the altitudes where EAS develops, the clouds do not attenuate the EAS signals.

Comparing different energy thresholds, the difference of the cloud impact slowly increases with energy, while it stays marginal in the energy of interest.

Table 1: Average cloud impact for different types of clouds for energy ranges above 5×10^{19} eV (top) and 7×10^{19} eV eV (bottom). In each case, a differential spectrum of $dN/dE \propto E^{-3}$ was assumed.

	H_C			
$E > 5 \times 10^{19}$ eV	2.5 km	5 km	7.5 km	10 km
$\tau = 5$	88%	66%	37%	18%
$\tau = 1.5$	89%	69%	43%	26%
$\tau = 0.5$	88%	82%	74%	70%
$\tau = 0.05$	90%	89%	89%	90%

	H_C			
$E > 7 \times 10^{19}$ eV	2.5 km	5 km	7.5 km	10 km
$\tau = 5$	98%	77%	44%	21%
$\tau = 1.5$	99%	83%	54%	39%
$\tau = 0.5$	100%	95%	88%	84%
$\tau = 0.05$	99%	100%	100%	99%

Table 2: Statistical distribution of clouds for τ and H_C from TOVS database [16] analyzed taking in account JEM-EUSO orbit [19].

	H_C			
τ	< 3 km	3–7 km	7–10 km	> 10 km
> 2	17.2%	5.2%	6.4%	6.1%
$1 - 2$	5.9%	2.9%	3.5%	3.1%
$0.1 - 1$	6.4%	2.4%	3.7%	6.8%
< 0.1	29.8%	0.03%	0.01%	1.2%

4 Discussion

In order to estimate the overall impact due to clouds, one needs to take into account how often the different types of clouds appear in FoV. From the TOVS data analysis for JEM-EUSO orbit, statistical distribution of clouds is summarized in Table 2 (see [19] for further details). The undesired clouds such as one with $\tau > 1$ and $H_C > 7$ km accounts for 20%, while $\sim 60\%$ cases are only low altitude clouds with $H_C < 3$ km whose influence to EAS is limited.

By the convolution of $\epsilon(E; H_C, \tau)$ with such information of cloud property distribution, the expected cloud impact on the trigger efficiency is obtained. In presence of cloud, however, the triggered events are needed to be selected with proper criteria of quality cut. In this work, we assumed observed EAS as 'quality event' if its maximum of development lies above the cloud-top altitude. In the case of clouds with $\tau < 1$, all triggered events are also accepted since the the maximum of development is measurable even with attenuated EAS signals. In such a case, angular reconstruction is little affected since it is based on the angular speed of moving spot corresponding to EAS track.

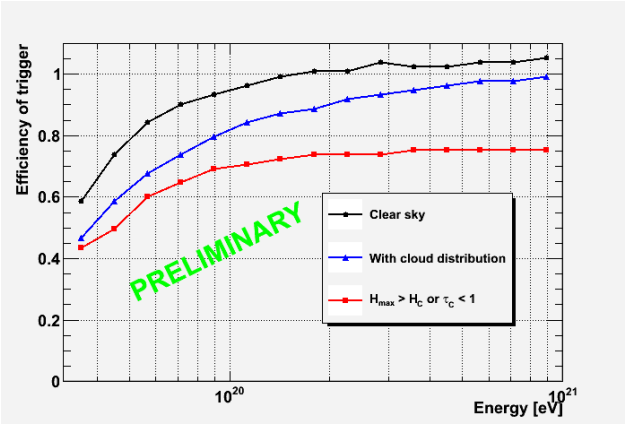


Figure 2: Preliminary trigger efficiency vs energy. The clear sky case is denoted by circles. Cloud-statistics average case is shown by triangles. The case for quality event is indicated by squares.

In Figure 2, the trigger efficiency is shown as a function of energy. For cloudy cases, all triggered events as cloud-statistics average is shown by triangles. The case of selection of quality event into those triggered events is also indicated by squares. For comparison, the clear sky case is shown by the circles.

For all triggered events, the efficiency increases with energy and approaches that of clear sky case at highest energies. For quality events, it increases up to $\sim 10^{20}$ eV and becomes almost constant at higher energies. This is because a certain fraction of the clouds with $\tau > 1$ exists at higher altitudes. From Table 2, for example, such clouds with $H_C > 7$ km accounts for 20%. Therefore a part of EAS develops below such type of clouds. The cloud impact for overall cloud-statistics is estimated to $\sim 70\%$ above $\sim 3 \times 10^{19}$ eV. This value is an important factor when one estimates the effective exposure over the mission (see [18, 20]). Similar estimate was carried out in EUSO mission and this result is in fair agreement apart from detailed difference in selection criterion. Currently, detailed study on reconstruction is in progress to take into account configuration of the JEM-EUSO mission. It should be mentioned that the main telescope of JEM-EUSO will be operated along with AM system. Utilization of these subsystem is investigated in parallel [8, 9].

5 Summary

In this work, the impact of the clouds in observation of UHECRs by the JEM-EUSO mission is investigated using ESAF simulation package with a test cloud assumption. The light curves for typical EAS with a stratus-test cloud shows the intense scattered signals of Cherenkov photons from the cloud-top. In the case of cirrus-like test cloud, there is attenuation of EAS signals that are emitted or scattered below the test cloud corresponding to the transmittance determined by the cloud's optical depth. For various cases, the trigger efficiency was estimated and compared with that of clear sky case. In the case of optically thick and high cloud, EAS signals are generally attenuated that results in smaller trigger efficiency. For optically thin ($\tau < 1$) cloud, a part of EAS does not trigger, while it keeps good visibility of EAS maximum. For the low altitude cloud, the influence is limited especially at higher energies. Taking into account the statistics of cloud property and the observability of the EAS maximum, the cloud impact to trigger aperture is $\sim 70\%$ above 3×10^{19} eV. The results herein are preliminary and further detailed studies are in progress along with utilization of the atmospheric monitoring system.

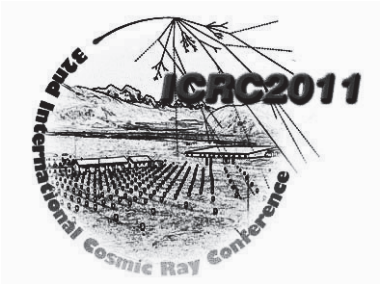
Acknowledgements

Sáez Cano thanks to University of Tübingen and RIKEN for their kind hospitality during her research stays. This work is supported by MICINN under projects AYA2009-06037-E/AYA, AYA-ESP 2010-19082, CSD2009-00064 (Consolider MULTIDARK) & AYA2011-29489-C03-01 and by Comunidad de Madrid under project S2009/ESP-1496. For computation, SPAS-UAH cluster was used.

References

[1] A. M. Hillas, Ann. Rev. Astron. & Astrophys.,22, 425 (1984).
[2] K. Greisen, Phys. Rev. Lett. 17, 748 (1966).
[3] G.Zatsepin and V.A.Kuzmin, J. Experimental and Theor. Phy., Lett. 4, 78 (1966).
[4] T. Ebisuzaki *et al.* in these proceedings (2011).
[5] Y. Takahashi *et al.* , New J. Phys. 11, 065009 (2009).
[6] O. Catalano et al. in Proc. of the 31th ICRC, Lodz (2009).
[7] J. Bayer et al., in these proceedings (2011).
[8] A. Neronov et al., in these proceedings (2011).
[9] J. A. Morales et al., in these proceedings (2011).
[10] C. Berat et al. Astroparticle Physics 33 (2010) 221-247.
[11] The EUSO Collaboration, *EUSO: Report on the Phase A Study* (2003).
[12] F. Fenu et al., in these proceedings (2011).
[13] M. Nagano et al., Astropart. Phys., 22, 235 (2004).
[14] F.X. Kneizys et al., *User's Guide to LOWTRAN 7*, AFGL-TR-0177, U.S. AIr Force Geophysics Laboratory, Hanscom (1988).
[15] A. N. Bunner, *Cosmic Ray Detection by Atmospheric Fluorescence*, Ph.D. thesis, Cornell University (1967).
[16] NOAA, TIROS Operational Vertical Sounder (TOVS) http://www.ozonelayer.noaa.gov/action/tovs.htm
[17] A. Zuccaro Marchi et al., in these proceedings (2011).
[18] K. Shinozaki et al., in these proceedings (2011).
[19] F. Garino et al., in these proceedings (2011).
[20] A. Santangelo et al., in these proceedings (2011).

32ND INTERNATIONAL COSMIC RAY CONFERENCE, BEIJING 2011



THE ESAF SIMULATION FRAMEWORK FOR THE JEM-EUSO MISSION

F. FENU[1,2], T. MERNIK[1,2], A. SANTANGELO[1,2], K. SHINOZAKI[2], M. BERTAINA[3], L. VALORE[4], S. BIKTEMEROVA[5], D.NAUMOV[5], G. MEDINA TANCO[6] ON BEHALF OF THE JEM-EUSO COLLABORATION
[1]*Eberhard Karls Universität Tübingen, Sand 1, 72076 Tübingen, Germany*
[2]*RIKEN 2 - 1 Hirosawa, Wako 351 - 0198, Wako, Japan*
[3]*Università degli studi di Torino, Via Pietro Giuria 1 - 10125 Torino, Italy*
[4]*Università degli studi di Napoli "Federico II"-Istituto Nazionale di Fisica Nucleare - Complesso Universitario di Monte Sant'Angelo - via Cintia 80126 Napoli, Italy*
[4]*JINR Joliot Curie 6, 141980 Dubna, Russia*
[5]*UNAM Ciudad Universitaria, Circuito de investigacion cientifica, Mexico D.F., Mexico*
fenu@astro.uni-tuebingen.de

Abstract: ESAF, the EUSO Simulation & Analysis Framework, was originally developed as the simulation and analysis software for the Extreme Universe Space Observatory - EUSO mission of ESA. More recently, ESAF has been extended and modified to simulate the JEM-EUSO mission. ESAF consists of several independent modules, which perform the shower simulation, the light transport in the atmosphere, the instrument and telemetry simulation, and eventually the analysis of the observed track in order to reconstruct the energy, arrival direction and Xmax of the event. In this paper, we present the ESAF event simulation structure. In particular we describe the shower generators, the atmospheric modeling, the simulation of the JEM-EUSO optics, sensors and electronics including the trigger algorithms developed to discriminate the good event signals from the background, allowing a fake trigger rate compliant with the JEM-EUSO telemetry constrains. We will also show some event describing it step by step through the entire detector.

Keywords: JEMEUSO, Simulation, Analysis, ESAF

1 Introduction. ESAF the Euso Simulation and Analysis Framework

The Euso Simulation and Analysis Framework (ESAF) is currently used as the simulation and analysis software for the JEM-EUSO mission [1][2]. It has been developed in the framework of the ESA-EUSO mission [3][4]. ESAF performs the simulation of the shower development, atmospheric transport, detector optics and electronics simulation. Furthermore, algorithms and tools for the reconstruction of the shower properties are included in the ESAF package. In the framework of the JEM-EUSO Phase-A study, we took all the necessary steps to implement the JEM-EUSO mission configuration. This is carried out in a coordinated effort between several groups which are actively collaborating in the software development and on the mission performances assessment. A general sketch of the ESAF structure is given in fig 1. ESAF is a C++, Object Oriented, root[1] based software. It has been written in a modular way in order to cope with the high complexity of the mission and with the rapidly changing instrumental design and science requirements. It consists of several independent modules: the LightToEuso, the EusoDetector, the Reco and the Analysis module. The LightToEuso module allows the simulation of the shower development and of the light transport through the atmosphere to the detector. The EusoDetector includes the simulation of all the detector components from Optics to the Electronics of the JEM-EUSO telescope. Once the trigger algorithms issued a trigger signal, the event is sent through telemetry to Earth for the event reconstruction. At this stage (the Reco framework) the reconstruction of the arrival direction, energy and type of primary particle is performed. The Analysis module is being developed. The executables of the software

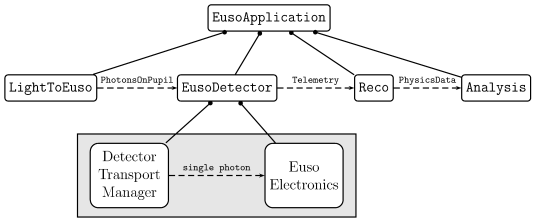


Figure 1: Basic ESAF scheme. Taken from [6]

1. Package developed at CERN for particle physics data analysis. [5]

have been divided in two parts: the Simu and the Reco file. The first performs the simulation of the real event from shower generation to telemetry while the second takes care of the reconstruction. This has been done in view of a future utilization of the reconstruction module which could be used for the analysis of real data.

2 The Simulation framework

In this section we will describe the simulation framework of the ESAF software. This part is meant to simulate all the physical processes which are related to the shower development, the light production and propagation, the detector and eventually the telemetry.

2.1 Event generators

Several shower simulators are implemented in ESAF, following parametrical and Monte Carlo approach. As parametrical generator, the Gaisser-Ilina-Linsley (GIL) function [7], is used to reproduce the profile as function of Energy and slant depth. Other generators such as the Monte Carlo simulator Corsika [8] and the Monte Carlo Conex simulator [9] are interfaced with ESAF. Consistency studies between all the different approaches have been performed and the appearance of some small inconsistency between the parameterization and the Monte Carlo simulators is still under investigation. With the different shower generators we are now able to generate showers of different primary. Neutrino showers can now be generated with the Conex generator and then analyzed by ESAF. Lidar events can be now generated in ESAF: specific methods have been developed and implemented to simulate photons at 355 nm emitted by laser sources, in parallel to methods in use for showers. Other sources of light (lightnings, TLEs[2], cities, meteors) cannot be simulated yet although test light sources can reproduce the effect of those events up to first approximation.

2.2 Atmospheric transport

Both Fluorescence and Cherenkov production is taken into account in ESAF. The simulated Fluorescence spectrum according to Nagano et al [10] is shown in Fig. 2. The Cherenkov production is taken into account following the standard Cherenkov theory. Both the ground reflected and the backscattered component are considered. All the photons are affected by Rayleigh scattering and ozone absorption. Furthermore, photons can reach the detector in indirect way after scattering. Optionally clouds can be simulated as constant layer of variable altitude thickness and optical depth. Non uniform cloud coverage is also included in ESAF. The effect of aerosols and dust has not been included in ESAF yet.

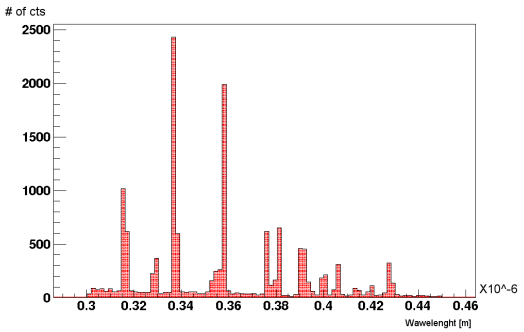


Figure 2: Photon spectrum simulated with ESAF. Both the typical Fluorescence emission lines and the Cherenkov (low level continuous spectrum) spectrum are visible. Fluorescence is calculated according to Nagano et al. [10]

2.3 Detector

Once the photons reach the detector they are taken over by the optics module. Several optics simulation approaches have been considered. The parametrical simulation module calculates analytically the position of the photon on the focal surface and adds to this position a random spread. This is intended to be the first approximation of the optics simulation and is basically the fast working tool to test the features of the different optics designs. Furthermore, the optics simulation code developed in RIKEN [11] is included in the simulation code. This ray-trace code is interfaced with the ESAF framework in order to transport every photon within the optics through a Monte Carlo simulation. In Fig. 3 an example of the generated RIKEN ray-trace Point Spread function can be seen. Several optics configurations have been included in the course of time to assess the performances. Another optics module is the Geant 4 optics module [12] which uses an interface with the Geant simulator to transport the photons from pupil to the focal surface.

In Fig. 4 we analyze the composition of the photon spectrum arriving at the pupil. As can be seen both direct fluorescence, reflected and backscattered Cherenkov are visible. Moreover we can observe in Fig. 5 the event through the entire detector from the pupil to detected counts regardless of the photon's kind.

Once the photons reach the focal surface they are transported through the filter and the optical adaptor before of reaching the photocathode. All the relevant effect including geometrical losses, inefficiencies of the adaptor (the BG3) and of the filter are taken into account. A parameteriza-

2. TLE: Transient Luminous Event. Transient event in the high atmosphere responsible for the production of huge amounts of light in the UV range. In this category we can consider Sprites, Jets, Elves and many other phenomena.

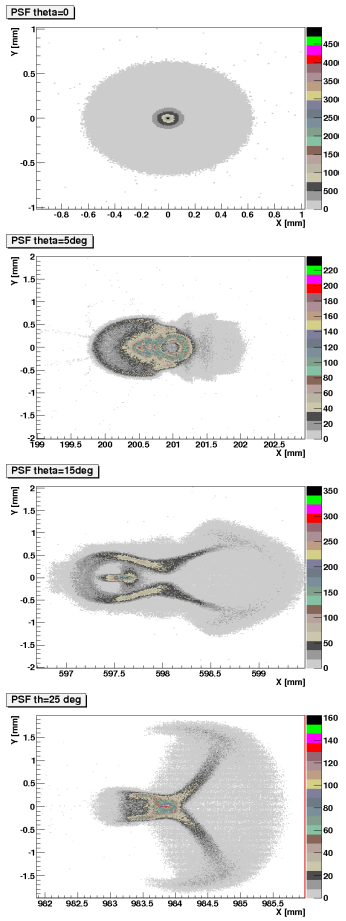


Figure 3: Point spread functions simulated with the RIKEN ray-trace code interfaced with ESAF for several inclination angles (0, 5, 15, 25 deg). On the axes the position in mm on the FS can be read.

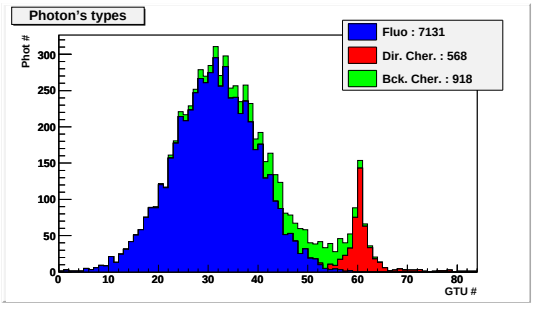


Figure 4: Composition of the photons at the detector pupil. Standard shower (10^{20}eV 60 deg) as simulated by ESAF with the GIL parameterization.

tion of the photomultiplier is included in the electronics part. All the effects like quantum efficiency (and its dependence from the photon inclination), collection efficiency and cross talk are also taken into account pixel by pixel within one Photomultiplier (PMT). The implemented Photomultiplier is the M64 Photomultiplier of Hamamatsu. In table 1 we give a resume of the most relevant parameters of

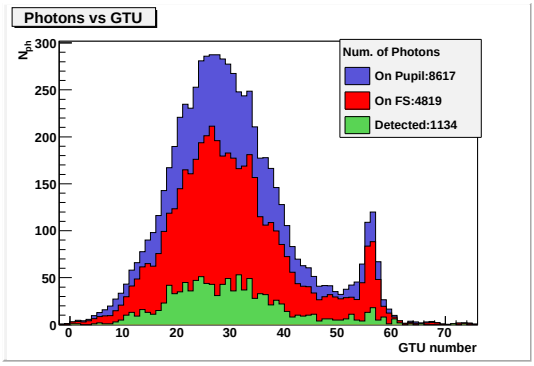


Figure 5: The event as seen through the detector. The Blue curve gives the number of photons as function of GTU # at the pupil. The red one tells how many photons reach the FS. The green one represents the counts. Standard shower (10^{20}eV 60 deg) as simulated by ESAF with the GIL parameterization.

the detector. More details can be found in [13]. The signal

Quantum Efficiency	$\sim 39.6\%$
Collection Efficiency	$\sim 80\%$
Cross talk	Negligible
Pixel Area	9 mm^2
Number of Pixels	64

Table 1: The most relevant parameters for the implemented M64 Photomultiplier

is then amplified by a parameterized gain and the resulting output current is collected and treated by the Front End Electronics. A threshold is set on the PMT output current in order to accept or reject the signal count.

2.4 Trigger

The trigger algorithm's duty is to filter the background in order to increase the signal to noise ratio. Being the telemetry limited, the instrument cannot afford the transmission of the entire Focal Surface data to Earth. The entire triggering scheme is therefore organized in a multiple step filtering. After the Front End Electronics identified a photon count a first search for persistency is done at the level of PDM [3]. This is called the first level trigger (L1). After at this level a trigger signal is issued data are sent at the next level: the so called Cluster Control Board [4] trigger. This is also called second level trigger (L2). Here the Fake Trigger Rate must be further reduced to fit with the telemetry constraints (from $\sim$ 1kHz to 0.1Hz on the entire Focal Surface). Several algorithms have been implemented and tested: the so called Linear Tracking Trigger (LTT) scheme and the Progressive Tracking Trigger (PTT) as well as the so called

3. Part of the Focal Surface consisting of 36 Photomultipliers.
4. Electronics board which operates on 324 Photomultipliers.

Cluster Control Board LTT trigger (CCB_LTT) [14]. Several combinations of trigger schemes have been tested and compared. Triggering efficiency for several detectors and different GTU length have been produced. Once the trigger has been produced the triggered events are sent through telemetry to the reconstruction framework. A more comprehensive review on the trigger scheme is given in [15].

2.5 Tilted mode

In order to further increase the exposure it might be useful to tilt the instrument. In this way the surveyed area will be increased by a large factor. Unfortunately the larger distance at which showers are observed under these conditions will significantly increase the energy threshold. Therefore tilting must be carefully studied in order to optimize the inclination of the instrument. The tilting angle also deeply affects the scientific output of the mission. Low tilting angles are more favorable to study Cosmic Rays in the GZK region while higher inclinations give us a larger exposure above 10^{20}eV. We started some preliminary activity to assess the most proper mission configuration and as a further step the tilted mode will be implemented in ESAF.

3 The Reconstruction framework

Aim of this framework is to analyze the detector response in order to identify the direction of arrival, the energy and the type of the primary. The first step consists in the identification of the signal inside the transmitted data. For this purpose both a clustering and a Hough module have been implemented. Then through fits procedures the direction of the primary is calculated. Several different fits algorithms have been included in ESAF. As last step the profile, X_{max} and the energy are reconstructed. A more comprehensive review of the reconstruction module is given in [16]. In Fig. 6 we see how the signal is treated after having been identified. A fit procedure is applied in order to find the arrival direction of the shower.

Figure 6: [figure missing here: see ICRC proceedings] The standard event arrival direction is here reconstructed. The event is seen after the clustering procedure while a fit is performed in order to find the arrival direction. (T. Mernik)

4 Conclusions

In this paper we described the ESAF simulation framework. After the short historical introduction we described the structure of the software and the physical models implemented in it. We showed how an event is treated by the ESAF simulation software by showing the key plots of the simulated event through the various steps of the detector simulation and of the reconstruction. Moreover we wish to remember that the ESAF package is available under the svn repository based in Lyon. We encourage interested people to contact the accounts manager at the address naumov@numail.jinr.ru.

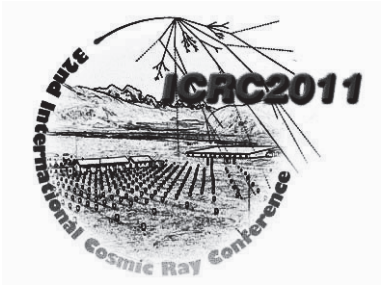
Acknowledgments

This work has been conducted by using the ESAF software which has been written by the ESAF developers team during the Phase-A study of the EUSO mission under the initiative by the European Space Agency ESA. We wish to thank RIKEN, Japan, for an allocation of computing resources on the RIKEN Integrated Cluster of Clusters (RICC) system. Moreover FF wishes to thank the Computational Astrophysics Laboratory for their kind hospitality.

References

[1] Y. Takahashi, New Journal of Physics, Vol. 11, N. 065009, 2009.
[2] T. Ebisuzaki et al., This ICRC contribution.
[3] A. Thea et al. ,"The EUSO Simulation and Analysis Framework", Proceedings 29th ICRC.
[4] C. Berat, "Full simulation of space-based extensive air showers detectors with ESAF", Astropart. Phys. Volume 33, Issue 4, May 2010, Pages 221-247
[5] http://root.cern.ch/drupal/content/documentation
[6] D. De Marco, M. Pallavicini, "The EUSO Simulation and Analysis Framework" EUSO internal document.
[7] N. P. Ilina et al. 1992, Sov. J. Nuc. Phys. 55 1540-1547
[8] D.Heck et al. 1998, "CORSIKA: a Montecarlo code to simulate Extensive Air Showers, Forshungszentrum Karlsruhe, 1998, Report FZKA, 6019
[9] T.Bergmann et al. 2007, Astropart. Phys., vol 26, pp. 420-432
[10] M. Nagano et al. 2003, Astropart. Phys., vol 20, pp. 293-309
[11] Y. Takizawa et al. 2011, This ICRC contribution.
[12] S. Biktemerova et al. 2011, This ICRC contribution.
[13] Y. Kawasaki et al. 2011, This ICRC contribution.
[14] J. Bayer et al. 2011, This ICRC contribution.
[15] O. Catalano and M. Bertaina, Proc. 31st ICRC, Lodz, Poland (2009).
[16] T. Mernik et al. 2011, This ICRC contribution.

32ND INTERNATIONAL COSMIC RAY CONFERENCE, BEIJING 2011



The ESAF Reconstruction Framework of UHECR Events for the JEM-EUSO Mission

THOMAS MERNIK[1,2], FRANCESCO FENU[1,2], DOMENICO D'URSO[3], ANDREA SANTANGELO[1,2], KLAUS BITTERMANN[1,2], KENJI SHINOZAKI[2], MARIO BERTAINA[4], SVETLANA BIKTEMEROVA[5], DMITRY NAUMOV[5], GUSTAVO MEDINA TANCO[6]
ON BEHALF OF THE JEM-EUSO COLLABORATION
[1]*Institut für Astronomie und Astrophysik, Kepler Center, Universität Tübingen, Sand 1, 72076 Tübingen, Germany*
[2]*RIKEN, 2-1 Hirosawa, 351-0198 Wako, Japan*
[3]*Università degli studi di Napoli and INFN Istituto Nazionale Fisica Nucleare, Complesso Universitario di Monte Sant'Angelo - Via Cintia 80126 Napoli, Italy*
[4]*Università degli studi di Torino, Via Pietro Giuria 1 - 10125, Italy*
[5]*JINR, Joliot-Curie 6, 141980 Dubna, Russia*
[6]*UNAM, Ciudad Universitaria, Circuito de la Investigacion Cientifica, Mexico D.F., Mexico*
mernik@astro.uni-tuebingen.de

Abstract: JEM-EUSO is a space based UV detector that will be mounted on the International Space Station (ISS) to monitor the earth's atmosphere searching for UHECR induced extended air showers (EAS). By evaluating the fluorescence and Cherenkov signal on the focal surface of the instrument the arrival direction, energy and nature of the primary can be determined. Due to the instantaneous aperture of 10^5 km^2 sr JEM-EUSO will be able to measure several hundreds of events at energies higher than $5*10^{19}$ eV. ESAF is a software for the simulation of space based UHECR detectors. It is configured to cover the specific aspects of the JEM-EUSO mission and to estimate its expected performance. ESAF can simulate every step of the generation and observation of an EAS - from the fluorescence track formation, the light transport in the atmosphere and through the instrument to the telemetry stage. The reconstruction chain covers the discrimination of the recorded track from background as well as the estimation of energy, arrival direction and Xmax for the determination of the UHECR species. In this paper we present strategies and algorithms implemented to estimate the spatial and energy resolution of JEM-EUSO as well as a selection of examples demonstrating the expected performance.

Keywords: JEM-EUSO, ESAF, Reconstruction, UHECR Events.

1 Introduction

The JEM-EUSO detector is a space based UHECR detector designed to be mounted on the Japanese Experiment Module "Kibo" on board the ISS [1]. It will monitor the earth's atmosphere from above to search for extended air showers generated by of cosmic rays in the energy range of 10^{19} eV to 10^{21} eV and possibly beyond. JEM-EUSO will reach an instantaneous aperture of approximately 10^5 km^2 sr [2] allowing a high statistics of events compared to ground based observations. Thus, JEM-EUSO is a key mission to explore the realms of extremely high energy cosmic rays far beyond the capabilities of any ground based UHECR observatory. More details can be found in [3].

ESAF - the EUSO Simulation & Analysis Framework, is a ROOT [4] based, modular software designed to simulate space based UHECR detectors. It has been developed in the context of the former EUSO mission [5]. Its modular structure allows to simulate any EUSO-like[1] instrument. The simulation comprises all physical processes relevant to UHECR measurement. Among these are the development of the resulting air shower, the production of fluorescence and Cherenkov light as well as propagation of photons towards the detector. Inside the instrument, simulations involve the propagation of photons through the optics, the response of the photomultiplier and electronics and the event reconstruction eventually. In this article we explain the reconstruction algorithms implemented in ESAF and present some results to demonstrate their achievement potentials.

2 The Reconstruction Framework

Cosmic ray induced EAS emit fluorescence light isotropically in all directions plus a beamed Cherenkov component. Parts of that light go directly to the telescope. Other com-

1. We define EUSO-like a space borne detector for the measurement of UHECR by the measurement of the fluorescence and/or Cherenkov light of EAS.

ponents are reflected diffusely from ground or scattered towards JEM-EUSO. The UV photons reaching the entrance pupil of the instrument propagate through the optics and activate the photomultiplier tubes arranged on the focal surface. When the readout electronics recognizes certain patterns a trigger is issued. Now the signal is processed and transmitted to earth for analysis and reconstruction. More details on the observation technique can be found in [2].

In ESAF different modules are dedicated to the single stages during the evaluation of the signal. First of all, the signal has to be disentangled from noise. Following that direction and energy reconstruction algorithms can be applied.

2.1 Pattern Recognition

The fluorescence signal will appear as a faint moving spot of the instruments focal surface embedded in the background generated by night glow, city lights, weather phenomena and other sources. The extraction of the signal track and the determination of its spatio-temporal behavior remains crucial for any further analysis aiming at reconstructing the arrival direction or energy of the primary. There are two possible algorithms for the pattern recognition:

- *Clustering* of data points in space and time to disentangle causally related data points from those distributed randomly.
- *Hough Transform*, developed to identify prefixed shapes within noise by transforming the relevant parameters to the so called Hough space and back.

Both are in principle capable to perform the required operation and have been implemented in ESAF.

2.2 Clustering

The approach of the cluster technique is to arrange data points into causal patterns by analyzing their minimum spanning tree (MST) which is in this case made of the Euclidean distance between them (fig. 1). A group of activated pixel is then identified as a cluster if their distance is less than a certain pre-adjusted threshold ξ. If this cluster is regarded as significant (large with respect to others) a line fit is performed to estimate its geometrical parameters [6].

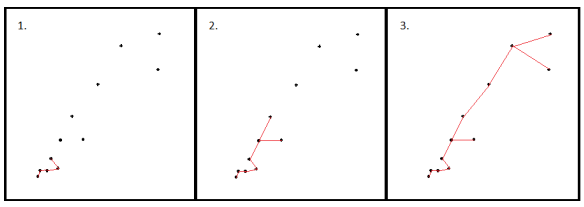


Figure 1: Clustering of data points: the size of the cluster depends on a threshold

2.3 Hough Transform

Initially designed for the detection of patterns in bubble chambers, the HT is an algorithm for the discrimination of certain shapes (even incomplete ones) from others, e.g. noise [7]. Here the item sought-after is a longish pattern that can be abstracted as a straight line. For each data point the HT assumes a number of lines passing through it. These lines can be parametrized by their distance from the origin of the coordinate system ρ and the angle θ between its normal and the x-axis (fig. 2, left). Transformed into the Hough space, a two dimensional parameter space spanned by ρ and ξ each data point represents a sinusoidal curve (fig. 2, right). The intersection points of the many sinusoidals are summed up in an accumulator. The intersection point that drews in most of the counts is then transformed back into the image space, where it corresponds to a straight line passing through as many data points as possible. Hence, when the signal track is identified a line fit estimates its parameters. This information is handed over to the direction reconstruction module.

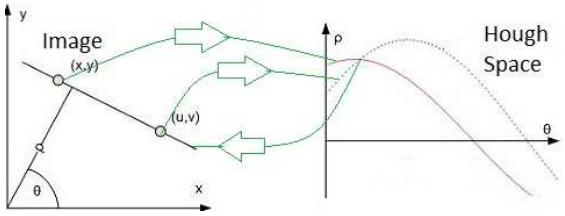


Figure 2: Simple example of a Hough transform for two data points.

2.4 Pulse Finder

Performances of pattern recognition algorithms can be further improved introducing a preliminary pulse finding step over each single camera pixel defining the associated time window validity. In each pixel, pedestal, variance and peaks of the recorded signal as a function of time are evaluated. Starting from a first guess time window defined around peaks, start and stop positions of signal are identified maximizing the signal to noise ratio. The procedure allows to make a pre-rejection of the noise and strongly reduces the probability to misleadingly identify a noisy pattern as a track.

3 Direction Reconstruction

From the geometrical properties of the signal track on the focal surface the arrival direction of the primary can be computed by a variety of methods implemented in ESAF as described in more detail in [8] and [9]. Fig. 3 shows the system of the EAS and the detector. In the current configuration there are 5 different algorithms implemented in ESAF. Two of them yield the most promising performance:

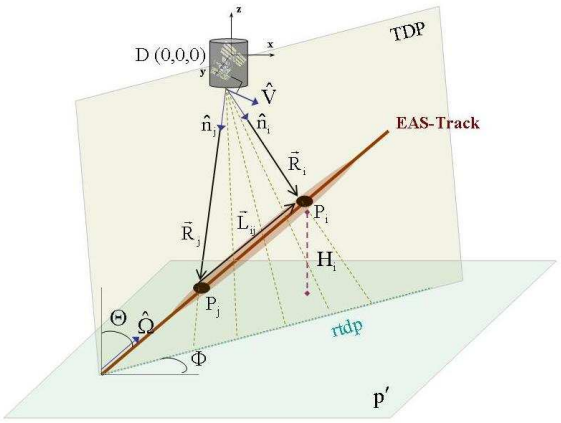


Figure 3: EAS observed with JEM-EUSO: Within the track-detector-plane (TDP), photons emitted at different times $t_j > t_i$ reach the detector from certain directions $\hat{n}_i$, $\hat{n}_j$ after traversing R_i, R_j in atmosphere. From the timing information and arrival angle of the shower photons, the direction of the primary $\hat{\Omega}(\Theta, \Phi)$ can be determined.

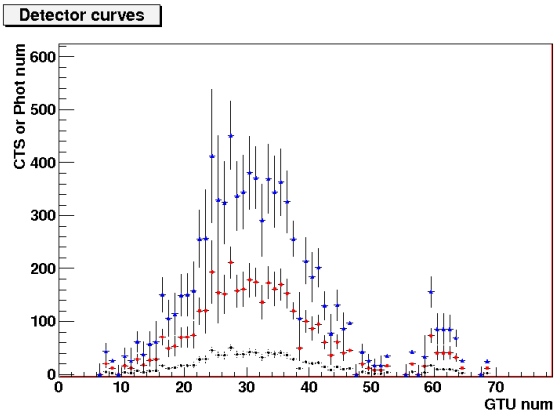


Figure 4: Energy reconstruction: Count distribution (black) is obtained by smoothing the clustering data. Focal surface light curve (red) and entrance pupil light curve (blue) are computed by taking into account the instruments efficiency.

- *Analytical Approximate 1*: angular velocities of the signal track int the x(t) and y(t) planes are linearly fitted. The arrival angle of the primary is derived by geometrical estimations.
- *Numerical Exact 2*: a χ^2 minimization is performed between the activation times of pixel induced by the actual signal to those induced by a signal track theoretically computed.

3.1 Energy Reconstruction

The ESAF package has an extensive module dedicated to the reconstruction of the energy of the primary as further described in [10].

Moreover, an alternative energy reconstruction module have been implemented by the Tübingen group. Starting from the reconstructed signal profile inherited from the pattern recognition we successively correct for the instrumental losses such as optical absorption in the lens system or inefficiency of the photomultipliers in order to get the photon's curve at the level of the entrance pupil of the optics (fig. 4). A parameterization both for the photomultipliers and for the optics response is required at this step. Using the reconstructed primary arrival direction and, if present, the timing of the Cherenkov mark we then reconstruct the position of the shower at each time. Using this information we can now correct the atmospheric effects and the geometrical loss which dim the signal. Several methods to reconstruct the geometry of the shower [2] have been implemented. Some of them use the timing of the Cherenkov mark, other make assumptions on the particle type or infer the position of the maximum from the shower width. Once the photon distribution within the shower has been reconstructed, assuming a certain fluorescence yield we can compute the number of charged particles in the shower. After that, the backscattered Cherenkov component is calculated and then subtracted from the contaminated electron curve. Eventually, a fit with a parameterization for the shower profile is performed. Having already calculated the Xmax (at the level of the electron curve reconstruction) - energy is the only remaining free parameter. Performing the fit therefore allows to give an estimate of the energy of the primary.

energy	$7 * 10^{19}$ eV, $1 * 10^{20}$ eV, $3 * 10^{20}$ eV
primary	proton
inclination Θ	30°, 45°, 60°, 75°
right ascension Φ	0° - 360°
statistics	1000 events each E/ Θ config.

Table 1: Configuration of study.

4 Some Examples

Currently the ESAF code is being updated to the most recent JEM-EUSO configuration. This includes improvements in the optical system as well as latest trigger algorithms (see [11]). Here we present a few examples of ESAF's reconstruction performance. For the angular resolution study only a certain subclass of events is considered as seen in tab. 1. For the energy resolution we limited outselves to standard events (E=$1 * 10^{20}$ eV, Θ=60°) All simulations have been carried out assuming an ISS altitude of 430 km. The the recently introduced PulseFinder has not been used in this particular study. Thus the examples presented here are rather conservative and may be regarded as preliminary.

2. Geometry means the position of the shower in the FOV at each time.

4.1 Spatial Resolution

γ^{68} is a measure of the angular resolution. 68% of all events have separation angle less than γ^{68}. Here we show the separation angle as function of E and Θ.

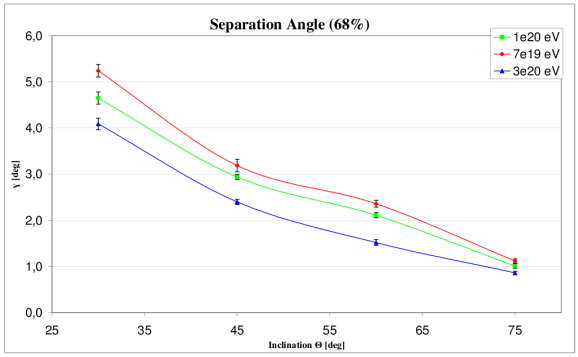


Figure 5: Angular resolution for different E ($7 * 10^{19}$,$1 * 10^{20}$, $3 * 10^{20}$ eV) and Θ (30°, 45°, 60°, 75°).

4.2 Energy Reconstruction

In fig. 6 we show the relative energy resolution for standard events (proton, E=10^{20} eV, Θ=60°). For details see [12].

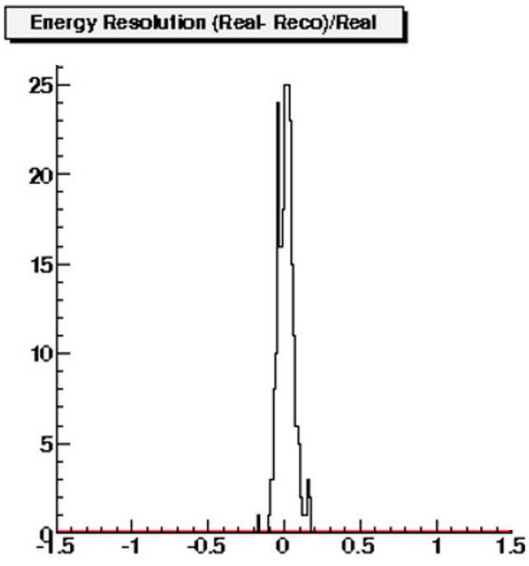


Figure 6: Energy resolution: $\frac{(E_{real}-E_{reco})}{E_{real}}$

5 Conclusion

ESAF is a powerful software and the tool of choice for the simulation and reconstruction of UHECR measeruments with space-based detectors. ESAF provides an independent and parallel assessment of the JEM-EUSO performance. A complete End-To-End simulation and analysis of a larger number of events including studies about different primaries and changing atmospheric conditions such as cloud coverage is in progress (see [13]). Due to relatively recently introduced improvements such as the PulseFinder technique, we expect significant improvements of the spatial and energy resolution in the near future.

Acknowledgements

This work has been conducted by using the ESAF software which was written by the ESAF developers team during the Phase-A study of the EUSO mission under the initiative by the European Space Agency ESA. We wish to thank RIKEN, Japan, for an allocation of computing resources on the Integrated Cluster of Clusters (RICC) system. Moreover TM wishes to express his gratitude to the Computational Astrophysics Laboratory of RIKEN for their kind hospitality.

References

[1] Y. Takahashi *et al.* , *The JEM-EUSO mission* in *New Journal of Physics*, Vol. 11, N. 065009 (2009)

[2] T. Ebisuzaki *et al.* , *The JEM-EUSO project: Observing extremely high energy cosmic rays and neutrinos from the International Space Station* Nucl. Phys. B (Proc.Suppl.) Vol. 175-176 p. 237-240 (2008)

[3] JEM-EUSO Collaboration, *Report on the Phase A Study 2010* (2011)

[4] R. Brun, *et al.* , *ROOT - An object oriented data analysis framework* in *Nuclear Instruments and Methods in Physics Research A*, Vol. 389, p. 81-86, (1997)

[5] EUSO Collaboration, *EUSO Report on the Phase A Study* (2003)

[6] M.C. Maccarone, *Cluster Analysis and Line Fits to Reconstruct EUSO Tracks* EUSO SDA-REP-002-0 (2002)

[7] P.V.C. Hough, *A Method for Faster Analysis of Bubble Chamber Photographs (Hough and Powell)* in *Instrumentation for High-Energy Physics* p. 242-+, (1961)

[8] C. Berat *et al.* , *Full simulation of space-based extensive air showers detectors with ESAF* in *Astroparticle Physics*, Vol. 33, Issue 4, p. 22 (2010)

[9] S. Bottai, *Some algorithms for direction reconstruction in EUSO* EUSO-SDA-REP-006-1

[10] P. Colin *et al.* , *EUSO Reconstruction Algorithms* EUSO-SDA-REP-016 (2003)

[11] F. Fenu *et al.* , *The ESAF Simulation Framework for the JEM-EUSO Mission*, in *This Conference Proceedings #592* (2011)

[12] A.Santangelo *et al.* , *Requirements and Expected Performances of the JEM-EUSO Mission*, in *This Conference Proceedings #991* (2011)

[13] K.Shinozaki *et al.* , *Estimation of Effective Aperture for Extreme Energy Cosmic Ray Observation by JEM-EUSO Telescope*, in *This Conference Proceedings #979* (2011)

32ND INTERNATIONAL COSMIC RAY CONFERENCE, BEIJING 2011

Simulation framework of STM code for development of JEM-EUSO instrument

KAZUHIRO HIGASHIDE[1,2],NAOYA INOUE[2],TAKAO SHIRAHAMA[2],KEISUKE NAGASAWA[2],
FOR JEM-EUSO COLLABORATION
[1]*RIKEN, 2-1 Hirosawa, Wako, Saitama 351-0198, Japan*
[2]*The Graduate School of Science and Engineering, Saitama University, Saitama 338-8570, Japan*
higashide@crsgm1.crinoue.phy.saitama-u.ac.jp

Abstract: The Extreme Universe Space Observatory installed on the Japanese Experimental Module at ISS(JEM-EUSO) is a science mission to investigate the nature and origin of Ultra-High-Energy Cosmic-Rays (UHECRs). The Saitama simulation is covering the End-to-End procedure for the JEM-EUSO mission to study the telescope performance, therefore it has been used as a tool especially for the development of the optics and focal surface devices. This implementation can contribute to the hardware development for seeking the best performance of the telescope. The code offers the data analysis routine for the simulated shower events, as well. In this report, the framework of this simulation code will be introduced and discussed.

Keywords: JEM-EUSO,Simulation,Ultra High Energy Cosmic Rays

1 Introduction

The Extreme Universe Space Observatory installed on the Japanese Experimental Module at ISS(JEM-EUSO) is a science mission to investigate the nature and origin of Ultra-High-Energy Cosmic-Rays(UHECRs)[1]. An UHECR interacts with an atmospheric nucleus and then produces an Extensive Air Shower (EAS). JEM-EUSO on board of the ISS at the altitude of about $430km$, captures the moving track of the fluorescent UV photons along EAS development.

JEM-EUSO telescope records EAS track with a time resolution of $2.5\mu s$ and a spatial resolution of $0.5km$ at ground. These timesegmented EAS images allow us determining EAS energies, their arrival directions and longitudinal profiles.

The End-to-End simulation code has been developed considering hardware characteristics of the JEM-EUSO optical system, the focal surface detector and the output signal control circuit.

The accuracies of cosmic ray energy, arrival direction and longitudinal development can be estimated by reconstructing EAS profiles with the most suitable algorithm; the End-to-End simulation code is also used for successive improvements of the hardware system to upgrade their accuracies.

2 STM code

The Shower and Telemetry Module(STM) code is End-to-End simulation code for JEM-EUSO. The STM code have three components(fig1): EAS generation, detector simulation and EAS event reconstruction part.This code was written by C language. Each parts of STM code are independent and joined by Perl.

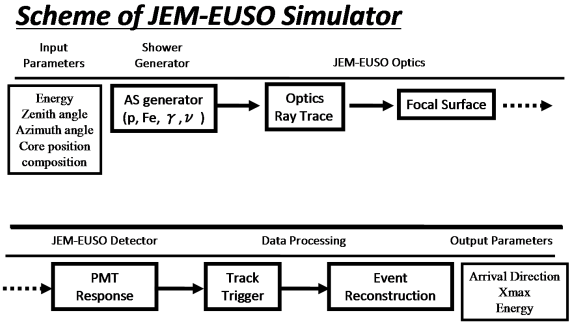


Figure 1: Scheme of STM code

2.1 EAS generation part

EAS generation code generates EAS longitudinal profile in atmosphere initiated by cosmic ray assumed chemical compositions, injected angle and energy. EAS has been generated by executing the code for various EAS longitudinal de-

velopments pooled in the EAS database made by AIRES or CONEX. Air fluorescence and Cherenkov light emissions are calculated taking into account their yields [2].they have wavelength 300-500nm. Absorption and scattering in atmosphere(rayliegh scattering, mie scattering and ozone absorption) are also calculated. And then the characteristics of the photons (wavelength, arrival time and spatial position of emission) on the optical lens of the telescope are evaluated. Figure 2 is sample of arrival time profile of photons on the optical lens.

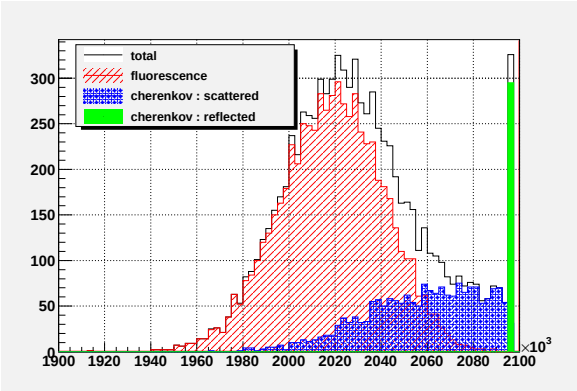


Figure 2: arivall time profile of photons on the optical lens of the telescope

2.2 Detector simulation part

In the detector simulation code, characteristics of hardware responses to incident photons, photoelectrons and analogue/digital signals have been taken into account. The detector simulation have optical raytrece, PDM layout on focal surface, PMT performance(QE, CE and etc.) and trigger algorithm for JEM-EUSO.

In optical raytrace simulation, main part of raytrace made by Y.Takizawa and N,Sakaki. We converted for STM code. Optical raytrace simulation has several lens design(old, baseline and advance design). Detail of Lens design is 2.65m diameter side cut model(minimum diameter is 1.9m), and PMMA or CYTOP material.

PDM layout on focal surface exists each lens design. It has gap of each PDM and PMT. Number of PDM is 137(baseline) or 143(advance) on focal surface and number of PMT is 36 on PDM. PDM length is 165mm and PMT length is 26.04mm. Figure3 is PDM layout thrown on earth. Area of a PDM on ground is about $40km \times 40km$ on center of forcal surface.

PMT simulation calculate number of photoelectron changed from photon with quantum efficiency, collection efficiency of PMT. It has raytrace of BG3 filter.

Trigger scheme have two step. First step of trigger was called progressive tracking trigger(PTT). Second step of trigger was called linear tracking trigger(LTT). Detail of PTT and LTT can be found in [3].

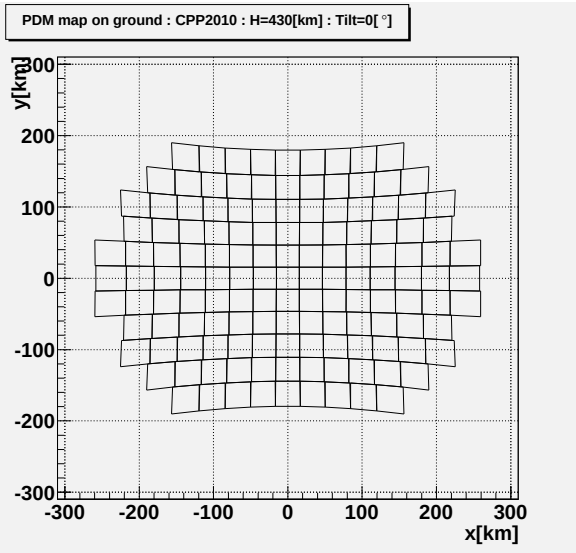


Figure 3: PDM layout thrown on earth

Finally pseudo-observational data including overall hardware responses will be generated. Figure4 is total photon counting efficiency(from injected photon to detected photoelectron) on pixel calculated by STM code.

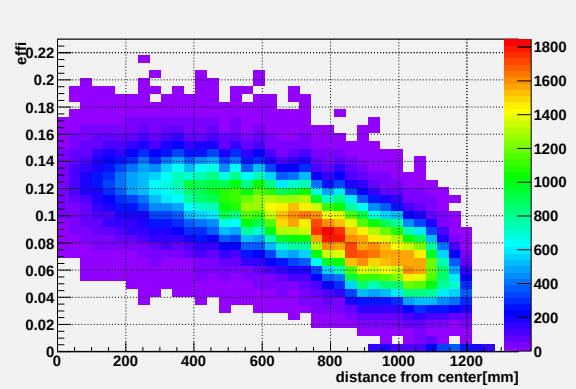


Figure 4: photon counting efficiency on pixel

2.3 EAS event reconstruction part

In addition, EAS event reconstruction code determines EAS energy, arrival direction and longitudinal development from simulated pseudo-observational data, and is used for evaluating their accuracies. This part also contributes as a feedback for the studies related to the development of analytical algorithms and hardware improvements aiming at the excellent telescopes capability with the best accuracies. Figure5 is a sample of reconstructed shower image calculated by STM code.

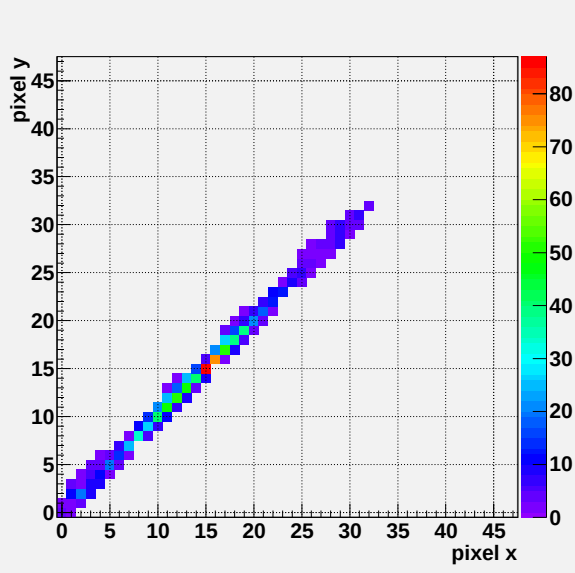


Figure 5: sample of reconstructed shower image calculated by STM code. energy=$10^{20}[eV]$. zenith angle=60[degree]]

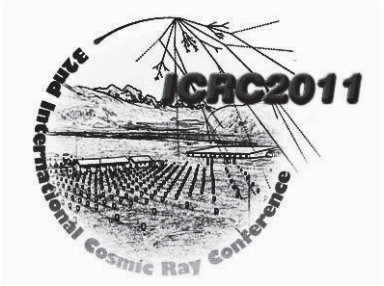
3 Conclusions

The STM code is End-to-End simulation code for JEM-EUSO mission. In this paper we described the STM code framework.

References

[1] T.Ebisuzaki, Proc. 32th ICRC, Beijing, 2011.
[2] Nagano et. al.: 2003, Astropart. Phys., 20, 293
[3] M. Bertaina, O.Catalano, Proc. 32th ICRC, Beijing, 2011.

32ND INTERNATIONAL COSMIC RAY CONFERENCE, BEIJING 2011



Estimation of effective aperture for extreme energy cosmic ray observation by JEM-EUSO Telescope

K. SHINOZAKI[1,2], M.E. BERTAINA [3], S. BIKTEMEROVA[4], P. BOBIK[5], F. FENU[6,1], A. GUZMAN[7], K. HIGASHIDE[8,1], G. MEDINA TANCO[7], T. MERNIK[6], J.A. MORALES DE LOS RIOS PAPPA[2], D. NAUMOV[4], M.D. RODRIGUEZ - FRIAS[2], G. SAÉZ CÁNO[2] AND A. SANTANGELO[6] ON BEHALF OF JEM-EUSO COLLABORATION

[1]*Computational Astrophysics Laboratory, RIKEN Advanced Science Institute, 2-1 Hirosawa, Wako 351-0198, Japan*
[2]*Space and Astroparticle Group (SPAS), University of Alcala, E-28807 Alcalá de Hénares, Spain*
[3]*Department of General Physics, University of Torino, Via P. Giuria 1, I-10125 Turin, Italy*
[4]*Joint Institute for Nuclear Research, Joliot-Curie 6, 141980 Dubna, Moscow Region, Russia*
[5]*Institute of Experimental Physics, Slovak Academy of Science, 040 01 Kosice, Slovakia*
[6]*Institut für Astronomie und Astrophysik, Eberhard-Karls Universität Tübingen, Sand 1, D-72076 Tübingen, Germany*
[7]*Institudo de Ciencias Nucleasres, Universitat Natcional Autonoma Mexico, Mexico City 04510, Mexico*
[8]*Department of Physics, Saitama University, Saitama 338-8570, Japan*

kenjikry@riken.jp

Abstract: JEM-EUSO (Extreme Universe Space Observatory on Japanese Experimental Module) is a space-based new type observatory to explore the extreme-energy-region Universe in particle channel. In the present work, we estimated the effective aperture of the current baseline configuration of the JEM-EUSO telescope in observing extreme energy cosmic rays. We tested the effect of the qualty cut among observed extensive air showers for cross-calibration with other experiments. We also demonstrated several advanges for the space-based JEM-EUSO observation.

Keywords: Extreme energy cosmic rays, JEM-EUSO, extensive air showers

1 Introduction

The origin and existence of extremely energetic cosmic rays (EECRs; referred to as ones with energies E_0 several $\sim 10^{19}$ eV and higher) remains an open puzzle in the contemporary astroparticle physics. Possible indications of sources or excess of EECRs in Celestial Sphere have been claimed by ground-based experiments [1, 2, 3], despite that capable sources are most powerful objects within limited distances by the Greisen-Zatseptin-Kuzmin effect [4, 5]. To investigate this puzzle, studies of energy spectrum and arrival directions of EECRs against their extremely low fluxes of 1 or fewer in km^2 per century, are essential. The size of observation area is therefore critical factor.

JEM-EUSO (Extreme Universe Space Observatory onboard Japanese Experiment Module) is the observatory for EECRs [6, 7]. The JEM-EUSO telescope will be accommodated on JEM/Exposed Facility of the International Space Station (ISS). The scientific objectives include astronomy and astrophysics through EECR channel and other exploratory objectives [8] such as detection of extreme energy gamma rays and neutrinos.

By means of air fluorescence technique, the observation of EECRs depends upon extensive air showers (EASs) phenomenon initiated by primary EECRs. This technique has been developed by several ground-based fluorescence telescopes, however, never been practiced in space. From the orbit, EAS event is observed as a luminous spot moving at the speed of light. For the event with an energy $E_0 = 10^{20}$ eV, for example, the EAS development results in emission of an order of 10^{16} fluorescence photons depending on the zenith angle θ of EAS. The telescope receives an order of thousands of photons per square meter aperture.

By monitoring night Earth with a wide field-of-view (FOV) telescope, a series of advantages and scientific merits are expected. When the JEM-EUSO telescope points to the nadir (nadir mode), unique geometry between EAS and telescope provides less uncertainty in EAS reconstruction due to well-constrained EAS-to-telescope distance. Observations over the orbit will cover the entire Celestial Sphere that allows searching any direction for EECR sources and for global arrival direction distribution. For scientific objectives, the most essential merit is the observation area far larger than ground-based telescope. We also plan to tilt the telescope off the nadir toward the horizon (tilt mode) that

enhances the projected FOV on the Earth's surface to allow more effective observation at higher energies.

In the present work, we focus on the aperture of the JEM-EUSO trigger system for EECR observation. We will discuss relevant issues to estimate the exposure of the data.

2 Apparatus and observation conditions

Apparatus The main part of the JEM-EUSO telescope consists of an $\sim$ 4-m^2-aperture optics with three Fresnel lenses [9] with aspherical curved focal surface (FS) covered by about 137 photodetector modules (PDMs) [10]. Each PDM is composed with 36 multi-anode photomultiplier tubes (MAPMTs) with ultra-bialkali photocathode with 64 channels [11]. PDMs are aligned on FS to maximize the observation area. In the baseline design, about 5000 MAPMTs are deployed and thus the total number of pixels is $\sim 3 \times 10^5$. symmetrically cut with a 40° segment. The spatial resolution for each pixel corresponds to $\sim 0.07^\circ$ or ~ 0.5 km on the Earth's surface for an orbit altitude $H_{\rm ISS} \sim 400$ km. For each pixel, data is acquired with every 2.5 μs (gate time unit) when the two consecutive levels of trigger schemes are activated[12]. These trigger schemes are referred to persistent track trigger (PTT) and line track trigger (LTT). Each scheme searches individual PDM for localized or aligned excesses of signals. Threshold levels for PTT and LTT are dynamically set to fit the rates within hardware requirement and telemetry budget.

Orbit and observation area The orbit of the ISS has an inclination $i = 51.6^\circ$ with $H_{\rm ISS}$ ranging in 278–460 km by the operational limit. The sub-satellite speed and period are $\sim$ 7 km/s and $\sim$ 90 minutes, respectively. Apart from effects by orbital decay and operational boost-up, the ISS motion is approximated as a circular motion with an eccentricity of practically 1. Among these elements, $H_{\rm ISS}$ is widely variable throughout its operation and so far has range between ~ 350 and ~ 400 km.

The 'observation area' of JEM-EUSO which depends upon tilting angle ξ off the nadir and $H_{\rm ISS}$ is estimated by ray trace simulations [9, 13] for isotropic light source viewed by the FS detectors. In the following we defined it as the projected area on the Earth's surface from which the main ray of photons are detected within outer most boundaries of the FS detector.

Figure 1 shows the observation area as a function of tilting angle for different $H_{\rm ISS} = 350, 400$ and 430 km.

For the baseline layout of 137 PDMs, the observation area $A_{\rm obs}^{\rm (nadir)}$ for nadir mode is a function of $H_{\rm ISS}$ expressed by:

$$A_{\rm obs}^{\rm (nadir)}[{\rm km}^2] \approx 1.4 \times 10^5 \cdot \left(\frac{H_{\rm ISS}}{400[{\rm km}]} \right)^2 \qquad (1)$$

With tilting angles ξ up to $\sim 40^\circ$, the observation area $A_{\rm obs}$ is approximated as follows:

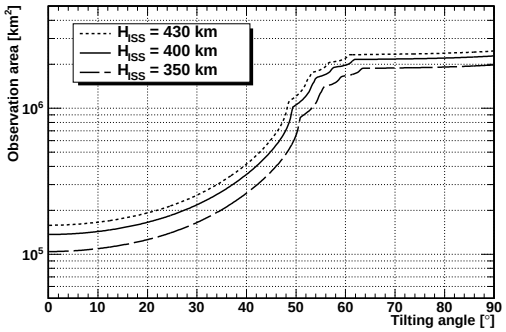


Figure 1: Observation area as a function of tilting angle for different altitudes of 400 km (solid line), 350 km (dashed line) and 430 km (dotted line).

$$A_{\rm obs}(\xi) \approx A_{\rm obs}^{\rm (nadir)} (\cos \xi)^{-b} \qquad (2)$$

where b ranges 3.2–3.4 for the altitude of interest. In this region $A_{\rm obs}$ increases with ξ. Around $xi \sim 40-50$ degrees depending upon $H_{\rm ISS}$, a part of FOV views the sky over the local horizon and $A_{\rm obs}$ saturates above $\xi \sim 60^\circ$.

Background and cloud impact The level of background (BG) noise is a key parameter to define the observation and schemes that yields the observation duty cycle η_0 as well. The first order constraint for η_0 is astronomically determined by the ISS transit over terminator. For $H_{\rm ISS} \sim 400$ km, the average fraction of nighttime is $\sim 33\%$ at the orbital altitude. By applying the upper limit of the BG flux in UV range of 300–400 nm less than 1500 photon m^{-2} sr^{-1}, η_0 corresponds to $\sim 20\%$ (see [15] for details). In this criterion, the average background flux is ~ 500 photons m^{-2} sr^{-1} ns^{-1} (referred to 'average BG level'). Note that the presence of the Moon with its phase close to New Moon is included in operational time as JEM-EUSO telescope is only affected by the illumination of Earth's surface.

The impact of clouds is estimated by the global secular statistics of the optical depth and cloud-top altitude [16] convolved with the trigger probability for each case. The trigger aperture for the time-average cloudy condition is $\sim 80\%$ above $\sim 5 \times 10^{20}$ eV in comparison with that for the cloud-free case. Applying quality cut for events with shower maximum above the optically thick clouds, the overall impact factor is estimated to be $\kappa_{\rm C} \sim 70\%$ above 3×10^{19} eV (see [17] for details).

3 Simulation and results

Simulation In the present work, we employed the ESAF (Euso Simulation and Analysis Framework) [18, 19] adapted into the present JEM-EUSO baseline configuration. The software is written in C++ using an object-

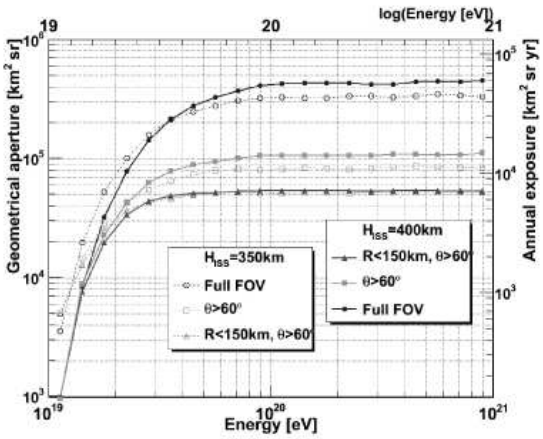


Figure 2: Geometrical aperture as a function of E_0. Open and closed circles indicate geometrical apertures for the ISS altitudes of 400 and 350 km, respectively. Squares and triangles show the cases of different geometrical cuts of $\theta > 60^\circ$ and $R < 150$ km, respectively. The vertical axis on the right represent annual exposure taking into account observation duty cycle and cloud impact.

oriented programming approach and runs on the ROOT package [20]. EAS generation is based on the GIL (Greisen-Ilina-Linsley) formulation [21] that reproduced the longitudinal development of hadronic showers simulated by CORSIKA [22] with QGSJET interaction model [23]. Fluorescence yield is a well recognized uncertainty for energy scale [24, 25]. In the present work, we assumed it by Nagano *et al.* [26]. To estimate trigger aperture, we simulated a large number of EAS uniformly injected into an area far larger than $A_{\rm obs}^{\rm (nadir)}$. $H_{\rm ISS}$ is set to be 350 and 400 km. Threshold levels for PTT and LTT trigger judgements need to fit within permissible fake trigger rates, while it is preferable to keep as low as possible. For optimizations of those parameters, we generated a large amount of noise simulations by STM code [13].

Geometrical aperture Unless otherwise noted, we define 'geometrical aperture' based on the probability satisfying second level LTT trigger condition by means of Monte Carlo simulations. The time-variant conditions such as cloud coverage or BG level are excluded in definition. In the present work, we assume the clear sky condition with average BG level. The exposure growth per given time may be evaluated by a product of η_0 and $\kappa_{\rm C}$ in the previous section. The estimation herein is a preliminary result for the current baseline detector configuration for the nadir mode.

For $N_{\rm trig}$ trigger events among simulated $N_{\rm inject}$ injected EECRs with an energy E_0, the corresponding geometrical aperture $A(E_0)$ is defined as follows:

$$A(E_0) = \frac{N_{\rm trig}}{N_{\rm inject}} \cdot S_0 \cdot \Omega_0 \qquad (3)$$

where S_0 and $\Omega_0 = \pi$ [sr] for $\theta = 0^\circ - 90^\circ$ are the area and the effective solid angle, respectively, in which uniform EAS flux is assumed. To evaluate full geometrical aperture, we applied $S_0 \gg A_{\rm obs}$ to take into account EAS crossing FOV with a core location out of the observation area.

By applying the geometrical selection for good quality events by core location distance R from the center of FOV and lower limit of zenith angle $\theta_{\rm cut}$, subset of geometrical aperture for a given energy is expressed as follows:

$$A_{\rm sub} \propto \int_0^{R_{\rm max}} \int_{\theta_{\rm cut}}^{90^\circ} \epsilon(\theta, \vec{r}) \cdot \sin\theta\cos\theta d\theta \cdot r dr \qquad (4)$$

where $\epsilon(\theta, \vec{r})$ is the probability of trigger at the location of $\vec{r}$ with respect to the correspoding position on Earth's surface to the center of FOV. The amount of light produced in EAS increases with zenith angle since the apparent EAS track becomes longer before being truncated at Earth's surface. In the inner part of FOV, higher efficiency in trigger is expected due to better focusing power of the optics along with shorter EAS-to-telescope distance.

Figure 2 shows the geometrical aperture as a function of E_0 for $H_{\rm ISS} = 400$ and 350 km. Effects of different geometrical cuts in θ and R are also demonstrated. The scale of annual exposure (growth in exposure by one-year operation) is also shown on the right by taking into account $\eta_0 = 0.2$ and $\kappa_{\rm C}$ = 0.7 (see caption and legend for details).

At highest energies, the geometrical aperture for full FOV is almost constant above $\sim (6-7) \times 10^{19}$ eV. The saturated aperture is determined by $A_{\rm obs}$ for given $H_{\rm ISS}$ and therefore the higher altitudes result in the larger apertures. Comparing annual exposure to the Auger (7000 km^2 sr yr) [14], it is expected to be ~ 9 times for $H_{\rm ISS} = 400$ km.

Applying $\theta_{\rm cut} = 60^\circ$ cut to full FOV, while the effective solid angle reduces to $\pi/4$ [sr], almost constant aperture is achieved above $\sim (4-5) \times 10^{19}$ eV. In addition, more stringent $R_{\rm max} = 150$ km cut extends such range down to $\sim (2-3) \times 10^{19}$ eV. It is worthy to mention that for lower $H_{\rm ISS}$ shorter EAS-to-telescope distances increases $\epsilon(\theta, \vec{r})$ for the same energy. This results in the larger apertures and enable better comparison with other experiments in more extended energy range.

Uniformity of exposure Unlike stationary ground-based observatories, global ISS orbit and better sensitivities for large θ EAS allow to scan the entire Celestial Sphere. The exposure distribution is practically flat in right accession. Apart from possible local or seasonal deviation from the global average of cloud coverage and BG level, the relationship between expected overall exposure and declination can be analytically expressed as a function of only $\theta_{\rm cut}$, knowing observable night time at a given latitude.

Figure 3 shows expected distribution of triggered events in declination for different $\theta_{\rm cut} = 0^\circ$, 45° and 60° cuts compared with uniform distribution.

For the case of $\theta_{\rm cut} = 60^\circ$ cut, minor excesses and deficit may arise in very limited parts near Celestial Poles and

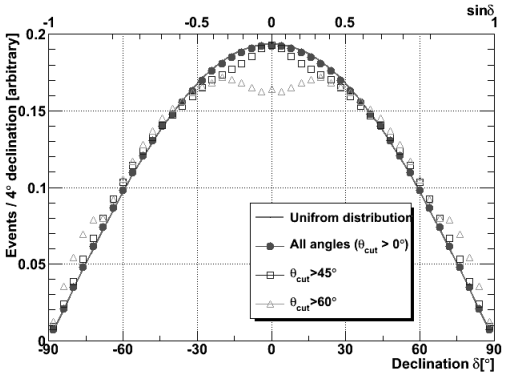


Figure 3: Declination δ distribution of triggered events for different $\theta_{\rm cut} = 0^\circ$ (circles), 45° (squares) and 60° (triangles) in comparison with uniform distribution (solid curve). The horizontal axis on the top shows $\sin\delta$ to indicate the solid angle coverage on the Celestial Sphere.

Equator, respectively. It is because sinuous variation in latitude of the orbit and JEM-EUSO stays longer in high latitudes. JEM-EUSO can achieve well constant exposures for full range of θ with which arrival direction analysis will be made. In the case of ground observatories, first of all they are constrained in observation of never-rising region below the local horizon and the correction factor for non-uniform observable region may even reach ~ 3.

4 Summary and discussion

In the present work, we simulated a large number of EAS to estimate the effective aperture for present baseline configuration and argued the relevant issues. $A_{\rm obs}^{\rm (nadir)}$ is proportional to the square of $H_{\rm ISS}$ which is highly dependent upon the ISS operation. In the mission, the science case has assumed $H_{\rm ISS}$ to be either ~ 400 km, or 430 km following the prediction at the time of EUSO mission [27]. In case of lower altitudes such as 350 km, $A_{\rm obs}$ is compensated by tilting $\sim 25^\circ$ to that of the nadir mode at 430 km altitude without dramatic change of EAS-to-telescope distance.

The geometrical aperture was estimated for clear sky condition. It is important to mention that applying geometrical cuts helps discriminate good quality events in the energy range $(2-3)\times 10^{19}$ eV at constant exposure with energy. Such subset of EAS data makes it possible to cross-check energy spectrum and performances with ground-based experiments at equivalent statistical power. Once it is carried, exposure at higher energies overwhelm by removing such cuts. Taking int account factors of η_0 and $\kappa_{\rm C}$, ~ 9 times annual exposure is expected in comparison with that of Auger. Particularly to increase the statistics at highest energies $\sim (3-5)\times 10^{20}$ eV, we plan to operate the telescope in tilt mode and also with higher BG level threshold.

The full coverage of EECR observation in Celestial Sphere is unique characteristics for the JEM-EUSO and moreover the overall exposure results in almost uniform at the first order. Such an advantage is more pronounced for arrival direction analysis, especially against spread EECR sources.

Some results shown herein are in progress. Further details on the general performance can be also referred in [28].

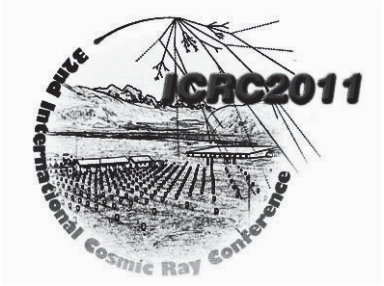
Acknowledgement

KS wishes to express his gratitude to University of Alcalá (UAH), Eberhard-Karls Universität Tübingen and University of Torino for their hospitality and excellent working conditions. Computation facilities of RICC (RIKEN Integrated Cluster of Clusters) System and of UAH-SPAS are acknowledged for efficiently performing simulations. The present work was supported in part by the Italian Ministry of Foreign Affairs, General Direction for the Cultural Promotion and Cooperation.

References

[1] M. Takeda *et al.* , Astrophys. J, 522, 255 (1999).
[2] J. Abassi *et al.* , Astropart. Phys., 30, 175 (2009).
[3] J. Abraham *et al.* (Auger Collaboration), Proc. 31st Int. Cosmic Ray Conf (Lodz), arXiv:0906.2347.
[4] K. Greisen, Phys. Rev. Lett. 17, 748 (1966).
[5] G.Zatsepin and V.A.Kuzmin, J. Experimental and Theor. Phy., Lett. 4, 78 (1966).
[6] Y. Takahashi *et al.* , New J. Phys. 11, 065009 (2009).
[7] T. Ebisuzaki *et al.* , in these proceedings, #0120.
[8] G. Medina-Tanco *et al.* , in these proceedings, #0956.
[9] A. Zuccaro Marchi *et al.* , in these proceedings, #0852.
[10] M. Casolino *et al.* , in these proceedings, #1219.
[11] Y. Kawasaki *et al.* , Nucl. Instr. and Meth., A564, 378 (2006).
[12] J. Bayer, in these proceedings, #0836.
[13] K. Higashide *et al.* , in these proceedings, #1240.
[14] Auger Collaboration, in these proceedings.
[15] P. Bobik *et al.* , in these proceedings, #0886.
[16] F. Garino *et al.* , in these proceedings, #0398.
[17] G. Saez Cano *et al.* , in these proceedings, #1034.
[18] C. Berat *et al.* , Astropart. Phys., 33, 221 (2010).
[19] F. Fenu *et al.* , in these proceedings #0592.
[20] R. Brun *et al.* , Nucl. Inst. Meth. A389, 81 (1997).
[21] N.P Ilina et at., Soviet J. Nud. Phys 55, 1540 (1992).
[22] D. Heck and J. Knapp 1998, Forschungszentrum Karlsruhe Report, FZKA 6019 (1998).
[23] S. Ostapchenko, Phys.Rev. D 74, 014026 (2006).
[24] Eg for review, F. Arqueros, J. Hörandel and B. Keilhauer, Nucl. Instr. Meth. A597, 1 (2009).
[25] N. Sakaki *et al.* , in these proceedings, #0520.
[26] M. Nagano *et al.* , Astropart. PHys., 22, 235 (2004).
[27] EUSO Collaboration, *EUSO Proposal: Report on the Phase A Study*, 2002.
[28] A. Santangelo *et al.* , in these proceedings, #0991.

32ND INTERNATIONAL COSMIC RAY CONFERENCE, BEIJING 2011



Precise Fluorescence Yield Measurement Using an MeV Electron Beam for JEM-EUSO Collaboration

D. MONNIER RAGAIGNE [1], S. DAGORET-CAMPAGNE[1],P. GORODETZKY[2], J. BARET[1], M. URBAN[1], C. BLAKSLEY[2], F. WICEK[1], T. PATZAK[2] AND S. BIKTEMEROVA[3] ON BEHALF OF THE JEM-EUSO COLLABORATION
[1]*Laboratoire de l'Accélérateur Linéaire, Univ Paris-Sud, CNRS/IN2P3, Orsay, France*
[2]*Laboratoire Astroparticule et Cosmologie, APC, Paris, France*
[3]*Joint Institute for Nuclear Research, JINR, Russia*
monnier@lal.in2p3.fr

Abstract: A new type of absolute measurement of the nitrogen fluorescence yield in the air will be performed at LAL using 3 items which will yield an unprecedented precision in all conditions of pressure, temperature, and pollutants. A 5 MeV electron beam will be provided by the new electron accelerator PHIL at LAL. As the fluorescence yield is proportional to the energy loss of the electrons, the contribution of secondary electrons (deltas) to the signal is much more important than the contribution of the primary electrons. It has therefore been chosen to use an integrating sphere, the basic property of which being that the probability to detect light is independent from where the light is produced inside the sphere. An output device on this sphere will be equipped with a set of optical fibers driving the fluorescence light to a Jobin-Yvon spectrometer equipped with an LN_2 cooled CCD. The fluorescence spectrum in the 300-430 nm range will be accurately measured in steps of 0.1 nm resolution. A PMT equipped with a BG3 filter (the same as on JEM-EUSO) will be set on the sphere to measure the integrated yield. The sphere will be monitored by a NIST photo-diode, and will be surrounded by a spherical envelope to create a temperature controlled chamber (a Dewar). With this setup it will be possible to vary the temperature from $-60^{\circ}C$ to $+40^{\circ}C$ and the pressure from 1 to 0.01 atm. The expected precision of the yield should be better than 5%.

Keywords: Ultra high-energy cosmic rays, air fluorescence technique, JEM-EUSO collaboration

1 Introduction

A precise measurement of the energy is essential for the study of ultra-high energy cosmic rays. Basically, two types of detectors are used for this purpose:

- Surface arrays which sample the shower tail: this method records the lateral development of the shower of secondary particles using an array of particle detectors.
- Fluorescence detectors which record the longitudinal development of the shower and observe the atmospheric fluorescence induced by charged particles in the shower.

The second method is currently the most precise one to estimate the energy of cosmic rays, and is used by the Fly's Eye experiment [1], HiRes [2], Telescope Array [3], and the Pierre Auger Observatory [4]. The future JEM-EUSO telescope [5] will also detect extensive air showers from the International Space Station with this method.

Fluorescence detectors provide a measurement of primary cosmic ray energy which is relatively model independent, as the fluorescence intensity is proportional to the electromagnetic energy released by the shower into the atmosphere. For the Pierre Auger Observatory, the uncertainty in the energy using the fluorescence method is around 22%, and the main source of systematic uncertainties comes from the limited accuracy in the measurement of the air-fluorescence yield. In the Pierre Auger Observatory[4] the uncertainty in the fluorescence yield contributes 14% to the total systematic error of the energy calibration. This parameter is thus a key for determining the energy of ultra-high energy cosmic rays detected by a fluorescence telescope. We will measure the fluorescence yield using a 5 MeV electron beam and calibrated detectors in order to improve the accuracy of this value to a precision of 5%.

2 Fluorescence Yield

Air-fluorescence photons are produced by the de-excitation of atmospheric nitrogen molecules excited by the shower electrons. Excited molecules can also decay by colliding with other molecules, using the process of collisional quenching. This effect increases with pressure, reducing fluorescence intensity.

Atmospheric effects, including pressure, temperature, and composition, must also be reproduced and studied in order to understand the real conditions present during the production of fluorescence photons within an extensive air shower. As the excitation cross sections show a fast decrease with energy, secondary electrons from ionization processes are the main source of fluorescence light. For this reason, it is necessary to simulate the production of fluorescence photons in order to evaluate the fiducial volume needed for interaction. The fluorescence spectrum consists of a set of molecular bands represented by a set of discrete wavelengths λ. The range of this spectrum is the near UV between 300 to 430 nm.

The fluorescence yield for a line, Y_γ, is defined as the number of photons emitted by the primary charged particle per meter of path. The deposited energy of an electron per unit of length is defined as:

$$\rho \frac{dE}{dX} \tag{1}$$

The number of photons produced with this energy depends on the fluorescence efficiency of the line, ϕ_γ:

$$Y_\gamma(photons/e/cm) = \phi_\gamma \frac{\rho}{h\nu} \frac{dE}{dX}. \tag{2}$$

This efficiency, ϕ_γ, depends on the lifetime of the level (de-excitation) and also on the effect of pressure, temperature, and composition [11].

The total fluorescence yield Y_{tot} is thus the sum of all Y_γ:

$$Y_{tot} = \sum_\gamma Y_\gamma. \tag{3}$$

Knowing both the fluorescence yield and its dependence on atmospheric properties accurately is essential in order to obtain a reliable measurement of the energy of cosmic rays in experiments using the fluorescence method [6], [7] and [8]. Studying the total spectrum of fluorescence emission is also fundamental for JEM-EUSO in order to optimize data analysis.

3 Principle of the experiment

3.1 Experimental Set-up

The aim of this experiment is to measure the fluorescence yield of each line with a 5% accuracy using an electron beam as a source of electrons (reproducing the electrons of an extensive air shower), an integrating sphere with control of pressure, temperature, and composition in order to measure atmospheric effects, and calibrated detectors.

The electron beam will interact with gas inside an integrating sphere. A fraction of the emitted fluorescence light will be detected and measured with both a Jobin-Yvon spectrometer equipped with an LN_2 cooled CCD, in order to study each spectral line separately, and also a photo-multiplier tube equipped with a BG3 filter (the same filter as the JEM-EUSO project).

The integrating sphere must be vacuum-tight and part of a dewar to allow studying the yield at low temperatures (down to $-60°C$).The basic property of the integrating sphere being that the probability to detect light is independent from where the light is produced inside the sphere The size of the sphere depends on pressure (due to the pressure dependence of the distance of ionization of secondary electrons and multiple scattering) from a few centimeters at 1 atm to a few decimeters at very low pressure (0.01 atm). The exact size of the sphere is determined using Geant4 simulations to reproduce multiple scattering and the mean free path of secondary electrons.

The source of electrons is an electron accelerator (PHIL) developed at the Laboratoire de l'Accélérateur Linéaire (LAL) and presented in the next section.

The calibration of the detectors is fundamental in order to obtain an accurate measurement of the fluorescence yield.

3.2 PHIL: the electron Beam

The "PHoto-Injector at LAL" ([9] and [10]) is an electron beam accelerator at LAL. This accelerator, which is primarily dedicated to the testing and characterization of electron photo-guns and high-frequency structures for future accelerator projects, can also be used to simulate the electrons emitted by an extensive air shower.

PHIL is currently a 6-meter-long accelerator with 2 diagnostic beam lines. The direct beam line will be used to inject electrons into an integrating sphere. An Integrating Current Transformer (ICT) will provide the estimated beam charge, beam size, and beam position measurement with high accuracy. The main characteristics of PHIL, for our configuration, have been summed up in the table 1. For the measurement of the fluorescence yield, precise knowledge of the source (energy, position, charge...) is an important part of the total accuracy. Using the PHIL accelerator, these parameters will be available with an accuracy of $\sim 2\%$.

3.3 Detectors

For the integrated measurement, fluorescence photons will be detected and counted by a photo-multiplier tube (PMT) with the same filter as in the JEM-EUSO project. The calibration of the detector is a key parameter in this kind of experiment. The overall PMT efficiency will be measured using a NIST photo-diode, accurate to 1.5%.

Spectral measurements are interesting because the effect of temperature, pressure, and composition are not the same for each spectral line. These effects are also interesting for the future JEM-EUSO project in order to study the signal to noise ratio, which changes with the wavelength.

The fluorescence lines will be measured using a Jobin-Yvon spectrometer equipped with a LN_2 cooled CCD.

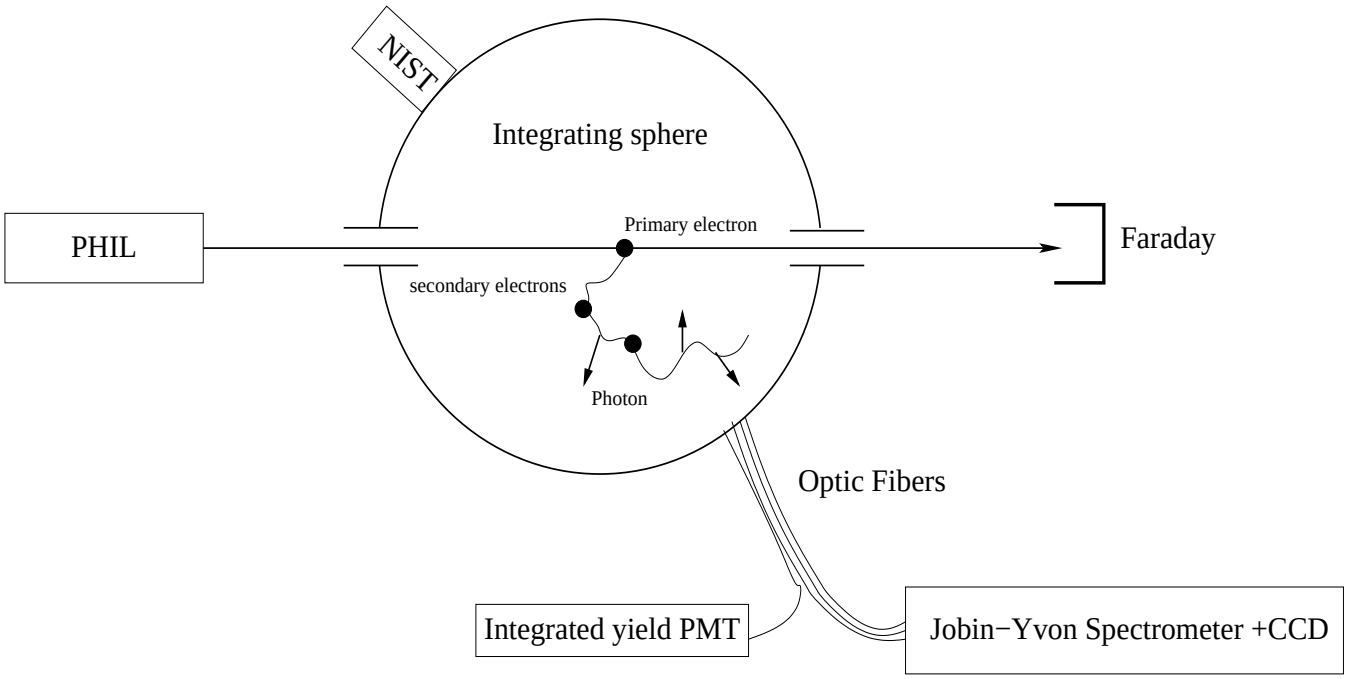


Figure 1: Design of experiment

Characteristics	Values
Charge per bunch	between 50 pC to 300 pC
Energy	3-5 MeV
Energy spread	less than 10%
Bunch length	a few ps
Beam transverse dimension	0.5 mm

Table 1: Characteristics of PHIL

The CCD will be calibrated using the calibrated photomultiplier tube at the second output of the spectrometer.

The patented method of calibration has been developed and used with success by G. Lefeuvre, P. Gorodetsky, and their collaborators, and is explained in the thesis of G. Lefeuvre (see [11] and [12]).

The expected accuracy of the detectors (PMT and CCD camera) should be around 2 %.

4 Summary

Th experiment will provide both the "integrated" measurement and "spectral" measurement of the fluorescence yield with high accuracy under a wide range of atmospheric conditions. The first step of the experiment will debug the measurement at 1atm. It will be performed during the next months and the study of atmospheric effects (temperature/pressure/composition) will be made during the year 2012.

A combined 2% accuracy for the detector and 2∼3 % accuracy for the charge of the electron beam will allow measurement of the fluorescence yield with an accuracy of up to 5%.

5 Acknowledgements

This work has been financially supported by the GDR PCHE in France, APC laboratory, and LAL. We also thank the mechanics, PHIL, and vacuum team at LAL for the construction of the fluorescence bench.

References

[1] D.J. Bird et al.,Astrophysical Journal,1994, **424**: 491-502

[2] C.Song,Z. Cao, B.R. Dawson , Astroparticle Physics, 2000, **14**: 7-13

[3] H. Tokuno, at al., Journal of Physics: conference Series, 2008, **120**: 120 062027

[4] The Pierre Auger Collaboration,Nucl. Instrum. Meth. , 2010 ,**A620**: 227-251

[5] Y. Takahashi and the JEM-EUSO Collaboration, New Journal of Physics, 2009, **11**(issue 6): pp.065009

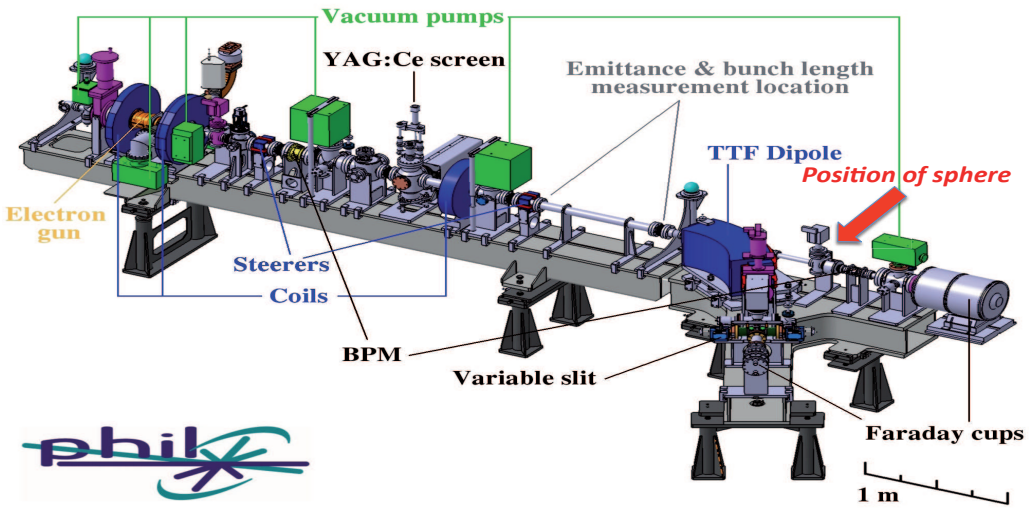
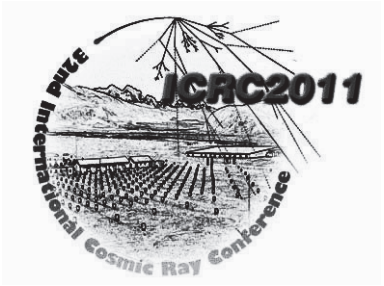


Figure 2: The PHIL accelerator: Futur position of the sphere is indicated with the red arrow

[6] J. Rosado, F. Blanco, F. Arqueros, astro-ph.IM, 2011, arXiv:1103.2022v1
[7] F. Arqueros, F. Blanco, J. Rosado, New Journal of Physics, 2009, 065011
[8] J. Rosado, F. Blanco, F. Arqueros, Astropart. Phys,2010, **34**, 164
[9] J. Brossard et al., Proceedings of Beam Instrumentation Workshop, 2010, Santa Fe, New-Mexico
[10] PHIL : http://phil.lal.in2p3.fr/
[11] Thesis of Gwenaelle Lefeuvre, University Paris7- Denis diderot, 2006, (ref. APC-26-06)
[12] G. Lefeuvre et al., Nucl. Instr. and Meth., 2007, **A578**, 78

32ND INTERNATIONAL COSMIC RAY CONFERENCE, BEIJING 2011



Fluorescence yields by electron in moist air and its application to the observation of ultra high energy cosmic rays from space

N. SAKAKI[1], A. ZINDO[1],M. NAGANO[2],K. KOBAYAKAWA[3] FOR THE JEM-EUSO COLLABORATION
[1]*Department of Physics and Mathematics, Aoyama Gakuin University, Sagamihara 252-5258, Japan*
[2]*Saitama-ken, Hasuda-shi, Higashi 5-8, 11-401, 349-0111, Japan*
[3]*Graduate School of Human Development and Environment, Kobe University, Kobe 657-8501, Japan*
sakaki@phys.aoyama.ac.jp

Abstract: In order to explore the ultra high energy cosmic rays above 10^{20} eV (UHECRs), huge detection area is crucial. In the near future, UHECRs will be observed from space in projects such as JEM-EUSO, to cover huge area, and fluorescent and Cherenkov light will be detected from extensive air showers (EASs) induced by UHECRs. Since those space-based experiments will observe most of EASs above sea, it is necessary to take the effect of humidity into account to obtain their longitudinal developments from the fluorescence yields along their trajectories. We have measured humidity dependence of life time and of fluorescence yields in air fluorescence for 10 lines between 300nm and 430nm with Sr90 source. The fluorescence yields decreased with higher humidity: for example, $\sim$20% decrease was observed for $\sim$100% relative humidity at 1000hPa. The reference pressures determined from the fluorescence yields and the life time were consistent with each other for each line. If our results are applied to the UHECR observation from space above sea, fluorescence yields will be reduced about 25% near the sea surface at low latitude in summer of US standard atmosphere 1966. Most of the observed EASs by JEM-EUSO will be inclined (the typical zenith angle is 60 deg.), so that the shower maximum will be far from the sea surface. Therefore, the decrease of the yield by humidity at shower maximum might be small but not negligible.

Keywords: Fluorescence yields, Extensive air shower, Ultra high energy cosmic ray, JEM-EUSO

1 Introduction

Ultra high energy cosmic ray enters the atmosphere and induces a cascade shower. The main component is electrons, which excite nitrogen and produces fluorescence photons in near ultra-violet region. So called air fluorescence method was proposed in 1960's to observe UHECRs. The fluorescence yields are nearly proportional to the deposited energy in the atmosphere. This method has been used by experiments such as Fly's eye[1], High resolution fly's eye (HiRes)[2], Pierre Auger Observatory (Auger)[3] and Telescope array experiment (TA)[4]. It will be also used in future experiments from space like TUS[5], JEM-EUSO[6], KLYPVE[7], S-EUSO[8]. The principle of the air fluorescence method is simple, however, it is not straightforward when we apply it to the real measurement. Because we need to understand a lot of factors, such as the fluorescence yields in various atmospheric conditions, atmospheric transmittance, systematics of the detector and so on. Above all, the knowledge of the fluorescence yields is fundamental.

We have started the measurement of the fluorescence yields in dry air and published the results[9, 10], because the experiments on ground so far have been performed in dry area like a desert. However, an observation from a satellite orbit will be main stream in the future because a huge exposure is required for the UHECR observation. Therefore, most of showers will be observed above sea and the fluorescence yield in moist air must be examined.

2 Fluorescence yields in moist air

When an electron passes through air, an excited state of N_2 or N_2^+ will be produced and then fluorescence photons will be emitted with a certain probability. The fluorescence yields (ϵ_i) for wavelength (i) per unit length by an electron is expressed as a function of pressure p:

$$\epsilon_i(p) = \rho \frac{\mathrm{d}E}{\mathrm{d}x} \left(\frac{1}{h\nu_i} \right) \cdot \varphi_i(p) \, , \qquad (1)$$

where ρ is the gas density, $h\nu_i$ is the photon energy, $\mathrm{d}E/\mathrm{d}x$ is the total energy loss of the electron. $\varphi_i(p)$ is the fraction of the energy emitted as photons to total energy loss[11]. Hereafter we omit the suffix i sometimes.

The reciprocal of the lifetime τ consists of three terms.

$$\frac{1}{\tau} = \frac{1}{\tau_r} + \frac{1}{\tau_q} + \frac{1}{\tau_c} \equiv \frac{1}{\tau_0} + \frac{1}{\tau_c} \, , \qquad (2)$$

where τ_r is the lifetime of transition with radiation from an excited state to a lower state, τ_q is that of internal quenching (internal conversion plus inter-system crossing) and τ_c is that of collision de-excitation. The reciprocal of τ_c is expressed by

$$\frac{1}{\tau_c} = p\sigma\sqrt{\frac{8}{\pi\mu k_B T}}\,, \tag{3}$$

where σ is the cross-section of collision de-excitation between molecules, k_B is the Boltzmann constant, T is temperature, and μ is the reduced mass of the two molecules. Here, the reference pressure, p', is defined as the pressure when τ_c equals to τ_0 and

$$\frac{1}{p'} = \tau_0\sigma\sqrt{\frac{8}{\pi\mu k_B T}}\,. \tag{4}$$

Let us consider the effect of water vapor. Then p' is related to τ_0 with

$$\begin{aligned}\frac{1}{p'} &= (f_{\rm n}q_{\rm nn} + f_{\rm o}q_{\rm no} + f_{\rm w}q_{\rm nw})\tau_o \\ &= \left(1-\frac{p_{\rm w}}{p}\right)\frac{1}{p'_{\rm dryair}} + \frac{p_{\rm w}}{p}\frac{1}{p'_{\rm H2O}},\end{aligned} \tag{5}$$

where f_n,f_o and f_w are proportional to partial pressures of N_2, O_2 and H_2O, respectively and normalized to $f_n + f_o + f_w = 1$. $q_{\rm nn}$, $q_{\rm no}$ and $q_{\rm nw}$ are the quenching rate constants of the collisional de-excitation between N_2^* (or N_2^{+*}) and N_2, O_2 and H_2O, respectively. $p_{\rm w}$ is water vapor pressure. $p'_{\rm dryair}$ and $p'_{\rm H2O}$ are the reference pressures for dry air and water vapor, respectively.

Then the lifetime and the fluorescence yield for each wavelength band are expressed with p' as

$$\frac{1}{\tau} = \frac{1}{\tau_o}\left(1+\frac{p}{p'}\right)\,, \quad \text{and} \tag{6}$$

$$\epsilon(p) = \frac{Cf_n p}{1+\frac{p}{p'}}\,, \tag{7}$$

where

$$C = \frac{1}{R_g T}\frac{{\rm d}E}{{\rm d}x}\left(\frac{1}{h\nu}\right)\cdot\varphi(0)\,. \tag{8}$$

$\varphi(0)$ corresponds to the fluorescence efficiency in the absence of collisional quenching[11] and R_g is the specific gas constant.

3 Experiment

A cubic chamber of 25 cm was used to keep air in various conditions[9, 10]. Decay electrons (0.85MeV on the average) from ^{90}Sr (74MBq) were collimated and the number of electrons which pass through the chamber was counted by a scintillation detector. Three 2" photomultiplier tubes (PMTs) selected for low noise were attached to three sides of the chamber to detect fluorescence photons through bandpass filters. The central wavelengths of the filters were 313, 325, 330, 337, 358, 370, 380, 391.4, 400 and 430 nm. The band widths were about 10 nm except the 391.4 nm filter with 5 nm width. The data were taken with the photon counting method. The charge of the signal from each PMT and the time difference between the electron signal and the photon signal were recorded for coincident events of an electron signal with signal from one of photon PMTs.

Air in the laboratory was taken into the chamber at various pressures between 1 hPa and 1000 hPa to determine the fluorescence yields in dry air. In order to study humidity dependence of the fluorescence yields, the total pressure was fixed at 30, 100 and 1000 hPa and the humidity was changed between 0% and 93% under the constant temperature around 20°C. In order to increase or decrease humidity, air was passed through water or silica gel. The humidity in the chamber was measured with two hygrometers, VAISALA HMP234 and Toplas TA502 which were confirmed to work also at lower pressure than 1 atmosphere by the manufacturers. Both hygrometers showed consistent humidity with each other during the measurement.

4 Results

Fluorescence yields per unit length per electron (ϵ) was derived with the following equation.

$$\epsilon = \frac{N_\gamma}{N_e l\eta f\Omega/4\pi({\rm QE})({\rm CE})}, \tag{9}$$

where N_γ is the number of detected photon signals, N_e the number of electron signals, η the transmission of the quartz window, f the transmission of the interference filter at the wavelength of the main nitrogen emission in study, Ω, QE and CE the solid angle, the quantum efficiency and the collection efficiency of the PMT, respectively, l the length of the fluorescence section. Fluorescence yields and lifetime at constant total gas pressure were measured and are shown in Figure 1 and Figure 2 respectively, as a function of water vapor pressure. Fluorescence yields and lifetime decrease with increasing water vapor pressure, because N_2 molecules are de-excited by collision with water molecules. These data are fitted by Eqs.(6) and (7), with the reference pressure in moist air expressed in Eq.(5), and then $p'_{\rm H2O}$ was determined. In this fitting process, $p'_{\rm dryair}$ was fixed to that determined from the dry air data[10]. $p'_{\rm H2O}$ derived from the yield data and the lifetime data are consistent with each other within 1-2 hPa.

Derived $p'_{\rm H2O}$ at $p = 30$ hPa for 10 lines are summarized in Figure 3. $p'_{\rm H2O}$ for 1N lines (391nm and 428nm) are about 0.4∼0.8 and are smaller than those for 2P lines, which are around 2-3 hPa. $p'_{\rm H2O}$ for 337nm and 358nm at total pressure 100 hPa and 1000 hPa were also determined. $p'_{\rm H2O}$ determined from the yield data at 30 hPa, 100 hPa and 1000 hPa are 1.36 hPa, 1.70 hPa and 1.66 hPa for 337 nm, and 1.23 hPa, 1.61 hPa and 1.27 hPa for 358 nm, respectively. Each error is 0.1-0.2 hPa. No significant pressure dependence of $p'_{\rm H2O}$ is observed. Our results are compared with those of AIRFLY[12], AIRLIGHT[13], Morozov *et al.* [14] and Pancheshnyi *et al.* [15, 16] in the same figure.

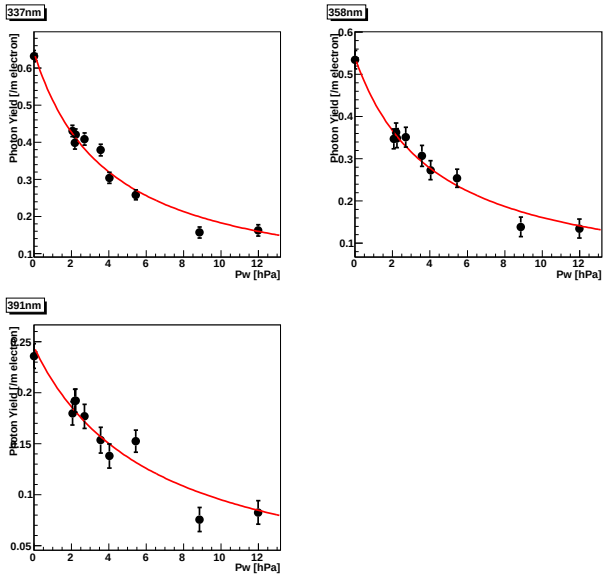


Figure 1: Fluorescence yields of 337nm, 358nm and 391nm lines as a function of water vapor pressure ($p_{\rm w}$) at p =30 hPa. Solid lines show the best fit curves by Eq. (7).

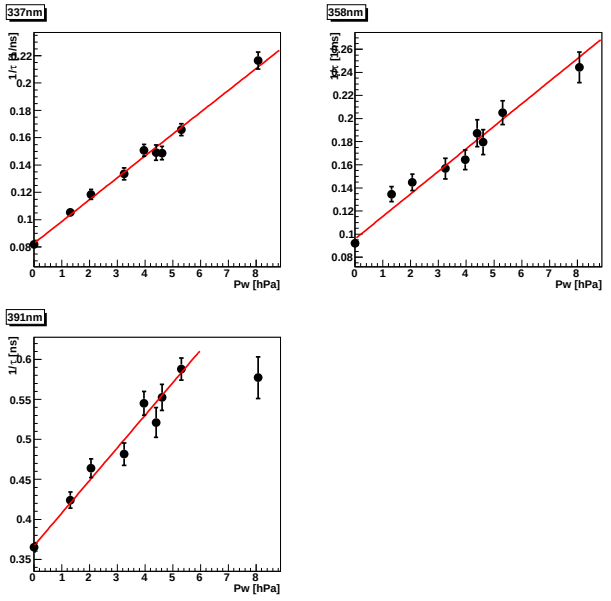


Figure 2: Reciprocal lifetime of 337nm, 358nm and 391nm lines as a function of water vapor pressure ($p_{\rm w}$)at p =30 hPa. Solid lines show the best fit curves by Eq. (6).

They are consistent one another, although the errors of our results are relatively large for some lines.

5 Application to UHECR fluorescence observation from space

US standard atmosphere 1976 model[17] (USstd76) has been used frequently in the field of UHECR observation. However there is only dry atmosphere model in the

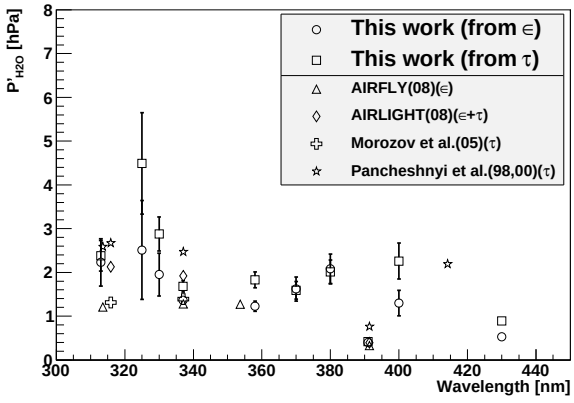


Figure 3: $p'_{\rm H2O}$ for 13 nitrogen lines. Our results are shown by circles (determined from the yield) and squares (from the lifetime). They are compared with those by AIRFLY[12] (triangles), AIRLIGHT[13](diamonds), Morozov *et al.* [14](crosses) and Pancheshnyi *et al.* [15, 16](stars).

USstd76. Therefore, we have used US standard atmosphere 1966 (USstd66) to see the humidity effect on fluorescence measurement from cosmic rays. Figure 4 shows water vapor pressure profile as a function of altitude. In winter at high latitude, water vapor pressure is relatively small, however, it increases up to 30 hPa, which corresponds to 80% relative humidity, in summer at low latitude.

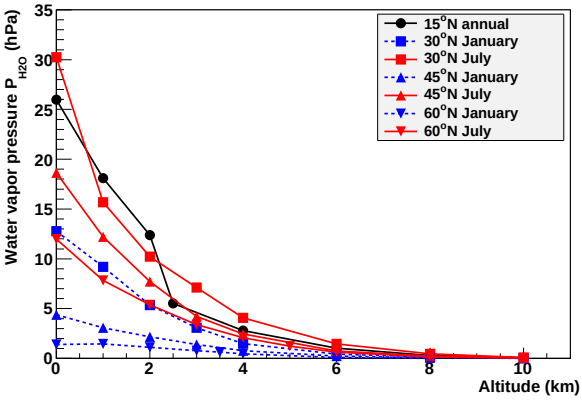


Figure 4: Water vapor pressure as a function of altitude from US standard atmosphere 1966 model. The data at 15°N are shown by solid circles, those at 30°N by solid squares, those at 45°N by solid triangles and those at 60°N by solid inverted triangles. January data are connected by dashed lines and July data are connected by solid lines.

Using not only the humidity data but also the temperature and pressure data of the USstd66 model, we have calculated expected total fluorescence yields between 300 and 430 nm as a function of altitude for winter and summer at four latitudes (15°N, 30°N, 45°N and 60°N). The flu-

orescence yields at each altitude was calculated with the following equation:

$$\epsilon = \left(\frac{\mathrm{d}E}{\mathrm{d}x}\right)_{0.85\mathrm{MeV}} \sum \frac{\varphi(0)\rho}{h\nu(1+\rho R_g\sqrt{293T}/p'_{20})}, \quad (10)$$

where p'_{20} is the reference pressure at 20°C, and p' is defined by Eq.(5). Mean p'_{H2O} from the yield data and from the lifetime was used for each line. The yield for USstd76 model (dry air) is normalized to one. The decrease of the yield in summer at low latitude is about 25% at sea level (see Figure 5). In order to see the influence of the humidity in USstd66 model, the ratio for dry air is shown in the same figure for the 30N° July profile (labeled with "(humidity=0)" in Figure 5). The yield agrees well with that of USstd76 within a few %. Therefore the decrease in yield for 30N° July is understood to be caused by humidity, not by the difference in temperature or pressure profile of both models.

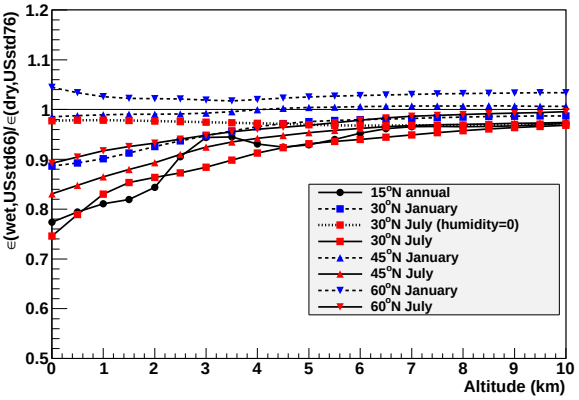


Figure 5: Ratio of total fluorescence yield between 300nm and 406nm in moist air from US standard atmosphere 1966 to that of US standard atmosphere 1976 (dry air) as a function of altitude. Same markers are used as in Figure 4.

For JEM-EUSO observation, median zenith angle of observed events will be around 60 degree. EAS with 10^{20} eV and $\theta = 60°$ is expected to reach its maximum development around 6 km high. The decrease due to humidity in summer is 10% or less there. For vertical showers, the maximum is lower, around 2-3 km high. The influence of humidity is larger, ∼15%. Showers produced by neutrinos are expected to develop horizontally near sea level and hence will be darker by 10% in winter and 25% in summer at low latitude.

6 Conclusion

In the future the UHECR observation from a satellite orbit is indispensable to obtain huge acceptance. Since most of EASs will be observed above sea, the influence of water vapor on the fluorescence yields must be investigated. We have measured the quenching of nitrogen fluorescence by water vapor for ten lines and applied the result to the various atmospheric conditions from US standard 1966 model. Fluorescence from the typical EAS observed by JEM-EUSO (zenith angle=60°) will be decreased by several percent at shower maximum in summer at low latitude. For horizontal showers near sea surface, as are induced by neutrinos, the decrease will be larger up to 25%. We have shown here only the decrease of the fluorescence yields by humidity at emission point. Since the attenuation in atmosphere is relatively small for space-based observations, the photon yield in moist air would be applicable with little modification.

The decrease in the fluorescence yields by humidity is not negligible especially in summer at low latitude. It is necessary to take into account the characteristics of the detector in each project to estimate how much the humidity influences on the observation actually.

References

[1] D.J. Bird *et al.* , Astrophys. J., 1994, **424**: 491–502.
[2] J.H. Boyer *et al.* , Nucl. Instr. Meth., 2002, **A482**: 457–474.
[3] J. Abraham *et al.* , Nucl. Instr. Meth., 2004, **523**: 50–95.
[4] J.N. Matthews *et al.* , Proc. 31st Intn'l Cosmic Ray Conf. (Łódź), 2009: #1386.
[5] V. Abrashkin *et al.* , Advances in Space Res., 2008, **41**: 2079–2088.
[6] Y. Takahashi *et al.* , New J. of Phys., 2009, **11**: 065009.
[7] B.A. Khrenov *et al.* , Phys. Atomic Nuclei, 2004, **67**: 2058.; L. Tkatchev *et al.* , Proc. 30th Intn'l Cosmic Ray Conf. (Merida), 2008, **5**: 873–876.
[8] A. Santangelo for the S-EUSO collaboration, Proposal for Super-"Extreme Universe Space Observatory", 2007.
[9] M. Nagano, K. Kobayakawa, N. Sakaki and K. Ando, Astropart. Phys., 2003, **20**: 293–309.
[10] M. Nagano, K. Kobayakawa, N. Sakaki and K. Ando, Astropart. Phys., 2004, **22**: 235–248.
[11] N. Sakaki *et al.* , Proc. 29th Intn'l Cosmic Ray Conf. (Pune), 2005, **7**: 85–88.
[12] M. Ave *et al.* , Nucl. Instr. Meth., 2008, **A597**: 50–54.
[13] T. Waldenmaier *et al.* , Nucl. Instr. Meth., 2008, **A597**: 67–74.
[14] A. Morozov *et al.* , Euro. Phys. J., 2005, **33**: 207–211.
[15] S.V. Pancheshnyi *et al.* , Chem. Phys., 1998, **294**: 523–527.
[16] S.V. Pancheshnyi *et al.* , Chem. Phys., 200, **262**: 349–357.
[17] "U.S. Standard Atmosphere 1976", U.S. Government Printing Office, Washington D.C., 1976.
[18] COESA, "US Standard Atmosphere 1966", U.S. Govern. Printing Office, Washington D.C., 1966.